Institut für Angewandte Photophysik
Fachrichtung Physik
Fakultät Mathematik und Naturwissenschaften
Technische Universität Dresden

Organic light-emitting diodes with doped charge transport layers

Dissertation
zur Erlangung des
Doktorgrades der Naturwissenschaften
(Doctor rerum naturalium)

vorgelegt von
Jan Blochwitz
geboren am 04.12.1970 in Meißen

Dresden 2001

Eingereicht am 18. Mai 2001

1. Gutachter: Prof. Dr. Karl Leo
2. Gutachter: Prof. Dr. Hans-Joachim Queisser
3. Gutachter: Prof. Dr. Dieter Neher

Verteidigt am 12. Juli 2001

Contents

Introduction 7

1 Basics, History & Motivation 9
1.1 Insight into an organic LED 9
1.1.1 The ideal situation in an inorganic LED 9
1.1.2 Layer structure of small organic molecule LEDs 10
1.1.3 Energetic situation in an OLED and physical processes 12
1.1.4 A comparison of the optoelectronic data of organic and inorganic LEDs 14
1.2 The development of organic light-emitting diodes in the past decade . . . 17
1.3 Present and future commercialization of OLEDs 19
1.4 Differences between polymer LEDs and small organic molecule LEDs . . . 20
1.5 The history of doping organic layers 22

2 Doping of organic layers: principles and effects 25
2.1 Doping basics 25
2.2 FTIR measurements and charge transfer 26
2.3 Model system: phthalocyanines doped with F_4-TCNQ 27

3 Experiment & materials 31
3.1 Organic materials used in this study 31
3.1.1 Materials and their properties 31
3.1.2 Purification of the materials 35
3.2 Determination of device efficiencies 35
3.3 Preparation of OLEDs in a single chamber HV-system, sample geometry . 38
3.4 Preparation of OLEDs in a multiple chamber ultra high vacuum system . 39
3.4.1 Motivation for the cluster tool 39
3.4.2 Setup of the cluster tool 40
3.4.3 Preparation of OLEDs in the cluster tool 40
3.5 Experimental aspects of the UPS/XPS-experiments 44
3.5.1 Analyzing system: Kratos 44
3.5.2 Substrates and their preparation 45
3.5.3 Preparation of mixed layers in the preparation chamber 45

4 UPS/XPS-experiments 47
4.1 Determination of the interface energy alignment by UPS/XPS-experiments 47
4.1.1 Basics 47
4.1.2 Evaluation of the spectra 54
4.2 Experimental results of the UPS/XPS-experiments 56
4.2.1 Doped and undoped ZnPc on ITO 56

4.2.2 Doped and undoped ZnPc on Au 61
4.2.3 Investigation of organic heterojunctions with doped layers 66
4.2.3.1 F_4-TCNQ on Au and ZnPc: HOMO determination . . . 66
4.2.3.2 Undoped and doped ZnPc on Alq_3 : energetic alignment . 68
4.2.3.3 Alq_3 on undoped and doped ZnPc: energetic alignment . 74
4.3 Conclusions from the UPS/XPS-experiments 76

5 OLEDs: Results and Discussion 79
5.1 OLEDs with F_4-TCNQ doped VOPc as hole transport layer prepared in the HV 79
5.1.1 Influence of the doping concentration 79
5.1.2 Improvement of quantum efficiency by introducing an electron blocking layer 85
5.2 Wide gap transport materials & electron injection layers: efficiency improvement 88
5.2.1 Screening of the doping efficiency of wide gap materials 88
5.2.2 Two layer OLEDs with doped wide gap HTLs 90
5.2.3 OLEDs with a doped wide gap HTL and an additional TPD blocking layer 94
5.3 The concept of the combination of transport layer doping and blocking layers 96
5.4 Preparation of OLEDs in a coupled UHV system 98
5.4.1 A comparison of OLEDs made in HV and in UHV 98
5.4.2 OLEDs with emitter layer doping 100
5.4.3 OLEDs with n-type doped electron transport layers 104
5.5 A lifetime test 108
5.6 A summary of the OLED experiments as a pathway to highly efficient OLEDs 110

6 Conclusions 113
6.1 Summary 113
6.2 Outlook 114

Appendix A Physical processes involved in OLED operation 115

Appendix B Simple approximations: j-V curves 127

Bibliography 131

List of Abbreviations 143

Acknowledgments 145

Parts of this work have been published in the following articles:

a) Articles

1. J. Blochwitz, M. Pfeiffer, T. Fritz, K. Leo. Low voltage organic light emitting diodes featuring doped phthalocyanine as hole transport material. *Appl. Phys. Lett.*, **73** (6) (1998) 729.

2. M. Pfeiffer, T. Fritz, J. Blochwitz, A. Nollau, B. Plönnigs, A. Beyer, K. Leo. Controlled Doping of Molecular Organic Layers: Physics and Device Prospects. *Advances in Solid State Physics*, **39** (1999) 77.

3. X. Zhou, M. Pfeiffer, J. Blochwitz, A. Werner, A. Nollau, T. Fritz, K. Leo. Very low operating voltage organic light-emitting diodes using a p-doped amorphous hole injection layer. *Appl. Phys. Lett.*, **78** (4) (2001) 410.

4. X. Zhou, J. Blochwitz, M. Pfeiffer, A. Nollau, T. Fritz, K. Leo. Enhanced hole injection into amorphous hole transport layers of organic light-emitting diodes using controlled p-type doping. *Adv. Funct. Mater.*, (in press) (2001).

5. J. Blochwitz, T. Fritz, M. Pfeiffer, K. Leo, D.M. Alloway, P.A. Lee, N.R. Amstrong. Interface electronic structures of controlled doped organic semiconductors. *Organic Electronics*, (accepted) (2001).

6. A. Werner, J. Blochwitz, M. Pfeiffer, K. Leo. Field dependence of thermally stimulated currents in Alq_3. *J. Appl. Phys.*, (accepted) (2001).

b) Patents

1. M. Pfeiffer, K. Leo, J. Blochwitz, X. Zhou. Lichtemittierendes Bauelement mit organischen Schichten. *Patent Application DE 100 58 578.7*, (2000).

Introduction and organization of the work

Organic dyes with a conjugated π-electron system usually exhibit semiconducting behavior. Hence, they are potential materials for electronic and optoelectronic devices. In particular since Tang et al. demonstrated highly efficient organic light-emitting diodes (OLEDs) in 1987 [1], organic semiconductors have received large attention because of the vision of large area and flat display-applications. Nowadays, such applications are already commercial on small scales (see Chapter 1.3).

Controlled doping of inorganic semiconductors was the key step for today's inorganic semiconductor technology. The control of the conduction type and Fermi-level is crucial for the realization of stable pn-junctions, the basic building block of all optoelectronic devices. This allows for optimized light emitting diode structures with operating voltages close to the optical limit (around 2.5V for a green emitting LED, Section 1.1.1). Despite that, organic light emitting diodes generally consist of a series of intrinsic layers based on organic molecules. All layers have different purposes which are shortly summarized in Section 1.1.2. All intrinsic organic charge transport layers suffer from non-ideal injection and noticeable ohmic losses. This leads to some basic differences in the charge carrier and potential distribution inside an OLED, compared to inorganic LEDs (Section 1.1.3). However, organic materials feature some technological advantages for device applications like low cost, an almost unlimited variety of materials, and possible preparation on large and flexible substrates. They also differ in some basic physical parameters, like the index of refraction in the visible wavelength region, the absorption coefficient and the Stokes-shift of the emission wavelength. An overview about the resulting differences between inorganic and organic light emitting diode applications is given in Section 1.1.4, whereas a more detailed view on the physical processes inside an OLED is given in Appendix A. Chapter 1.2 summarizes the key steps of the OLED improvement over the past decade. The OLED research is split in two fields: the OLEDs based on vacuum sublimed small molecule layers and the field of polymer LEDs (PLEDs) based on spin coated polymers. We restrict our discussion to the improvement of non-polymeric OLEDs. Differences between the two organic technologies are explained in Chapter 1.4. Despite the key importance of doping for the realization of optoelectronic devices based on inorganic semiconductors, electronically doping of organic semiconductors has only been scarcely addressed[1]. The reader may find a possible explanation for this and a short overview about doping of organic materials in Chapter 1.5. Our aim is the lowering of the operating voltages of OLEDs by the use of doped organic charge transport layers.

The present work is focused mainly on the p-type doping of weakly donor-type molecules with strong acceptor molecules by co-evaporation of the two types of molecules in a vacuum system. Chapter 2 introduces the idea of doping organic layers. The electrical properties of the model system of a phthalocyanine matrix doped with the strong accep-

[1]Sometimes, organic layers mixed with emitter molecules are named 'doped layers'. Therefore, the p- or n-type doping of organic charge transport layers is referred to as 'electronically doping' or 'doping' in this work. In contrast, doping with emitter molecules will be named 'emitter doping'.

tor molecule tetrafluoro-tetracyano-quinodimethane (F_4-TCNQ) are presented. Section 3.1 introduces the materials involved in this study and two important purification methods. Section 3.2 gives an overview about the definition of efficiencies relevant for OLED applications and their measurement. Sections 3.3 and 3.4 summarize the preparation techniques of the light emitting devices in a single chamber high vacuum (HV) and in a multiple chamber ultra-high vacuum (UHV) system, respectively, whereas the experimental setup of the UPS/XPS-experiments is described in Section 3.5.

In order to understand the improved hole injection from a contact material into a p-type doped organic layer, ultraviolet photoelectron spectroscopy combined with X-ray photoelectron spectroscopy (UPS/XPS) was carried out (Chapter 4). The principles of the determination of the energetic level alignment from UPS/XPS-data are introduced in Section 4.1. The experimental results of the UPS/XPS measurements on doped zinc-phthalocyanine (ZnPc) and their interpretation follows in Section 4.2. Measurements were done on the typical transparent anode material for OLEDs, indium-tin-oxide (ITO) (4.2.1) and on gold (4.2.2). The effect of doping on internal interfaces of OLEDs is discussed in Section 4.2.3.

Chapter 5 is dedicated to OLEDs containing doped transport layers. Their performance improves successively from a simple two-layer design with doped phthalocyanine as hole transport layer (Section 5.1.1) over a three-layer design with an electron blocking layer (Section 5.1.2) until OLEDs with doped amorphous wide gap materials, with and without additional electron injection enhancement and electron blocking layers (Chapter 5.2). Based on the experience with the first OLEDs featuring doped hole transport layers, an ideal device concept which is based on realistic material parameters is proposed in Section 5.3. The effect of the preparation of OLEDs in a more sophisticated multiple chamber UHV system on device efficiency and stability is addressed in Section 5.4.1. Very high efficient OLEDs with still low operating voltage have been prepared by using an additional emitter dopant molecule with very high photoluminescence quantum yield in the recombination zone of a conventional OLED (Section 5.4.2). Finally, the question of a further decrease of the operating voltage by n-type doping of the electron transport layer is investigated in Section 5.4.3. A lifetime test in Section 5.5 shows that doping does not decrease the lifetime of an OLED. All OLED results are summarized in Section 5.6. They give a pathway to very low voltage *and* high efficiency organic light-emitting diodes.

Figure 1: *An organic LED showing the logo of the Technical University of Dresden.*

1 Basics, History & Motivation

First, this Chapter introduces the ideal energetic situation in a doped inorganic semiconductor LED as a motivation for the doping of organic LEDs. The layer structure of common OLEDs and the theoretical basis for the description of the charge transport, exciton recombination and decay phenomena in disordered organic systems is briefly outlined. Basic differences to inorganic LEDs are pointed out. The applicability of organic materials is addressed. A summary of the historical development of LEDs based on organic semiconducting materials is given. Many improvements were achieved by intensive worldwide research on new structural and chemical ideas up to the recent first commercial applications of OLEDs in flat organic displays. A comparison between polymeric LEDs and small organic molecule LEDs is given. Previous works on doping organic molecular layers are shortly reviewed.

1.1 Insight into an organic LED

1.1.1 The ideal situation in an inorganic LED

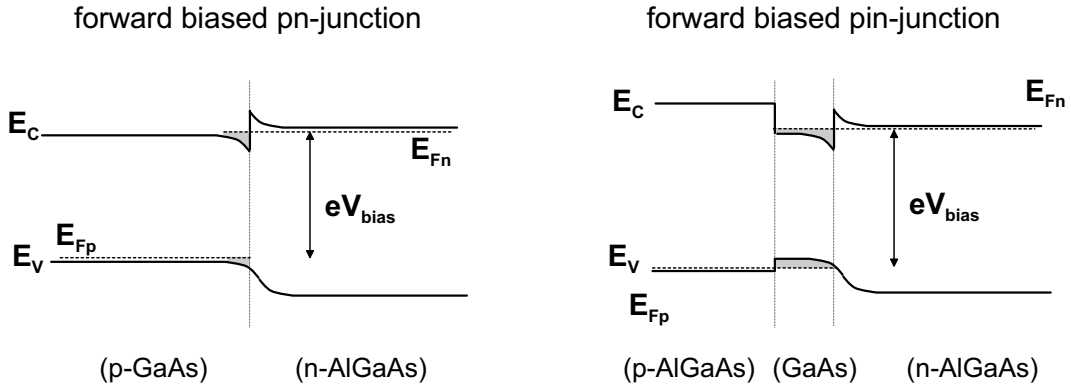

Figure 1.1: *Energy band diagrams under high forward bias (flat band behavior) for two possible inorganic LED setups: (left) pn-heterojunction with heavily doped transport layers. At their interface, a high concentration of holes and electrons builds up with electron injection into p-GaAs from n-AlGaAs. (right) A p+pn or pin double heterojunction. Here, the outer layers are heavily doped, whereas the inner layer with the smallest band gap is weakly doped. Electrons and holes are confined inside the low band gap region which emits light. This design is preferentially used for inorganic laser diodes because it allows additional optical confinement due to refractive index changes at the interfaces.*

Figure 1.1 shows the ideal energetic situation which is realized in inorganic LEDs. Especially in the case of a double heterojunction (right side), the carriers are easily injected

from the contacts (not shown) into heavily doped transport layers and then into an active layer with a smaller band gap, which allows effective carrier confinement. Due to the high conductivity in the outer heavily doped regions, the operating voltage is close to the energy of the emitted light divided by the electronic charge (around 2.5V for green light emission). At that point, the LED shows flat band behavior and a very steep current-voltage curve.

In contrast, undoped organic materials have their Fermi-energy deep inside the HOMO-LUMO gap. They show low conductivities and inefficient charge injection from electrodes into the organic materials. Therefore, several organic layers with distinct properties have to be used. Additionally, the layers have to be extremely thin (typically below 100nm) in order to minimize voltage drops inside the device which would increase the operating voltage of the device. Furthermore, for organic solids the optical emission originates from excitonic states in contrast to inorganic semiconductors, where direct transition between valence and conduction states is the dominant process. The excitonic gap is in general smaller than the transport gap. As a consequence of all these effects, the operating voltage of OLEDs is generally higher. The current-voltage curves are less steep due to space charge limited currents inside the organic layers.

1.1.2 Layer structure of small organic molecule LEDs

In principle, an organic light emitting diode consists of a sequence of organic layers between two electrodes, an anode for hole and a cathode for electron injection, respectively. Schematically, the basic layers are assigned to the following functions (see Figure 1.2):

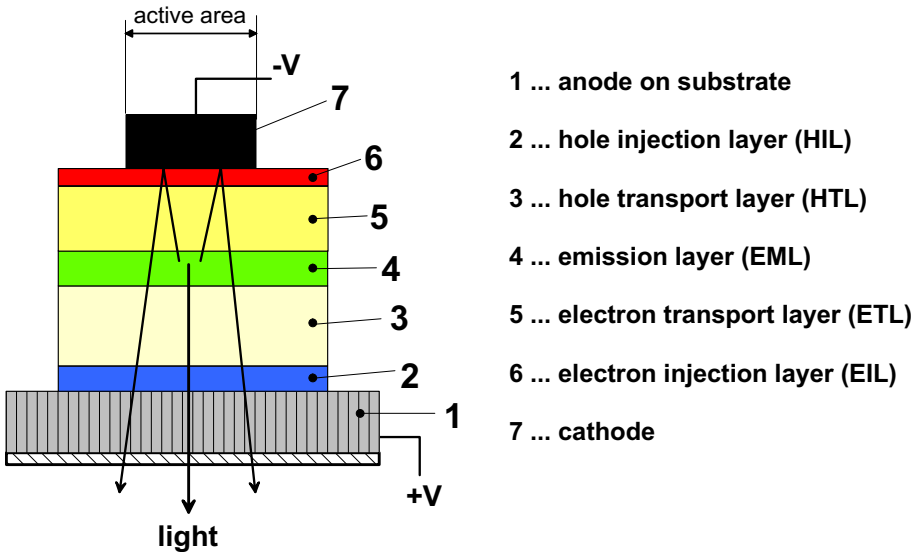

Figure 1.2: *Principle layer sequence of an OLED and the purpose of the layers.*

Under positive bias, holes are injected from the anode and electrons from the cathode. The charge carriers drift through the transport layers and meet in the emission layer. There, they form excitons (neutral excited states or bound electron-hole pairs) which show a certain probability to decay radiatively.

In order to achieve a high efficiency (emitted photons per injected electrons), the layers have to fulfill certain requirements. The hole injection layer (2=HIL) has to ease hole injection from the anode into the hole transport layer (3=HTL). This might be achieved by choosing the energetic level of the highest occupied molecular orbital (HOMO) to be in between the HOMO of the HTL and the ionization potential of the anode. For the simple picture given in Figure 1.3, the HOMO and LUMO levels are treated similar to valence and conduction bands in inorganic semiconductors and the vacuum level is assumed to be aligned. The reader should keep in mind that this is a very rough approximation (see Chapter 4). The hole transport layer should have a high hole mobility and must hinder electrons coming from the cathode from reaching the anode (this would result in a 'shunt' current). Additionally, the transmission of all organic layers have to be high in the emission wavelength region. The HOMO and LUMO (lowest unoccupied molecular level) positions of the emission layer (EML) have to make hole and electron injection from the neighboring layers possible. Additionally, the photoluminescence efficiency (ratio of radiatively recombining excitons to created excitons) of the emissive material should be high and the emission should be red-shifted to the absorption (Stokes-shift). The properties of the electron transport (ETL) and electron injection (EIL) layers should be complementary to those of the HIL and HTL (i.e suitable LUMO levels, high electron mobility). The anode should have a high ionization potential to inject holes into the HOMO of the HIL. Accordingly, the cathode should be a low work-function metal like magnesium or calcium. Finally, at least one electrode must be transparent for visible light in order to achieve a high light outcoupling efficiency. For that reason, in most cases, indium-tin-oxide (ITO) is used as transparent anode.

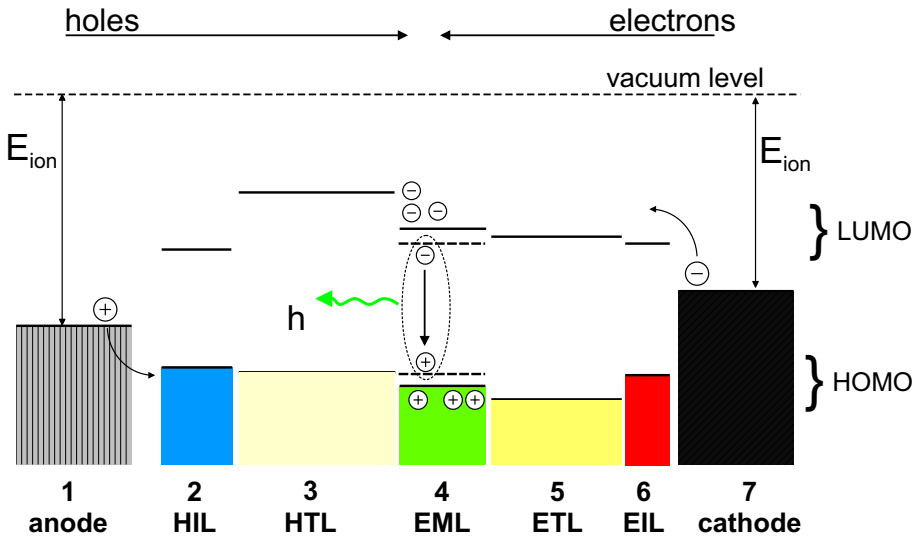

Figure 1.3: *Schematic view on a favorable energetic situation in an OLED.*

Almost all realized OLEDs consists of less layers than proposed in Figure 1.2. This is due to the fact that some organic materials combine several of the properties mentioned above in one layer. E.g., in the Tang-device from 1987 (layer sequence: ITO-anode/TPD/Alq_3/Mg:Ag-cathode [1]) TPD serves for hole injection, hole transport and electron blocking, whereas Alq_3 features reasonable electron transport, electron injection

and light emission capabilities. The exciton recombination and light emission zone is inside Alq_3 near the interface to TPD. This is known from the fact that the electroluminescence spectrum of this device equals the photoluminescence spectrum of Alq_3. In the most simple case, as done for polymers a long time, only one layer has to fulfill all necessary tasks. This can only lead to high quantum efficiencies if this single layer is able to inject and transport holes as good as electrons (for most organic materials, however, hole mobility is higher than electron mobility). Otherwise the emission zone would be near to one electrode and excitons would be quenched (decay non-radiatively).

1.1.3 Energetic situation in an OLED and physical processes

A key difference between the (nominally undoped) organic and the common inorganic light-emitting diodes is the way charge carriers are injected and transported. In the latter case, charge carriers originate from the dopants of a pn-junction (donors in the n-type and acceptors in the p-type region), while in the former case carriers need to be injected from the electrodes. Additionally, the mobility of charge carriers in organic layers is low, due to the relatively weak intermolecular van-der-Waals forces and hence small orbital overlap between neighboring molecules. As a result, the potential and charge profiles in the devices are quite different. The carrier concentration is nearly a constant in the neutral regions outside the depleted region of an inorganic pn-junction. In contrast, in organic devices, carriers are concentrated near the electrodes and their concentration drops rapidly away from this interface (space charge limited behavior).

Figure 1.4 shows a schematic comparison of the net charge and potential distribution in the case of (a) an insulator, (b) an inorganic pn-homojunction and (c) a typical organic double layer LED. No charge carriers are injected into the insulator. The (low) net charge density is due to polarized dipoles. The external field is more or less evenly distributed over the sample. For an inorganic pn-junction, charges are injected very easily through a quasi ohmic Schottky-contact between a metal and the heavily doped semiconductor. Net charges are formed in the depletion region at the pn-junction (see also Figure 1.1). Almost no voltage drop is observed outside the depletion region. Carrier recombination, and hence electroluminescence, takes place near the depletion region under forward bias [3].

In contrast, charges are injected and space charge regions are formed in an OLED. The net charge density drops away from the contacts. In a double-layer device with properly chosen material combinations, like it is shown in Figure 1.4, injected charges will be blocked at the internal interface. Thus, the recombination takes place near that interface [4]. For common organic diodes, a substantial voltage drop outside the emission zone is present. This reduces the slope of the current-voltage curves and lowers power efficiencies at higher operating voltages.

By intentionally doping the organic charge transport layers, in analogy to inorganic pn-junction-diodes, the disadvantage of usual OLEDs should be overcome. The present work is focused on that topic.

The optoelectronic behavior of an organic light emitting diode is determined by a complicated interplay between several effects:
(i) The injection of charge carriers from the anode and the cathode into the neighbored organic layers,

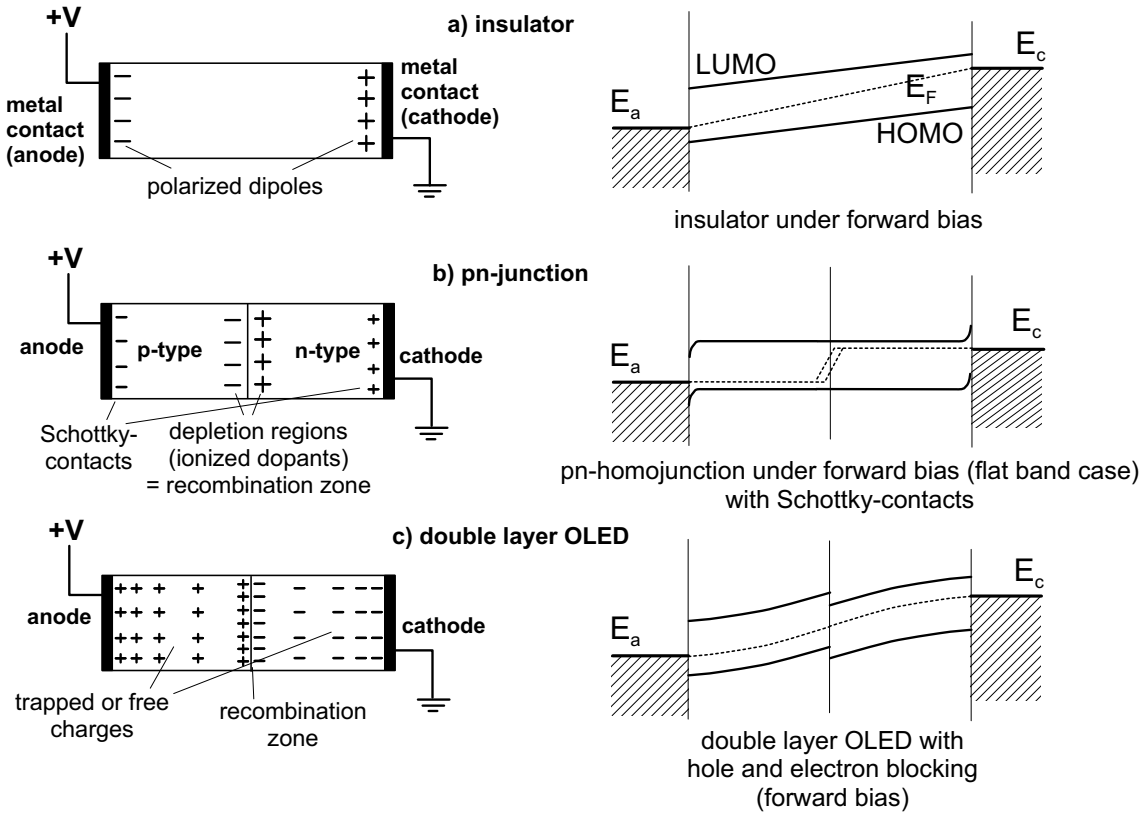

Figure 1.4: *Illustration of the net charge distribution (left) and energy level alignment under forward bias (right) differences between an inorganic pn-junction device (b) and a typical organic double layer device (c). For comparison, the case of an ideal insulator (a) is shown as well. [2, 3, 4]*

(ii) the redistribution of the electric field inside the organic layers (in a way to reduce the charge injection at the electrodes) on applying a bias voltage,
(iii) the build-up of space charges at internal interfaces,
(iv) the field and temperature dependent mobilities of the charge carriers,
(v) the field assisted internal barrier crossing of charge carriers,
(vi) the creation of excitons at internal interfaces,
(vii) the creation of excitons in the bulk, and
(viii) the radiatively or non-radiatively decay of excitons.
Since organic materials exhibit electronic traps due to structural disorder or impurities, charging and discharging of the traps also play an important role in device operation. Furthermore, the energy transfer from host to guest molecules in mixed layers, which are often used in order to enhance the radiative decay of excitons, may influence the overall electronic behavior of an OLED. The aim of an OLED parameter optimization is to lower the operating voltage and, simultaneously, to increase the device efficiency.

In Appendix A, a more detailed discussion of the physical processes involved and their currently favored theoretical description is briefly reviewed.

Due to the variety of effects and material parameters, it is generally not possible to deduce an analytical model of the operation of a complex OLED-structure which would

be able to predict the temperature and voltage dependence of the current and the electroluminescence yield. This makes it difficult to evaluate the measured current-voltage behavior of such devices. The only possible way to gain a predictive insight into a complex OLED structure is to set up a numerical model based on some properly determined material parameters, like the mobility for charge carriers in the involved organic layer, trap densities and distributions, and the energetic alignment at the internal interfaces. Such a numerical model (see e.g. [4, 5, 6, 7, 8, 9, 10, 11]) was not the focus of this work. However, the literature status of this topic is reviewed in Appendix A.

An analytical description of the current-voltage and emission-voltage behavior of an OLED is only possible if the OLED has a very limited number of internal interfaces and a predominantly unipolar charge transport. Appendix B gives an overview of the current-voltage curves that can be expected in the case of a single layer device where predominantly one type of charge carriers is injected and transported.

1.1.4 A comparison of the optoelectronic data of organic and inorganic LEDs

Table 1.1 gives a comparison of relevant data for the operation of a typical inorganic LED (nitride technology: InGaN as active medium) and a typical organic light-emitting diode (Alq_3 doped with quinacridone as emitter, see Chapter 5.4.2). Note that inorganic LEDs can be regarded as point sources of light, whereas organic LEDs are typical areal emitters. Therefore, the light emission of organic LEDs is mostly measured as luminance (in cd/m^2) and for inorganic LEDs as luminous intensity (in candela) or total luminous flux (in lumens). This difference motivates the forecast that organic LEDs will not replace inorganic ones, but will find completely new applications (for examples see Section 1.3).

From Table 1.1, one might get the feeling that inorganic LEDs perform better than

Table 1.1: *Comparison of a typical inorganic LED and an OLED (described in Chapter 5.4.2). See text for detailed discussion*

LED:	inorganic = point emitter	organic = areal emitter
emitting material (color)	InGaN (green)	Alq_3:QAD (green)
operating voltage (V)	3.6	3.4 (for 100cd/m^2)
power efficiency (lm/W)	14-20	10 (at 100cd/m^2)
external quantum efficiency (photons/electron in %)	4-6	2-3 (at 100cd/m^2)
diode area	approx. 0.1 mm^2	100μm^2 .. $>$ 0.1m^2 (in principle), typically: 2mm^2
luminance (cd/m^2)	20x10^6	100 .. $>$ 10^5 (at higher voltages, low power efficiency)
current density (mA/cm^2)	2x10^4	0.9 (for 100cd/m^2)
lumen output (single LED)	approx. 1 Lm	0.6 mLm (2mm^2, 100cd/m^2)

organic ones in almost every point. But here, the possibility to integrate the LEDs in large arrays at reasonable costs is not addressed. For a typical monitor-screen one would need 1280x1024 pixels on an area of approx. 15-20inch. It is not possible to integrate highly efficient inorganic LEDs on such large dimensions, but taking an array of single inorganic LEDs would be much to costly. Nevertheless, because of their outstanding brightness, arrays of single inorganic LEDs are currently used for very large area (>10m^2) displays in a daylight environment. Additionally, inorganic LEDs are suitable for devices where high quality optical systems are essential (e.g. projection systems [12]).

In contrast, organic LEDs are the superior choice for large and flat direct view display applications in room-light environment, such as laptop monitors or television screens. Their power efficiency and operating voltage are in the range of the best inorganic LEDs, but the preparation processes are much more cost-effective. Inorganic LEDs need perfectly ordered layers (e.g. single crystalline) on small highly reflecting substrates to achieve a very high performance in terms of efficiency. Despite that, organic materials used in OLEDs are simply sublimed in vacuum onto low temperature and large area substrates and can be relatively easily patterned [13, 14, 15]. The technology is compatible to existing CMOS (complementary metal-oxide semiconductor) driver technology [16].

The reason for the high cost-factor of inorganic LEDs is the index of refraction n of the materials involved. For typical inorganic LEDs (given here for GaN and InN, green wavelength region) n is in the range of 2.5 up to 3.2, Si shows values in excess of 4 [17]. In contrast to that, the prototypical emitter-material of organic LEDs, Alq_3, has an index of refraction of 1.72 [18]. The most simple classical ray optics approximation for the outcoupling efficiency η_o of an LED considering the losses by total internal reflection (assuming outcoupling into air, no absorption and scattering, no reflection at the opposite contact, no Fresnel-losses) yields:

$$\eta_o = \frac{1}{2}\left(1 - \frac{\sqrt{n^2-1}}{n}\right) \approx \frac{1}{4n^2}\,. \tag{1.1}$$

This simple approximation gives 2.1% outcoupling efficiency for inorganic LEDs ($n = 3.5$) and 9.3% for organic LEDs ($n = 1.72$). From this viewpoint, organic LEDs have an advantage of 300-400%. Additional losses from surface reflection (Fresnel-losses) and absorption in the several μm thick layers of inorganic LEDs (typical OLED layer thicknesses are in the range of 100-200nm) enhance this difference. The outcoupling efficiency of OLEDs may additionally be enhanced by microcavity effects due to the low total organic layer thickness (including ITO) [19]. However, the advantage of OLEDs regarding outcoupling efficiency is reduced by the spin statistics. The internal quantum efficiency of typical OLEDs where only the singlet excitons contribute to the light emission is restricted to 25% (more details in Section 5.4.2). Very efficient inorganic LEDs are optimized by sophisticated layer and substrate structures which make use of scattering, wave-guiding effects [20] and anti-glare layers. The need for such optimized structures is the reason for the comparatively high prize and the small substrate area of inorganic LEDs. Thus, organic light emitting diodes are the superior choice for low cost displays with a high pixel number and density in room-light environment.

Organic semiconductors have other unique properties, which makes them more suitable than inorganic semiconductors for certain applications. Firstly, some fluorescent dyes like Alq_3 emit strongly red-shifted to their absorption, which minimizes reabsorption losses. Additionally, due to their high fluorescence yield, only thin layers are needed (around

20nm). Secondly, other organic dyes feature an extremely high absorption coefficient, which makes them suitable for very thin organic photovoltaic cells [21, 22].

In addition to the physical properties, there are some technological aspects, which have stimulated large research efforts in that field: organic semiconductors are relatively cheap to synthesize, easy to apply to large surfaces (whether vacuum sublimed at temperatures below 500 °C or spin casted at room temperature), thus, it is possible to prepare them onto flexible substrates. There exists a wide variety of chemical substances and the possibility to fine-tune their properties by chemical methods.

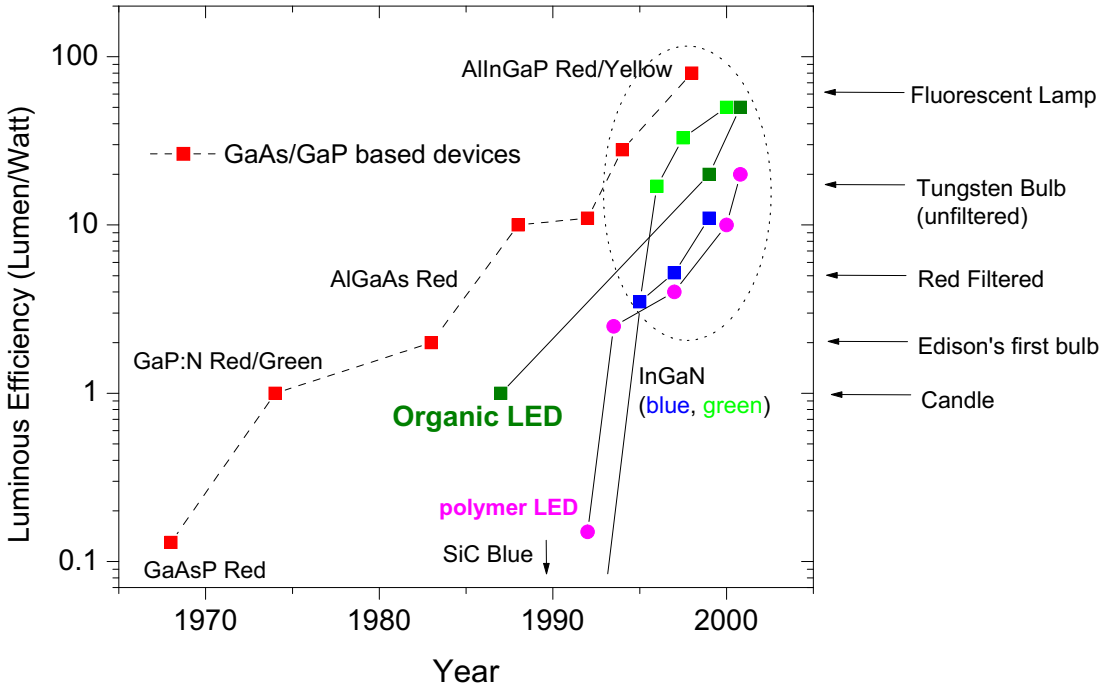

Figure 1.5: *Evolution of organic and inorganic LEDs. Shown is the increase in power efficiency over the years. Conventional inorganic LEDs based on the GaAs/GaP technology are complemented by the newer nitride technology (e.g. InGaN). Organic technology is divided in small molecule organic LEDs (OLEDs) and polymer LEDs (PLEDs). source: [23]*

The success story of organic light-emitting diodes is mainly driven by the rapid development of their optoelectronic parameters that approaches and even passing the optoelectronic properties of the well established inorganic LEDs (see Figure 1.5). Most recent inorganic green emitting LEDs (commercially available in high quantities) based on the nitride-technology reach up to 20 lumens per Watt (lm/W). To date, the best OLEDs with doped emission layers reach 5-10 lm/W (see Section 5.4.2). Meanwhile, also OLEDs with more than 30 lm/W were demonstrated by the use of phosphorescent emitter materials

[24, 25].

1.2 The development of organic light-emitting diodes in the past decade

Electroluminescence, the generation of light by electrical excitation, was first realized in organic semiconducting materials (namely in 1 to 5 mm thick anthracene single crystals) in the 1960s [26, 27]. Helfrich et al. solved the problem of electron injection into the organic material (at that time only the hole injection from a solution of potassium-iodine was efficient) by using a solution of negative anthracene ions. This was the first experimental proof that electroluminescence needs bipolar charge injection into the device, the capture of oppositely charged carriers in a recombination zone and the radiative decay of the thus created excited electron-hole pairs (excitons).

However, the recombination efficiency was rather low. It took until the late eighties before more intense research was stimulated by the work of Tang et al. from the Kodak group [1]. Their electroluminescence device (total thickness of 135 nm) is still the prototype for today's highly developed OLEDs. It consisted of the hole injection contact indium-tin-oxide (ITO), which is a highly doped transparent inorganic semiconductor, an aromatic diamine (TPD) as hole transport material, an emissive layer of aluminium-tris-(8-hydroxy-quinolate) (Alq_3) and a magnesium-silver alloy (Mg:Ag) as electron injection contact. All layers were sublimed in a vacuum system and were amorphous. The large success of this diode can be attributed to the superior choice of the materials involved: (1) Alq_3 shows a high photoluminescence-efficiency which is strongly red shifted to the absorption, (2) the diamine layer keeps the emission zone away from the light-quenching contacts, and (3) ITO and Mg:Ag show efficient injection of holes and electrons, respectively, into the neighboring organic layers. Despite the fact that ITO and Alq_3 exhibit disadvantages in terms of stability, these materials are still widely used for organic light emitting diodes. The LED of 1987 needed 5.5V to reach a luminance of 100 cd/m^2 (common monitor and cathode-ray-tube brightness) and had a current efficiency (see Chapter 3.2) of approx. 2 cd/A. The green emission originates from the Alq_3 layer. This breakthrough in device efficiency *and* operating voltage was the take-off for intense research on organic semiconductors and their use for organic light-emitting diodes (for an overview of early works see [28]).

In 1990, Burroughes et al. [29] from the Cambridge group followed up with a highly efficient OLED based on polymers (PLEDs). Their prototype emitter material was poly(p-phenylene-vinylene) (PPV), which, similar to Alq_3, emits in the green wavelength region. The main steps of improving PLEDs in the 1990s were then:

1) 1991, the use of a very low work-function metal (Calcium) as cathode material (Brown & Heeger [30]).

2) Around 1995, the development of elegant organometallic coupling procedures (such as the Suzuki condensation coupling) to make high-purity conjugated polymers (for a detailed review, see [31]).

3) Since 1994, the use of chemically doped conjugated polymers (conducting polymers) as hole injection layer between the anode and the emissive polymer layer (e.g. [31, 32, 33, 34]).

4) The ongoing development of new polymers, like copolymers based on PPV or the class of polyfluorene (e.g. [35, 36, 37]), with improved luminescence efficiencies.

All these efforts have lead to polymer LEDs with power efficiencies of up to 16-22 lumen per watt at very low operating voltages in the range of 2.5-3.5 Volts for 100 cd/m^2 [36, 31].

For polymer LEDs, the number of layers is usually restricted to two, since the solvent of every new spin casted layer must not dissolve the underlying polymer layer. In contrast, organic LEDs made with small molecules can consist of as many layers as needed for best performance. Hence, the optimization of OLEDs can be done by utilizing new molecular layers with appropriate properties. From this point of view, the research efforts towards lower driving voltage and higher efficiency after the breakthrough work of Tang et al. can be split in three main points:

(1) The improvement of hole injection and transport,
(2) the progress regarding light emission layers, and
(3) the advances in electron injection.

Important steps for the improvement of hole injection and transport were: (a) The introduction of specially suited hole injection layers (mainly phthalocyanines). Their purpose is to lower the energetic barrier for hole injection from the ITO-anode into the hole transport layer (e.g. TPD) [38, 39] and to improve the contact between the hole transport layer and the ITO-anode, thus increasing device stability [40]. More recent low voltage small molecule LEDs use polymeric hole injection layers (see Section 1.5). (b) The solution of stability problems of some hole transport materials (layers from glass forming materials easily crystallize at their low glass transition temperature, which roughens the layer and may detach the top contact) by the development of star-shaped molecules (so-called Starbursts) which form very smooth, glass-like layers [41, 42, 43]. (c) The third main issue of improving hole injection into the organic layers was the controlled preparation of the ITO-anode. It is long known that the preparation of the ITO can both change its work-function and surface roughness drastically [44]. Nevertheless, ITO is still the common choice of the OLED-community due to its availability (because of the large scale use by the liquid crystal industry), high transmission (>90% at 550nm) and low resistivity. Up to now, no other material is able to combine all these properties better than ITO. Today, it is believed that oxygen plasma treatment [45] or UV-ozone cleaning [46] of ITO leads to best OLED-performance.

In the beginning 1990s, intense research, mainly in Japan, was done to find other chelate metal complexes than Alq_3, which can emit in the blue, green and red wavelength region (for a review see [47]). However, more successful for improving OLED efficiency was the use of emitter dopants [48]. Here, an organic molecule which shows excellent photoluminescence properties in solution is blended by a small amount of approx. 1 weight-% into an OLED-transport-layer. Thus, energy is transferred from the host molecule to the guest [49, 50], or excitons are directly created on the guest molecule [51, 52]. With emitter doping, the typical efficiency of OLEDs with pure Alq_3 as emitter of up to 5cd/A [53, 54, 55] could be increased to over 10cd/A [56, 57, 58].

In order to achieve even higher efficiencies, one has to overcome the spin statistics problem. In usual organic emitter molecules, only the singlet states can emit radiatively, the 75%-created triplet excitons decay non-radiatively [59, 60]. Very recently, there was

first evidence that this spin statistics can be altered dramatically be the different formation cross-section of singlet and triplet excitons [61]. However, the most recent approach to increase the efficiency of OLEDs is the use of the strong spin-orbit coupling of phosphorescent materials. Here, radiative emission from both singlet and triplet states occurs and efficiencies in excess of 30cd/A and 20-30lm/W can be achieved [24, 25, 62, 63, 64]. Yet another advantage of these types of emitter molecules is that usually their emission spectrum is much narrower than that of singlet emitters. Thus, a better color purity can be achieved in OLED-display applications.

Another intense field of research is the improvement of electron injection into organic layers. Since the use of low workfunction metals like magnesium and cesium would lead to diodes unstable under ambient conditions, aluminium (Al) or an alloy of silver and magnesium (Mg:Ag) are the preferred cathode materials. Unfortunately, especially for Al, the electron injection is not efficient and the OLED device suffers from imbalanced electron-hole density in the emission zone. The first attempt to overcome this problem was the introduction of a thin insulating layer (preferentially Al_2O_3) between the molecular electron transport layer and the cathode [65, 66] (for explanations see also: [67, 68]). A more pronounced effect on driving voltage and efficiency of an OLED had the introduction of a lithium-fluoride (LiF) interlayer [53, 69] (for an explanation of the effect see [70, 71, 72]). The origin of the LiF-effect as a kind of n-type doping became clear with the work of Kido et al. [54] who mixed Li-atoms directly into the electron transport layer near the metal electrode and obtained the same effect (for detailed explanations see also [73, 74] and Section 5.4.3).

Additionally, much work has been done on improving device stability and lifetime. The foci of these studies are, among others, on (1) better control of the ITO substrate, (2) more stable organic materials, (3) sophisticated driving schemes of the OLEDs [40, 75, 76], and (4) the use of multi-heterostructures or intermixed layers [77, 78, 79, 80].

The present work deals mainly with the improvement of hole injection and transport by using p-doped hole transport layers. This is the first step towards an OLED, where both electron and hole transport layers are n-type and p-type doped, respectively. As we will see, doping of transport layers reduces operating voltages and hence increases the lifetime of the devices. It is shown that even very efficient OLEDs with reasonable low driving voltage can be further improved by p-type-doping of the hole transport layer.

1.3 Present and future commercialization of OLEDs

In 1997, Pioneer commercialized for the first time a low content information display based on the technology of organic light-emitting diodes, namely a passiv matrix driven 256x64 green monochrome display [81]. Soon after, Pioneer started to equip high class car stereos with multi-color dot matrix displays based on organics (with distinct blue and green emission zones) [82]. Today, many companies perform research in the field of passiv or active driven matrix displays based on small organic molecules or polymers, and hence, new applications are short before market initiation (Philips, Pioneer, IBM, Seiko-Epson, Sanyo-Kodak [83], Siemens, Covion, Idemitsu-Kosan [13], e-magin). This first applications will be mainly in the field of portable or car electronics, in smart cards,

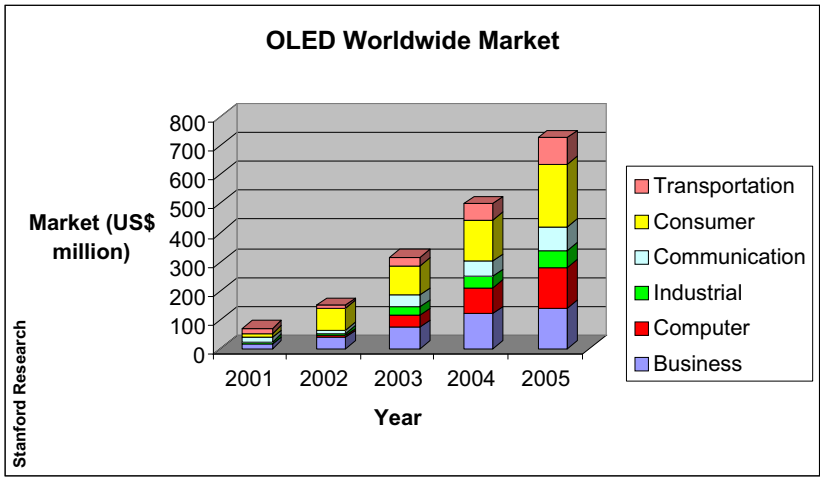

Figure 1.6: *Market potential of OLED based applications until 2005.*

as small displays for digital cameras, camcorders and mobile phones, as backlights for existing display technologies and in head-on displays.

However, flat panel display applications for consumer and computer purposes have the main market potential (up to almost one billion US$ until year 2005). This market will explode with the availability of high resolution large and flat organic displays, capable of displaying information at video rates, operating at low voltages and consuming very little energy, which makes them suitable for battery powered applications (see Figure 1.6). The great advantage of OLED displays from a consumer point of view is that they are self-emitters and thus viewing angle independent. In contrast to that, the established liquid crystal displays only changes the polarization state of the illuminating light, an effect which is strongly viewing angle dependent.

Further applications beyond displays are in sight. All-organic thin layer devices such as transistors and diodes used for integrated circuits have already been realized [84, 85, 86, 87, 88]. Additionally, due to the fact that the power efficiency of OLEDs can exceed that of incandescent lamps and approaches that of discharge lamps, application of the OLED technology for lighting purposes is also very promising.

1.4 Differences between polymer LEDs and small organic molecule LEDs

The present work deals exclusively with organic layers prepared in vacuum from low molecular weight organic semiconducting materials. The field of organic semiconductors comprises also an additional field, namely polymeric semiconductors. The main difference between this two classes of materials from a technological point of view is that polymers are usually prepared by spin coating from a solution onto the desired substrate with following heating/drying cycles.

This results in some differences, which are summarized in Table 1.2.

Organic materials based on vacuum sublimable small molecules (their sublimation temperature is in the range of 100-500 ^{o}C) can be cleaned repeatedly until the purity

Table 1.2: *Comparison of some technological and physical properties of small molecules LEDs (OLEDs) and polymer LEDs (PLEDs). The data are valid for small molecule LEDs without electrical doping and for PLEDs featuring a p-type doped hole injection layer like the system PEDOT:PSS.*

LED / properties	OLED	PLED
preparation	vacuum sublimation	spin coating under atmosphere
advantages	control of purity & compatibility to CMOS technology	cheap (patterning by printing)
disadvantages	expensive vacuum system needed, mask alignment problems for multi-color OLED-displays	impurity & solubility incompatibilities
conductivity	undoped: $<10^{-8}$S/cm	same, but conducting polymers are possible by chemical doping
injection behavior (see also Chapter 4)	no level bending, interfacial dipols favor electron injection [89]	level bending assumed = easier injection [90]
mobilities (at around 1MV/cm, strongly field dependent!)	10^{-5} .. 10^{-3} cm^2/Vs (see Section 3.1.1)	same order (e.g. [91])
LED operating voltage (see Sections 1.2 & 1.5)	4.5-6V (for 100cd/m^2)	2.5-3.5V (for 100cd/m^2)
lifetime	>10.000h	comparable except for blue (after solving solvent problems)

shows the desired level. Furthermore, their storage and processing in vacuum conserves this purity (for more details see Section 5.4.1). In contrast, polymer layers sometimes suffer from intrinsic impurities originating from their synthesis or remainders of the solvents. This is especially true for blue light emitting polymers. Furthermore, it is difficult to spin coat more than two polymer layers because of the demand for solution incompatibility among consecutive layers. To prevent this limitation, mixed layers of a matrix polymer and several transport molecules are sometimes used, but they suffer from decreased mobilities [92]. Additionally, it is more difficult to spin coat polymer layers uniformly on substrates greater than 5 inches and preserves their high quality. The efficiency of polymer LEDs prepared by alternative technologies like ink-jet or screen printing is generally lower as compared to their spin cast counterparts [93].

Nevertheless, the operating voltage of polymer LEDs is usually lower than for comparable OLEDs. Two explanations can be given: (1) Such low-voltage polymer LEDs feature

conducting polymers (like PEDOT:PSS) as injection layers and (2) from photoelectron spectroscopy measurements, it is known that polymer layers exhibit band or level bending at metal contacts, which eases charge carrier injection into the device. The reason for that behavior might be intrinsic impurities, i.e a kind of unintentional doping.

At the present, it is not clear which technology succeeds or if both technologies will co-exist. Both show some advantages and comparable device performances. Hence, the choice of the material systems should depend on the application in mind. From a research point of view, OLED devices have a higher degree of reproducibility since they allow total control over the layer sequence, sharper interfaces than polymer LEDs and an easier purification of the materials. Nevertheless, some basic experiments, like the optical detection of charge carriers in an active layer, use polymeric layer. Polymers in solution can be electrochemically doped and it is therefore easy to determine the absorption spectrum of the charged molecules [94]. Knowing their spectrum it is possible to detect the signal of injected charge carriers.

1.5 The history of doping organic layers

The breakthrough for optoelectronic devices based on inorganic semiconductors was made possible by the development of doping. From that time on, the conduction type and level could be tuned more or less independently of the intrinsic material properties and unintentional impurities. Despite this key importance of doping for inorganic semiconductor technology, there were only very little attempts to dope organic semiconductor materials. This is mainly due to three reasons:

1) Organic semiconductors (molecules with a conjugated π-electron system [95]) are mostly intrinsic, i.e. they have no free charge carriers. Nevertheless, most layers of organic semiconductors show a higher mobility for one type of charge carriers (holes or electrons). This might be due to impurities or structural defects in the molecular layer. Thus, the designer of an organic device is able to choose materials by their intrinsic mobility preferences as to be a hole or an electron transporter.

2) The doping of organic layers by mixing them with atoms (analogous to the mixing of silicon single-crystals with bromine or other atoms) or gases does not lead to stable layers since the dopant can easily diffuse and layered pn- or pin-junctions can not be prepared.

3) As we will see later (Section 5.2.1), the choice of an efficient molecular matrix/dopant system is a trial and error process. The prediction of the doping efficiency is not possible from the energetic position of the appropriate molecular levels (e.g. for p-type doping the HOMO-level of the matrix and the LUMO-level of the dopant molecule). Other effects influence the doping efficiency, too.

The doping effect, which from a phenomenological point of view means the increase of conductivity of a semiconductor layer by addition of small amounts of a different material, was already demonstrated on weakly donor-like organic semiconductors like the phthalocyanines (Pc's). Exposing them to strongly oxidizing gases like iodine or bromine leads to very high conductivities [96]. Unfortunately, these small dopants can easily diffuse through the entire layer, thus not enabling the preparation of stable pn-junctions, which are the main building blocks of semiconducting optoelectronic devices. It is also well known

that the conductivity of organic dyes can be influenced by doping with donor or acceptor molecules having an extended π-electron system. Phthalocyanines e.g., have been p-type-doped with acceptor molecules like ortho-chloranile [97], tetracyano-quinodimethane (TCNQ) [98] and dicyano-dichloro-quinone (DDQ) [99, 100, 101]. Because of the relatively weak effect of the dopant TCNQ on the conductivity of the Pc's, only high molecular doping ratios between 1:20 and 1:1 were studied. A maximum conductivity of $6x10^{-6}$S/cm was achieved at a doping ratio of 1:5. Oligothiophenes have been doped with DDQ [102] and polyacetylene with AsF_5 [103]. Apart from that, only a few attempts have been described in literature to apply molecularly doped dye layers in semiconductor devices, namely rectification diodes [102, 104]).

To the authors knowledge, all attempts of using p-type doped organic semiconductors in organic light emitting diodes have been limited to polymeric layers up to now, whereas the other active layers of the LED have been polymeric or vacuum sublimed organic molecule layers. The following material systems were tested: (1) Already in the 1980s, Hayashi et al. inserted a doped poly(3-methylthiophene) layer between the anode and a perylene emitter layer (device efficiency was rather poor) [105]. (2) Yang, Heeger [32] and at the same time Antoniadis [106] introduced doped polyaniline for polymer LEDs. (3) $FeCl_3$ doped polythiophene was used by Romero et al. [107], (4) iodine doped MEH-PPV (poly[2-methoxy,5-(2'-ethyl-hexyloxyl)-1,4-phenylene vinylene]) was used [108], and (5) Yamamori et al. showed thick hole transport layers of polycarbonate doped with a chloroantimonate (TBAHA) [109, 110] to be used in OLEDs. Furthermore, and more recently, Kido et al. used $FeCl_3$ doped polymer layers [111] and Ganzorig et al. doped a spin-coatable form of TPD with $SbCl_5$ [112]. Nowadays, the most common and widely used hole injection and transport layer in bi-layer polymer LEDs is a mixture of poly(3,4-ethylenedioxythiophene) and poly(4-styrenesulfonate) (PEDOT:PSS) [113] (commercially available from Bayer). A more recent approach uses an electrochemically doped film of poly(4,4'-dimethoxy-bithiophene) (PDBT [34]) as stable hole injection layer in poyfluorene PLEDs.

The clear-cut conclusion from the works mentioned above is that doping of transport layers is necessary to achieve low operating voltages of OLEDs and PLEDs. The operating voltage needed to achieve a brightness of approx. 100cd/m^2 in OLEDs without doping is in the range of 4.5-6V [110, 112]. It is below 3-4V for polymer LEDs using doped hole injection layers [31].

The focus of this work is on p-type doping of different small molecule vacuum deposited organic semiconducting layers with an organic acceptor molecule, namely tetrafluoro-tetracyano-quinodimethane (F_4-TCNQ), and their use as hole injection and transport layers in OLEDs. It will be shown in the next Chapters that this doping leads to organic light-emitting diodes with very low operating voltages *and* high light emitting efficiencies.

2 Doping of organic layers: principles and effects

This Chapter outlines the idea of doping organic layers by a co-evaporation of matrix and dopant molecules. The present state of understanding of the effect is described. The method of Fourier transformed infrared spectroscopy (FTIR) is able to yield information about the first step of the doping reaction. The basic electrical properties of a p-type doped model system are summarized. The conductivity of the doped layers is strongly enhanced and the Fermi-level shifts towards the transport states, in analogy to inorganic semiconductor doping.

2.1 Doping basics

From a chemical point of view, the p-type doping of a more or less electron donating matrix molecule M with an electron attracting (acceptor like) dopant molecule A can be described with the mass action law:

$$M + \widetilde{M}A \rightleftharpoons M + [\widetilde{M}^+A^-] \rightleftharpoons M^+ + \widetilde{M}A^- \quad , \tag{2.1}$$

where M is a random matrix molecule, $\widetilde{M}$ is a matrix molecule next to a dopant A. The first step of the reaction (2.1) is the initial charge transfer describing the electron transfer from a matrix molecule to the nearest acceptor molecule. This intermediate local charge transfer state $[\widetilde{M}^+A^-]$ may dissociate into a quasi-unbound state, which means that the matrix molecule carrying the positive charge is too far away from the ionized dopant molecule to feel coulombic attraction anymore. Thus, the positive charge can move through the organic layer by hopping and the density of M^+ determines the density of free equilibrium holes $p_{f,0}$ in the layer. Doping of M with A is efficient if the balance of the above reaction is on the right side, i.e. the density of free holes $p_{f,0}$ approaches the doping density N_A. Reaction (2.1) describes the case of p-type doping, however, it is obvious that n-type doping may be described similarly.

How does the free hole density depend on doping? The chemical mass action law is equivalent to the physical laws regarding carrier statistics in doped semiconductors. Thus, one might argue that as long as $p_{f,0} \ll N_A$, the model of *deep acceptors* is applicable, which means that the dopants are only partially ionized or that most holes are bound to charged acceptors. If $p_{f,0} \approx N_A$ the limit of *shallow acceptors* should be reached. But is this true for our organic doping systems?

In a standard semiconductor picture, the Fermi energy E_F and the hole density $p_{f,0}$ are related to the energetic positions of the acceptor E_A and the hole transport state E_h of the matrix molecules in the case of deep acceptors by:

$$E_F(T) = \frac{E_A + E_h}{2} + \frac{k_B T}{2} \ln \frac{N_h}{N_A} \quad , \tag{2.2}$$

where N_h is the effective density of states at E_h. The free hole density is:

$$p_{f,0} = \sqrt{N_A N_h} \exp\left(-\frac{\Delta E}{2k_B T}\right) \quad , \tag{2.3}$$

in Boltzmann-approximation, where $\Delta E = E_A - E_h$. In accordance with equation (2.3), the hole density in the *deep acceptor limit* should increase with the *square-root* of the doping density and should be *thermally activated*. The above equations only hold for $\Delta E \gg k_B T \ln(N_h/N_A)$.

However, in the opposite case of shallow acceptors, E_F and $p_{f,0}$ are determined by

$$E_F(T) = E_h + \frac{k_B T}{2} \ln \frac{N_h}{N_A} \quad , \tag{2.4}$$

and

$$p_{f,0} = N_A \quad . \tag{2.5}$$

In the case of *shallow acceptors*, the free hole density should increase *linearly* with the doping density and should *not be thermally activated*. For high doping densities, in the range of $N_h/N_A = 100$, ΔE would have to be below 0.1eV to reach the shallow acceptor limit at room temperature. Assuming a Coulomb binding potential appropriate to describe the binding energy E_B of the initial charge-transfer (CT) state, one gets:

$$E_B = \frac{1}{4\pi\epsilon_0\epsilon_r}\frac{e^2}{r} \quad , \tag{2.6}$$

where r is the distance of the positive and negative charge after separation of the CT-state and ϵ_r is the relative dielectric constant of the organic medium ($\epsilon_r \approx 3$). This equation treats the electronic polarization effect of the CT-state and the free charge carriers in a continuum approach, which is applicable if the distance r exceeds a few lattice constants [95]. According to equation (2.6), a binding energy of $\Delta E = 0.1$eV would correspond to a distance of the charge carriers within the CT-state of 5nm.

Since this is much larger than the distance between two neighboring molecules, one would expect the model of deep acceptors to be appropriate to describe the doping effect in organic molecular layers. It should be stated here that the models above describe inorganic semiconductors well, but it is questionable if they do so for organic semiconductors.

For the molecular doping ratios applied in this study (matrix molecules to doping molecules ratio between 300:1 and 30:1) the morphological and structural behavior of the doped layer is mainly determined by the matrix molecules. For further details see the diploma thesis of B. Plönnigs [114].

2.2 FTIR measurements and charge transfer

We investigate the first step of reaction (2.1) by Fourier transformed infrared spectroscopy (FTIR). Upon a charge transfer from the matrix molecule to the dopant molecule, the charge distribution of that dopant is changed, which changes the binding forces between the atoms in the molecule. Hence, the frequency changes of various vibrational modes (which lie in the infrared spectral region) of the dopant molecule provide information

about the degree of charge transfer Z. Z is defined by two limiting cases, where $Z = 0$ means that the dopant is uncharged, whereas $Z = 1$ means that one electron is totally transferred to the dopant. Z-values between 0 and 1 indicate a partial charge transfer, meaning that one electron occupies an orbital which can be described as a linear combination of orbitals of both molecules.

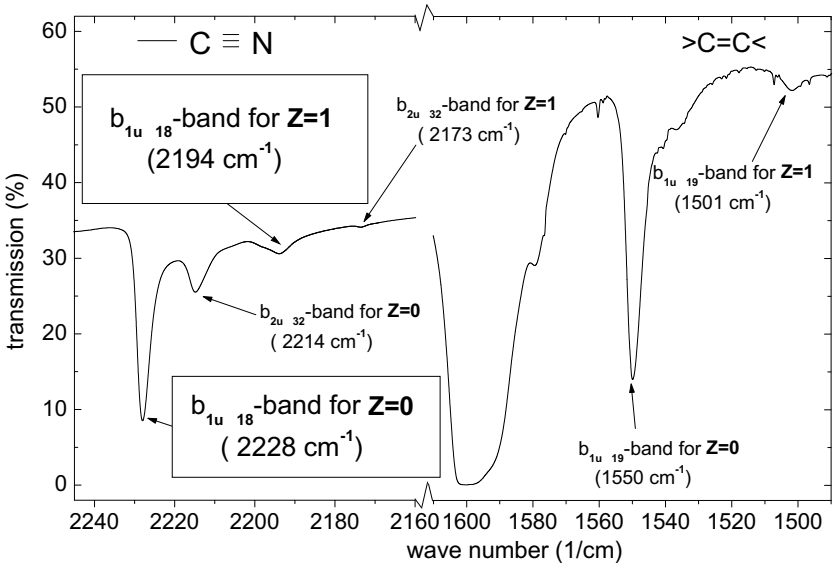

Figure 2.1: *FTIR spectrum of a mixed pellet of KBR and F_4-TCNQ-powder (taken from [114]).*

For the strong acceptor dopant F_4-TCNQ, a linear wave-number dependence of the peak shift for several peaks in the F_4-TCNQ spectrum was found from comparison of FTIR and X-ray diffraction measurements [115, 116]. To investigate the degree of charge transfer between several matrix molecules and F_4-TCNQ, we used mainly the in-plane C-N stretching mode $b_{1u}\nu_{18}$ of F_4-TCNQ at 2228cm^{-1} ($Z = 0$) and 2194cm^{-1} ($Z = 1$), respectively. This is due to the following advantages for that mode: (i) It is IR-active (non-vanishing transition dipole moment), (ii) sensitive with respect to the charge state of F_4-TCNQ, and (iii) no additional matrix absorption around these wave-numbers takes place. Figure 2.1 shows an example of a typical FTIR spectrum for F_4-TCNQ mixed into a pellet together with non-IR-absorbing KBr. The $b_{1u}\nu_{18}$ mode shows two peaks, the main one at 2228cm^{-1}, which indicates no charge transfer and an additional second one at 2194cm^{-1}, which results from a total charge transfer state ($Z = 1$) of the radical salt $K^+F_4TCNQ^-$.

2.3 Model system: phthalocyanines doped with F_4-TCNQ

Before applying the doping concept to OLEDs, basic research on doping was mainly done by our group on a model system of zinc-phthalocyanine (ZnPc) or vanadyl-phthalocyanine (VOPc) doped with 2,3,5,6-tetrafluoro-7,7,8,8-tetracyano-quinodimethane (F_4-TCNQ, for

materials properties see Section 3.1.1). A short summary should make the reader familiar with the basic behavior of the model system regarding electrical measurements which was published in detail in refs. [95, 117, 118].

The conductivity σ of undoped ZnPc is below 10^{-10}S/cm in vacuum, in fact too low to be measured in a our coplanar contact geometry (Chapter 3.3). For undoped VOPc, the conductivity was determined to be $\sigma \simeq 10^{-12}$S/cm in sandwich geometry. Leaving a nominally undoped sample for some days in air results in a conductivity of about 10^{-7}S/cm. Here, the origin of the extrinsic carriers is oxygen doping. Upon intentional electronically doping, already at a concentration of 0.2mol% the conductivity for the system ZnPc/F_4-TCNQ reaches 10^{-4}S/cm, and reaches 2x10^{-6}S/cm for VOPc/F_4-TCNQ. The conductivity of both ZnPc and VOPc increases super-linearly with the doping ratio (see Figure 2.2). It is thermally activated with a constant activation energy in the temperature range of 20 °C to 100 °C. With increasing doping the activation energy of the conductivity decreases and is almost a factor of two smaller for ZnPc compared to VOPc. The conductivities are low compared to crystalline semiconductors because of the lower mobility.

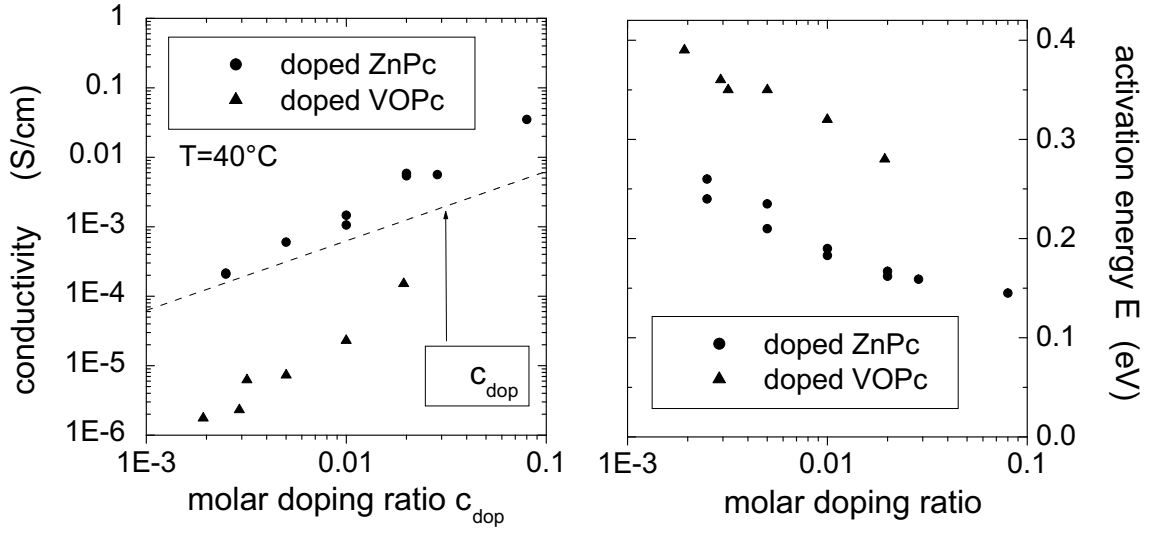

Figure 2.2: *(left) Conductivity (the dashed line represents linear dependence) and (right) activation energies of the conductivity (constant in a temperature range from 20 °C to 100 °C) for ZnPc and VOPc doped with F_4-TCNQ measured in coplanar contact geometry (taken from [95]).*

Since the degree Z of charge transfer was determined to be 1 for both ZnPc and VOPc doped with F_4-TCNQ, the difference between VOPc and ZnPc doping can not be explained by different ionization energies. Within a variable range hopping approach described in [119], the differences seem to be related to different degrees of delocalization of the states in the tail of a Gaussian distribution of transport states.

Seebeck (or: thermopower) measurements can be used, in order to determine the conduction-type and the energetic distance between the Fermi-level and the transport

level in the doped molecular layers [95]. For the Seebeck effect, one measures the voltage V_{see} arising if two contacts of a semiconductor are held at two different temperatures (mean temperature T, difference ΔT). The Seebeck-coefficient S is defined as:

$$S(T) := \lim_{\Delta T \to 0} \frac{V_{see}(T, \Delta T)}{\Delta T} \quad . \tag{2.7}$$

The Seebeck-coefficient is positive for holes as majority charge carriers in the semiconductor, negative for electrons. If one assumes that hole transport takes place by hopping in an energetically small distribution of transport states around E_h (or, similar, in a very small band) and transport is homogeneous in the sample, then the Fermi-level E_F and the hole density p are related to the Seebeck-coefficient by [95]:

$$S(T) := \frac{E_F(T) - E_h}{eT} = \frac{k_B}{e} \ln\left\{\frac{N_h - p(T)}{p(T)}\right\} \simeq \frac{k_B}{e} \ln\left\{\frac{N_h}{p(T)}\right\} \quad , \tag{2.8}$$

where N_h is the density of transport states. The approximation in the right part of equation (2.8) is equivalent to the Boltzmann approximation. From equation (2.8), one can easily derive the activation energy of the hole density.

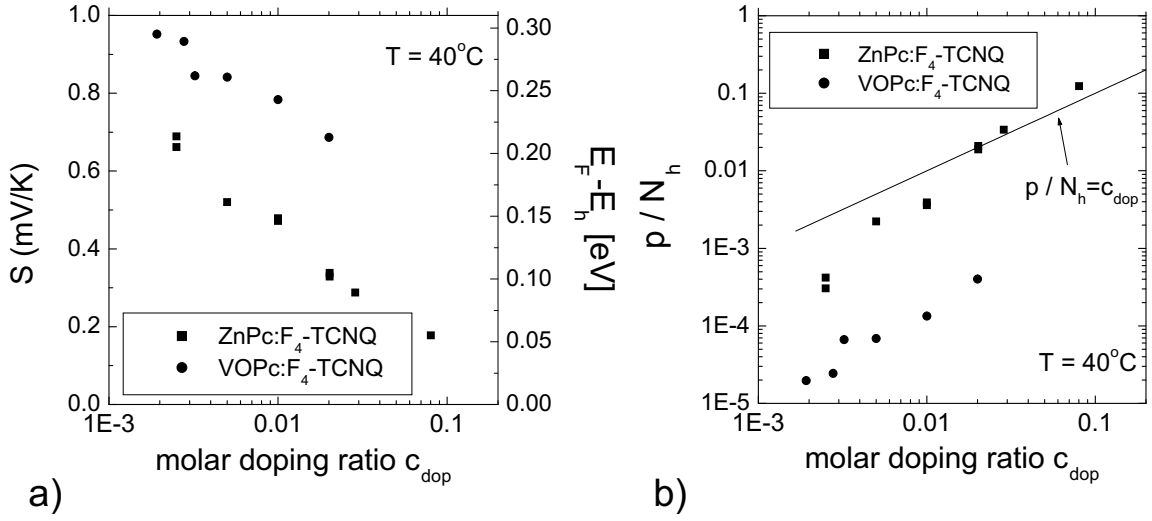

Figure 2.3: *(a) Seebeck coefficient (left axis) and energetic difference between the Fermi-level E_F and the hole transport state E_h (right axis) versus doping ratio and (b) calculated hole density per total density of states N_h at the transport state E_h versus doping density. Additionally the line for 100% doping efficiency ($c_{dop} = p/N_h$) is shown (taken from [95]).*

Results of the Seebeck measurements are shown in Figure 2.3. The Seebeck-coefficient S is always positive, indicating hole transport. S continuously decreases with increasing dopant concentration c_{dop}, showing that the Fermi-level approaches the transport level. The calculated hole density p shows a slightly super-linear increase with dopant concentration c_{dop}. Furthermore (not shown in Figure 2.3), the Seebeck-coefficient is almost independent of temperature for ZnPc, hence the hole density is not thermally activated. In contrast, the Seebeck-coefficient for VOPc is thermally activated with a small activation

energy of about 0.1eV (compare with the activation energy of the conductivity of >0.3eV). The fact that the conductivity of doped VOPc is low compared to that of doped ZnPc is also reflected in the Seebeck-measurements. The doping efficiency can be calculated from the ratio of the density of free holes to the density of dopant molecules assuming that N_h equals the density of matrix molecules. It is low for VOPc-samples, whereas it seems to reach 100% for highly doped ZnPc samples ($c_{dop} > 1\%$). The assumption about N_h, however, is probably not justified (cp. [119]).

In summary, the measurements on the p-type doping model system reveal:

- The conduction is p-type.
- The transport level is several k_BT below the Fermi-level (0.1eV for ZnPc and 0.2eV for VOPc at doping ratios of 2-3%).
- The hole density is temperature independent for doped ZnPc and thermally activated with a small activation energy for doped VOPc.
- The conductivity increases strongly super-linearly with the dopant concentration. The hole density increases only slightly super-linearly.
- The generation of free charge carriers by doping is much more efficient for ZnPc than for VOPc.

A comparison of the results of these electrical measurements with the basic considerations in Section 2.1 leads to the conclusion that the standard semiconductor model of shallow acceptors seems to be more adequate, since the hole density is not or only weakly thermally activated and the doping concentration dependence follows more a linear than a square-root behavior. In fact, the super-linear increase of conductivity and hole density with doping ratio could recently be explained by Männig et al. with a disorder model [119], based on the assumption of shallow acceptor states. Nevertheless, the finding of shallow acceptors is still in clear contradiction to the naive estimations of the binding energy of a charge transfer complex between matrix and dopant molecules from coulombic attraction as described in Section 2.1.

A rough estimation of the dopability of a matrix/dopant system is possible by the measurement of the degree Z of charge transfer together with a conductivity-determination of undoped and doped samples. This criterion is used later (Section 5.2.1) to chose suitable matrix molecules for doped hole transport layers in OLEDs.

3 Experiment & materials

This Section describes how the experiments with organic light emitting diodes were performed. First, all organic materials used in this study will be introduced together with their relevant physical properties. Since it turned out to be an important issue, the question of the purification of organic materials used for OLEDs will be addressed. An overview about the definition and determination of the relevant optoelectronic efficiencies is presented which gives the basis for comparing OLED properties. Next, the preparation of organic devices in a single chamber high vacuum system is described. For more complicated layer structures with p- and n-type doping in different layers, one needs a multiple chamber vacuum system (cluster tool). The setup of such a system and the preparation of organic devices in the cluster tool are described. Finally, the experimental setup for the ultraviolet- and X-ray photoemission spectroscopy measurements to investigate doped organic layers on inorganic conductive substrates is described.

3.1 Organic materials used in this study

3.1.1 Materials and their properties

The chemical structures of the molecules used in this study are given in Figures 3.1, 3.2 and Figure 3.3. For most OLED-samples, we used Alq_3 as emitter material (Figure 3.2 top left), because of the broad literature database of OLEDs using Alq_3 as emitter. Alq_3 has this importance for the OLED research because it combines three important properties: (i) a large Stokes-shift (hence, no re-absorption of emitted light occurs), (ii) a relatively high electron mobility and (iii) proper positions of the HOMO and LUMO-levels, respectively, which fit to other OLED materials. Nevertheless, it has also one big disadvantage: the positive charged state of Alq_3 is chemically unstable [120]. Hence, most of the OLEDs with pure Alq_3 as emitter suffer from short lifetimes [121]. In Section 5.4.2, we will discuss the effect of some emitter-dopants (like QADs) on the quantum efficiency of OLEDs.

As shown in [95], the acceptor molecule F_4-TCNQ (Figure 3.1) is one of the most effi-

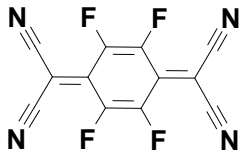

F_4-TCNQ:
2,3,5,6-tetrafluoro-7,7,8,8-tetracyano-quinodimethane
$C_{12}N_4F_4$

Figure 3.1: *Molecular structure of the p-type dopant used in this study: the strong acceptor molecule F_4-TCNQ .*

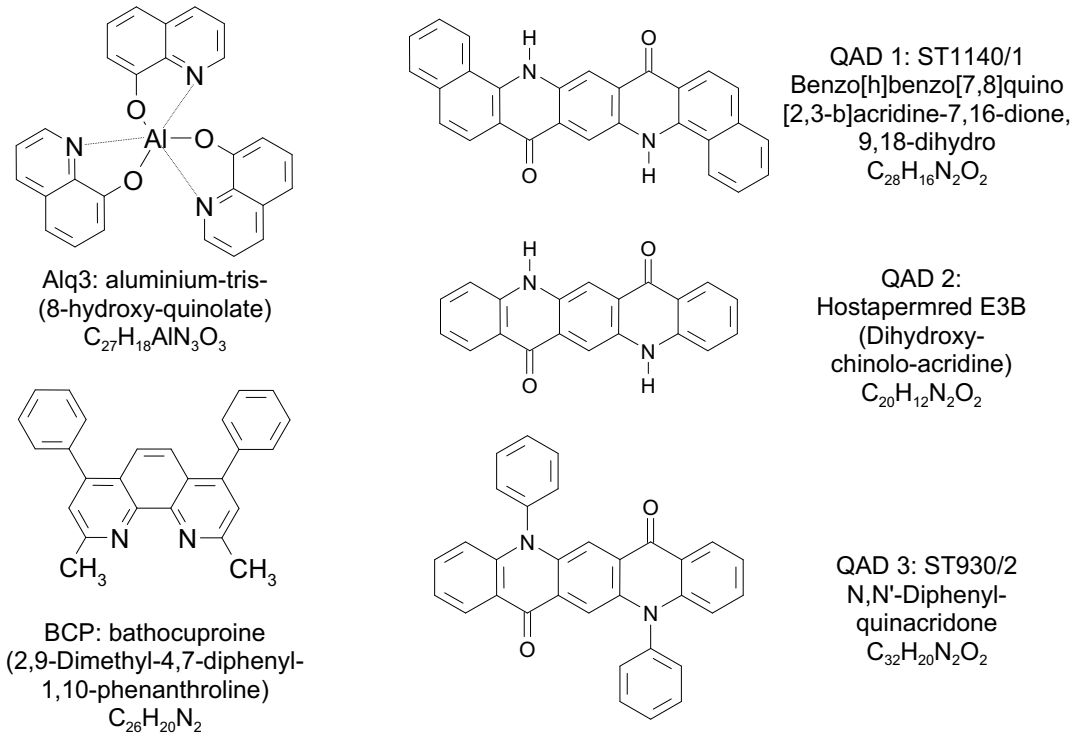

Figure 3.2: *Molecular structure of the emitter and electron transport materials used in this study. BCP is known as hole blocking and electron transport material, whereas the QAD's are emitter dopant molecules.*

cient p-type dopants. Hence, F_4-TCNQ was used exclusively during this study. Its doping effect in molecular layers of various potential OLED-hole transport materials (Figure 3.3) was tested (see Section 5.2.1).

Some of the basic properties (taken from literature) of these materials are listed in Table 3.1. The position of the HOMO and LUMO levels of the molecular layers is of special importance for their use in OLEDs. Furthermore, the mobility for majority carriers must be high for electron and hole transport materials. Most materials used in OLEDs are amorphous to make sure that they form smooth layers. Their glass transition temperature (the temperature above which the layers are getting crystalline) is usually in the range of below 100 ^{o}C (TPD) to above 150 ^{o}C (Alq_3). The crystallization is believed to be a major lifetime limiting process for OLEDs, because it roughens the surface which may result in contact delamination.

Throughout the whole study, we used indium-tin-oxide (ITO) as hole injection contact (anode) and aluminium (Al) as electron injecting contact (cathode). ITO shows a work-function of 4.4eV [122] up to 4.9eV [123] in dependence of the surface treatment prior to deposition of the organic layers [45, 46]. Solvent cleaned ITO as we use it here should have a low ionization potential around 4.4eV. Al has a work-function of approx. 4.2eV [89]. If Al is used in combination with a small lithium-fluoride (LiF) inter-layer the work-function is lowered by approx. 0.7eV [72].

The ITO substrates used for the OLED-samples in the present study were delivered by Jenoptik GmbH Jena (Germany) and had a sheet resistance of approx. 10 $\Omega/\Box$. They

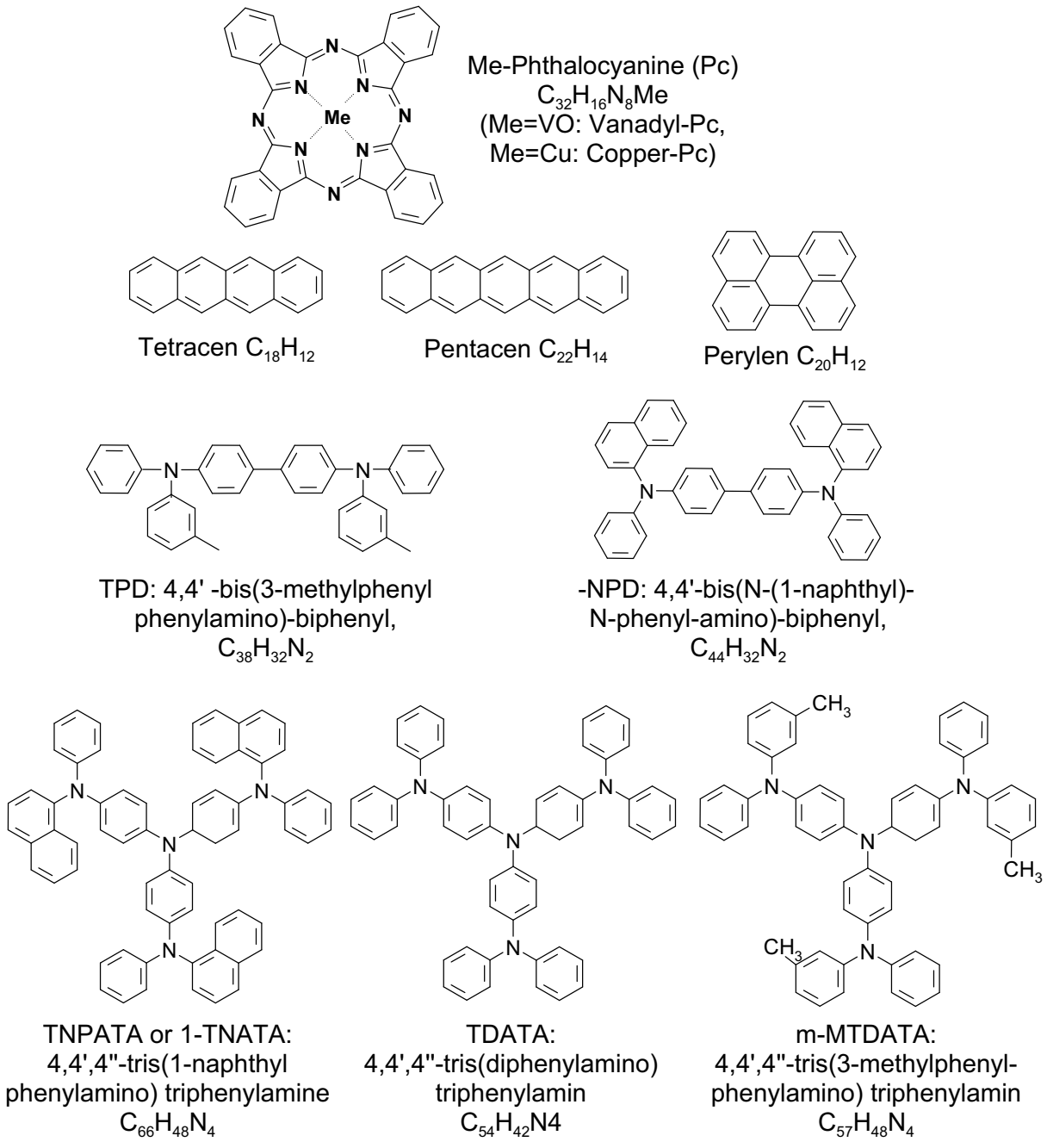

Figure 3.3: *Molecular structure of the hole transport materials used in this study. The bottom three materials are called 'Starbursts' due to their shape.*

were ex-situ cleaned in an ultrasonic bath with ethanol, acetone and de-ionized water, dried, and residual dust particles were removed with a cleaning polymer (Opticlean, LOT Oriel GmbH). For samples made in the UHV-system, the ITO substrates were heated at 120 ^{o}C over-night.

Table 3.1: *Some material properties relevant for OLED-application. Note that the LUMO values are taken from measured HOMO-positions and optical gap measurement. The given values for the density ϱ are used to calculate the layer thickness from quartz-thickness monitor measurements.*

material	supplier	HOMO	LUMO	mobility (at RT)	other properties
Alq_3	Aldrich and Syntec	5.7eV [122] - 6.0eV [124]	3.1eV [122]	$\mu_n \leq 5\text{x}10^{-5}$ cm^2/Vs [125, 126], $\mu_p < 0.01\mu_n$ [127]	ϱ = 1.4g/cm^3, amorphous layers, sublimes, EL at 525nm
QADs	Syntec, in house	?	?	-	optical absorption fits to EL of Alq_3, emission red shifted by 5-30nm
BCP	Aldrich	6.7eV [24]	3.2eV [24]	$\mu_n < \mu_{n,Alq3}$	ϱ = 1.3g/cm^3, amorphous, melting
F_4-TCNQ	Aldrich, Acros	8.3eV (sec. 4.2.3)	$\approx$ 5.1eV [117]	-	sublimation already at $T \approx 90\,^o$C
VOPc	in house	5.3eV [128]	3.9eV [128]	μ_p=1.5x10^{-3} cm^2/Vs (doped [117]), $\mu_n \ll \mu_p$	ϱ = 1.54g/cm^3, polycrystalline, several phases possible [95], not flat due to the oxygen
ZnPc	Aldrich	5.0eV [128]	3.4eV [128]	similar VOPc	ϱ = 1.6g/cm^3, polycrystalline, two phases, flat
TPD	Syntec	5.4eV [122]	2.4eV [122]	μ_p=1x10^{-3} cm^2/Vs [126], $\mu_n \ll \mu_p$	ϱ = 1.3g/cm^3, amorphous glassy material, melting
TDATA MTDATA TNATA	Syntec	5.1eV [43, 129]	$\leq$ 2.4eV	μ_p=3x10^{-5} cm^2/Vs [129], $\mu_n \ll \mu_p$	ϱ = 1.3g/cm^3, amorphous glassy material, melting
Tetracen	Aldrich	5.4eV [130]	2.4eV [130]	?	ϱ = 1.3g/cm^3, polycrystalline
Pentacen	Aldrich	5.1eV [130]	2.9eV [130]	?	ϱ = 1.5g/cm^3, polycrystalline
Perylen	Aldrich	5.4eV [131]	2.3eV [132]	?	ϱ = 1.3g/cm^3, polycrystalline
α-NPD	Syntec	5.7eV [124]	2.6eV [124]	$\mu_p = 1/2\ \mu_{p,TPD}$ [126], $\mu_n \ll \mu_p$	ϱ = 1.3g/cm^3, amorphous glassy material, melting

3.1.2 Purification of the materials

The purification of organic materials is of large importance for the efficiency and stability of light emitting diodes, as will be discussed for some examples in Section 5.4.1. The success of polymer light emitting diodes was strongly coupled to the development of new synthetic approaches for the production of high purity polymeric materials.

In contrast to polymers, sublimable small molecule organic materials can be cleaned to nearly 100% purity. This is mainly done by a vacuum gradient sublimation technique, which in this study was used for the materials Alq_3, VOPc, ZnPc, TPD, QAD, BCP, and partly the Starburst molecules.

The material is placed at one end of a fused-silica tube, which is evacuated to high vacuum (approx. 10^{-5} mbar). The tube is heated in a multi-zone furnace, where an outer copper tube ensures a smooth temperature gradient. The temperature of the different zones is controlled in a way that the organic material sublimes from the outermost hottest zone (temperature slightly above the sublimation point) and resublimes in the colder zones. The different components of the initial material are then spatially separated and can be collected separately. This technique also works for glass-forming and melting materials (TPD, Starbursts), although the efficiency of the method is low then.

For the latter materials, which evaporate from a melt, a better technique is the zone refinement. There, the raw material is melted into a glass rod under an inert atmosphere. In the zone refinement device, a temperature profile is established with alternating zones of temperatures above and below the melting point. The glass rod is moved back and forth. By successive melting and solidification of certain zones in the material, impurities are forced to move to the outer part of the glass rod, leaving a purified central part of the material behind. This technique was used for the Starburst materials TDATA and m-MTDATA for samples made in the UHV-system.

The success of the purification of organic materials can be seen from different facts: (i) the purified materials can be vacuum sublimed without residues, (ii) the backward current in organic Mip-diodes (anode/intrinsic material/doped material/cathode) is much smaller, if purified materials were used, and (iii) the light emitting efficiency of OLEDs using purified material is higher compared to unpurified ones.

Additionally, the evaporation sources have to guarantee a uniform temperature distribution in the crucible with the material inside, in order to keep the high purity during the vacuum-preparation of the samples. Otherwise, the organic material may be cracked due to local high temperatures and the crack components may again act as impurities in the active layers.

3.2 Determination of device efficiencies

Since most applications of organic light emitting diodes will be related to visible light emission (e.g. illumination, signs and displays), the optical characteristics of OLEDs are usually given and compared in photometric, not in radiometric units. Therefore, the sensitivity of the human eye has to be involved in the calculation of light emission and output efficiencies. The spectral response of the human eye under daylight conditions (referred to as photopic or cone vision) was standardized by the International Lighting Commission (CIE) in 1924. They deduced from experiments with a representative number of persons the photopic spectral luminous efficiency function $V(\lambda)$. This yields

the connection between the four radiometric fundamental quantities (radiant flux Φ_e in Watts, radiant intensity I_e in W/steradiant, irradiance E_e in W/m^2, and radiance L_e in W/(m^{2}sr)) and their photometric equivalents (luminous flux Φ_V in lumen, luminous intensity I_V in lm/sr=cd, illuminance E_V in lm/m^2=lux, and luminance L_V in lm/(m^2 sr)=cd/m^2). As an example, the connection between radiant flux and luminous flux is defined by the following equation (others equivalent):

$$\Phi_V \;=\; K_m \int_{380nm}^{770nm} \Phi_e(\lambda)\, V(\lambda)\, d\lambda \quad , \tag{3.1}$$

where $K_m = 683$lm/W is a conversion constant. To easily convert radiometric and photometric quantities, the radiation luminous efficacy K_r is defined. Since the total radiant flux can be written as $\Phi_e = \int_0^\infty \Phi_e(\lambda)d\lambda$ the radiation luminous efficacy can be defined as follows:

$$K_r \;=\; \frac{\Phi_V}{\Phi_e} \;=\; K_m \frac{\int_{380}^{770} \Phi_e(\lambda)V(\lambda)d\lambda}{\int_0^\infty \Phi_e(\lambda)d\lambda} \quad . \tag{3.2}$$

The radiation luminous efficacy is not an efficiency, but gives the effectiveness of a beam of radiation in stimulating the perception of light in the human eye. Typical values of K_r are about 500lm/W for small band green light emission (typical for LEDs), about 125lm/W for red, about 75lm/W for a typical saturated blue, and is 220lm/W for a constant white light emission (for an overview about this topic see e.g. [133]).

OLEDs are mainly characterized by three efficiency values:

(1) The system luminous efficacy K_S (in lm/W) gives the ratio of total light output in lumens to the electrical power in Watts. In this work it is also referred to as luminous or power efficiency η_P.

(2) The current efficiency η_c (in cd/A), defined by the ratio of the luminous intensity in forward direction $I_{V,0}$ and the current flowing through the OLED (same as luminance in forward direction $L_{V,0}$ divided by current density).

(3) The quantum efficiency η_Q (in %), defined as the ratio between the number of emitted photons and the number of injected electrons.

The third value is a radiometric one, whereas (1) and (2) are photometric values. These definitions have the consequence that the same quantum efficiency for a red, green and blue emitting OLED gives strongly different current and luminous efficiencies, due to different radiation luminous efficacy of the three LEDs.

Let η_c be the current efficiency in cd/A at an operating voltage V. Then, the power efficiency η_P can be calculated by:

$$\eta_P \;=\; \frac{f_D\,\pi}{V}\,\eta_c \quad , \tag{3.3}$$

where f_D is a factor which depends on the angular distribution of the light emitted from the substrate into one half-sphere:

$$f_D \;=\; \frac{1}{\pi I_{V,0}} \int_0^{\pi/2} \int_{-\pi}^{+\pi} I_V(\vartheta,\varphi)\, \sin\vartheta d\varphi d\vartheta \quad , \tag{3.4}$$

where $I_{V,0}$ is the luminous intensity in forward direction and $I_V(\vartheta,\varphi)$ is the angular distribution of the emitted light. If one assumes a Lambertian emission with $I_V(\vartheta,\varphi) =$

$I_{V,0} \cos \vartheta$ (which is approximately the case for an OLED neglecting micro-cavity and Fresnel-loss effects [134]), f_D equals one.

The quantum efficiency η_Q is related to the current efficiency η_c by:

$$\eta_Q \;=\; f_D \pi \, \eta_c \, \frac{e}{K_r E_{mean}} \quad , \tag{3.5}$$

where E_{mean} is the average photon energy, in a first order approximation related to the wavelength of maximum emission λ_{max} by $E_{mean} = h\,c\,/\,\lambda_{max}$, where h is the Planck-constant and c the speed of light.

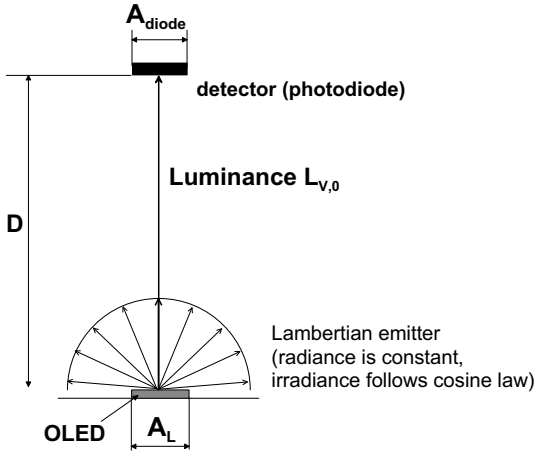

Figure 3.4: *Experimental setup to measure the luminous intensity in forward direction of an OLED.*

In order to obtain the current efficiency of an OLED, one needs to know its luminance in forward direction $L_{V,0}$ (in cd/m^2, $L_{V,0} = I_{V,0}/A_L$). The experimental setup used for the present work is schematically drawn in Figure 3.4. A photodiode (area A_{diode}, transmission of their windows τ, relativ spectral sensitivity $s_{r,diode}(\lambda)$) is placed above an OLED (area A_L, emission spectrum $\phi(\lambda)$) at a distance D. The photodiode is connected to an amplifier circuit, which generates a voltage V_{diode} proportional to the irradiance of the photodiode. The photodiode/amplifier-unit has to be calibrated (experimentally or from data sheets). This calibration can be expressed by a sensitivity of the photodiode/amplifier-unit at the wavelength of maximum sensitivity S_{max} in irradiance-Watt per voltage V_{diode}. Then the luminance in forward direction can be calculated to:

$$L_{V,0} \;=\; K_r \, V_{diode} \, \frac{S_{max}}{FF} \, \frac{D^2}{\tau \, A_L A_{diode}} \quad , \tag{3.6}$$

where K_r accounts for the conversion of the radiometric irradiance measured by the photodiode to the photometric luminous intensity that wants to be calculated (equation (3.2)). FF is a fill-factor which weights the emission spectra of the OLED with the spectral sensitivity dependence of the photodiode: $FF = \int \phi(\lambda) s_{r,diode}(\lambda) d\lambda \,/\, \int \phi(\lambda) d\lambda$. The values of K_r and FF depend on the emission spectra of the measured OLED. Formula (3.6) yields a good approximation only for $D >> A_{diode}$ and $D >> A_L$.

3.3 Preparation of OLEDs in a single chamber HV-system, sample geometry

The first part of the samples were prepared in a single chamber high vacuum system (at a base pressure of around 2x10^{-6}mbar) driven by a combination of oil containing rotary backing pumps and turbo molecular pumps. It could be equipped with up to 4 evaporation sources (for organic materials or metals) and one more source for the dopant material. The organic materials were vacuum sublimed from fused silica crucibles heated by tungsten wires. Hence, the temperature distribution was uneven inside the crucibles, e.g. resulting in black colored residues from Alq_3. Aluminium was evaporated from a tungsten wire. The system had to be vented to exchange samples and Al-material. Doped layers were prepared by *co-evaporation* (see Figure 3.5). Typical evaporation rates of organic materials were 1-2Å/sec for the matrix and, depending on the doping ratio, below 1-2 Å/min for the dopant material. The rates and layer thicknesses are monitored by quartz oscillators together with control units from Leybold-Inficon. To measure the rates of matrix and dopant molecules independently, one thickness monitor was placed in a short distance above the dopant source (only 'visible' by the dopant source), whereas the second one is placed near the sample position. Geometry factors were determined by a test evaporation with a third thickness monitor at the place of the sample. Source-sample distances were in the range of 15-25cm and much larger than the sample diameter (15 by 15mm), assuring even material thickness over the whole sample area. Typically, a time of >15min was waited between the evaporation of consecutive layers.

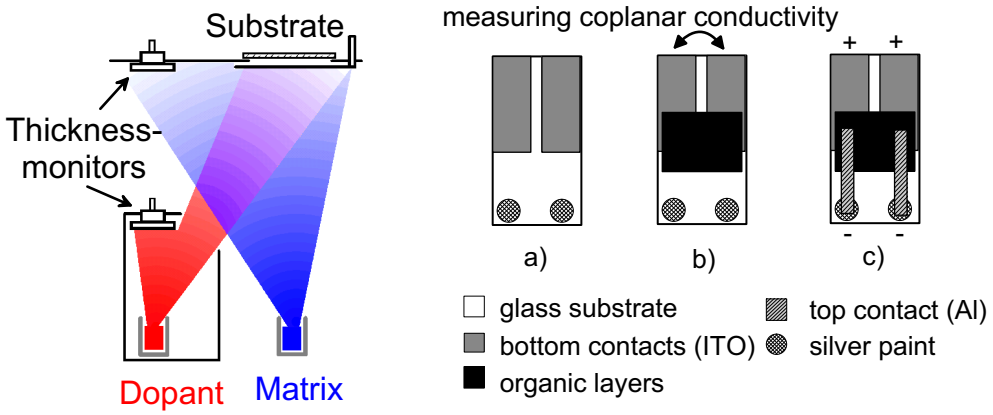

Figure 3.5: *(left) A schematic view on the method of co-evaporation to make doped organic layers. (right) The geometry and preparation steps of sandwich type OLED-samples: a) substrate with structured bottom contacts (ITO), b) after evaporation of the organic layers, c) with top contacts (Al). The overlap of the bottom and the top contact determines the active area of the OLED. The glass substrate is mounted into a teflon sample holder, which in the case of the UHV-system can be transferred between different chambers.*

The densities of ZnPc, VOPc, Tetracen, Pentacen and Perylen (see Table 3.1) were calculated from the crystal structure and molar masses, whereas the density of Alq_3 was determined by an independent thickness determination via thin layer absorption/reflection measurements in a UV-VIS spectrophotometer (Shimadzu UV-3100). The other densities

given in Table 3.1 are mean values for standard amorphous OLED-materials. To calculate a molar doping ratio from measured nominal thickness values of the quartz thickness monitors, a fictitious density is assumed for the dopant, namely the density of the matrix corrected by the ratio of the molar masses (e.g. 0.73 g/cm^3 for F_4-TCNQ in VOPc).

The electrical and optical behavior of the OLED-samples was determined in-situ. Therefore, four electrical sample-contacts were connected in-situ via molybdenum or stainless steel clamps, silver paint and a feed-through to a source-measure unit (Keithley SMU 236), allowing to prepare 2 complete samples on one substrate. The light intensity was measured by a calibrated photodiode with integrated amplifier (Laser Components LCI-5UV) in a setup according to Section 3.2. The calibration was done with a thermopile of known sensitivity and a spectral-calibrated halogen lamp. The photodiode can be moved to fine-adjust to the position directly above the OLED-sample. Because of the two base contacts on the substrate, the planar conductivity of the first organic layer on the conductive substrate could be measured during its evaporation (Figure 3.5). Typical device areas were 2mm^2.

3.4 Preparation of OLEDs in a multiple chamber ultra high vacuum system

3.4.1 Motivation for the cluster tool

Because of the restrictions given by a single chamber high vacuum preparation system regarding the amount of possible evaporation sources and the need to vent the system after every prepared sample, a new, more extensive vacuum system was needed. The setup of the system has been worked out and realized as part of this work in co-operation with BESTEC GmbH, Berlin, Germany.

The advantages of the new multiple chamber ultra high vacuum system (cluster-tool) are as follows:

- The main advantage is the possibility to prepare p-doped, n-doped and metallization layers in different chambers without breaking the vacuum. This prevents the dopants from getting mixed, which would reduce the doping efficiency drastically and make reproducible experiments impossible. Additionally, more complex sample structures are possible.

- Because of the possibility to transfer the sample holder (made from Teflon or ceramics) into load-locks (small vacuum chambers which can be vented and re-evacuated quickly), the evaporation chambers only need to be vented in case of re-filling the sources with raw material. This opens up the possibility to degas all sources (and hence purify the organic material) a sufficiently long time before making the first organic layer. Additionally, the sample can be transferred into a dry nitrogen glove box and may be encapsulated there in order to get an air-stable device. This can then be operated in air for a long time or investigated by other experimental techniques.

- Since every chamber can be operated independently, several users can make their preparation and measurements at the same time.

3.4.2 Setup of the cluster tool

The setup of the coupled ultra-high vacuum system (cluster tool) is sketched in Figure 3.6. All chambers are arranged around a central handler chamber (I), responsible for the transfer of the sample holder from and to all chambers. The width of the transfer tubes is 100mm allowing for sample sizes of 1 by 1 inch. The samples are mounted on Teflon or ceramic sample holders which have connection terminals for easy electrical connections inside the vacuum systems. Sample holders can be introduced into the system via two load locks. One is placed inside a dry nitrogen glove box (II). The other one (III) is connected to a sample transport box for the transfer of samples to another vacuum system without breaking the vacuum. Four outer chambers are dedicated to sample preparation: one for the metal layers (IV), one for intrinsic (undoped) layers (V), one for p-type doped organic layers (VII) and one for n-type doped organic layers (VIII). Chamber VI differs from chambers V,VII and VIII in the design of the evaporation sources. The 6 metal evaporation sources are electrically heated tungsten or ceramic boat-evaporators and one e-beam evaporator, respectively (see Figure 3.7). The boats can be refilled in-situ from a material storage box by means of a manipulator. The four organic evaporators in the chambers V,VII and VIII are placed in 4cm wide coolable tubes and can easily be exchanged and refilled, breaking the vacuum of only one chamber. In the chambers IV,V,VII and VIII, the sample holder can be connected to electrical and thermocouple feed-throughs via spring contacts (see Figure 3.8). Additionally, he may be connected to a cooling/heating station allowing to control the sample temperature between -150 ^{o}C and +150 ^{o}C . A mass-spectrometer can be connected to all evaporation chambers. Furthermore, the metallization chamber (IV) is equipped with a calibrated photodiode (Hamamatsu S1227-33BQ) connected to an amplifier unit. This allows for in-situ light-output measurements after the preparation of an OLED-sample. Chamber VI is used as a storage chamber for up to 8 samples.

The system is pumped by an oil-free combination of diaphragm backing pumps and turbo-molecular main pumps allowing for a base pressure of 5x10^{-9}mbar.

3.4.3 Preparation of OLEDs in the cluster tool

Basically, the way to prepare OLED-samples follows the one described in Section 3.3 with the following differences:

(i) The ITO substrates were heated to 120 ^{o}C over night. They were allowed to cool down to approx. 30 ^{o}C before evaporating the first organic layer.

(ii) All organic sources (except the F_4-TCNQ source) were held at temperatures above 150 ^{o}C at least one night before making the first organic layer. This reduces the water content of the organic materials. Additionally, due to the fact that the evaporation chambers are rarely vented, the material purity is enhanced by vacuum storage. Furthermore, the emitter material Alq_3 was stored in a high vacuum system between its purification by gradient sublimation and the introduction of the material into the cluster-tool.

(iii) The base pressure of the evaporation chambers was between 5x10^{-9} mbar and 1x10^{-8} mbar.

(iv) A new sample holder design allows to make 3 samples on one substrate. For the results given in Chapter 5, the best of the three was chosen.

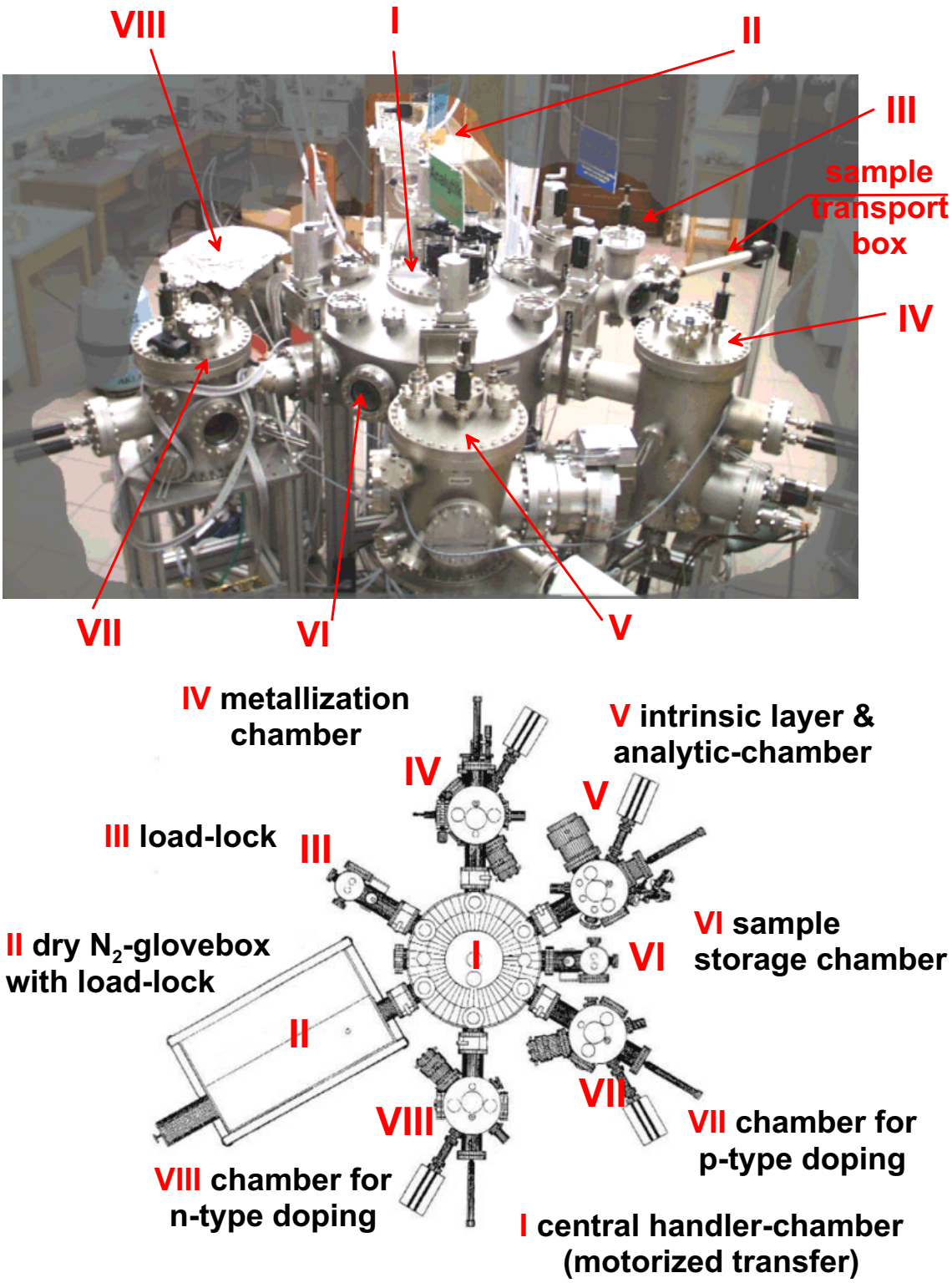

Figure 3.6: *Photograph (top) and a schematic view (bottom) onto the cluster tool designed for the preparation of organic multi-layer devices. The purpose of the different chambers is indicated.*

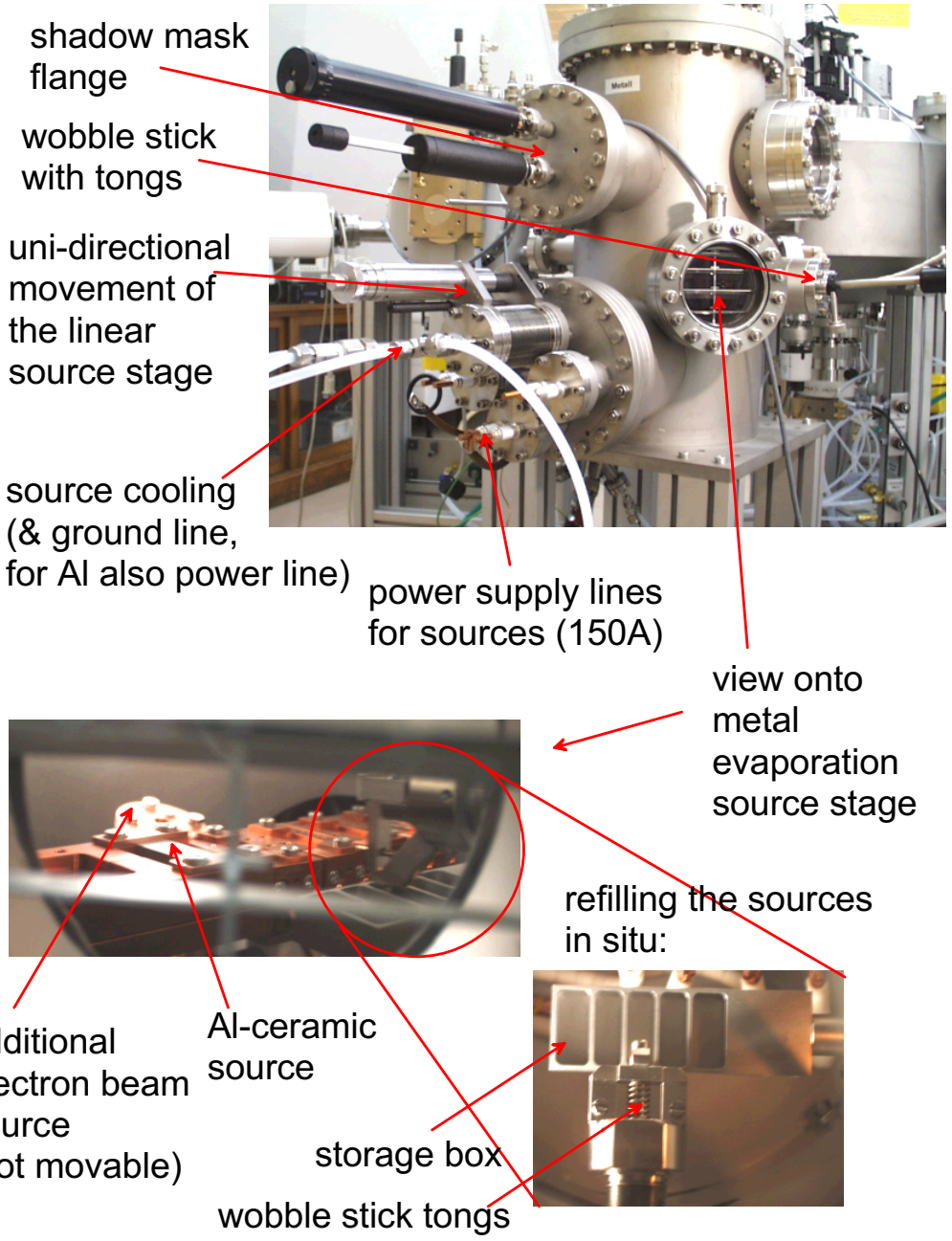

Figure 3.7: *View onto the metal chamber with the metal evaporation source stage. The whole stage can be moved to align the metal evaporator under the sample stage. The ground contact posts of the 4 standard evaporation sources (heated tungsten boats for Au, Ag, Mg and LiF or others) are cooled. In the case of the Al evaporator (a ceramic boat), both contact posts are water cooled to prevent temperature damage. The metal evaporation boats can be refilled in situ from a storage box via a wobble stick. Additionally, a small electron beam evaporator is equipped in the chamber.*

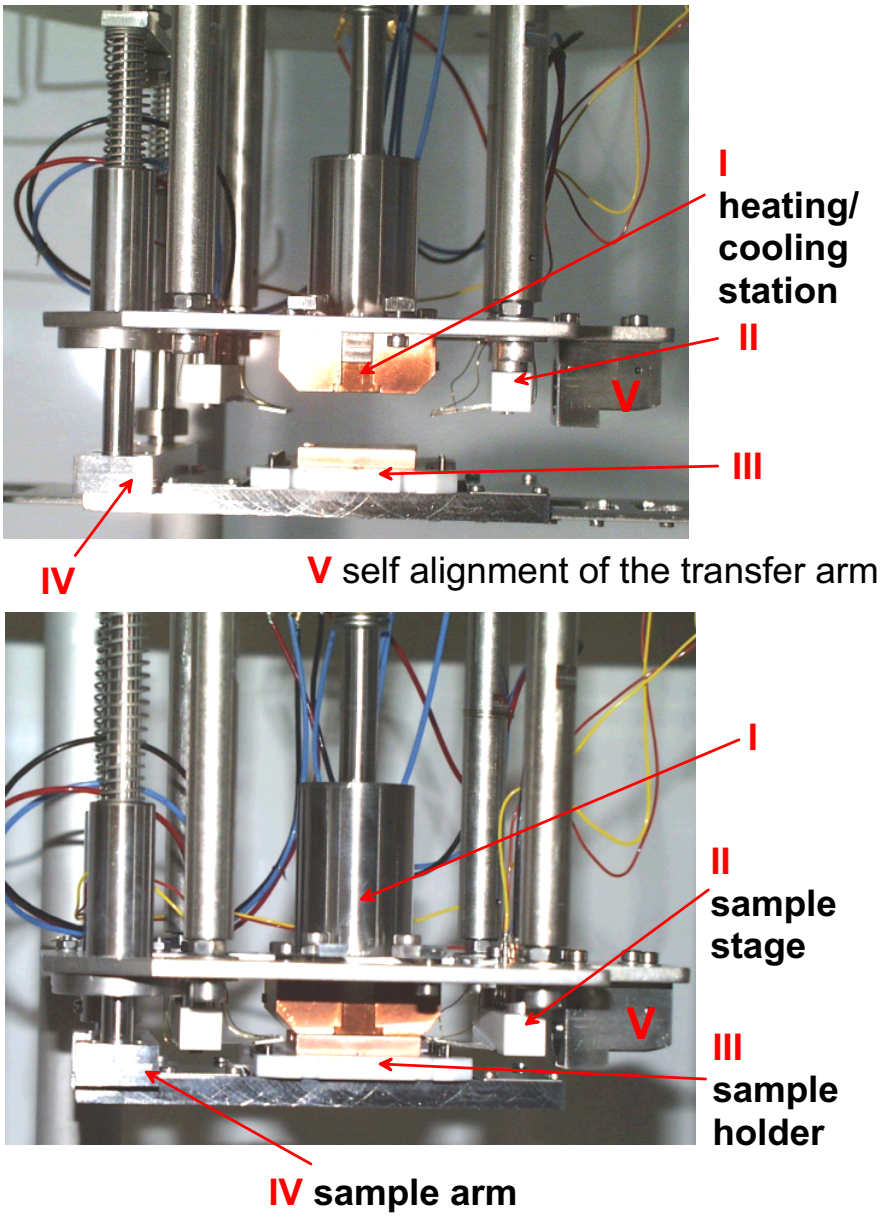

Figure 3.8: *The sample stage of all evaporation chamber (shown ex situ). Top: before the sample is connected electrically and thermally to the sample stage and the heating/cooling station (heating by shielded halogen lamps, cooling by a liquid nitrogen flow through the stainless steel block). Bottom: after connection by moving up the sample stage. The sample holder is transferred via the not shown handler arm (located in the handler chamber) which is self aligned in V. The electrical connection is made via spring clamps mounted at the sample stage and a connection terminal at the sample holder. The thermal connection can be improved by using an eutectic indium-gallium compound for better thermal contact between the copper block mounted on the heating/cooling station and the copper block tightly contacted with the sample to be heated/cooled. The sample stage also features adjustable shadow masks for the evaporation of organic or metal layers.*

(v) New evaporation sources for organic materials were used, which have a higher temperature evenness. This was achieved by using either graphite crucible heated by outer tungsten wires or using quartz crucibles with a small top hole inside an electrically heated tungsten foil. The evenness of this evaporation sources is proved by the fact that Alq_3 now evaporates without residues left behind in the crucibles.

(vi) During the preparation of a sample, the sample holder was transferred from chamber VII (p-type doped HTL layers) into chamber V (intrinsic blocking layers) and later into chamber VIII (emitting layers and n-type doped ETL layers). Finally the top contacts were evaporated in chamber IV where also the electroluminescence and current-voltage measurements were done.

3.5 Experimental aspects of the UPS/XPS-experiments

3.5.1 Analyzing system: Kratos

The basic design of a photoelectron spectrometer consists of several parts mounted together in a vacuum system: a sample holder, a UV-light source for ultraviolet photoelectron spectroscopy (UPS), an X-ray source for XPS and an electron detector. One needs an ultra-high-vacuum system basically for two reasons:

- The results of UPS and XPS measurements are strongly influenced by surface contaminations since both techniques are very surface sensitive. The time needed to cover a clean surface with a monolayer of a gas with a molecular weight of 28 (N_2) at room temperature depends on the partial pressure p (in mbar) of that gas in the vacuum system [135] as:

$$t_C\,[sec] \approx \frac{10^{-6} mbar}{s\,p} \quad , \tag{3.7}$$

  where s is the sticking coefficient ($s = 0..1$). Hence, a pressure of approx. 10^{-10}mbar yields a monolayer coverage time of 1 hour (assuming $s = 1$). This time is sufficient for a typical UPS/XPS experiment.

- Air (or oxygen) strongly absorbs radiation in the energy range above 6eV. Therefore, this radiation range is also called vacuum ultraviolet (VUV). Since there exists no VUV transparent hermetic window material, the UV-source has to be placed inside the same vacuum-system, where the sample and the spectrometer are situated.

For our experiments, we used a Kratos 'Axis 165 Ultra' UPS/XPS ultra high vacuum system (at the Chemistry Department of the University of Arizona in Tucson/USA). The X-ray source is a monochromatized Al-K_α radiation source (energy $h\nu = 1486.6$eV) with an approximate line width of 0.35eV FWHM. The excitation spot at the sample is 3 by 3mm, the sampling size only 300 by 700μm. The X-ray source was operated at 15kV acceleration voltage with an emission current of 15mA. The UV-light is generated by a differentially pumped resonance Helium(I)-discharge lamp with an energy $h\nu = 21.21$eV. The Helium was purified in a liquid nitrogen cold-trap before entering the discharge region. The beam spot diameter is approx. 1cm. The UV-intensity could not be varied (approx. 5x10^{14} photons/cm^2). The spectrometer is a concentric hemispheric electrostatic analyzer

with multichannel channeltron-detection of the electrons (the latter is used to enhance the signal to noise ratio for UPS-measurements). The typical pass energy for a high resolution XPS-measurement of a single XPS-peak was 10eV, whereas the pass energy for UPS measurements was held at 5eV. The base pressure of the analyzer chamber was approx. 10^{-9}mbar. The sample holder is independently grounded and was held (only during UPS-measurements) at -5V bias voltage of the sample with respect to the spectrometer. This is necessary to separate secondary electrons originating from the sample and the spectrometer, respectively [135]. The sample holder is moveable in all 3 directions to adjust the focus position of the spectrometer. This adjustment was done by optimizing the spectrometer signal with the bare substrate before each measurement and was held constant afterwards.

A preparation chamber with a base pressure of 10^{-7}-10^{-8}mbar is connected to the analyzer chamber. The sample needs to be transferred into the preparation chamber after each UPS/XPS-measurement. After evaporation of the next organic layer (which takes some seconds for the first very thin layer up to some hours for the last thick layer), the sample has to be transferred back for the measurement. This way, the evolution of the UPS and XPS-spectra with increasing layer thickness could be followed.

3.5.2 Substrates and their preparation

All substrates were ultrasonically cleaned with the three solvents chloroform, acetone and ethanol and dried for one hour in air. Afterwards, they were introduced in the load lock of the vacuum chamber and left there overnight. Finally, the Au and ITO-substrates were cleaned by argon-sputtering in the analyzer chamber immediately before evaporating the first organic layer. The success of the sputtering was tested by an XP-scan across the carbon C1s range (around 300eV binding energy), since most solvents and contaminations contain carbon. The sputtering was stopped after the disappearance of the C1s-peak. For gold, this took almost half an hour (at 10^{-7}mbar Ar-pressure, 1-2kV acceleration voltage and 10mA emission current), whereas for ITO 2-4 minutes were sufficient (at 1kV and 5mA). Note that a long Ar sputtering changes the workfunction of the ITO substrate.

The size of the substrates was approx. 15 by 15mm. In case of ITO on glass as substrate, the ground connection was done by a stainless steel clamp.

3.5.3 Preparation of mixed layers in the preparation chamber

The organic layers were vacuum sublimed with a constant and very low growth rate of 2-6Å/min for the matrix molecules and 0.1-0.2Å/min for the dopants. The investigated thickness range was 2Å for the first layer (first growth step, sub-monolayer coverage) up to approx. 200Å for the thickest layers. A monolayer coverage of ZnPc is reached at a nominal thickness of 8.5Å, assuming the sticking coefficient to be unity and assuming the bulk density value at the interface. The evaporation rate was measured with a free standing 10MHz-quartz thickness monitor (QCM) which had a resolution of 0.1Hz (which is approx. 0.03Å coverage for an organic layer density of 1.6 g/cm^3). The sublimation sources were resistance heated ceramic boats with shutters. All organic materials (except the dopant F_4-TCNQ) were cleaned by gradient sublimation. Doped layers were prepared by co-evaporation of the matrix and dopant molecules. The molar doping ratio for the doped samples was chosen to be approximately 1:30 for two reasons: (i) Because of the low

evaporation rate of the matrix, an even lower rate of the dopant was difficult to control. (ii) A lower content of the fluor containing dopant in the matrix would have made the measurement of the XPS-F1s peak impossible. The evaporation rate of the two sources was independently measured by only one QCM through opening/closing the appropriate source shutters. The temperature of the sources was held constant during every growth step. Additionally, the evaporation rates were checked between every two growth steps.

4 UPS/XPS-experiments

In order to reveal the energetic situation inside a light emitting diode, the method of a combination of ultraviolet and X-ray photoelectron spectroscopy (UPS/XPS) is used which is described in the beginning. Next, the evaluation of the UPS and XPS spectra is described. Following that, the results of UPS/XPS measurements on the junctions (1) doped and undoped ZnPc on ITO, (2) doped and undoped ZnPc on Au and (3) doped and undoped ZnPc on and below Alq_3 are presented. The parallel interpretation of these experiments shows that doping leads to a level bending in organic semiconductors in good agreement with the standard inorganic semiconductor theory. Doping shifts the Fermi-level towards the transport state (for p-type doping the HOMO level) which alters the injection behavior. This explains the more efficient hole injection from conductive substrates into doped organic layers observed for the OLEDs, which will be presented in Chapter 5.

4.1 Determination of the interface energy alignment by UPS/XPS-experiments

4.1.1 Basics

Ultraviolet photoelectron spectroscopy (UPS) is a powerful tool to reveal the energetic situation at a semiconductor/metal or semicondcutor/semiconductor interface [135, 136]. Since the measurement is very surface sensitive, layer-by-layer growth of the semiconductor under investigation gives all information about the evolution of band- or level bending in the semiconductor in dependence of the distance to the underlying substrate. Additional X-ray photoelectron spectroscopy (XPS) measurements enhance the sensitivity of the method to different physical and chemical processes which might occur at the semiconductor/metal interface. Recently, UPS and XPS have been used by several groups to investigate metal/organic [90, 137, 138, 139] and organic/organic [124, 140, 141, 142, 143] interfaces in more detail.

Both spectroscopic methods are based on the fundamental quantum hypothesis of Einstein. It relates the maximum kinetic energy E_{kin}^{max} of an electron escaping from a sample to the light frequency ν of the impinging radiation. For metals, the Einstein relation reads:

$$E_{kin}^{max} = h\nu - \Phi_S \quad , \tag{4.1}$$

where Φ_S is the work function (potential barrier at the interface) of the sample investigated. This process is the so called 'photoemission' of an electron by electromagnetic radiation or the 'photoionization' of a sample. More generally, the kinetic energy E_{kin} of an electron escaping from an N-electron system (leaving a system with N-1 electrons

behind) is given by $E_{kin} = h\nu - [E(N-1) - E(N)]$, where $E(N)$ and $E(N-1)$ denote the energies of the system with N and $N-1$ electrons, respectively.

The difference between UPS and XPS is given by the frequency of the exciting electromagnetic radiation, which is in the far-UV for UPS (energies between 10 and 40 eV) and in the X-ray-range for XPS (energy about 1000-2000eV). Thus, UPS releases valence electrons bound in the outer shells of atoms, molecules, and solids, whereas XPS releases electrons from core levels of atoms. Hence, UPS is especially suitable to determine the position and shape of the highest occupied molecular level (HOMO) of a molecule or molecular solid. XPS is very sensitive to changes of the chemical bonds of molecular atoms due to the so called chemical shift of the core level orbitals.

The surface sensitivity of UPS and XPS measurements originates from the low mean free path of electrons with energies between 10 and 2000eV due to scattering of the photo-emitted electrons within the solid. For a large number of different materials, a general curve of the escape depth as a function of the electron energy could be deduced (see Figure 4.1). The large penetration depth of the exciting radiation and the low mean free path of the emerging electrons is the reason for the large background-signal from secondary electrons (electrons that are scattered at least once inside the solid) in UPS and XPS spectra.

Figure 4.2 illustrates the various electronic potentials involved in an UPS or XPS experiment in the case of a semiconductor located on a metal substrate. On the right side the electron spectrometer (which measures the kinetic energy of the photo-emitted electrons emerging from the sample) with the workfunction Φ_D is sketched. An external voltage

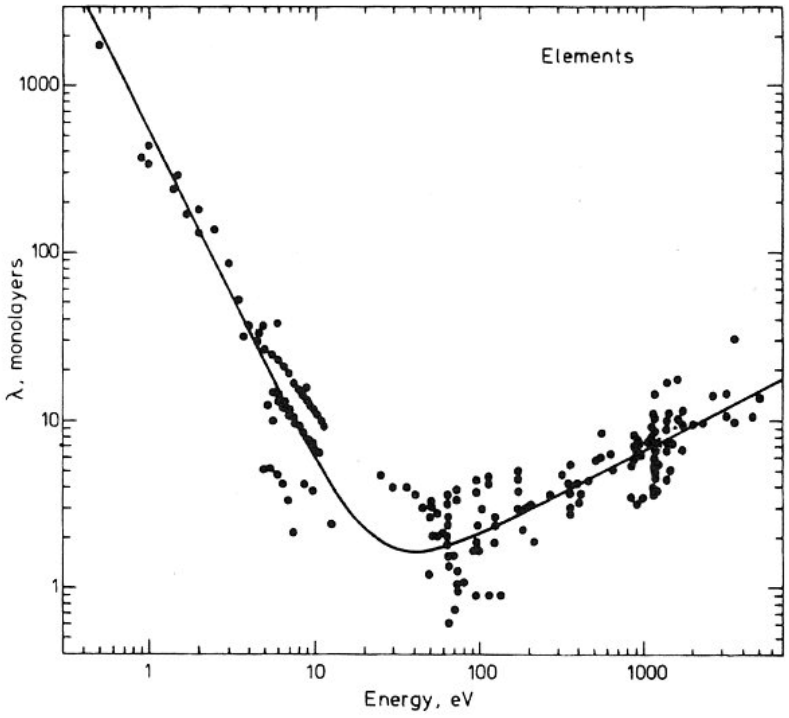

Figure 4.1: *Mean free path of electrons in solids as a function of their energy. The data points reflect electrons originating from different elements (taken from [144]).*

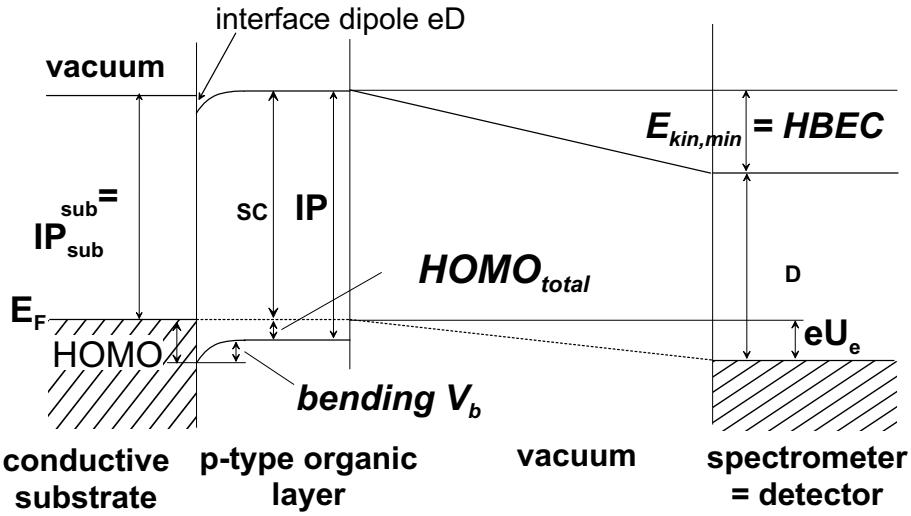

Figure 4.2: *Common energy level diagram for photoelectron spectroscopy including a metallic-substrate with a semiconductor on top (here a p-type doped organic semiconductor) and the spectrometer (see text for a detailed description of the mentioned values).*

U_e is supposed to be applied between the sample (metal substrate) and the spectrometer. Before more intense research activities on organic/metal interfaces started in the 1990's, vacuum level alignment (no interface dipole) and no level bending was generally assumed for junctions with organic semiconductors. For this simple case, the injection barrier for holes is given by the difference of the ionization potentials of the metallic substrate and the organic layer. Already from the first UPS-experiments it became clear that this assumption is not valid for almost all metal/organic heterojunctions [89, 124, 145].

Figure 4.3 shows typical UP-spectra for (i) a metallic substrate (in this case gold), (ii) a thin organic layer on the metallic substrate and (iii) a thick organic layer on top of the substrate (i.e. thick enough that no signal contribution from the underlying substrate can be measured). Two energies determine the position and width of an UP-spectrum. For the Au-spectrum as an example, the electrons with the highest kinetic energy (right side of the spectrum shown in Figure 4.3) originate from the Fermi-edge of the substrate (E_F in Figure 4.2). The cutoff E_{kin}^{min} of photoemission at the low kinetic energy side of the UP-spectrum is determined by electrons with a binding energy just low enough to be photoexcited to the vacuum level of the sample, which is the highest theoretically observable binding energy in an UPS-experiment (therefore also the name HBEC = high binding energy cutoff). Nevertheless, these electrons are mostly secondary electrons from states with lower binding energies. If a thin organic semiconducting layer is brought onto the metallic substrate, the signal from the substrate is reduced and new spectral features appear. In the case of level bending, these new features shift with increasing thicknesses of the organic layer (as sketched in Figure 4.2) because their energetic distance to the (aligned) Fermi-level changes. For thick organic layers, the features of the underlying substrate disappear (due to the short mean free path of the electrons inside solids) and well resolvable peaks near the former position of the Fermi-edge can be attributed to the electrons originating from the HOMO-levels of the molecules in the organic semiconductor (see the right peak in Figure 4.3). It should be noted that the high kinetic energy onset of

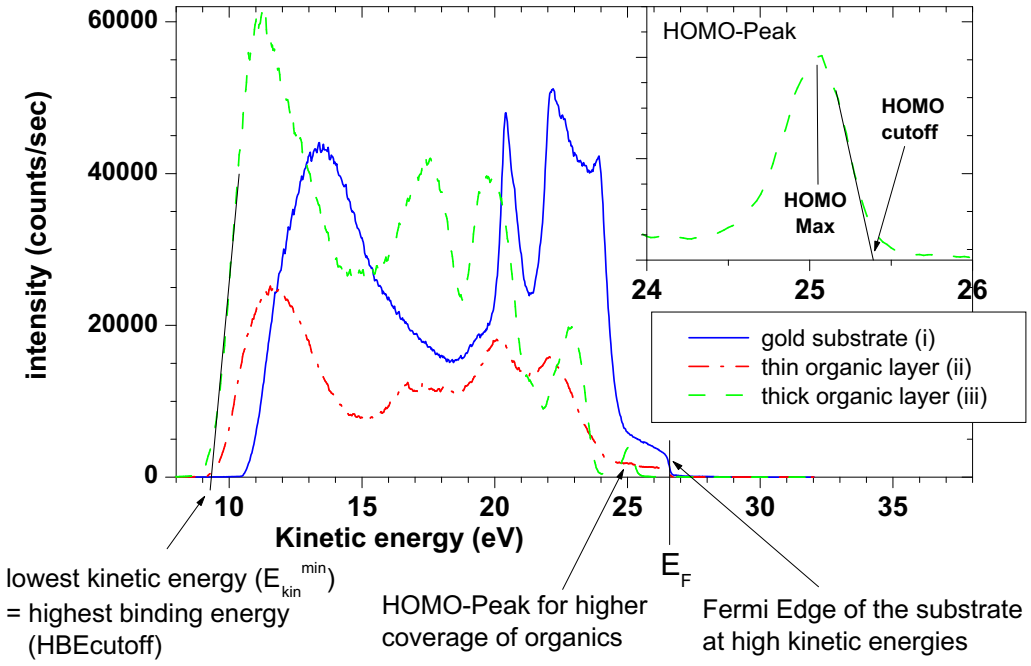

Figure 4.3: *Typical UP-spectra for (i) a blank gold substrate, (ii) a thin organic layer (ZnPc) on top of the Au substrate (thickness smaller than escape depth of the electrons) and (iii) a thick organic layer (ZnPc) on top of the Au substrate.*

the highest kinetic energy peak in an UP-spectrum of an organic material is not identical to the highest molecular orbital (HOMO) of a single molecule but is somehow related to it. Thus, the entire peak will be called HOMO peak for short in the following. The shape of this HOMO peak is determined by all solid state effects that are intrinsic properties of the molecular solid under investigation (for further details, see the discussion at the end of this Section). Since the photoelectron emission for organic and inorganic semiconductors starts at the HOMO-level or valence band edge, there is no direct measure of the Fermi-level inside the semiconductor. It must be determined from the assumption of Fermi-level alignment with the underlying conductive substrate, which is not necessarily true for some weakly conductive organic materials.

In principle, the level bending behavior of an organic semiconductor near the substrate could be seen by a shift of the whole UP-spectrum with increasing thickness of the organic overlayer. The expression 'level bending' refers to an electrostatic shifting of energy levels relative to the Fermi-level of a layer by a net space charge density inside the layer. Unfortunately, other processes at the interface between the organic semiconductor and the substrate, like the formation of interface dipoles, can affect the low kinetic energy onset of the photoemission. Thus it is sometimes not possible to separate these processes unambiguously. Here, the additional information from XPS might help. If level bending occurs, the position of core level peaks of the molecules that forms the layer in which

the level bending takes place should ideally shift the same way the whole UP-spectrum is shifting. Moreover, for the case of an organic/organic heterojunction, XPS helps to decide whether the level bending takes place in the under- or the overlayer. For underlayer level bending, all XPS peaks of elements belonging to both organic layers should shift together during the establishment of the equilibrium energy alignment with increasing overlayer thickness [141]. In the case of overlayer level bending only the overlayer core level peaks shift. Additionally, from a change of the peak shape of the XPS-peaks, one can retrieve information regarding chemical reactions of the different molecular species at the interface.

From the basic considerations above, a way to determine the energetic alignment at an organic semiconductor/conductive substrate interface can be deduced according to Figure 4.2. We follow here mainly the evaluation scheme given by Schlaf et al. [141, 146].

Values which can be directly taken from the UP-spectra in a kinetic energy scale are E_{kin}^{min} (or HBEC), the difference $\Delta HOMO$ of the HOMO cutoff energy (see inset of Figure 4.3) to the Fermi energy of the underlying substrate and the ionization potential IP. The latter is calculated from the width of the whole spectrum according to:

$$IP = h\nu - (E_{kin}^{max} - E_{kin}^{min}) \quad , \tag{4.2}$$

where $h\nu$ is the energy of the exciting radiation. For the conductive substrate, E_{kin}^{max} is the kinetic energy of the photoelectrons emitted from the Fermi edge of the conductive substrate ($E_{F,sub}$), for the organic overlayer, E_{HOMO}^{cutoff} is taken as E_{kin}^{max}. With the assumption of Fermi level alignment over the entire organic layer, the total energy balance equation of the measuring system is:

$$E_{kin}^{min} = \Phi - \Phi_D - eU_e \quad , \tag{4.3}$$

where U_e is the external voltage between the sample and the spectrometer, Φ_D the detector workfunction and Φ the workfunction of the outermost layer. Without an organic coverage, Φ is the workfunction of the substrate Φ_{sub} which equals the ionization potential IP_{sub} and hence the actual detector work function can be calculated:

$$\Phi_D = IP_{sub} - E_{kin,sub}^{min} - eU_e \quad . \tag{4.4}$$

Now, the workfunction $\Phi = \Phi_{SC}$ at a certain thickness of the organic semiconductor overlayer can be obtained from the HBEC. Equations (4.2)-(4.4) yield:

$$\Phi_{SC} = E_{kin}^{min} + IP_{sub} - E_{kin,sub}^{min} = E_{kin}^{min} + h\nu - E_{F,sub} \quad . \tag{4.5}$$

In order to reveal the energy alignment at the organic semiconductor / conducting substrate interface, one has to measure the development of the HBEC and the HOMO peak cutoff in the UP-spectra and the shifts of suitable element peaks in the XP-spectra with increasing thickness of the organic overlayer. From these values, one can deduce the difference $\Delta HOMO_{total}$ between the substrate Fermi-level and the HOMO cutoff energy of the thickest organic overlayer (assuming that for higher thicknesses no further shift of the spectrum takes place). Furthermore, the ionization potential $IP_{organic}$ for a thick overlayer and the difference of the HBEC between the thick organic layer and the substrate (ΔE_{HBEC}) as well as the total level bending $V_{b,total}$ in the space charge region in the organic layer near the substrate can be deduced. The latter can either be obtained from the shift of the whole UP-spectrum or from the shift of suitable elemental peaks,

as described above. The difference $\Delta HOMO$ between the HOMO energy of the organic material and the Fermi energy of the substrate directly at the interface which gives the Schottky barrier height can then be calculated:

$$\Delta HOMO = \Delta HOMO_{total} - V_{b,total} \quad . \tag{4.6}$$

Additionally, the interface dipole energy can be obtained from:

$$eD = -[\Delta E_{HBEC} - V_{b,total}] = -[\Delta HOMO - (IP_{organic} - IP_{sub})] \quad . \tag{4.7}$$

In the equation above, a negative sign for eD was chosen if electrons are accelerated across the interface away from the substrate (following [89] and [147]).

To deduce the following energy level alignment schemes in accordance with Figure 4.2, the following values were measured or calculated: (i) the ionization potential IP_{sub} of the substrate (from the width of the substrate UP-spectrum: equation (4.2)), (ii) the ionization potential $IP_{organic}$ of the thick organic overlayer, (iii) the distance $\Delta HOMO_{total}$ of the HOMO cutoff energy at thick organic layer coverage to the Fermi-energy of the substrate and (iv) the level bending value V_b. The values of $\Delta HOMO$ and eD can then be calculated according to equations (4.6) and (4.7).

Before closing this Section, a short discussion about two important points discussed controversially in the literature should be given here (e.g. [89, 138]): (i) The question wether one should take the HOMO onset or the maximum of the HOMO-peak as a relevant energy measure for the interpretation of the UPS-data. This is closely related to the origin of the broad HOMO-peaks in a typical UP-spectrum of organic solids. (ii) The applicability of the concept of level or band bending in order to interpret the energy alignment of organic semiconductor/metal junctions.

(i) There are several effects which in principle could broaden an UPS signal of a hypothetically sharp molecular state (like the HOMO). First, there is the resolution-limitation of the electron spectrometer which was some years ago in the range of 1eV and, hence, very important. Today, this effect can be neglected. Second, the limited lifetime of photo-generated holes causes a symmetric broadening of the HOMO-peak. If this would be the decisive factor, the peak maximum would have to be evaluated, since the onset would have no physical meaning.

The following effects are connected with the nature of a molecular solid. First, small bands might be formed in organic solids for the case of stronger interactions between neighboring molecules (especially if the degree of ordering is high, e.g. in molecular single crystals). As for inorganic semiconductors (band-edge picture), the HOMO peak onset would have to be taken for the determination of both the ionization potential of the organic solid and the determination of the interface barrier for charge injection from a conductive substrate into the organic layer. Secondly, there are the processes of electronic relaxation inside the molecule and inside the solid. However, these relaxation processes are faster than the release of a photoelectron and, thus, should not influence the HOMO peak shape. In contrast, the phononic relaxation of molecular and crystal vibrations takes place at a comparable time scale [135]. Similar to optical spectroscopy, Franck-Condon satellites might be resolved in the UP-spectrum if the spectrometer resolution is high enough (see Figure 4.4a). Vibrational energies of molecules amount to some 100meV and can be seen in UPS experiments on molecular gases [135]. The vertical transition which

is observed with the highest intensity and therefore mainly determines the peak position does not necessarily lead to the relaxed final state. Taking into account that only the adiabatic transition S_{0-0} is fully relaxed, the HOMO-peak onset would have to be chosen for the determination of the ionization potential.

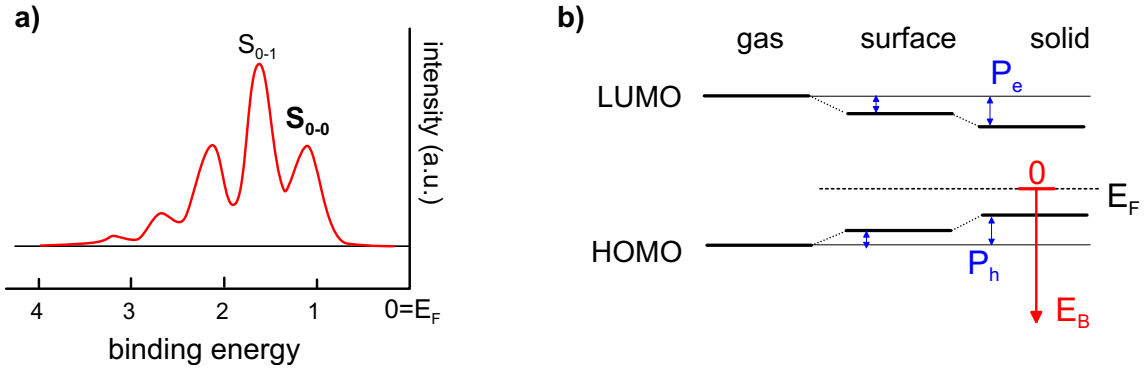

Figure 4.4: *(a) A schematic view on Franck-Condon satellites of a molecular UP-spectrum. Only the S_{0-0} transition is fully relaxed (adiabatic transition). In this example the S_{0-1} transition is the vertical transition with the highest intensity. (b) Energetic situation at the surface and in the bulk of a molecular solid: the binding energy of the HOMO is smaller in the bulk.*

Yet another effect is sketched in Figure 4.4b. The influence of the polarization energies P_e and P_h for electrons and holes in the bulk is higher compared to molecules at the surface of an organic solid. Hence, the binding energy of the HOMO in the bulk is smaller. As one is interested in bulk conditions, the HOMO-onset is the reasonable value.

From the effects listed above, it seems that mainly the phononic relaxations and band effects are relevant. Therefore, one might expect a non-symmetric shape of the HOMO-peak of an organic solid. Despite that, measured HOMO-peaks can often be described fairly well with mixed Gaussian-Lorentzian-peak shapes. This might be due to the fact that all mentioned effects together with disorder in molecular solids (which leads in a first order approximation to a Gaussian distribution of the density of states) and signals from deeper layers contribute to the UP-spectrum and finally a complicated, but in first-order-approximation symmetric, HOMO-peak shape results.

For reasons mentioned above we measure the high kinetic energy cutoff of the HOMO-peak to deduce the ionization potential. Furthermore, we believe that for the explanation of injection phenomena into organic solids, the adiabatic energy transition of the photoexcited electron is of exclusive importance. This means that the final state of the molecular crystal after the photoionization process should be the phononic ground state. However, some groups choose the HOMO maximum as the relevant energetic level [148] to explain charge carrier transport phenomena in disordered molecular layers, distinguishing rather arbitrarily between ionization potential (where still the cutoff is used) and the HOMO-position. One should keep in mind that, as described above, the width and shape of the HOMO peak does not directly reflect the width of the transport state distribution.

(ii) The term 'level bending', as we use it in this work, is an equivalent of the expression 'band bending' used for inorganic semiconductors to describe electrostatic effects of a net space charge density (Poisson's equation). As we will see later, the inorganic semiconduc-

tor band bending concept describes our experimental findings for the Schottky-junction between doped organic layers and conductive substrates well.

Nevertheless, one needs to keep in mind that the underlying physical process might not be similar to band bending. This is especially true for the case of nominally undoped organic layers on metals. The origin of level shifts in intrinsic organic layers on metal substrates is still a subject of great controversy in literature (compare [146, 149, 150, 151] and [152, 153, 154, 155]). Hill et al. explained the observed level shift of 0.4eV over a distance of 30Å from the contact in an Alq_3 layer on top of a magnesium substrate by polarization screening of the organic molecules in front of a metal [155]. The same group found a HOMO level shift of approx. 0.8eV over 30Å for PTCBI (perylenetetracarboxylic bisimidazole) on magnesium [153], which they interpreted as interface dipole due to a chemical reaction or a distortion of the organic molecules. In another publication [152], they carefully investigated the development of the first organic monolayer. They suggest that HOMO position and XPS peak shifts in that thickness range relates to the development of the interface dipole during the grow of the first monolayers of metal-quinolates on Ag. For this effect, the UPS HOMO shift and HBEC shifts have to be in the same direction. In contrast, Schlaf et al. explained a level shift of 1.5eV over a distance of approx. 300Å in Gaq_3 (tris-(8-hydroxy-quinolate)gallium) on platinum with an electrostatic level bending effect [146]. This level bending might be due to an unintentional n-type doping of the organic layer. For this material combination, they additionally found a strong interface dipole.

4.1.2 Evaluation of the spectra

From the UP-spectra of the conductive substrate and the organic overlayers, the following values were determined: (i) the position and width of the Fermi edge of the conductive substrate, (ii) the high binding energy cutoff of all layers, (iii) the HOMO-peak position of all organic layers and (iv) the Homo-peak onset for all organic layers (if possible).

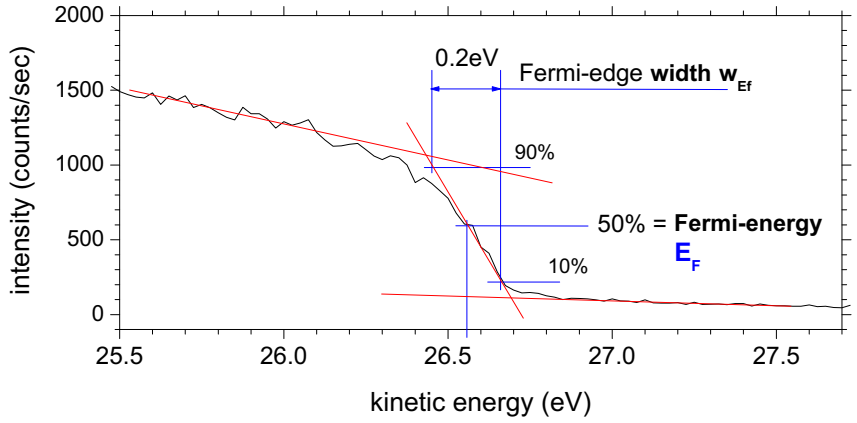

Figure 4.5: *A typically Fermi edge measured for an uncovered Au-substrate.*

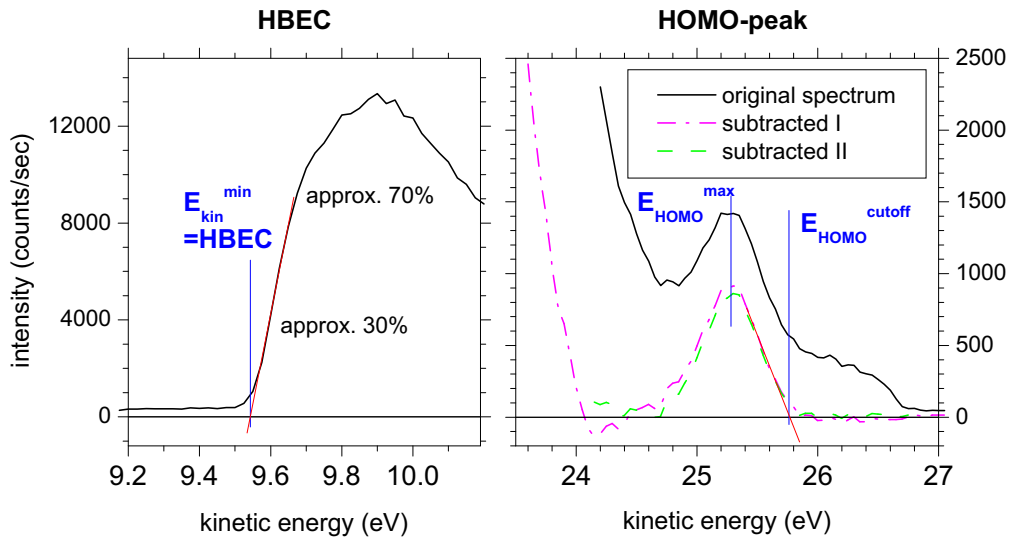

Figure 4.6: *The determination of the high binding energy cutoff ($HBEC = E_{kin}^{min}$) and the HOMO peak maximum (E_{HOMO}^{max}) and cutoff (E_{HOMO}^{cutoff}) positions from the UP-spectrum of a 96 Å thick ZnPc-layer on Au (left=high binding energy part; right=low binding energy part with HOMO-peak). The three spectra of the right figure refer to (i) the measured spectrum, (ii) the substrate background corrected spectrum ('subtracted I') and (iii) the both substrate background and secondary electrons background corrected HOMO-peak spectrum ('subtracted II').*

The Fermi-edge of a typical Au-substrate is shown in Figure 4.5. The 10%-90% width of the Au Fermi-edge is approx. 200meV. According to the Fermi-Dirac statistics a width of $\approx 4.4kT$ would be expected, i.e. 110mV at room temperature. Therefore, the resolution of the instrument can be approximated to be 90meV. Hence, calculating a width of the UP-spectra from the high binding energy cutoff and the HOMO-peak cutoff results in ionization potentials 0.09eV too high. Throughout this work, results are not corrected for this error. The Fermi-energies E_F are measured in the center of the Fermi-edge slope. The signal to noise ratio at the Fermi-edge of an ITO substrate is smaller compared to an Au Fermi-edge but can still be clearly resolved. It should be noted here that for a constant spectrometer workfunction the measured Fermi energy is independent of the substrate.

The high binding energy cutoff ($HBEC = E_{kin}^{min}$) was determined by the energy-axis intersection of a straight line fitted to the slope of the spectrum in the range of approx. 30% to 70% of the peak height (see Figure 4.6). The HOMO-peak of an organic overlayer was treated as follows: The intensity of the substrate signal can be evaluated in a spectral region where no overlayer signal is present for the thickest organic layer coverage (see spectrum 'subtracted I' in Figure 4.6). After subtraction of the substrate background signal, the background of the secondary electrons is subtracted by a polynomic fit to the surrounding of the HOMO-peak. The resulting HOMO-peak shape (see spectrum 'subtracted II' in Figure 4.6) can be approximated by a Gaussian peak. The maximum of the HOMO-peak E_{HOMO}^{max} is deduced from a corresponding peak fit. The HOMO-

peak onset (or cutoff) E_{HOMO}^{cutoff} is determined by fitting a straight line to the slope of the HOMO-peak (in accordance with the HBEC-determination). The measurement error of this procedure is less than 20meV, hence better than the resolution of the spectrometer.

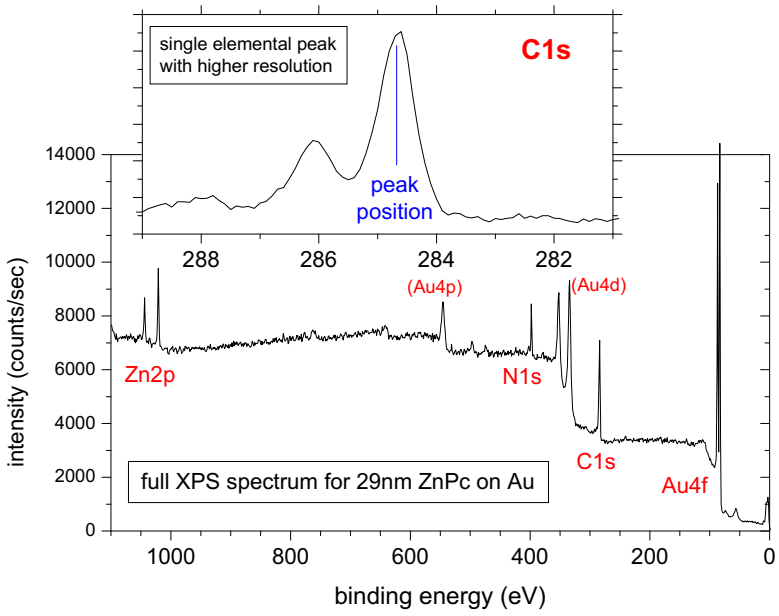

Figure 4.7: *XP-spectrum of 290Å ZnPc on top of an Au-substrate. The inset shows the structure of the XPS signal from the 1s-electrons of carbon (C1s, measured with a higher resolution). The different maxima belong to differently bound carbon atoms inside the ZnPc molecule. The actual maximum position was determined by a peak fit procedure described in the text. In case of level bending in the molecular layer in front of the substrate, the peak position of all XPS-peaks of the molecular layer must shift in parallel, whereas the Au-peak positions should remain constant.*

Figure 4.7 shows a typical XP-spectrum of an organic material on top of an Au-substrate. The XPS peak positions (and widths) were determined by fitting the data with several Gaussian/Lorentzian (70:30) line shapes after subtracting the background.

4.2 Experimental results of the UPS/XPS-experiments

4.2.1 Doped and undoped ZnPc on ITO

Phthalocyanines, especially copper-phthalocyanine (CuPc), are widely used as hole injection layers in OLEDs (see e.g. [38, 39, 62]) due to the fact that their HOMO energy (5.0-5.3eV) lies between the workfunction of the typical transparent anode ITO (4.4-4.9eV) and the HOMO of typical hole transport materials like TPD or NPD (5.4-5.6eV). This leads to a stepwise and, hence, more efficient injection of holes from the anode into

the hole transport layer. Here, we investigate the energetic behavior of the junction between doped and undoped ZnPc and ITO. ZnPc has properties similar to CuPc (CuPc: HOMO=5.2eV, LUMO=3.5eV [128]). We have chosen ZnPc as the model system for the first UPS/XPS investigations since it shows a high doping efficiency with F_4-TCNQ (see

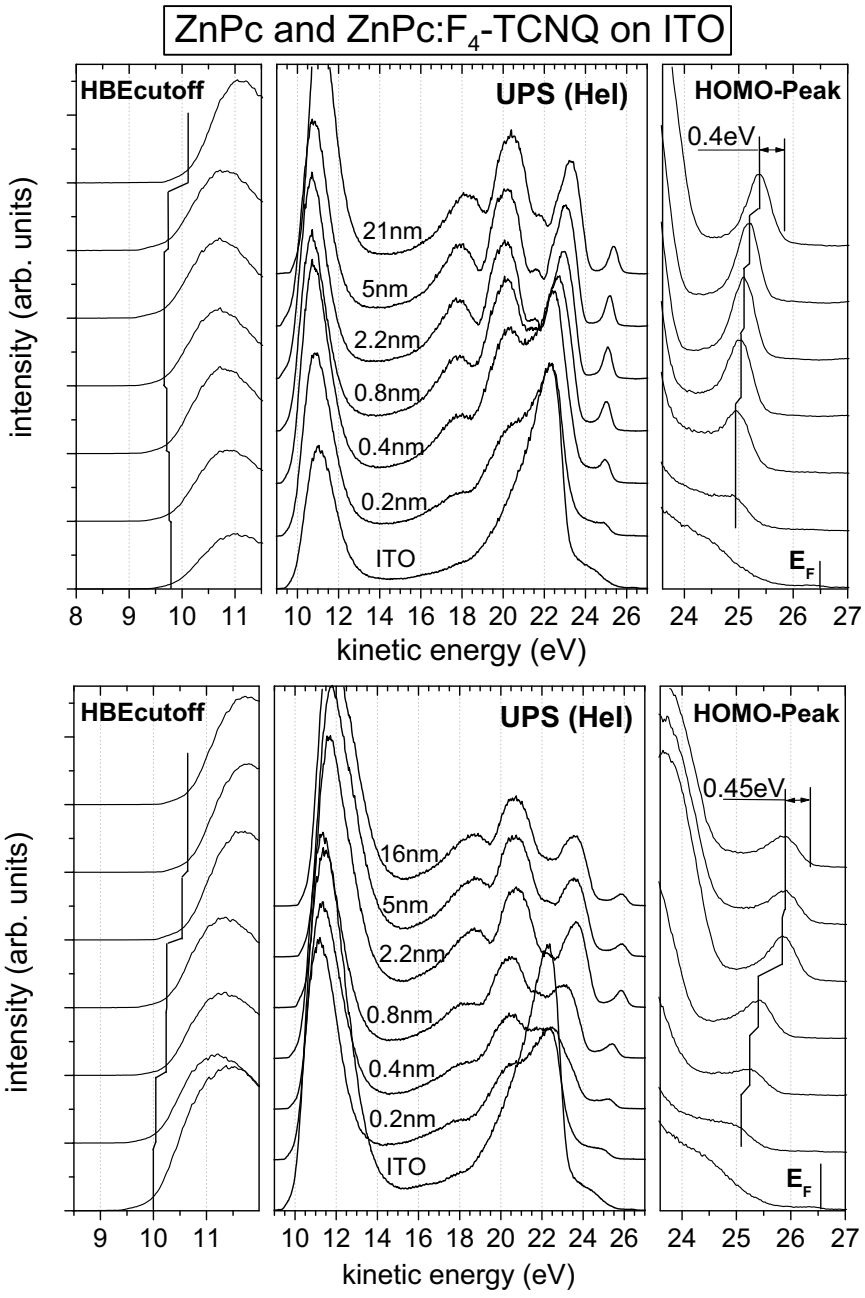

Figure 4.8: *Evolution of the UP-spectra for (top) ZnPc on ITO and (bottom) F_4-TCNQ-doped ZnPc on ITO. The vertical lines mark the shifts of the high binding energy cutoff and the HOMO peak shift. The values 0.4eV and 0.45eV mark the (constant) HOMO-peak width (i.e. the distance of the peak maximum to the cutoff).*

Section 2.3).

Figure 4.8 (upper part) shows the development of the UP-spectra for undoped ZnPc on ITO as a function of the ZnPc layer thickness. The data are shown on an uncorrected kinetic-energy scale. The lowest spectrum is for bare ITO with a Fermi edge at E_{kin}=26.5eV. The ZnPc HOMO-peak appears at $E_{\mathrm{kin}} \cong 25$eV (maximum value) and shifts slightly towards lower binding energies at higher coverage. The width of the HOMO peak does not change systematically. No other features in the energy gap range of the UP-spectra are observed, which would point towards a chemical reaction at the interface or polaronic states [153]. On the high binding energy side, the cutoff first shifts slightly to higher and later back to lower binding energies, indicating an interface dipole layer (opposite to the space charge layer developing later).

Figure 4.8 (lower part) shows the development of the UP-spectra for ZnPc doped with F_4-TCNQ on ITO. The molecular doping ratio is approx. 30:1. The HOMO shift is larger but in the same direction as compared to undoped ZnPc on ITO. The HBEC shifts in the same direction as the HOMO.

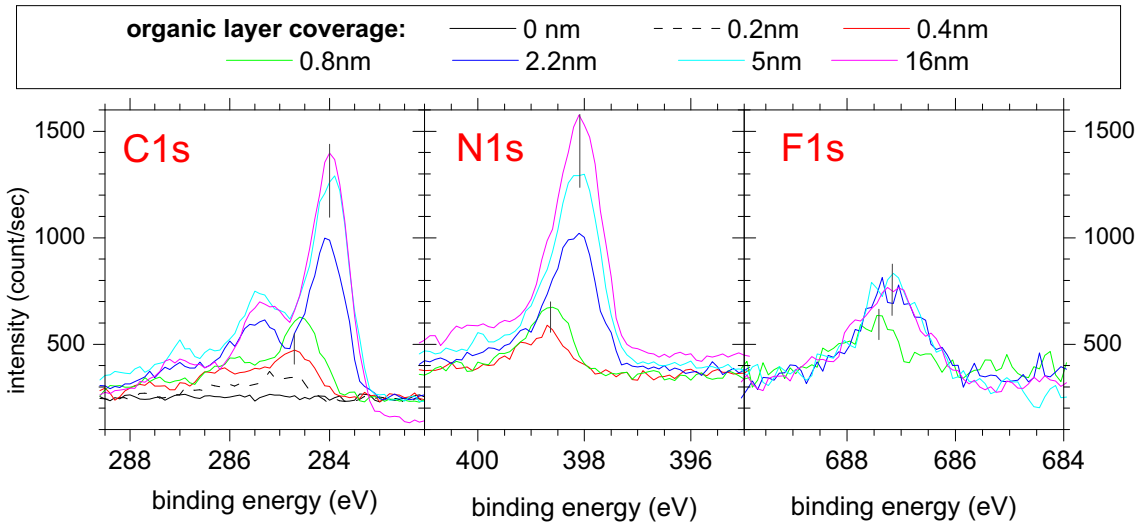

Figure 4.9: *Development of the XP-spectra with increasing organic layer coverage of F_4-TCNQ doped ZnPc on ITO for the three elemental peaks C1s, N1s and F1s. The background level of the F1s peak was renormalized to fit to the presentation.*

Figure 4.9 gives some examples of XP-spectra for doped ZnPc on ITO. Shown is the development of the spectra for the signal peaks originating from C1s, N1s and F1s electrons. The first two belong to the ZnPc matrix whereas the latter belongs to the dopant F_4-TCNQ. They all shift in the same direction. However, the peak position of the F1s peak for very low organic layer coverage could not be determined because of a low signal to noise ratio. This is due to the low cross-section of the F1s electrons and the low concentration of dopant molecules in the matrix.

UPS and XPS shifts are summarized in Figure 4.10. The left column refers to undoped ZnPc on ITO, the right part to doped ZnPc on ITO. The top part shows all relevant XPS

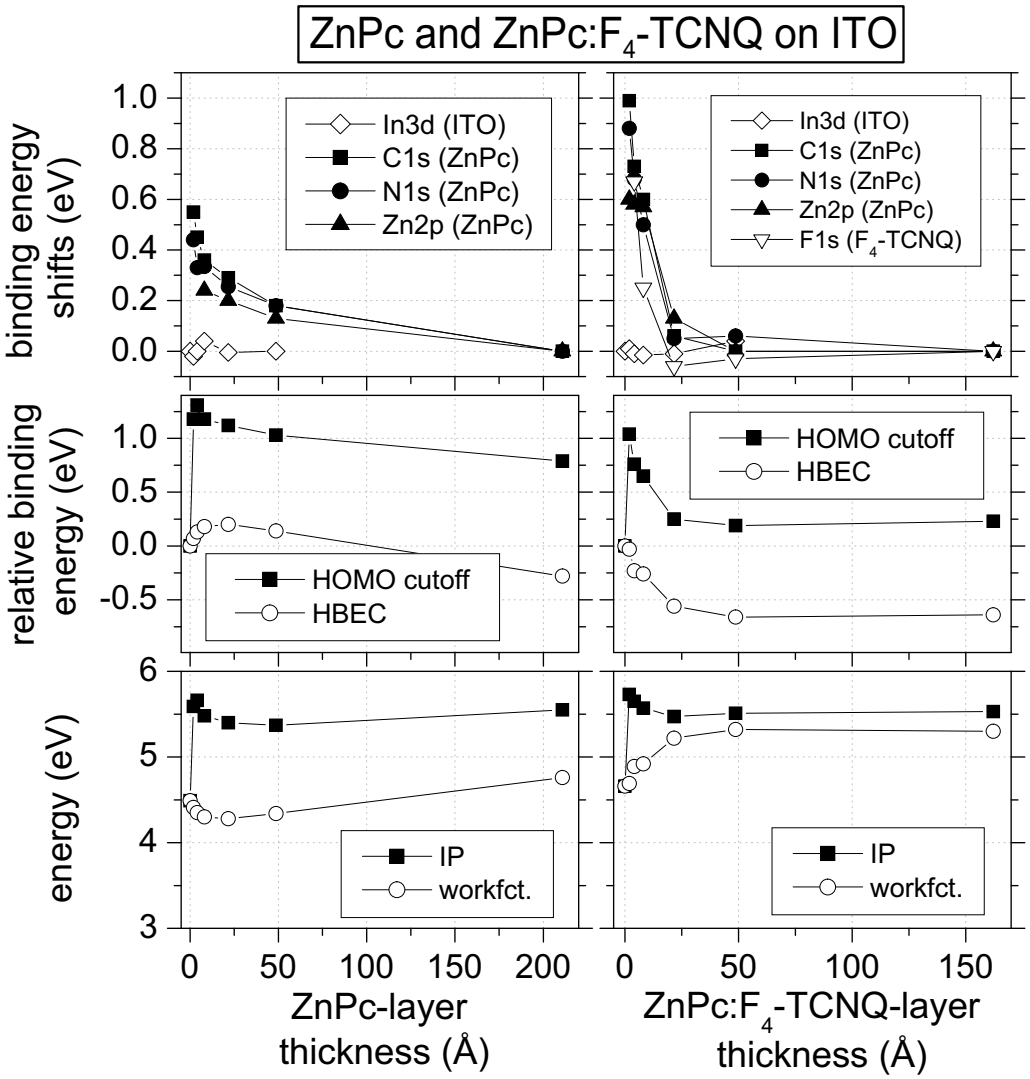

Figure 4.10: *UPS energy shifts and XPS peak shifts for (left) ZnPc on ITO and (right) doped ZnPc on ITO. The shifts are positive in direction of higher binding energy. XPS zero energy is defined at the peak position for zero organic coverage for elemental peaks originating from the substrate and at highest coverage for elemental peaks originating from the organic overlayer. The zero energy of the HOMO cutoff is defined as the Fermi-energy of the substrate. Zero energy of the HBEC is the HBEC position without organic coverage. The shift of the HBEC-energy indicates the presence of an interface dipole and level bending during the growth of the overlayer. The workfunction is measured relative to the vacuum level.*

peak shifts on a binding energy scale. For XPS peaks belonging to the substrate zero shift is defined at the peak position without overlayer coverage. For overlayer XPS-peaks, zero shift is defined at the highest overlayer coverage. The graphs in the center show the shifts of the HOMO cutoff on a binding energy scale relative to the Fermi edge position

of the substrate and the change in the HBEC relative to the position of the HBEC of the substrate. The bottom graphs summarize the development of the ionization energy IP and the workfunction Φ_{SC} of the organic layer. Note that the region where UPS and XPS peak positions are changing is much smaller in the doped case, indicating a smaller space charge layer width at the interface.

Figure 4.11 shows the energy diagrams derived from the photoemission data for the case of nominally undoped ZnPc (left) and for ZnPc doped with F_4-TCNQ (right) on ITO substrates. The measured level shifts are treated as an electrostatic level bending effect. For its determination from UPS and XPS experiments, the measurement of the peak position at very low coverage is an intrinsic problem. Thus, the level bending was calculated as a mean value of the peak-shifts for peaks which were reliably observable for the lowest organic coverage (namely the C1s and N1s peaks). For the experiments discussed here, the HOMO shifts agree with the level bending values obtained from XPS within error. In both the undoped and the doped case, we observe an interface dipole of about -0.3eV, with a direction corresponding to electron transfer to the ITO. It should be noted here that, for nominally undoped ZnPc on ITO, the change of the peak positions between 50Å and 200Å is most probably (at least partly) caused by extrinsic effects. This cannot be sample charging, since the shifts are in direction to lower binding energies. These possible extrinsic effects is accounted for by the larger experimental errors given in Figure 4.11 for the ionization potential $IP_{organic}$ and the total HOMO shift $\Delta HOMO_{total}$ as compared to doped ZnPc on ITO.

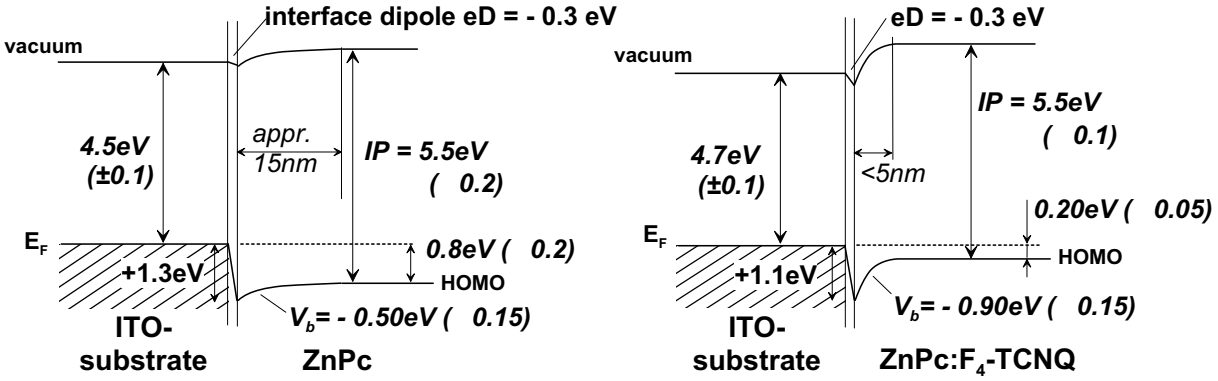

Figure 4.11: *Energy level scheme as obtained from UPS and XPS for the contact between ITO and ZnPc. The left side shows the energetic structure for the undoped case; the right side for ZnPc p-type doped with F_4-TCNQ.*

Summarizing the data presented above, the main observations are the following:

1. The Fermi level in the doped ZnPc layer is shifted towards the HOMO states by about 0.6eV compared to the undoped case, clearly showing the effect expected from efficient doping and backed by the Seebeck measurements on p-type doped organic layers (Chapter 2.3).

2. Accordingly, we observe a much higher level bending in the doped case compared to the undoped case.

3. The width of the space charge layer is reduced in the doped case compared to the undoped case. Although these values are more qualitative, one clearly sees a reduction of the width of the space charge layer from >15nm in the undoped to <5nm in the doped case. With the observed level bending of $V_b = -0.9$eV and the nominal doping density of 1:30 ($N_A = 1/30\, N_{mol} \approx 5\text{x}10^{19}\text{cm}^{-3}$), the width w of the space charge layer can be calculated from standard semiconductor theory (e.g. [156]):

$$w = \sqrt{\frac{2\varepsilon\varepsilon_0}{e}\,\frac{1}{N_A}\,V_b} \quad . \tag{4.8}$$

   Choosing $\epsilon = 4$ [98] results in a width w of the space charge layer for the doped case of 2.8nm, which is in reasonable agreement with the experiment. The origin of the level shift in the undoped case remains unclear since for level bending a much wider space charge layer than 15nm should be observed. From 0.4eV level bending and 15nm space charge layer width, a dopant density of 1:2000 can be calculated which is above the expected trap density for ZnPc purified by gradient sublimation. The origin of such a behaviour for intrinsic organic layers on metal substrates is still a subject of great controversy in literature (e.g. compare [149, 150, 151] and [152, 153, 154, 155]). In the case of phthalocyanines an unintentional p-type doping with residual oxygen is possible. However, our previous doping experiments (Section 2.3) show a conductivity for air-exposed ZnPc which is very much below that of a F_4-TCNQ doped ZnPc layer at a doping ratio of approx. 1:2000.

4. The interface dipole is of the same sign and very similar magnitude for doped and undoped ZnPc. This gives evidence that the interface dipole is mainly caused by a charge transfer reaction between ZnPc and ITO.

5. The ionization potential is not affected by doping. Note that the measured ITO ionization potential differs for the undoped and the doped case, although it is physically the same substrate with the same cleaning procedure. However, it is known from literature that the ITO workfunction can change dramatically by small surface modifications (see e.g. Kim et al. [45]), like they may caused by different sputtering times.

4.2.2 Doped and undoped ZnPc on Au

Additional UPS/XPS-experiments were carried out for which a poly-crystalline gold-foil was used as the substrate. They help to further clarify the doping effect of F_4-TCNQ in ZnPc.

Again, Figure 4.13 (upper part) shows the development of the UP-spectra for undoped ZnPc on Au as a function of the ZnPc layer thickness. The Fermi-energy of the gold is again at approx. 26.5eV. The ZnPc HOMO-peak maximum appears at approx. 1eV below the Fermi-edge and shifts to lower kinetic (higher binding) energies at higher coverage. The width of the HOMO peak is comparable to that of undoped ZnPc on ITO. On the high binding energy side, the cutoff shifts monotonically to higher binding energies, indicating an interface dipole layer in the same direction as the possibly present level bending in the organic layer.

The lower part of Figure 4.13 shows the development of the UP-spectra for ZnPc doped with F_4-TCNQ on Au. Here, the HOMO peak appears for low coverage at the same energy as for the undoped case, but shifts towards lower binding energies with increasing coverage. The HBEC shift behavior is somewhat more complex. A strong shift of the HBEC when the first organic layer was evaporated points towards an interface dipole similar to the undoped case. The HBEC shifts then back to lower binding energies. However, it shifts later again to higher binding energies before the shift saturates at approx. 6nm organic layer thickness.

Figure 4.12 show some examples for the XP-spectra development of the most important elemental peaks for doped ZnPc on Au. The F1s spectra had a very low signal to noise ratio. In fact, it was not possible to determine the peak position of the F1s peak for doped ZnPc on Au. This effect points towards a reaction of F at the Au-surface, which might also lead to the complex behavior of the HBEC at thicknesses below 20Å. However, the signal from the Zn2p electrons was also weak at very low coverage. Hence, the level bending value was only determined from the shifts of the C1s and N1s peaks.

Figure 4.14 summarizes the UPS/XPS experiments of undoped and doped ZnPc on a poly-crystalline Au-substrate. One clearly sees that the level bending (taken from both XPS and UPS data) is inversed upon doping.

The evaluation of the data yields the energy alignments sketched in Figure 4.15. The main observations are:

1. The distance of the Fermi level to the HOMO level is decreased upon doping from 1eV down to 0.25eV (as for ZnPc on ITO).

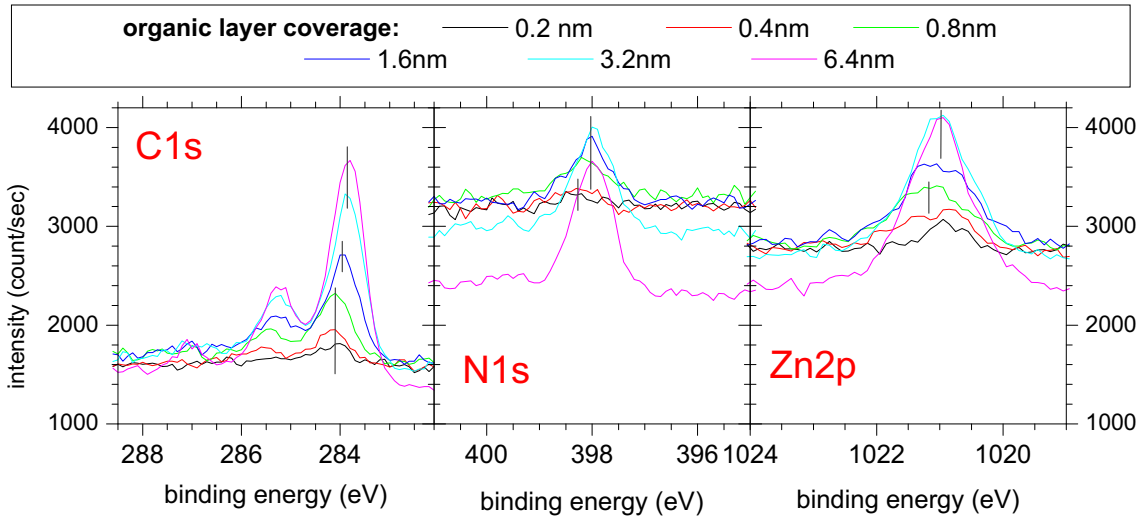

Figure 4.12: *Development of the XP-spectra with increasing organic layer coverage of F_4-TCNQ doped ZnPc on Au for the three elemental peaks C1s, N1s and Zn2p (originating from ZnPc-molecules).*

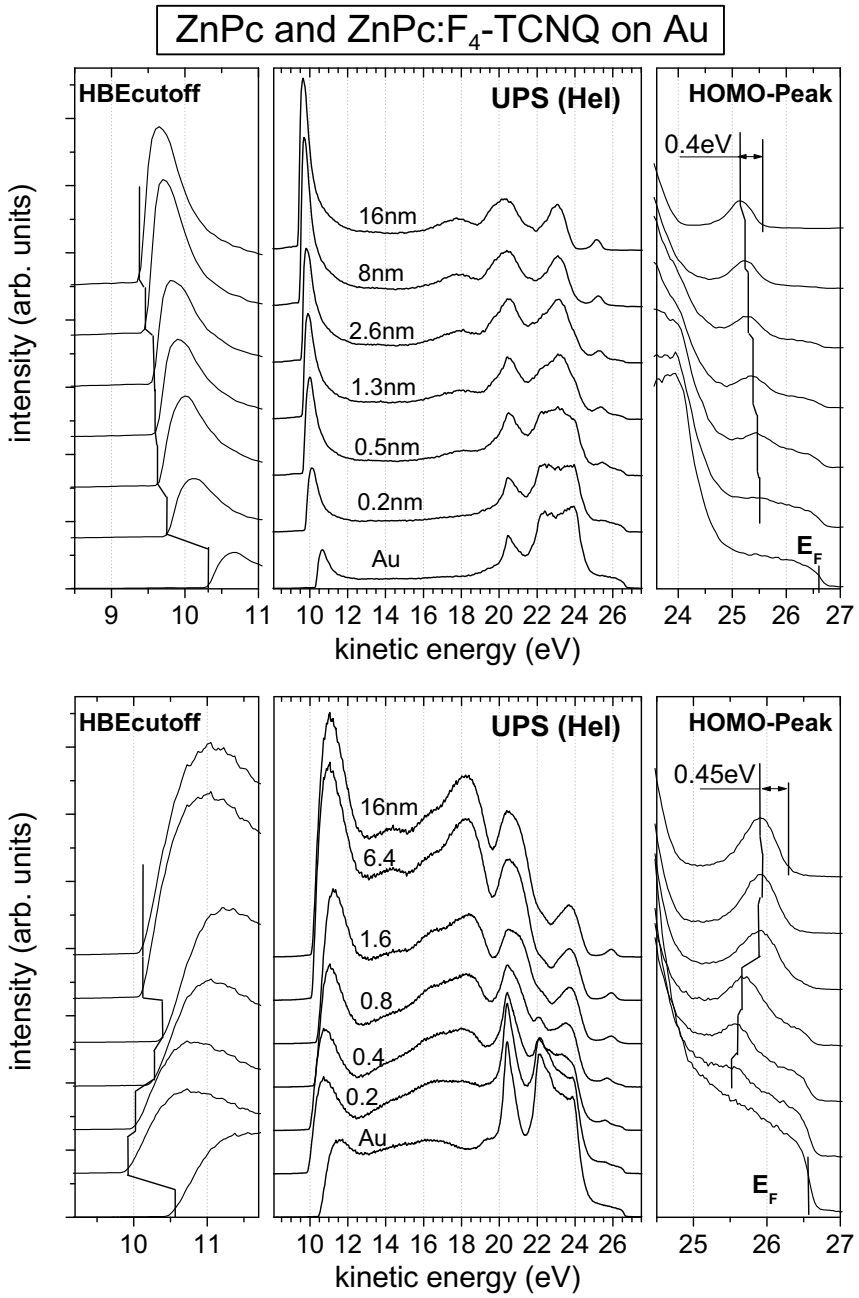

Figure 4.13: *Evolution of the UP-spectra for (top) ZnPc on Au and (bottom) F_4-TCNQ - doped ZnPc on Au. The vertical lines mark the shifts of the high binding energy cutoff and the HOMO peak shift. The values 0.4eV and 0.45eV mark the (constant) HOMO-peak width (i.e. the distance of the peak maximum to the cutoff).*

2. Generally, we expect an ohmic behavior for the Au-semiconductor contact because of the higher Au workfunction as compared to ITO. This is indeed the case for the undoped sample (left), where an accumulation layer near the interface is observed (positive level bending). For the doped layer (right side of fig.4.15), however, the

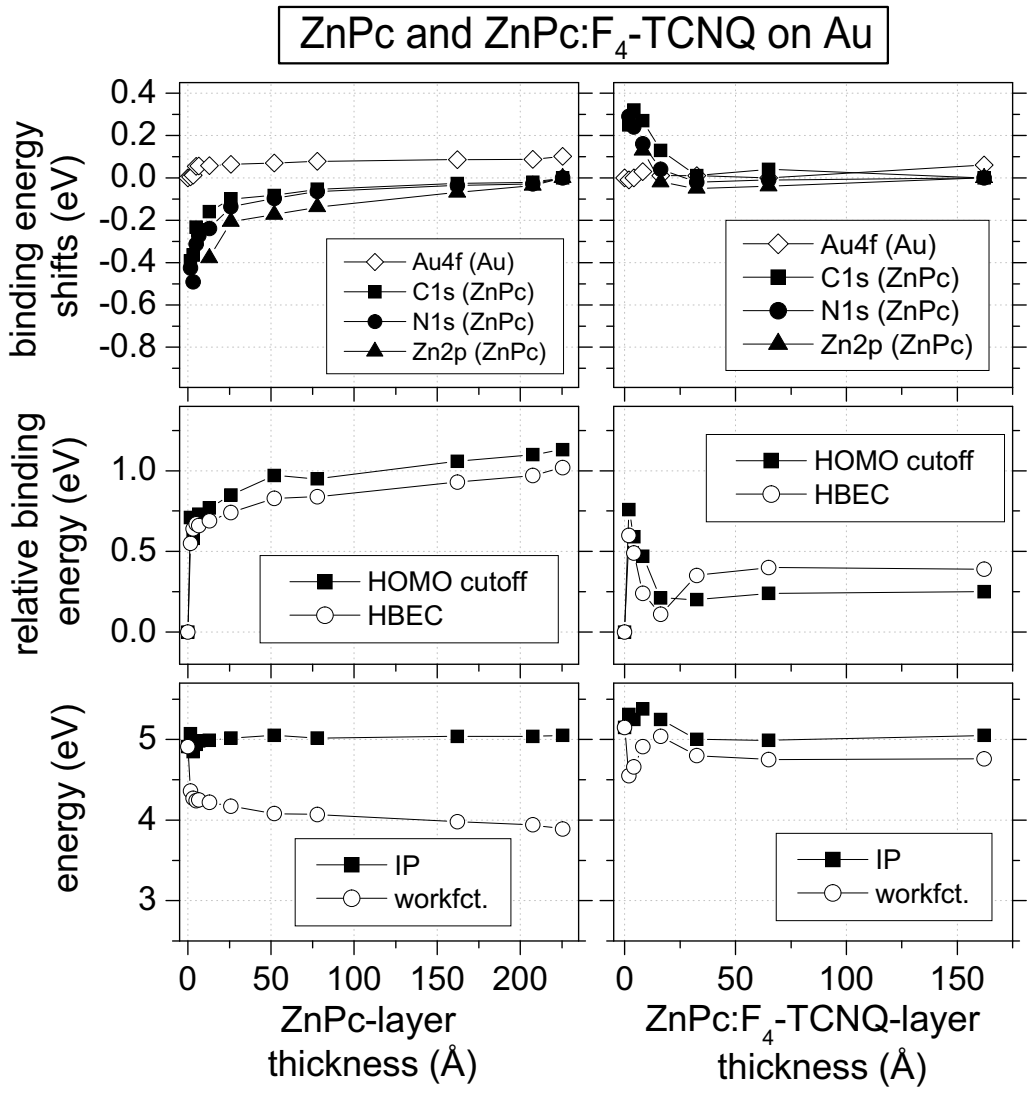

Figure 4.14: *UPS energy shifts and XPS peak shifts for (left) ZnPc on Au and (right) doped ZnPc on ITO.*

shift of the Fermi level leads to a depletion layer near the interface caused by a level bending in opposite direction as compared to the undoped case.

3. The interface dipole of the doped and undoped sample changed in accordance with the workfunction change of the substrate. This implies that doping does not change the interface dipole (which is surprising taking into account the possible reaction of F with Au at the interface). However, the origin of the change in the substrate workfunction is not clear since the same substrate and identical cleaning procedures were used.

4. Although the ionization potential does not depend on doping, it is approx. 0.45eV lower (5.05eV) for ZnPc on Au than for ZnPc on ITO (5.5eV). Schlettwein et al.

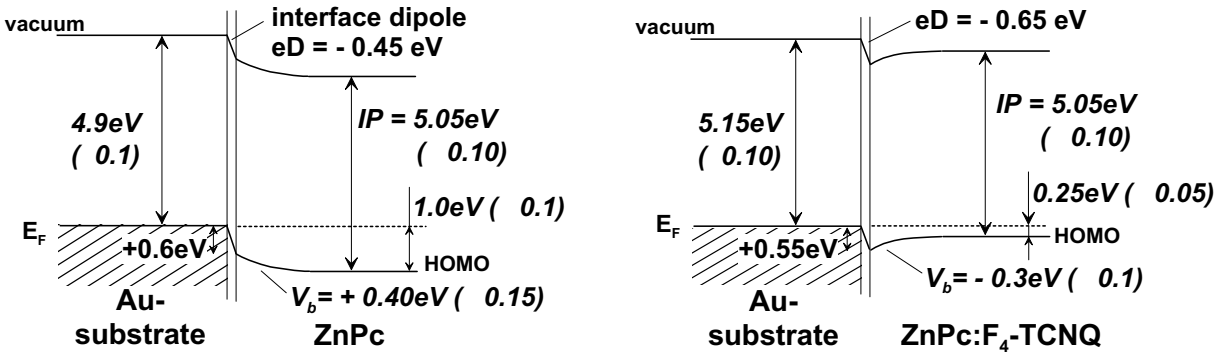

Figure 4.15: *Energy level scheme as obtained from UPS/XPS experiments for the junction between Au and ZnPc. The left side shows the energetic structure for the undoped case; the right side for ZnPc p-type doped with F_4-TCNQ.*

[157] found an ionization potential of ZnPc on Ag and on Au of 5.3eV. Since they took the maximum of the HOMO-peak to calculate the ionization potential, this has to be corrected by the half-width of the ZnPc-HOMO peak (approx. 0.4eV), which yields 4.9eV for the ionization potential of ZnPc on Au. Lee et al. [142] found an ionization potential of CuPc on NPB (bis-(naphtyl)-diphenyl-biphenyl-diamine) of 4.8eV. The reason for the different ionization potential of ZnPc on Au and ITO is not clear. Different ZnPc growth modes on the ITO and on the Au-substrate would be a possible explanation but they can hardly explain the huge difference. This problem, however, does not affect our conclusions regarding the doping effect.

For comparison, we have performed transport experiments on samples with contacts between gold and doped ZnPc which confirm the UPS/XPS study and show how the contact properties can be adjusted by doping: Nominally undoped ZnPc forms an ohmic contact with Au (see literature [158]), whereas p-type doped ZnPc leads to a weakly blocking contact, which is expected from the electrostatic level bending caused by the downwards shift of the Fermi level. The contact behavior of doped ZnPc to Au was determined from current-voltage measurements on the sample structure: Au/60nm undoped ZnPc/440nm doped ZnPc/Au (preparation and measurements under high vacuum, see Figure 4.16). The additional thin undoped ZnPc layer is needed to increase the width of the space charge layer in order to see the weak blocking behavior of the Au / doped ZnPc junction (compare [95] for the same experiments on vanadyl-phthalocyanine). Choosing the Au contact near the undoped interlayer as anode, injection limited rather than space charge limited currents were seen under positive bias in a voltage range of 1-5V (see Figure 4.16). In the case of a 600nm thick undoped ZnPc layer between two Au contacts (investigated in air to increase the current through the device) symmetric current voltage curves were found with a space charge limited behavior between 1 and 5 Volts ($j \sim V^{1.7}$). This is a strong evidence for ohmic injection of the majority carriers (in this case holes) into the organic layer. For more details regarding current-voltage curves of single organic layer samples, see also Appendix B.

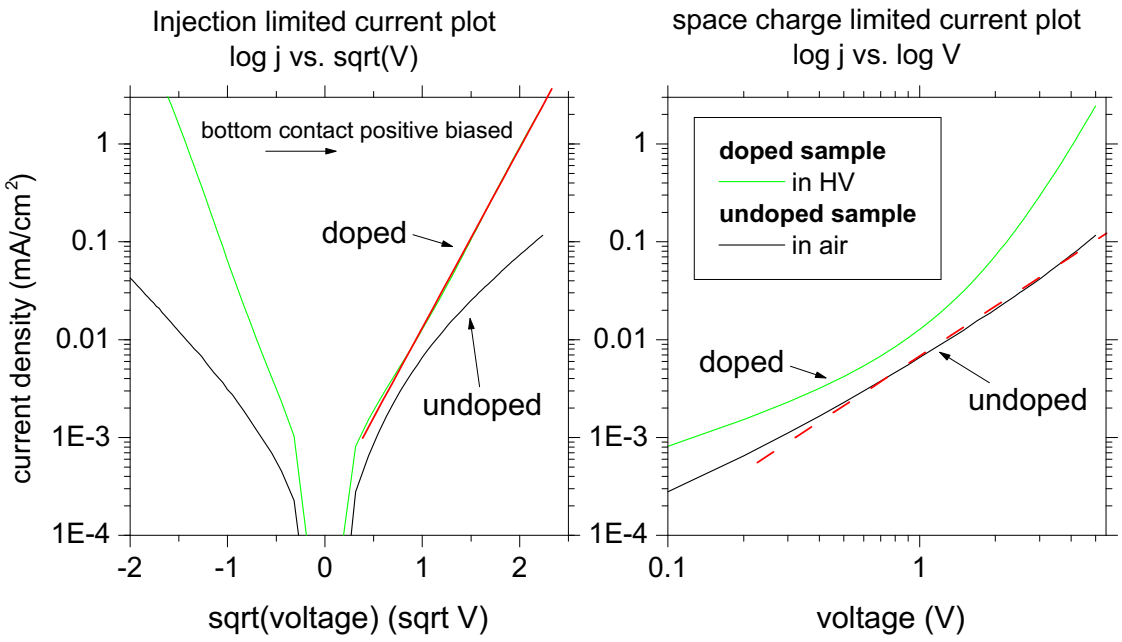

Figure 4.16: *Current-voltage curves of a doped sample (green curves, layer structure: Au bottom contact / 60nm undoped ZnPc / 440nm F_4-TCNQ doped ZnPc / Au top contact) and an undoped sample (black curves, layer structure: Au / 600nm ZnPc / Au). The left picture shows a log-lin plot which yields a linear fit for injection limited currents ($j \sim \exp V$), the right one shows a log-log plot, which gives linear fits for space charge limited currents under ohmic injection ($j \sim V^i$, $i > 1$).*

4.2.3 Investigation of organic heterojunctions with doped layers

4.2.3.1 F_4-TCNQ on Au and ZnPc: HOMO determination

Our standard dopant material F_4-TCNQ shows island-like growth on most substrates. However, to determine the ionization potential, UPS/XPS investigations on pure F_4-TCNQ layers on gold foil and ZnPc were carried out. Together with optical absorption measurements, this yields an approximation of the LUMO level of F_4-TCNQ.

a) F_4-TCNQ on polycrystalline Au-foil

The HOMO-peak of F_4-TCNQ was only visible for nominal layer thicknesses above 400Å and the XPS signal for Au was still visible at a nominal thickness of approx. 900Å. Both effects are strong hints for island-like layer growth. Hence, we did not try to evaluate level bending effects from the development of the XPS-peaks. The conductivity of pure F_4-TCNQ layers was measured to be below 10^{-8}S/cm [104], thus only a small level bending should be expected. Furthermore, between 400Å and 900Å nominal layer thickness, all elemental XPS-peaks and HOMO peaks were visible and did not shift.

The ionization potential of a nominally 900Å thick F_4-TCNQ layer on Au was determined to be $IP = 8.35eV \pm 0.1eV$ and the distance of the HOMO cutoff to the Fermi-

level (assuming an aligned Fermi-level over the whole organic layer) was $IP - \Phi_{SC} = 2.85eV \pm 0.1eV$.

Several effects point towards a chemical reaction of F_4-TCNQ with the underlying Au substrate: (i) The elemental peaks of carbon and nitrogen show additional features below thicknesses of 30Å that vanishes at a higher coverage. (ii) The F1s peak shifts between 30 and 400Å, whereas the C1s peak, the N1s peak and the HBEC of the UP-spectra do not. Hints for a possible reaction of F_4-TCNQ with Au were already seen for doped ZnPc on Au (see 4.2.2).

b) F_4-TCNQ on ZnPc

In order to compare the ionization potentials of F_4-TCNQ on different substrates, we performed the same experiments on a layer of 24nm ZnPc on polycrystalline Au. Since ZnPc is an organic material, one would expect a less pronounced interaction between F_4-TCNQ and the substrate and more closed layers of F_4-TCNQ. This is indeed the case, which can be seen from the fact that the HOMO-peak of F_4-TCNQ is already clearly visible for 200Å nominal layer thickness. However, since the ionization potential of F_4-TCNQ is higher than that of ZnPc, the F_4-TCNQ HOMO peak is buried under a strong ZnPc signal. This hinders the determination of the HOMO peak position for a lower coverage.

On depositing the first F_4-TCNQ molecules on top of the thick ZnPc layer, the elemental peaks of carbon, nitrogen and zinc and the HOMO peak position of the ZnPc layer shift all together by approx. 0.5eV to lower binding energies. This indicates a doping of the ZnPc by diffusion of hot F_4-TCNQ molecules or a strong interface dipole caused by a charge transfer of holes to the ZnPc layer. A shift of 0.5eV towards the Fermi level is in rough agreement with the shift of the HOMO-level for doped ZnPc compared to undoped ZnPc as determined above for the ITO and Au substrates.

The ionization potential and the distance of the HOMO cutoff to the Fermi-level for a nominal thickness of 440Å are $IP = 8.3eV \pm 0.1eV$ and $IP - \Phi_{SC} = 2.9eV \pm 0.1eV$. This is in very good agreement with the results for F_4-TCNQ on Au.

A level shift in the F_4-TCNQ layer could not be observed since the HOMO peak of F_4-TCNQ was only visible above 200Å nominal layer thickness whereas the C1s and N1s peaks of F_4-TCNQ are overlayed with strong contributions of the same elemental peaks from the underlying ZnPc substrate. Nevertheless, the XP-spectra for fluorine show two slightly different peak shapes below and above 30Å, which again indicates a chemical reaction with the ZnPc-substrate. However, it may also reflect the charged and the uncharged state of F_4-TCNQ.

c) An estimate of the LUMO position of F_4-TCNQ

From the measured values of IP and $IP - \Phi_{SC}$, we derive a F_4-TCNQ workfunction of $\Phi_{SC} = 5.4eV$. From this we can deduce an upper limit estimate for the LUMO position. Assuming F_4-TCNQ to be a strong n-type semiconductor (LUMO near the Fermi-energy), the electron affinity should be below 5.4eV.

It is possible to compare this value with a LUMO position deduced from the optical gap of the F_4-TCNQ layer. For this purpose, a nominally 400Å thick F_4-TCNQ layer was vacuum sublimed onto a quartz substrate. The layer was not uniform as can be seen with the eyes. However, optical absorption measurements (see Figure 4.17) yield an onset of absorption at 505nm, which correspond to an optical gap of 2.45±0.05eV. This value is

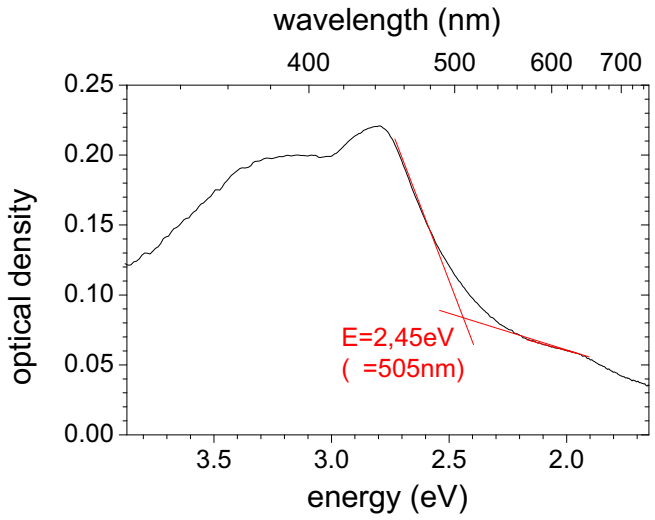

Figure 4.17: *Optical absorption spectra of a 400Å thick F_4-TCNQ layer on a quartz substrate. Indicated is the determination of the optical gap from the onset of absorption.*

smaller than the distance of the HOMO level to the Fermi-level as determined from UPS experiments. Hence, the exciton binding energy which determines the difference between the optical and the electrical gap should be higher than 0.5eV, which is a reasonable value for organic materials.

For comparison, Pfeiffer [95] estimated the LUMO position of F_4-TCNQ from the known LUMO position of the unfluorinated form of F_4-TCNQ (TCNQ shows a LUMO of 4.5eV taken from redox-potential measurements in solution [159]) and a comparative study with other molecules with fluorine-substituents [160] to be around 4.85eV.

As a conclusion, the LUMO position of a F_4-TCNQ molecular layer should be in the order of 4.85 to 5.4eV.

4.2.3.2 Undoped and doped ZnPc on Alq_3 : energetic alignment

UPS/XPS experiments were done on undoped and F_4-TCNQ doped ZnPc on Alq_3 to obtain insight into the energetic alignment of doped layers on other organic materials suitable for OLED-applications. We first tried to investigate the junction of ZnPc on Alq_3, although the layer sequence in common OLEDs is the other way around (i.e. Alq_3 on top of ZnPc). However, since the ionization potential of ZnPc is lower than that of Alq_3, it is possible to evaluate the new emerging HOMO-peak of ZnPc at a very low ZnPc coverage (see Figures 4.18 and 4.19). The disadvantage of this approach is that Alq_3 is more sensitive to UV and X-ray radiation and thus charging and damaging are more serious problems. For that reason, two different experiments have been done: (i) A layer growth with only doing UPS measurements in between two growth steps, drastically shortening the exposure time of the sample to UV and X-ray radiation (an UPS scan needs typically 5 minutes, whereas a full XPS investigation needs more than half an hour). This experiment yields relatively stable UP-spectra, which was checked by repeating the UPS experiments

at the highest coverage, resulting in a charging shift of less than 50meV to higher binding energies. (ii) In the second experiment, XPS and UPS scans were done between two growth steps, but only the XPS scans were evaluated to determine the level shift for the first experiments. This can be done because we observed that XPS scans are more stable regarding damage of the organic layer. This was clarified by the fact that XPS-peaks did not shift after repeating the experiments at a coverage where UPS-peaks already shifted slightly.

In order to deduce the energetic alignment of an organic/organic junction, the same equations as for the alignment of an organic layer on a conductive substrates are valid. Only the substrate values in equations (4.2) to (4.7) has to be exchanged by the values of the underlying organic layer. Furthermore, Fermi-level alignment with the metallic substrate right at the bottom (this was a polycrystalline Au-foil for all following experiments) is assumed for the following calculations.

a) undoped ZnPc on Alq_3

In the XPS experiments, no shift of the elemental peaks of aluminium, oxygen and nitrogen (belonging to Alq_3) was observed upon evaporating ZnPc on top of a 200Å thick Alq_3 layer. Despite that, the elemental peaks of zinc and nitrogen (belonging to ZnPc) did shift between 2Å and 160Å by -0.5eV towards lower binding energies (for data see Figure 4.19, left pictures). Hence, the total level shift of $V_b = -0.5eV$ takes place in the ZnPc layer. A shift in this direction can not be explained by charging effects and may be due to level bending.

The results of the independently performed UPS measurements point in the same direction. A shift of the ZnPc-HOMO by -0.55eV was observed between 2Å and 50Å (due to the different position of the HOMO-peaks of Alq_3 and ZnPc, the ZnPc HOMO peak could already be clearly resolved at very low thicknesses, see Figure 4.18). No HOMO shift was observed for the HOMO-peak of Alq_3 which could be resolved up to a nominal overlayer thickness of 4Å. The ionization potentials of the thickest Alq_3 and the thickest undoped ZnPc layer were determined to be 5.85 and 4.85eV, respectively. The distances of the HOMO cutoff to the Fermi-level were 1.7 and 0.4eV, respectively. The large distance of the HOMO-level to the Fermi-level in Alq_3 indicates the known fact that Alq_3 tends to behave as a n-type organic semiconductor. Comparing the latter value of 0.4eV with the former measurements ($IP - \Phi_{SC}$ was 0.8 and 1eV for doped ZnPc on ITO and Au, respectively) shows that the presence of an Alq_3 underlayer alters the measured position of the Fermi-level. A change of the HOMO levels in the direction to lower binding energies can not be explained by a simple positive charging of the topmost organic layer. Thus, the origin of the observed behavior is not clear in the moment. One explanation would be some mechanism of p-type doping process occurs which might be due to a charge transfer of electrons from Alq_3 to ZnPc and photoexcitation of electrons from ZnPc leaving free holes in the ZnPc layer behind. These charges re-distribute in analogy to the case of an intentionally p-type doped ZnPc layer. The 'photo-doping' interpretation is also supported by the observation that the shift of the HOMO peak of ZnPc starts beyond 8Å ZnPc thickness. However, a doping of the topmost organic layer or an influence of a photovoltage established at the Alq_3/ZnPc interface should also shift the XPS-peaks of the intrinsic underlayer, as will be seen in the next Section. Such a behavior could not been observed. An unintentional doping of the ZnPc layer by residual F_4-TCNQ molecules in the preparation chamber can also not be excluded.

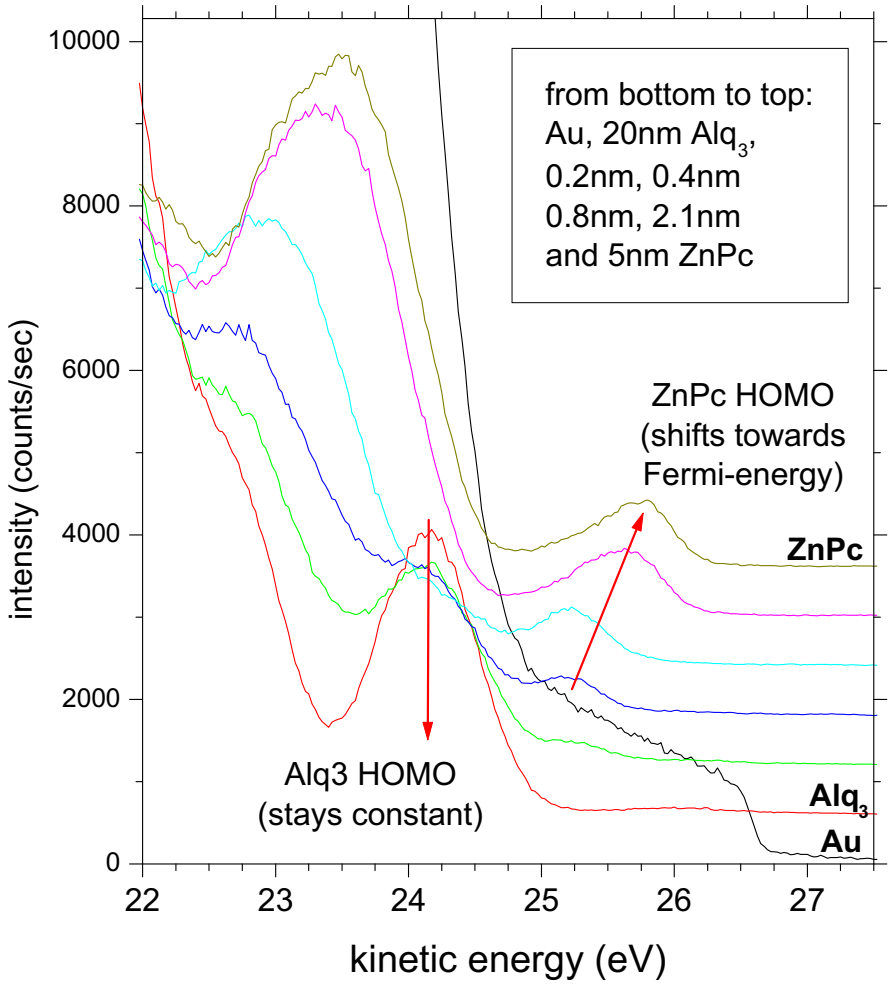

Figure 4.18: *UP-spectra evolution of undoped ZnPc on top of Alq_3. The bottom substrate is a polycrystalline Au-foil. With evaporation of the overlayer ZnPc the Alq_3 HOMO peak vanishes (but, in this case, stayed at constant position), whereas the ZnPc HOMO peak arises more near to the Fermi-energy of the underlying Au-substrate, due to the more p-type conduction and its lower ionization potential. With further growth of the ZnPc overlayer its HOMO peak shifts to even higher kinetic energies.*

The HOMO cutoff difference $\Delta HOMO$ directly at the interface of Alq_3 and ZnPc can be calculated from the total HOMO shift and the level shift value (equation 4.6) to be -0.8eV towards lower binding energies (coming from the underlayer). From this value, the interface dipole could be calculated to be -0.2eV (equation (4.7)). For most organic heterojunctions except junctions between very strong acceptors and donors, a small interface dipole is observed indicating vacuum level alignment over the junction [89, 143]. The energy alignment at the interface of undoped ZnPc on top of Alq_3 deduced from the above described observations is drawn schematically in Figure 4.20, left picture.

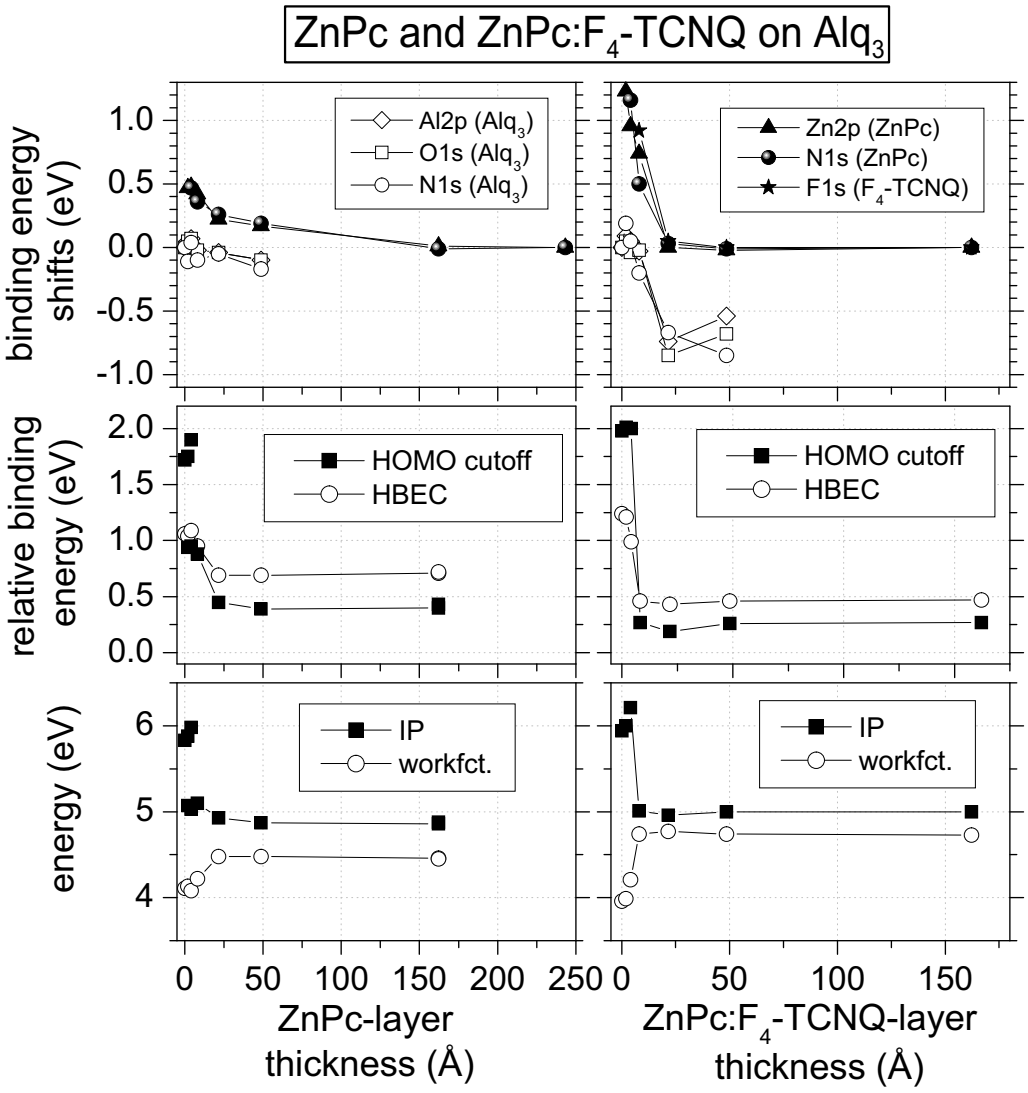

Figure 4.19: *UPS energy shifts and XPS peak shifts for (left) ZnPc on Alq_3 and (right) F_4-TCNQ doped ZnPc on Alq_3. Note that for undoped ZnPc on Alq_3 and a low overlayer coverage the HOMO cutoff energies for Alq_3 and ZnPc could be determined at the same time.*

The energetic alignment directly at the interface can also be deduced from the UP-spectra at thicknesses before the HOMO peaks start to shift, for the presented experiment at 0.2-0.4Å overlayer thickness. This approach circumvents the problems with the not explainable level shift in the nominally intrinsic ZnPc layer. The evaluation gives a HOMO difference between Alq_3 and ZnPc directly at the interface of -0.8eV and an interface dipole of zero, which corresponds well with the energy alignment scheme deduced from a thick overlayer coverage and including level bending (Figure 4.20, left side).

b) doped ZnPc on Alq_3

For F_4-TCNQ doped ZnPc (molecular doping level 1:30) the level shift takes mainly place in the Alq_3 layer, in contrast to the junction above of undoped ZnPc on Alq_3 where level shift took place in the ZnPc layer. This could be deduced from the XPS peak shifts of the elemental peaks of ZnPc and Alq_3 (see Figure 4.19, right pictures for the experimental data). The XPS peaks from atomic levels of the Alq_3 and the ZnPc:F_4-TCNQ layer (N1s with a contribution from Alq_3 and from ZnPc, Al2p, O1s, Zn2p, F1s) shift by approx. -0.95eV ($\pm 0.20eV$) towards lower binding energies (which again can not be explained by charging). There is a tendency of larger shifts in the doped ZnPc layer (Zn2p and N1s peaks of ZnPc) than in the Alq_3 layer (Al2p, O1s and N1s peaks of Alq_3). However, one can assume in a reasonable approximation that the same shift appears for the under- and the overlayer XP-spectra. According to the work of Schlaf et al. [141] this indicates a level bending only in the underlayer (in this case the Alq_3 layer), since the shift of all elemental peaks after the evaporation of the first part of the organic overlayer is the sum of under- and overlayer shifts.

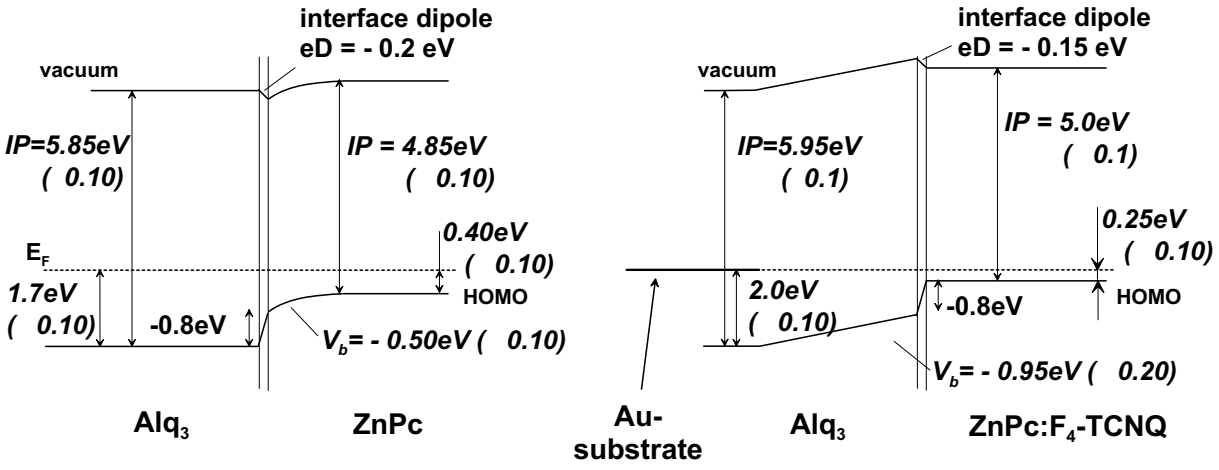

Figure 4.20: *Scheme of the energy alignment of undoped ZnPc (left) and F_4-TCNQ doped ZnPc (1:30) (right) on top of Alq_3 deduced from a combined UPS/XPS study. The level shift obtained from XPS measurements takes place inside the ZnPc layer for undoped ZnPc on Alq_3 and inside the Alq_3 layer for doped ZnPc on Alq_3. Again, the HOMO level of the doped ZnPc shifts towards the Fermi energy. Note that for doped ZnPc on Alq_3 the level shift inside the Alq_3 is caused by a potential drop over the Alq_3 layer due to Fermi level alignment between the substrate and the organic overlayer.*

Almost no hint for level bending was found in the UP-spectra, which is in clear contradiction to the huge level shift deduced from the XP-spectra. Both, the Alq_3 and the ZnPc HOMO should shift. Unfortunately, the HOMO position of the underlying Alq_3 layer could only be resolved until 4Å overlayer thickness. The main contribution of the XPS peak shift of the aluminium and oxygen peaks of Alq_3 was observed between 8 and 20Å. If one evaluates the position of the 5th and 6th maxima of the UP-spectra belonging to the Alq_3 underlayer, one sees evidence for a shift of the Alq_3 UP-spectra to higher binding energies between 8 and 20Å in qualitative agreement with the XPS results. However, since the underlayer signal is buried under a large contribution of the UPS-signal from

the overlayer, this shift can not be quantified. Thus, we conclude that the UPS shifts only could not be resolved, although they are present as can be deduced from the XPS results. The discrepancy in the HOMO and the XPS-peak shifts might be explained as follows: The escape depth of high energetic XPS-electrons is higher than that of UPS-electrons (Figure 4.1). If one assumes island like growth of the ZnPc on top of Alq_3 (what is not unusual for organic materials), the UP-spectrum of the ZnPc when it is firstly observed may belong to higher thickness as the nominal one. Hence, the HOMO-peak position in the equilibrium state more away from the interface is measured. The explanation by different probing depth in UPS and XPS, respectively, is supported by the fact that the underlayer XPS-peaks could be resolved until a nominal thickness of 50Å which is above the typical escape depth. As can be concluded from the XPS results, the Fermi level equilibrium between substrate and organic overlayer is reached at approx. 25Å overlayer thickness with a total level bending of -0.95eV in the Alq_3 layer.

To deduce the energetic alignment at the interface of doped ZnPc on top of Alq_3, the following values were determined from the UP-spectra: The ionization potential of the thickest Alq_3 and doped ZnPc layers were $IP_{Alq3} = 5.94eV$ and $IP_{ZnPc} = 5.0eV$, which are slightly above the values for undoped ZnPc on Alq_3. The distances of the HOMO cutoff to the Fermi-level were 2.0 and 0.25eV, respectively. The latter gives strong evidence that the Fermi-level is aligned over the whole organic layer thickness, since it agrees very well with that values obtained for doped ZnPc on Au and ITO (0.3eV and 0.2eV, respectively). The total HOMO cutoff difference between the under- and the overlayer $\Delta HOMO_{total}$ was -1.75eV towards lower binding energies (coming from the underlayer). From the latter and the level shift value the HOMO-level difference between Alq_3 and ZnPc directly at the interface is obtained to be $\Delta HOMO$ =-0.8eV, which is the same as for undoped ZnPc on Alq_3. The interface dipole amounts to -0.15eV. Thus, as for the junctions of doped and undoped ZnPc on Au or ITO, the interface dipole is not changed upon doping.

The equilibrium energy alignment at the interface of doped ZnPc on top of Alq_3 (assuming that the total level shift of -0.95eV occurs in the Alq_3 layer) is drawn schematically in Figure 4.20, right side. It includes the underlying Au substrate. The observed level shift in Alq_3 is caused by a potential drop over the intrinsic Alq_3 between the Au-foil substrate and the doped ZnPc overlayer. From the ionization potential of the thick Alq_3 layer on top of the Au-substrate ($IP_{Au} = 5.15eV$) and the total HOMO cutoff difference between Au and Alq_3 ($\Delta HOMO_{total} = 2.0eV$), a very large interface dipole at the Au/Alq_3 junction of $eD = -1.2$eV can be calculated, neglecting level bending effects inside the Alq_3 layer near the Au interface. However, the influence of the latter was not carefully investigated. It can be seen from Figure 4.20 that doping does not change the HOMO-alignment directly at the interface Alq_3/ZnPc and the interface dipole. Doping changes the amount and place of the level bending because of Fermi-level alignment of two consecutive organic semiconducting layers with the underlying metallic substrate.

The presented experimental results of a combined UPS/XPS investigation of doped ZnPc on Alq_3 shows the importance of using additional information from the XPS experiments to conclude the equilibrium energy alignment from UPS results. Due to the slightly different escape depth of XPS and UPS electrons and the possibility of island growth, peak shifts not visible in the UP-spectra might be clearly resolvable in the XP-spectra. This is especially true, if the level bending or shift takes place in the underlayer material due to a Fermi-level alignment induced by the overlayer material.

4.2.3.3 Alq_3 on undoped and doped ZnPc: energetic alignment

For junctions between organic materials and, in particular, low workfunction metals it is known that the deposition sequence of the layers (metals on top of organics or the other way around) alters the interface energy alignment due to a possible reaction between the involved molecules and atoms or a doping of the organic layers [89, 138]. Even for organic/organic junctions this behavior has already been observed [124]. Thus, we investigated the junction between ZnPc and Alq_3 in the layer sequence Alq_3 on top of undoped and doped ZnPc (on Au-foil as the substrate defining the Fermi energy). Yet another reason to investigate the junction of Alq_3 on top of ZnPc is that in common OLED structures the emission layer (Alq_3) is evaporated on top of the hole transport layer (ZnPc).

Here, we performed only an UPS study since there was no time to redo the experiment carefully with XPS investigation.

a) Alq_3 on undoped ZnPc

The HOMO peak of ZnPc can be reliably resolved until a thickness of 32Å. No shift takes place in that thickness region. The Alq_3 HOMO level could only be resolved for thicknesses above 32Å. No HOMO shift was observed. Thus, from UPS measurements only it has to be concluded that no level bending takes place, neither in the ZnPc under- nor in the Alq_3 overlayer (for data see Figure 4.21, left side).

The values needed to obtain the energy alignment at this interface are: (i) the ionization potential for 220Å thick undoped ZnPc on the bottom Au-foil $IP_{ZnPc} = 5.2eV$, (ii) the ionization potential of the 240Å thick Alq_3 on top of ZnPc $IP_{ZnPc} = 5.95eV$, (iii) the distance of the HOMO cutoff to the Fermi-level $IP - \Phi_{SC}$ which is 0.65eV for ZnPc and 1.5eV for Alq_3. Hence, the difference between the HOMO cutoff of ZnPc and Alq_3 is 0.85eV in accordance to the opposite evaporation sequence described above. The calculated interface dipole is almost zero ($eD = -0.1$eV). An possibly present, but not measured, level bending would alter this value. It is noted here that for the junctions between copper-phthalocyanine (CuPc) and bis-(naphtyl)-diphenyl-biphenyl-diamine (NPB) or bathocuproine (BCP), no interface dipole was observed, too [142, 161].

Figure 4.22 (left side) shows the energy alignment deduced from the UPS-experiments on Alq_3 on undoped ZnPc. As compared to the inverse layer structure of undoped ZnPc on Alq_3, the alignment regarding HOMO difference and interface dipole directly at the interface is almost the same. The fact that the interface dipoles point in different directions may be attributed to larg errors in the exact determination of the level shift for both experiments.

b) Alq_3 on doped ZnPc

Again, level bending is neither observed from shifts of the ZnPc HOMO (which could be observed until 12Å Alq_3 coverage) nor from shifts of the Alq_3 HOMO (which could be observed starting at 4Å Alq_3 coverage, see Figure 4.21, right side). The values to conclude the energy alignment at the interface are: (i) the ionization potential for 160Å thick F_4-TCNQ doped ZnPc (1:30) on the bottom Au-foil $IP_{ZnPc} = 5.1eV$, (ii) the ionization potential of the 200Å thick Alq_3 on top of doped ZnPc $IP_{ZnPc} = 5.95eV$, (iii) the distance of the HOMO cutoff to the Fermi-level $IP - \Phi_{SC}$ which is 0.3eV for doped ZnPc and 1.3eV for Alq_3. Hence, the difference between the HOMO cutoff of ZnPc and Alq_3 is 1.0eV. The interface dipole is calculated to be -0.15eV. Again, possibly present level bending might

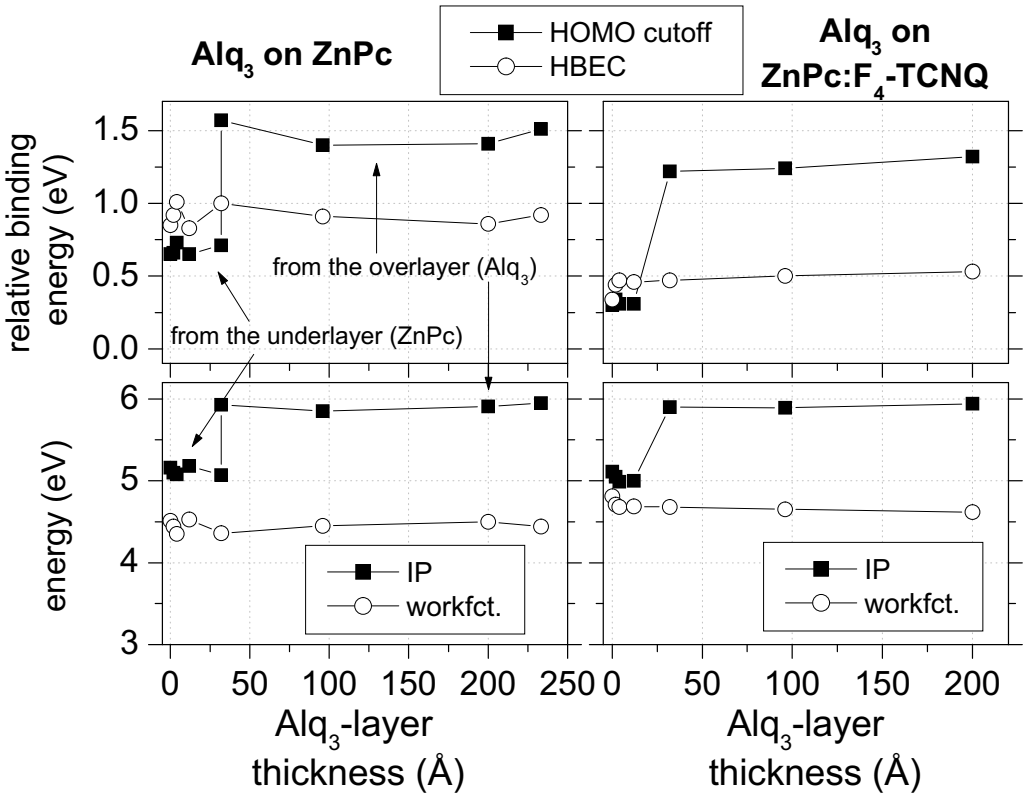

Figure 4.21: *UPS energy shifts for (left) Alq_3 on undoped ZnPc and (right) Alq_3 on F_4-TCNQ doped ZnPc. No level bending can be deduced from this UPS data. The work-function stays almost constant what indicates vacuum level alignment at the interfaces.*

change this value. Nevertheless, for all junctions between Alq_3 and ZnPc the interface dipole is almost zero.

Figure 4.22 (right side) shows the energy alignment deduced from the UPS-experiments on Alq_3 on doped ZnPc. The comparison with the undoped case (left side) shows that the effect of the 0.35eV change in the distance between the HOMO level of doped and undoped ZnPc (from 0.65eV down to 0.3eV) on the interface alignment is reduced by the fact that also the distance of the HOMO level to the Fermi-level in Alq_3 has changed by 0.2eV (from 1.5eV down to 1.3eV). The latter might be by some mechanism of p-type doping of the Alq_3 layer on top of the doped ZnPc (which should be reflected in a level bending in additional XPS experiments) or to a pinning of the Alq_3 Fermi-level at the doped ZnPc surface at a different energetic position due to new dopant induced gap states at the Alq_3 interface. The remaining part of the change in the distance of the HOMO-level to the Fermi energy is reflected in a change of the HOMO distance between the ZnPc and the Alq_3 layer, which is now slightly increased from 0.85eV to 1eV. Nevertheless, since the errors of the interface alignment determination are in the range of this changes, a definite answer to the question whether the energetic alignment at the interface is changed upon doping or not can not be given. It seems that doping does not change the interface dipole,

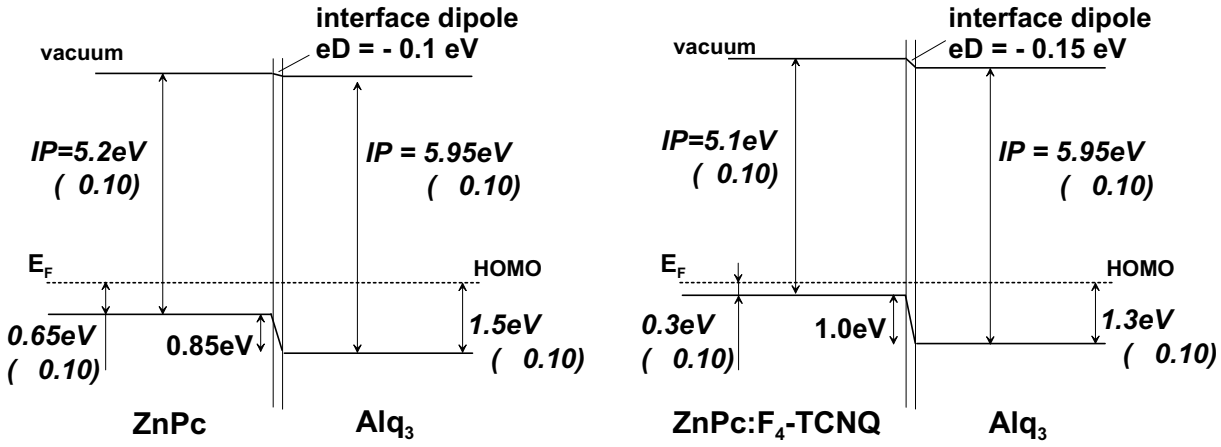

Figure 4.22: *Scheme of the energy alignment of Alq_3 on undoped ZnPc (left) and F_4-TCNQ doped ZnPc (1:30) (right) deduced from only UPS-experiments. No level bending was observed in the UP-spectra for both cases. Doping changes the HOMO distance to the Fermi-level in the doped ZnPc layer and seems to pin the Fermi-level in the overlayer Alq_3 layer at slightly lower values. Additionally, the barrier for hole injection from ZnPc into Alq_3 is slightly enhanced upon doping (see text for further details).*

which has been observed for all junctions with or without doping throughout this work. However, doping seems to change the barrier for hole injection from the doped ZnPc into Alq_3 and changes the Fermi-level pinning in the neighbored intrinsic layer.

4.3 Conclusions from the UPS/XPS-experiments

From the experiments of doped ZnPc on ITO and on gold-substrates described above, it can be deduced that the organic system ZnPc:F_4-TCNQ behaves rather similar to inorganic semiconductor matrix/dopant systems:
(i) The Fermi-energy comes closer to the transport energy (the HOMO),
(ii) the built-in potential is changed accordingly, and
(iii) the depletion layer becomes very thin because of the high space charge density in the doped layer.
This behavior favors charge injection from the contact into the organic semiconductor due to a very small Schottky barrier.

For a complete overview over the effects of doping of one layer in an organic/organic heterojunction more intensive research is needed. In particular, the question how doping influences the level shift and bending in the nominally undoped layers, the origin of the discrepancy between UPS and XPS results for some junctions, the origin of the charging/photodoping phenomena and the question whether doping changes the Schottky barrier for charge injection directly at the organic/organic interface or not need to be further addressed. However, some conclusions are possible:
(i) For all investigated organic heterojunctions between ZnPc and Alq_3, the assumption of vacuum level alignment seems to be valid.
(ii) The distance between the Fermi-level and the transport level is reduced upon inten-

tional doping similar to the junctions of organic layers on conductive substrates.
(iii) Doping of the topmost organic layer leads to Fermi-level alignment with the conductive substrate. This results in a potential drop inside the intrinsic organic layer which can be seen in a level shift of the XPS peaks.
(iv) For some special cases of organic heterojunctions the additional information about level bending or level shifts taken from XPS experiments is essential to yield the correct interface energy alignment.

For all thick layers of doped ZnPc, the distance between the Fermi-level and the HOMO level determined from the HOMO cutoff of the ZnPc UP-spectra was between 0.2eV and 0.3eV (nominal doping ratio of about 30:1 ZnPc to F_4-TCNQ molecules). From Seebeck measurements this value was determined to be approx. 0.1eV for doped ZnPc and 0.2eV for doped VOPc. The larger distance observed in UPS experiments can be explained by the fact that for the Seebeck effect only the transport in the upper most tail states of the density of states distribution accounts which can not be resolved in UPS.

5 OLEDs: Results and Discussion

In this Chapter, results about OLEDs with doped transport layers are presented. Doping improves their optoelectronic properties, like operating voltage and device efficiency. The basic effect of doping is shown first for a simple two-layer device with a p-type doped hole transport layer. The insertion of a third layer, the electron blocking layer at the hole side, is needed to increase the device efficiency. Then, the p-type doping is extended to amorphous wide gap hole transport materials. A similar blocking layer as before also improves the device efficiency of the OLEDs with wide gap HTLs. Therefore, a concept to achieve high efficiencies and *low operating voltages is formulated. It makes use of doped charge transport layers and suitable blocking layers.*
This is followed by a survey of the OLED-samples prepared in a new multiple chamber UHV system. We compare properties of similar samples made in the single chamber HV-system and prepared in the multiple chamber UHV-system which show the importance of material purity and handling on device properties. A further step towards higher device efficiencies is the doping of the emitter layer with emitter dopants. This effect is shown for different quinacridone-type molecules. A first step towards n-type doping of the electron transport layer is shortly presented. Finally, a joint evaluation of all OLED layer sequences is done. The device improvement from simple two-layer structures to sophisticated structures with additional electron injection layers and emitter dopants demonstrates the way to achieve highly efficient organic light emitting diodes.

5.1 OLEDs with F_4-TCNQ doped VOPc as hole transport layer prepared in the HV

5.1.1 Influence of the doping concentration

a) Optoelectronic properties

We demonstrate the effect of p-type doping the hole transport layer of an OLED on the optoelectronic device properties. As an example, we chose a two-layer system consisting of the F_4-TCNQ doped hole transport layer vanadyl-phthalocyanine (VOPc) and the electron transport and emission layer Alq_3 sandwiched between an ITO anode and an aluminium cathode. A series of OLEDs with different doping ratios (from 1:280 up to 1:34), but identical layer structure and thicknesses was prepared in a single chamber high vacuum system. The doping density range was chosen from the conditions that a noticeable effect should be achieved but no change of the crystal structure occurs. The latter is known to be true from electron diffraction studies for doping ratios below 5% [114]. All organic materials except the dopant F_4-TCNQ were purified once by vacuum gradient sublimation. Alq_3 was delivered by Sigma-Aldrich GmbH, Germany. Current-voltage

and luminance voltage characteristics were recorded in-situ. Additionally, the electroluminescence spectra were recorded in-situ by a multi channel detector system (OSMA, Princeton Instruments). It turned out that the emission spectra of the OLEDs were independent of the doping ratio and almost identical to the photoluminescence spectra of an approx. 71nm thick pure Alq_3 layer on a glass substrate. This indicates that the emission is from the Alq_3 layer near to the VOPc-Alq_3 interface. The layer structure together with the photoluminescence spectra of the Alq_3 layer, the electroluminescence spectra of the OLEDs and the absorption spectra of a 200nm thick VOPc layer are given in Figure 5.1.

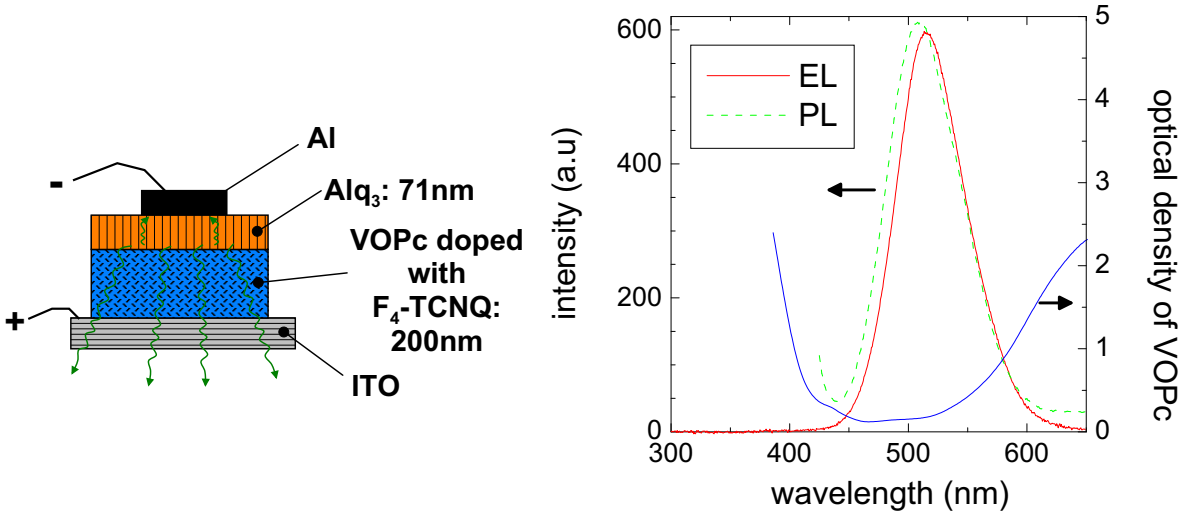

Figure 5.1: *(left) OLED-layout for the investigation of the effect of doping the HTL VOPc with F_4-TCNQ. The molecular doping ratio was varied from undoped to 34:1. (right) The photoluminescence spectra (PL) of a pure Alq_3 layer, a typical electroluminescence spectra (EL) of all OLEDs and the absorbance spectra of a 200 nm thick VOPc layer are shown.*

The current density j vs. voltage V and luminance in forward direction $L_{V,0}$ vs. voltage V characteristics are depicted in Figure 5.2. Shown are results for doping ratios from 1:34 to 1:280 (molecular ratio of F_4-TCNQ to VOPc), compared to an OLED-device with an undoped VOPc-layer. One can see that already slight doping strikingly decreases the operating voltage, hence increasing the power efficiency. Also, the $j-V$ and $L_{V,0}-V$ characteristics are strongly dependent on the doping ratio of the hole transport layer. The luminance of the OLED with the undoped VOPc as HTL could not be measured due to the short lifetime of the OLED at voltages necessary to reach a measurable light emission.

Table 5.1 summarizes the results of the study of the doping concentration influence. The voltages to reach a current density of 10mA/cm^2 and to get a light output of 100cd/m^2 (typical monitor brightness) are strongly decreased by doping the VOPc layer. This is caused by two effects: It is obvious that the series resistance of the device is considerably reduced due to the much higher bulk conductivity of the hole transport layer. As an example, the conductivity of the doped VOPc layer with the highest doping concentration

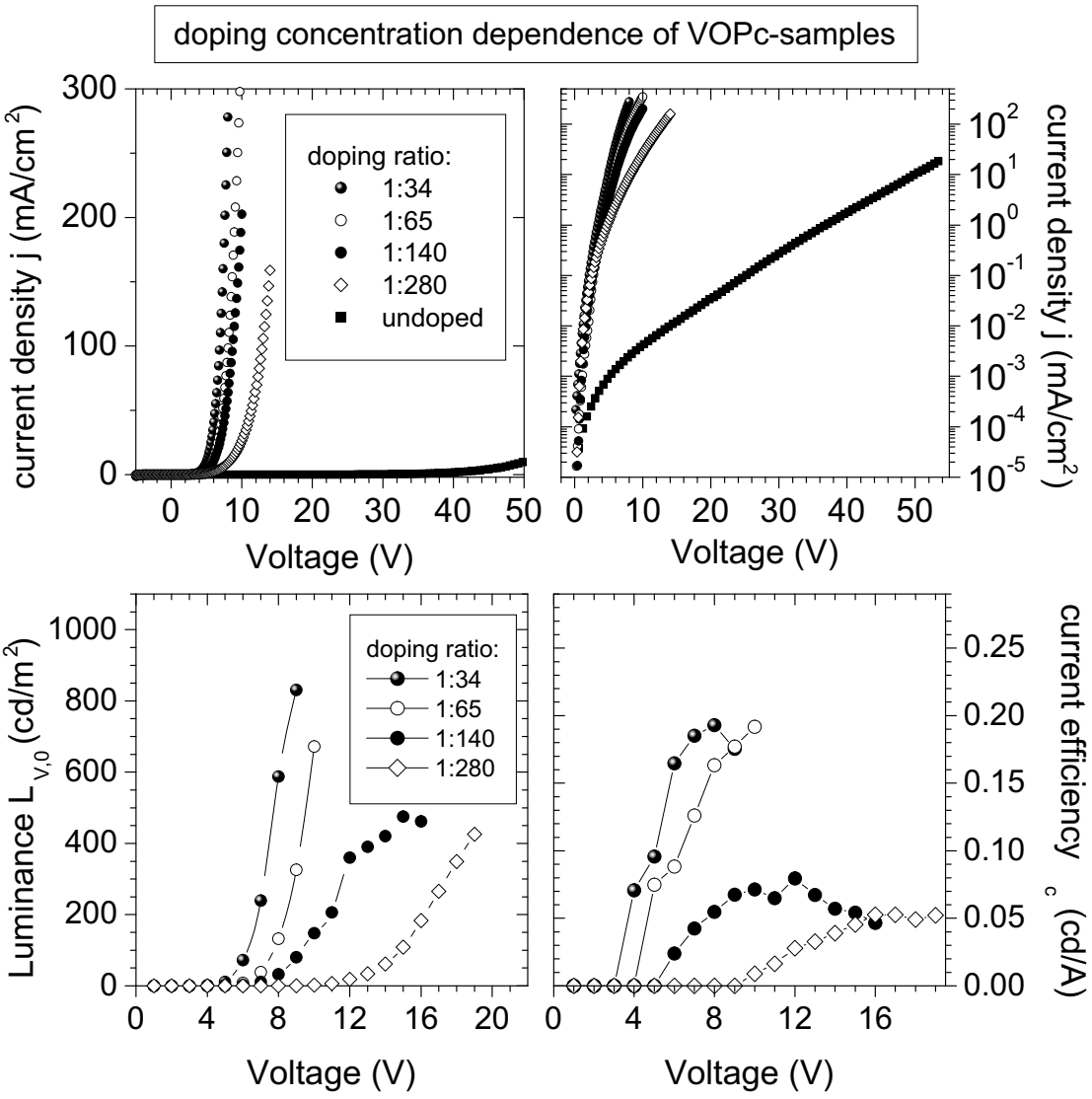

Figure 5.2: *Top: current density j vs. voltage V characteristics for the OLED structure ITO/200nm doped VOPc/71nm Alq_3/Al for several molecular doping ratios (left: linear scale, right: logarithmic current scale). Bottom: Luminance in forward direction $L_{V,0}$ vs. voltage V characteristics (left) and the dependence of the current efficiency η_c on the applied voltage V (right) for these OLEDs.*

is approx. 1x10^{-4} S/cm (Figure 2.2) which would result in a voltage drop over a 200nm thick doped VOPc layer of 12mV at a current density of 60mA/cm^2. This voltage drop can be neglected for the measured operating voltages between 5 and 15V. The second effect is deduced from the results of UPS/XPS investigations (see Chapter 4). Doping leads to a thinner space charge layer near the contact in the doped organic layer which enables more efficient tunnel injection of holes from the ITO into the doped HTL. This is similar to the quasi-ohmic behavior of Schottky contacts to highly doped inorganic semiconductors.

Nevertheless, the operating voltages of the OLEDs are still well above those expected from the energy of the emitted light, which is 2.4V for the emission wavelength of Alq_3. The main reasons are probably the inefficient electron injection into and the bad electron transport inside the Alq_3 layer.

Table 5.1: *Voltages V to reach a certain current density j and luminance in forward direction $L_{V,0}$ for various doping ratios of the doped VOPc hole transport layer (OLED layer sequence: ITO/200nm doped VOPc/71nm Alq_3/Al). Additionally, the current, power and quantum efficiencies η_c, η_P and η_Q are given. The latter is calculated under the assumption that the OLEDs are ideal Lambertian emitters and the medium wavelength of the emitted light of all OLEDs is 515nm. For η_c also the maximum value is given in brackets. The radiation luminous efficacy K_r for the pure Alq_3 emitting OLEDs was calculated from the electroluminescence spectra to be 420 lm/W.*

sample	V (V) for $j = 10$ mA/cm^2	V (V) for $L_{V,0} = 100$ cd/m^2	j (mA/cm^2) for $L_{V,0} = 100$ cd/m^2	η_c (cd/A) at $L_{V,0} = 100$ cd/m^2 and max.	η_P (lm/W) at $L_{V,0} = 100$ cd/m^2	η_Q (%) at $L_{V,0} = 100$ cd/m^2
undoped	50.0	not measurable	-	-	-	-
1:280	8.2	14.9	220	0.04 (0.05)	0.01	0.015
1:140	6.0	9.3	140	0.07 (0.08)	0.024	0.025
1:65	5.8	7.7	63	0.16 (0.19)	0.064	0.05
1:34	5.0	6.2	59	0.17 (0.19)	0.086	0.06

Table 5.1 also gives the current densities necessary to obtain a luminance of 100cd/m^2 and the calculated efficiencies at this brightness. The current efficiency of the OLED strongly increases with the doping ratio for dopant concentrations from 1:282 to 1:65, but this increase is weakening for larger dopant concentrations. Additionally, the efficiency seems to have a maximum value at a certain voltage, which is clearly visible in the η_c vs. V curves for the doping ratios 1:140 and 1:34.

The current efficiency is mainly determined by the balance and total number of holes and electrons in the emission zone, because the recombination is a bipolar process (see Appendix A, point e). Thus, the efficiency enhancement upon doping can be explained by an increased number of holes that are injected into the Alq_3 layer so that the probability that an electron meets a hole in the Alq_3 layer before it enters the VOPc layer is increased. The maximum of the current efficiency can be explained as follows: Due to the missing energetic barrier, electrons can easily be injected into the VOPc layer (see energy diagram in Figure 5.3, left picture). There they are able to recombine non-radiatively or they may reach the anode. Hence, a maximum should be expected at that voltage where the density of injected electrons, which is strongly dependent on the bias voltage, and the density of holes, which is less dependent on bias voltage due to doping, are balanced. Additionally, at high voltages holes may reach the cathode without recombining in the Alq_3 layer what also decreases the efficiency [162]. A possible explanation for the low increase of the current efficiency between the doping ratios 1:65 and 1:35 is doping-enhanced exciton

quenching at the Alq_3-VOPc interface, as it is also known for dye-metal interfaces. This explanation is supported by the observation that the dopant F_4-TCNQ in an Alq_3 layer quenches the photoluminescence of Alq_3 [163].

In spite of the remarkable improvement of the electroluminescence efficiency upon doping, the absolute value of the efficiency is still very much below the best results reported in literature for OLEDs emitting from a pure Alq_3 layer (around 2-5 cd/A, see e.g. [1, 53, 54, 55]). The major reason for the lower efficiency of these diodes is that the simple two-layer design does not prevent negative carriers from reaching the anode. This again is due to the missing energy barrier for electrons at the Alq_3-VOPc interface. This reduces the probability of exciton formation in Alq_3 and thus the light emission.

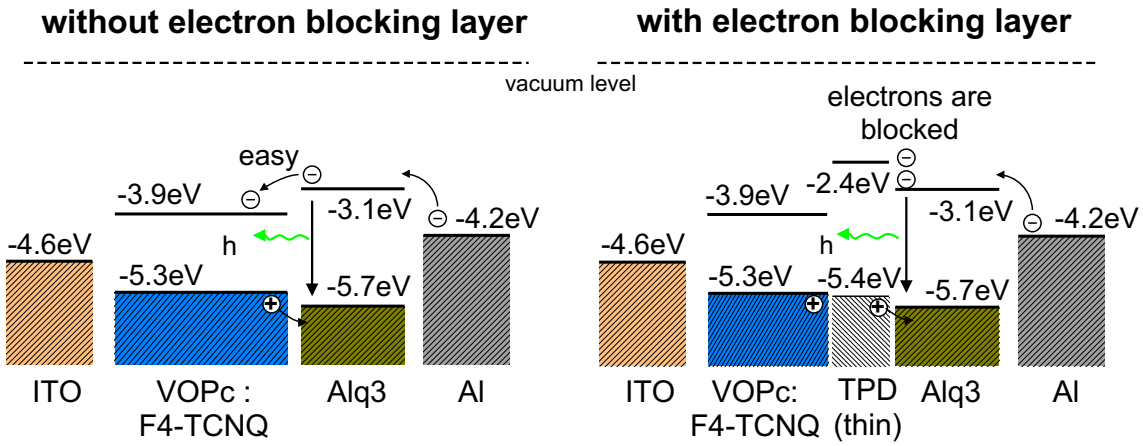

Figure 5.3: *Schematic energy alignment (assuming vacuum level alignment) for OLEDs containing a VOPc hole transport layer without (left) and with (right) an electron blocking layer (TPD).*

We can summarize the main results on OLEDs with a p-type doped hole transport layer prepared by co-evaporation as follows:

- The operating voltage of the doped OLEDs is lowered drastically compared to undoped OLEDs and
- the power efficiency is improved by doping the transport layer.

This basically has the following technological advantages:

- It allows the use of thicker hole transport layers, which reduces short circuit problems.
- The ohmic heating of the OLED is reduced because of a lower voltage drop in the doped layer. This should result in longer device lifetimes.
- A slight change of the anode workfunction (e.g. by special pre-treatment of the ITO anode) should not change the charge injection into the device, because of the highly doped organic semiconductor in front of the anode material.

b) Current-voltage curves

Figure 5.4 shows two current-voltage curves of OLEDs of the previous doping concentration series in more detail. The principal behavior of all OLEDs having a doped hole transport layer is identical; as an example the curve for the 1:65 doped VOPc layer is given. Thus, for a reasonable high doping ratio, the current voltage behavior of OLEDs with doped HTL is determined by the intrinsic Alq_3 layer. This is to be expected because the conductivity of the Alq_3 layer is very much below that of the doped VOPc layer. The absolute value of the current flow is determined by the bipolar recombination rate in the device and can be several orders of magnitude higher than in an unipolar device consisting of only the Alq_3 layer [130]. At very low bias voltages, one recognizes an ohmic region (ohmic conduction of thermally generated charge carriers). At higher operating voltages the j vs. V curve of the 1:65 doped sample is steeper, following the space charge limited dependence $j \sim V^6$ of an exponential trap distribution (see Appendix B). The trap filled limit, where Child's law $j \sim V^2$ should hold, is not reached at voltages

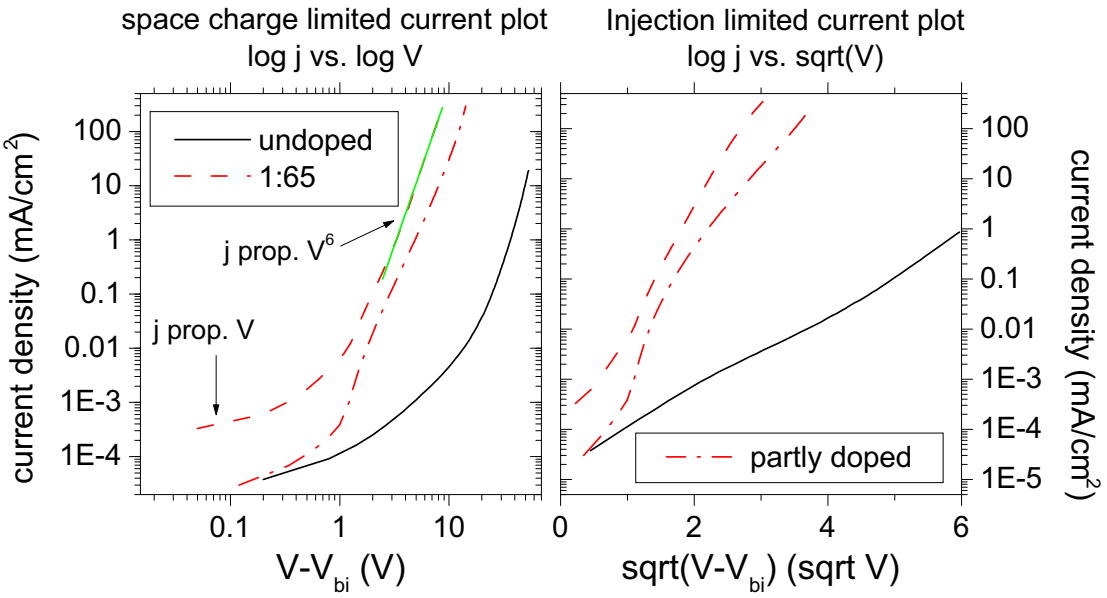

Figure 5.4: *Current voltage curves of the OLEDs with an undoped VOPc layer (black, solid line) and with a 1:65 doped VOPc layer (ITO/VOPc/Alq_3/Al, red, dashed line) in (left) a double logarithmic plot (to check for space charge limited currents) and (right) in a $log(j)$ vs. $\sqrt{V - V_{bi}}$ plot to check for injection limitations. For comparison, the current voltage curve of a partly doped device with the layer sequence ITO/25nm doped VOPc 1:34/175nm undoped VOPc/Alq_3/Al is shown (red, dash-dotted line). The built-in voltage V_{bi} for the undoped device was approximated by the workfunction difference of the ITO and the Al cathodes (0.4eV), whereas the built in voltage for the OLEDs with a doped VOPc layer was calculated from the workfunction difference of the doped VOPc layer (estimated from UPS/XPS experiments to be 0.3eV above the HOMO-level) and the Al cathode, which results in 0.8eV.*

where these devices are stable. Similarly, Burrows et al. observed a space charge limited current behavior (with $j \sim V^6$ at room temperature) in OLEDs with the layer sequence ITO/TPD/Alq_3/Mg:Ag [164, 165]. However, deviations from this behavior in our OLEDs between 0.3 and 2V might be due to the fact that aluminium instead of Mg:Ag is used as cathode material. Thus, no ohmic contact for electron injection is expected in the low voltage region because of the higher Al-workfunction. Note that the behavior of the OLEDs at low voltages between 0 and 3 V, where no light is emitted, shows no systematic dependence on the doping ratio (Figure 5.2). This is evidence for short circuit path in the OLEDs or other parasitic effects, which determine the current flow at low voltages.

The current-voltage curve of the undoped sample is somewhat different to the curve of the doped sample. Firstly, the current density at a given voltage above 3V is more than three orders of magnitude lower. Secondly, the current voltage curve does not seem to follow the SCL model (left graph in Figure 5.4) but rather shows an injection limited behavior. However, it is not clear from the right graph of Figure 5.4, whether this is due to thermionic emission over an image charge potential, where $j \sim \exp\sqrt{V - V_{bi}}$ is expected. Both effects can be due to the fact that charge injection from the not specially pre-treated ITO into undoped VOPc is the limiting factor in this device. This is supported by the fact that an OLED with only 25nm 1:34 doped VOPc near the ITO and 175nm thick undoped VOPc layer near Alq_3 rather shows a space charge limited behavior (cp. Figure 5.4, partly doped sample). However, a detailed analysis of the charge injection and transport behavior would demand thickness and temperature dependent current-voltage investigations and the inclusion of recombination and bipolar injection effects in the theoretical description. This would also be necessary to clarify the SCL behavior seen in the doped samples (for further details see e.g. [130, 166]).

5.1.2 Improvement of quantum efficiency by introducing an electron blocking layer

As it was seen in the preceding Section, the efficiency of OLEDs using VOPc doped with F_4-TCNQ as hole transport layer is generally low. This behavior can be explained by the fact that electrons can easily reach the anode contact because they are not blocked at the interface Alq_3-VOPc. We thus expect that the electroluminescence efficiency can be remarkably increased by inserting a thin electron blocking layer with a larger band gap but similar HOMO-level than VOPc. This conditions are fulfilled for the well investigated amorphous hole transport material TPD. Because of their large HOMO-LUMO distance (at least larger than the transport gap of the emitter material), such materials are commonly referred to as wide gap materials. The situation is depicted in the schematic energy diagram of such an OLED using an additional thin TPD electron blocking layer (Figure 5.3, right diagram).

Figure 5.5 gives the luminance in forward direction $L_{V,0}$ vs. voltage V and current efficiency η_c vs. voltage curves for two OLEDs: The 1:34 doped VOPc sample from the preceding Section and a second one with an additional 20nm thick TPD interlayer. As expected, the maximum current efficiency is increased by a factor of 3 up to almost 0.6 cd/A. Additionally, the OLED with the amorphous TPD interlayer showed a higher stability and could be operated at higher voltages without the danger of damage[1]. The

[1]it should be noted here that also the OLED without TPD could be operated at higher voltages than

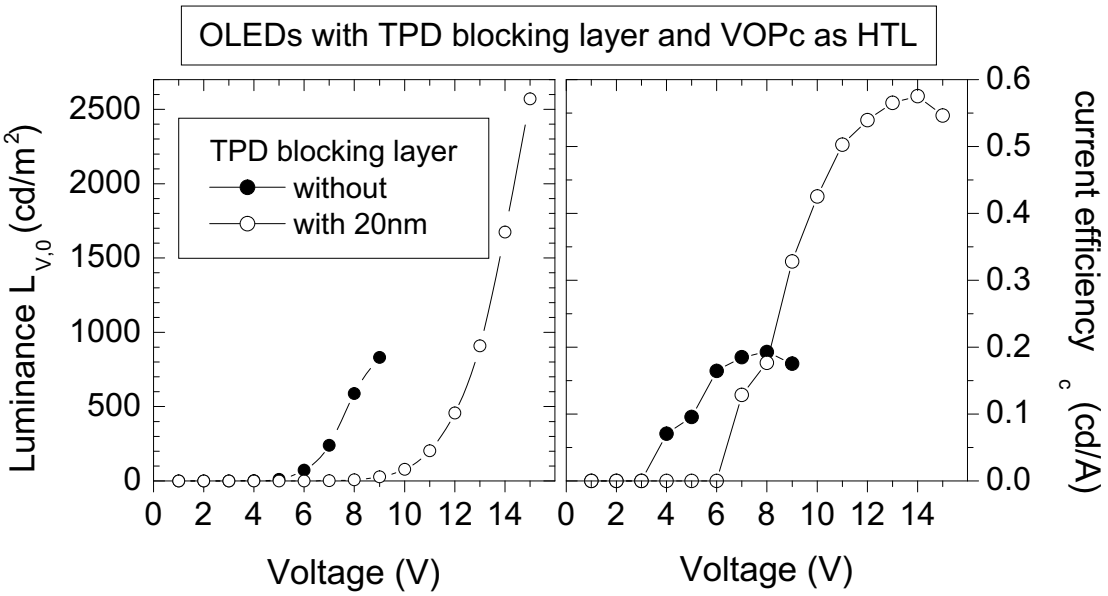

Figure 5.5: *(left) Luminance in forward direction $L_{V,0}$ vs. voltage V characteristics for the OLEDs ITO/200nm doped VOPc/71nmAlq_3 /Al and ITO/200nm doped VOPc/20nm TPD/71nmAlq_3 /Al (molecular doping ratio 1:34). (right) The dependence of the current efficiency η_c on the applied voltage V for these OLEDs.*

Table 5.2: *Survey of the optoelectronic behavior of the two OLEDs described in Figure 5.5. Calculations were done as described in Table 5.1.*

sample	V (V) for $j = 10$ mA/cm^2	V (V) for $L_{V,0} = 100$ cd/m^2	j (mA/cm^2) for $L_{V,0} = 100$ cd/m^2	η_c (cd/A) at $L_{V,0} = 100$ cd/m^2 and max.	η_P (lm/W) at $L_{V,0} = 100$ cd/m^2	η_Q (%) at $L_{V,0} = 100$ cd/m^2
without TPD	5.0	6.2	59	0.17 (0.19)	0.086	0.06
with TPD	9.25	10.1	23	0.43 (0.57)	0.13	0.15

OLED with the TPD interlayer reaches its maximum current efficiency at higher luminance. From the fact that electrons are blocked at the Alq_3-TPD interface, and thus the charge balance is relatively independent of the applied voltage [167], it is expected that the efficiency vs. voltage dependence has a plateau after reaching its maximum value, which is not seen in the data of Figure 5.5 (right picture). Most probably, this is caused by exciton quenching at impurities in the Alq_3 layer. Evidence for this gives the later observed efficiency plateau of similar OLEDs prepared in the multiple chamber UHV system

shown in Figure 5.5, however, the change in operating voltage with time was more critically in this case

(see Section 5.4.1).

However, as can be seen in Table 5.2 and Figure 5.5, the TPD interlayer also increases the operating voltage due to the much lower conductivity of intrinsic TPD compared to doped VOPc. This leads to a lower increase of the power efficiency η_P upon inserting the TPD layer.

Additional experiments with an only 5nm thick TPD interlayer gave almost no effect on current efficiency and operating voltage. This gives evidence that TPD does not form closed layers on the relatively thick polycrystalline VOPc layer. Hence, it is impossible to optimize the TPD layer thickness to maximize the power efficiency for this OLED layer setup.

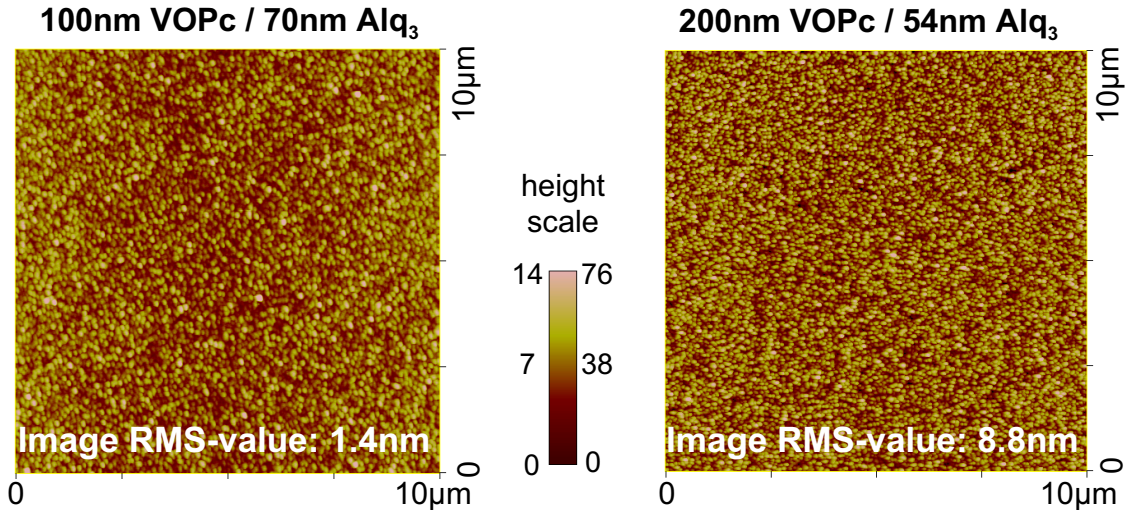

Figure 5.6: *Atomic force microscopy (AFM) scans of surfaces of (left) ITO/100nm VOPc/70nm Alq_3 and (right) ITO/200nm VOPc/54nm Alq_3. Note the different height scales of the two pictures. The 200nm thick VOPc layer shows spikes up to 70nm height whereas the 100nm thick VOPc layer shows only spikes up to 12nm. The latter is in the range of the roughness of the underlying ITO substrate.*

The first results with the use of an amorphous wide gap hole transport material showed the potential for improvements of the device concept featuring doped hole transport layers. Thus, the dopability of wide gap materials will be investigated in the following Sections to replace the thick phthalocyanine layers. There are two more reasons why phthalocyanines are not suitable for OLED application:

- Because of the low HOMO-LUMO gap of all phthalocyanines, they show strong absorption in the red and orange spectral region (see the absorption spectra of VOPc in Figure 5.1). Thus, thick phthalocyanine layers are no good candidates for full color OLED applications.

- Phthalocyanines generally form polycrystalline layers, which tend to island and needle growth at nominal thicknesses above approx. 100nm. Evidence for that was found in the behavior of the OLEDs with a 5nm thick TPD interlayer where almost no change in the optoelectronic properties was observed. Even stronger evidence

gave the following experiment: Decreasing the thickness of the doped VOPc layer lead to an increase of the operating voltage. This can only be explained with a higher effective Alq_3 layer thickness when the VOPc layer gets smaller. The origin of this behavior might be a drastically increased roughness of the thick VOPc layer, which indeed can be seen from AFM investigations of the VOPc/Alq_3 surface (Figure 5.6). The higher roughness of the VOPc underlayer may lead to a higher density of current paths through the Alq_3 overlayer which are shorter than the nominal layer thickness. Since the voltage drop over the Alq_3 layer is much higher than that in the doped VOPc layer, a decrease in VOPc-layer roughness would lead to a decrease of the density of shorter current paths and an increase of the effective Alq_3 layer thickness. Such a lateral inhomogeneous thickness can also partly explain the relatively low absolute value of the current efficiency, even with a TPD interlayer.

5.2 Wide gap transport materials & electron injection layers: efficiency improvement

5.2.1 Screening of the doping efficiency of wide gap materials

There are two main reasons why we wish to p-type doped amorphous wide gap materials: (i) their blocking behavior for electrons (cp. Section 5.1.2), and (ii) the better film forming capabilities of such materials which reduce pin-hole and instability problems. In the following, the results of a doping efficiency screening of such materials are presented. To quickly evaluate their dopability by F_4-TCNQ, the planar conductivity of a doped layer at room temperature and the degree Z of charge transfer (investigated with FTIR spectroscopy) of a doped organic layer on a KCl substrate were investigated. The known OLED wide gap hole transport materials TPD, α-NPD and a Starburst derivative (TNPATA) were investigated together with tetracene, pentacene and perylene from the class of homocyclic aromatic molecules. The wide gap hole transport materials exhibit amorphous layer growth in a glassy state. These materials start to crystallize at the glass transition temperature which is above 60 ^{o}C for all investigated materials.

Figure 5.7 summarizes the experiments. Not shown are values for copper-phthalocyanine (CuPc) which is widely used in OLEDs as hole injection layer. As in the case of ZnPc and VOPc, it can be efficiently doped (Z=1) and shows a slightly higher conductivity than VOPc (8x10^{-9} S/cm at a doping ratio of 1:33). Additionally, two other Starburst-derivatives, namely m-MTDATA and TDATA (for chemical structures see Figure 3.3) were investigated and their room temperature conductivity at a molecular doping ratio of 1:60 was determined to be 7x10^{-7}S/cm and 4x10^{-7}S/cm, respectively.

It can be concluded from that survey that a high degree of charge transfer is necessary for efficient doping. In the case of the homocyclic molecules perylene, tetracene and pentacene, the degree of charge transfer increases with decreasing ionization energy and a higher Z value leads to higher conductivities. The conductivity of doped pentacene almost reaches the value of VOPc, however, it shows a degree of charge transfer well below 1. The same behavior (increasing Z with decreasing ionization energy) is seen for the class of di- and triphenylamines (NPD, TPD and TNPATA). However, their conductivity is generally low. This drastic difference to the doped layers of the phthalocyanines or pentacene can not be explained sufficiently by their low mobility values in the range of 10^{-3} to 10^{-4}

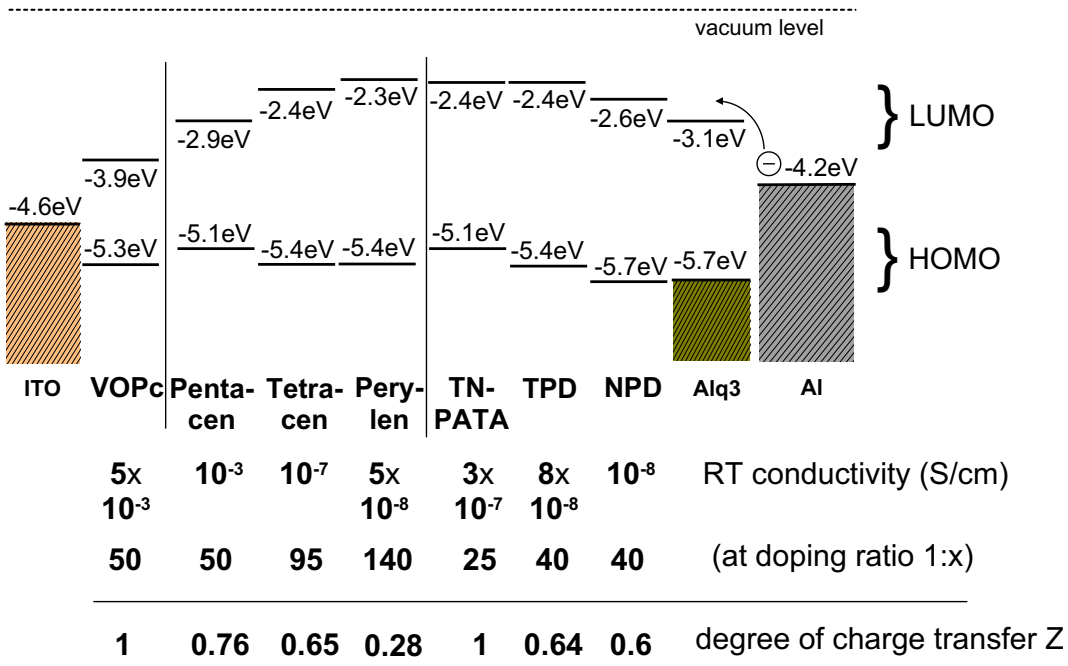

Figure 5.7: *Planar conductivity (200nm thick layers) at room temperature and degree of charge transfer Z of several potential hole transport materials doped with F_4-TCNQ at the given molecular doping ratio. The HOMO and LUMO levels of the investigated materials are shown schematically (see Section 3.1.1). The conductivity of all undoped layers was below 5x10^{-9}S/cm.*

cm^2/Vs [168]. Obviously, the second step of reaction (2.1), namely the separation of local charge transfer states into a mobile hole and an ionized acceptor is inefficient for these glassy amorphous materials, which exhibit weakly interacting π-electron systems. Maennig et al. explained the conductivity difference by different width of the distribution of states (DOS). A small DOS width causes the transport to take place far away from the Fermi energy [119]. Furthermore, the same HOMO position neither leads to similar degrees of charge transfer nor to similar conductivities, as one can see from a comparison of pentacene and TNPATA or of tetracene, perylene and TPD. The arrangement of the dopant molecules with respect to the matrix molecules might play a role, here. However, no general rule for the choice of a suitable matrix material to be efficiently doped with F_4-TCNQ can be concluded from the above observations.

Now, the question arises if such doped wide gap hole transport materials like TNPATA can be used in a typical OLED. Assuming a HTL layer thickness of 200nm and a current density of 10mA/cm^2 (which allows for 100cd/m^2 luminance at a current efficiency of 1cd/A), the voltage drop over this layer with a conductivity of 3x10^{-7} S/cm should only be 0.7V. This is small compared to the operating voltage of typical OLEDs. Hence, such a layer should act quite similar to the doped VOPc layer in the preceding Sections. This is shown in the following.

5.2.2 Two layer OLEDs with doped wide gap HTLs

Starburst derivatives were chosen as an amorphous model system for doping based on the results describes above. The unsubstituted Starburst derivative TDATA [41] was used for the following experiments because of its availability in larger amounts. TDATA was purified in house by the vacuum gradient sublimation technique. The samples were prepared in the single chamber high-vacuum system. For the results following, Alq_3 from Syntec GmbH, Germany was used, purified in house by the gradient sublimation technique.

a) OLEDs with Al cathodes

A doping concentration dependence study was performed similarly to the study of doped VOPc in the preceding Section. The layer sequence of the samples was ITO/200nm TDATA: F_4-TCNQ/65nm Alq_3/Al. The current density j vs. voltage V curves and luminance in forward direction $L_{V,0}$ vs. voltage curves are depicted in Figure 5.8. In the bottom right graph, the dependence of the current efficiency η_c on the operating voltage V is also shown. With increasing doping concentration, the hole injection from the untreated ITO into the TDATA layer is improved and the conductivity in the TDATA layer is increased. The simple calculation above has shown that even low doping ratios raise the conductivity to levels where the influence of the bulk resistance becomes small for the voltage range where noticeable light is emitted. A further increase of the doping concentration of TDATA from 1:62 to 1:33 does not significantly change the current voltage curves of the OLEDs indicating that the injection is not further improved.

Table 5.3 summarizes the most important optoelectronic data of the doping concentration series.

Table 5.3: *The optoelectronic data of OLEDs with a F_4-TCNQ doped wide gap hole transport layer with different doping concentrations: ITO/200nm F_4-TCNQ doped TDATA/65nm Alq_3/Al.*

molecular doping ratio	V (V) for j = 10 mA/cm^2	V (V) for $L_{V,0}$ = 100 cd/m^2	j (mA/cm^2) for $L_{V,0}$ = 100 cd/m^2	η_c (cd/A) at $L_{V,0}$ = 100 cd/m^2 and max.	η_P (lm/W) at $L_{V,0}$ = 100 cd/m^2	η_Q (%) at $L_{V,0} = 100$ cd/m^2
	doped TDATA as HTL and Al cathode					
undoped	33.5	34.8	15.3	0.65 (0.69)	0.059	0.20
1:250	8.0	11.3	45.8	0.22 (0.22)	0.061	0.07
1:62	6.2	9.5	69.5	0.14 (0.14)	0.046	0.04
1:33	6.15	9.4	87.9	0.11 (0.11)	0.037	0.03

The operating voltage to reach a light output of 100 cd/m^2 is decreased from above 30V to below 10V upon doping. Note that this decrease is not as high as in the case of doped VOPc as hole transport layer (Section 5.1.1) where the operating voltage was decreased to almost 6V. Together with the desired decrease of operating voltage we observe an undesired decrease of device efficiency from 0.7 cd/A (maximum value) in the undoped case down to only 0.1 cd/A at the highest doping ratio. This might have three reasons: (i) the dopant F_4-TCNQ directly at the interface acts as a quenching species for

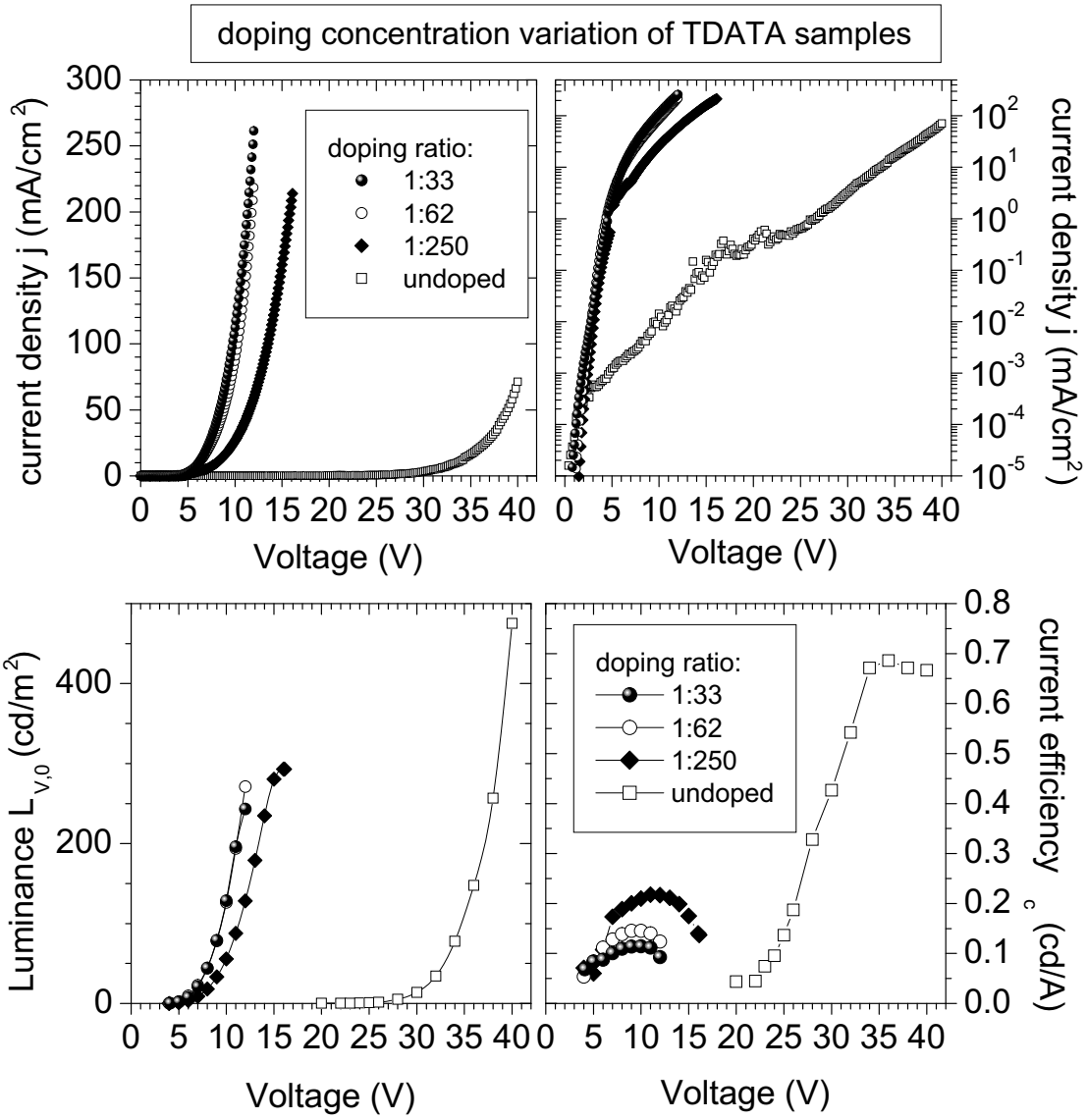

Figure 5.8: *Current voltage curves in a linear scale (top left) and a log-lin scale (top right) as well as luminance in forward direction $L_{V,0}$ vs. voltage V (bottom left picture) and current efficiency η_c vs. voltage curves (bottom right pictures) for OLEDs with the layer sequence: ITO/200nm F_4-TCNQ doped TDATA/65nm Alq_3/Al and several doping ratios of the TDATA layer .*

excitons at the interface Alq_3-TDATA, (ii) doping increases the probability for an electron to be injected into the doped TDATA layer, leading to non-radiative recombination in the organic layer or at the anode contact, and (iii) an increased probability of exciplex formation due to the high hole concentration at the interface. All these effects would lower the device efficiency.

Despite the problems with the lowered efficiency, the doping concentration study at

the sample structure ITO/200nm doped TDATA/65nm Alq_3/Al shows the potential of using doped wide gap materials in OLEDs to decrease their operating voltage.

a) OLEDs with Al cathode and a LiF interlayer

As was seen from the results of OLEDs with p-type doped hole transport layers, the hole injection and transport is strongly enhanced upon doping. To further improve the optoelectronic properties of OLEDs, their electron injection and transport must be improved. The first approach would be the use of cathode-metals with a lower workfunction like calcium or magnesium. Ca is widely used for polymer LEDs and improves their properties significantly. The disadvantage of this approach is the low stability of such highly reactive cathodes against environmental influences. In 1997, the Kodak group inserted a small layer of lithium-fluoride (LiF) in between the electron transport layer and the aluminium cathode [53]. This drastically improved the electron injection. First, this effect was explained by a better injection through a small (less than 1nm) insulating layer [71]. It was found later that the effect is less pronounced for Mg cathodes [69] and for an inverse layer sequence (LiF on top of Al). Nowadays, the interplay of two processes that enhance electron injection is verified. Firstly, LiF on top of aluminium lowers the workfunction of Al by about 0.7eV [72] making the combination of LiF and Al a lower workfunction cathode. Secondly, by evaporating hot Al atoms on top of LiF, the LiF is cracked and Li atoms diffuse into the underlying organic layer and cause a n-type doping [74]. The doping works especially well for Alq_3 as organic layer. It also works for other reactive metals, like titanium. Furthermore, other I-VII or I-VI insulating compounds might be used, like cesium-fluoride [169] or lithium-oxide [25]. Up to now, the role of residual water on the LiF surface is still unclear. Heil et al. [72] stated that water is necessary for an exothermic chemical reaction that leads to doping, whereas Mason et al. [74] stated a possible chemical reaction without the need of water. However, only a monolayer of water would be necessary to start the reaction of Alq_3 and LiF. This monolayer is adsorbed quickly even in a vacuum chamber with a base pressure of $5x10^{-9}$mbar.

Figure 5.9 shows the current density j vs. voltage V curves and luminance in forward

Table 5.4: *Survey of the optoelectronic behavior of two layer OLEDs with a wide gap HTL and an additional LiF electron injection layer made in the HV system: ITO/200nm F_4-TCNQ doped TDATA/65nm Alq_3/1nm LiF/Al. Calculations were done as described in Table 5.1.*

molecular doping ratio	V (V) for j = 10 mA/cm^2	V (V) for $L_{V,0}$ = 100 cd/m^2	j (mA/cm^2) for $L_{V,0}$ = 100 cd/m^2	η_c (cd/A) at $L_{V,0}$ = 100 cd/m^2 and max.	η_P (lm/W) at $L_{V,0}$ = 100 cd/m^2	η_Q (%) at $L_{V,0}$ = 100 cd/m^2
	TDATA as HTL, LiF/Al as cathode					
undoped	26.1	27.5	13.9	0.72 (0.78)	0.082	0.22
1:250	5.9	8.5	38.7	0.26 (0.35)	0.10	0.08
1:62	4.05	6.7	64.5	0.16 (0.21)	0.08	0.05
1:33	4.25	6.7	77	0.13 (0.16)	0.06	0.04

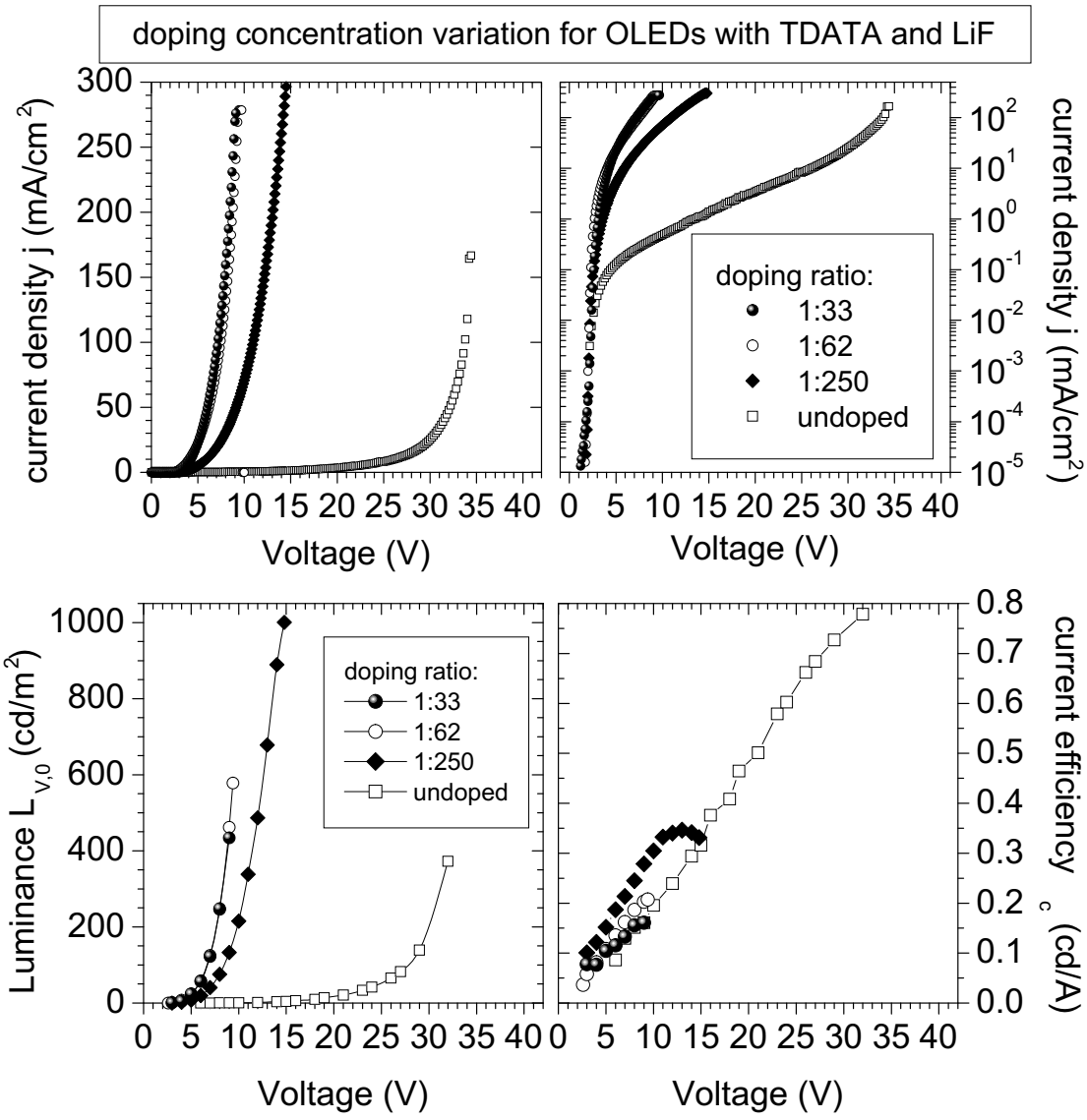

Figure 5.9: *Current voltage curves in a linear scale (top left) and a log-lin scale (top right) as well as luminance in forward direction $L_{V,0}$ vs. voltage V (bottom left picture) and current efficiency η_c vs. voltage curves (bottom right pictures) for OLEDs with differently doped TDATA and an additional nominally 1nm thick LiF layer between Alq_3 and aluminium cathode (layer sequence: ITO/200nm F_4-TCNQ doped TDATA/65nm Alq_3/1nm LiF/Al).*

direction $L_{V,0}$ vs. voltage curves together with the dependence of the current efficiency η_c on the operating voltage V for OLEDs with the layer sequence ITO/200nm doped TDATA/65nm Alq_3/1nm LiF/Al and a varying doping concentration. The most relevant results are listed in Table 5.4. As shown also by other groups [69, 170] the operating voltage of the OLEDs with LiF interlayer are decreased compared to OLEDs without LiF

interlayer. Comparing OLEDs with 200nm doped TDATA (doping level 1:33) as hole transport layer, an operating voltage (for a luminance of 100cd/m^2) of 9.4V without LiF, but of only 6.7V with LiF interlayer is obtained. Despite that, the current efficiency of OLEDs with a LiF interlayer has only been slightly increased (in the 1:33 doped case from 0.11cd/A up to 0.16cd/A). The tendency to lower efficiency with increased doping is the same as in the case of the OLEDs without the LiF interlayer. Obviously, this effect is not related to the quality of electron injection and charge balance in the emission zone but results from the interface between TDATA and Alq_3. As can be seen from literature, OLEDs with the interface Starburst-Alq_3 show in tendency lower device efficiencies than devices with NPD-Alq_3 or TPD-Alq_3 interfaces [162, 42, 43]. The lower efficiency has been attributed to the exciplex formation between the excited state of Alq_3 and the ground state of the Starburst derivatives leading to increased nonradiative exciton decay [171, 172, 173].

5.2.3 OLEDs with a doped wide gap HTL and an additional TPD blocking layer

We have learned in Section 5.1.2 that the introduction of a thin layer with better suited properties helps to avoid electron injection into the hole transport layer. One might ask whether this concept also improves OLEDs with wide gap hole transport layers. It is known from literature that OLEDs with TPD as hole transport layer show higher efficiencies than Starburst-OLEDs. Thus, a doping concentration series of OLEDs with F_4-TCNQ doped TDATA as hole injection and transport layer, Alq_3 as emitting layer and LiF/Al as cathode material together with an additional 10nm thin TPD layer between TDATA and Alq_3 was investigated. Figure 5.10 shows the current density j vs. voltage V curves and luminance in forward direction $L_{V,0}$ vs. voltage curves. The dependence of the current efficiency η_c on the operating voltage V is also shown. The layer sequence is: ITO/100nm doped TDATA/10nm TPD/65nm Alq_3/1nm LiF/Al. Investigated were two doping concentrations and one undoped sample for comparison. The relevant optoelectronic data are summarized in Table 5.5 (series 2).

Table 5.5: *Survey of the optoelectronic behavior of OLEDs with a wide gap HTL, an LiF/Al cathode and an electron blocking layer made in the HV system: ITO/100nm F_4-TCNQ doped TDATA/10nm TPD/65nm Alq_3/1nm LiF/Al. Calculations were done as described in Table 5.1.*

molecular doping ratio	V (V) for j = 10 mA/cm^2	V (V) for $L_{V,0}$ = 100 cd/m^2	j (mA/cm^2) for $L_{V,0}$ = 100 cd/m^2	η_c (cd/A) at $L_{V,0}$ = 100 cd/m^2 and max.	η_P (lm/W) at $L_{V,0}$ = 100 cd/m^2	η_Q (%) at $L_{V,0}$ = 100 cd/m^2
	wide gap OLED with TPD blocking layer and LiF/Al cathode					
undoped	9.0	9.0	10.0	1.0 (1.0)	0.35	0.31
1:500	5.55	5.3	8.3	1.2 (1.7)	0.71	0.37
1:50	3.35	3.4	9.1	1.1 (1.3)	1.0	0.34

As expected from our previous experiments, the operating voltage is again strongly

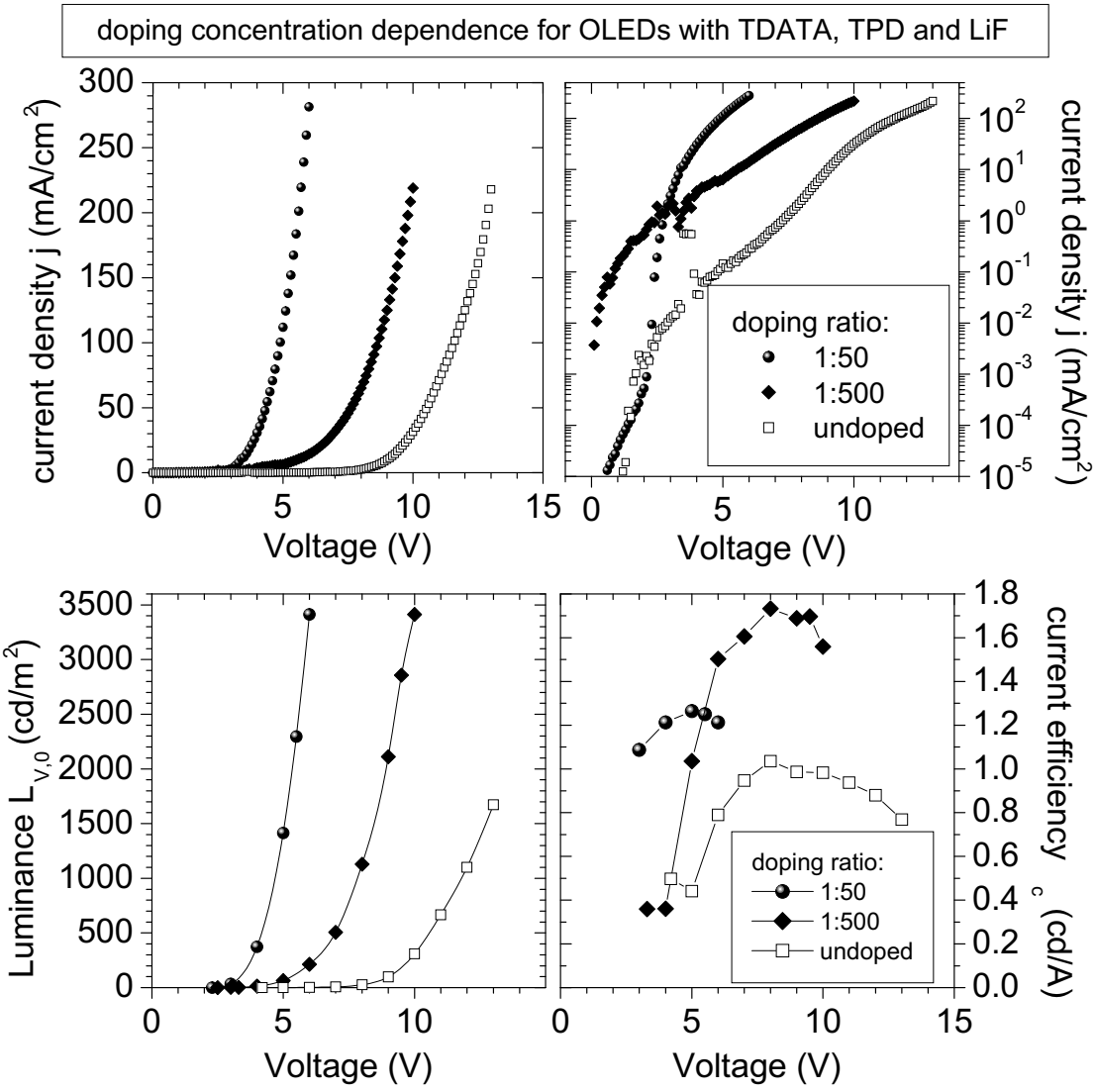

Figure 5.10: *Further efficiency improvement by the introduction of a more suitable blocking layer (10nm TPD): current voltage curves in a linear scale (top left) and a log-lin scale (top right) as well as luminance in forward direction $L_{V,0}$ vs. voltage V (bottom left picture) and current efficiency η_c vs. voltage curves (bottom right pictures) for the OLED layer sequence: ITO/100nm F_4-TCNQ doped TDATA/10nm TPD/65nm Alq_3/1nm LiF/Al and different doping concentrations of TDATA.*

decreased upon doping. Because of the lower total thickness of the hole transport layers (110nm instead of 200nm), the operating voltage of the undoped sample is only 9V (for 100cd/m^2). This supports the limiting role of an undoped hole transport layer in conventional OLEDs. Additionally, the efficiency of the undoped device (1cd/A) is higher than the undoped device without the TPD interlayer (0.78cd/A), again indicating the crucial role of the interface to Alq_3. What is most important is the fact that with a 10nm thin

TPD layer, the current efficiency is even enhanced upon doping. It reaches a maximum value of 1.7cd/A for the low doping ratio 1:500 and still 1.3cd/A for the higher doping ratio of 1:50. For the latter, the operating voltage to reach 100cd/m^2 is 3.4V, which is better than any other OLED reported in literature based exclusively on vacuum sublimed small molecular layers (compare to [56]). The power efficiency is 1lm/W which is more than 10 times the power efficiency of the device without the TPD blocking layer and almost 30 times the efficiency of the OLEDs without LiF and TPD layers. Again, the dependence of the current efficiency on voltage shows a maximum. The rise in current efficiency at small voltages can be attributed to the improved charge balance in the light emission zone due to more efficient electron injection at higher voltages. The decrease of current efficiency at even higher voltages might be due to impurities in the light emitting Alq_3 layer.

The effect of introducing a TPD blocking layer between Alq_3 and the doped hole transport layer on the optoelectronic properties of doped OLEDs emphasize the importance of a suitable material combination next to the emitting layer. This leads to the formulation of a general concept of using doped hole and electron transport layers in conjunction with suitable blocking layers which is described in the next Section.

5.3 The concept of the combination of transport layer doping and blocking layers

The left side of Figure 5.11 shows an almost ideal energetic situation for a three-layer OLED. It is analogous to the situation in inorganic LEDs. The emission zone forms a potential wall, where charge carriers are captured and are not able to escape without recombination.

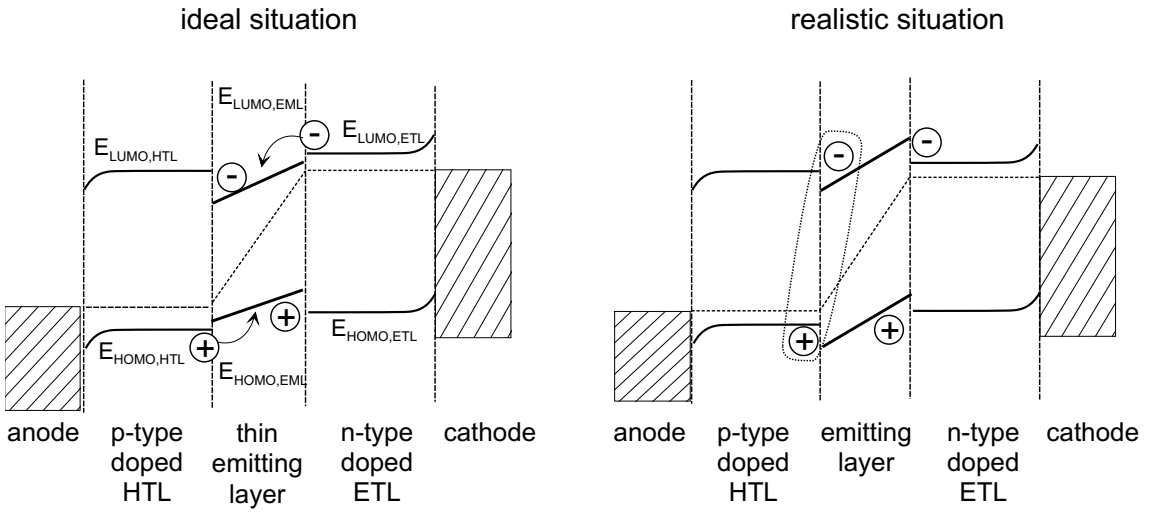

Figure 5.11: *(left) An almost ideal energetic setup of an OLED under forward bias. (right) The same situation, drawn using a parameter-set of realistic materials. The dotted line should indicate the possibility to form an interface exciplex.*

Due to the p- and n-type doping of the hole and electron transport layer (HTL and

ETL) and the apparent band bending at the metal/organic Schottky-junction, electrons and holes can be easily injected from the anode/cathode into the organic layers, although there is an energy barrier for hole and electron injection. Additionally, because of the high density of intrinsic carriers due to doping, the ohmic resistance of the transport layers can be neglected. If, furthermore, no barrier for hole injection from the HTL into the emitting layer (EML) and also no barrier for electron injection from ETL into the EML exists, the whole device should operate at voltages close to the theoretic limit of the energy of the emitted radiation and should show very steep current-voltage curves.

Generally, this ideal behavior is difficult to achieve in practice for several reasons: (i) Since the energy of light in the visible wavelength region is 2-3eV, the transport layers must have larger band gaps (i.e. HOMO-LUMO distances), which rules out many organic materials consisting of molecules large enough for thermally stable devices. (ii) Barriers for holes between the HTL/EML and for electrons between ETL/EML have to be avoided. Thus, the HOMO level of the HTL material ($E_{HOMO,HTL}$) and the LUMO level of the ETL material ($E_{LUMO,ETL}$) must be low/high (like it is sketched in Figure 5.11, left side). Such materials would need extremely strong acceptor/donator molecules to dope them. Especially n-type dopants (donator-HOMO near $E_{LUMO,ETL}$) tend to be unstable because their LUMO level approaches the vacuum level.

Using more realistic material parameters leads to a situation sketched in the right side of Figure 5.11. Here, charge carriers of opposite signs are blocked at the interfaces between the charge transport and the emission layer and accumulate there. This may lead to non-radiative quenching processes, e.g. exciplex formation of free charges on distinct molecules [172, 173, 174, 175] and direct quenching of excitons by dopants via Förster-transfer. Here, exciplex formation is the creation of an interface charge transfer exciton (hole located on material A, electron on material B) that can not transfer his energy to a Frenkel bulk exciton (cp. Appendix A, point g). Altogether, the quantum efficiency of such an OLED may be low (cp. Section 5.2.2).

To avoid such problems, the concept of additional blocking layers is introduced here [176]. Such blocking layers should be thin (because they are undoped and have low conductivities), but thick enough not to be tunneled through in the case of transport materials with energy levels that allow for minority carrier tunneling and otherwise thick enough to form closed layers. Additionally, their HOMO/LUMO positions needs to be adjusted in a way drawn schematically in Figure 5.12.

The conditions for a good blocking layer are given at the example of a blocking layer at the hole side (BLh):

(1) The majority carriers (holes) are predominantly blocked at the interface between the doped hole transport layer (HTL) and the blocking layer, which means that the barrier for hole injection from the blocking layer to the emitting layer (EML) should be low. This criterion is a consequence of the energetic situation faced in realistic materials.

(2) Minority carriers (electrons from the cathode side) have to be blocked very efficiently at the EML/BLh interface, since electrons that enter the BLh can reach the anode without further barriers.

(3) The LUMO of the HTL should be considerably higher than the LUMO of the EML (as sketched in figure 5.12). If this is fulfilled, the thickness of the BLh can be minimized and electrons are still efficiently blocked.

(4) No additional non-radiative decay channels should be created by the new interface between the emission layer and the blocking layers. That means that the charge transfer

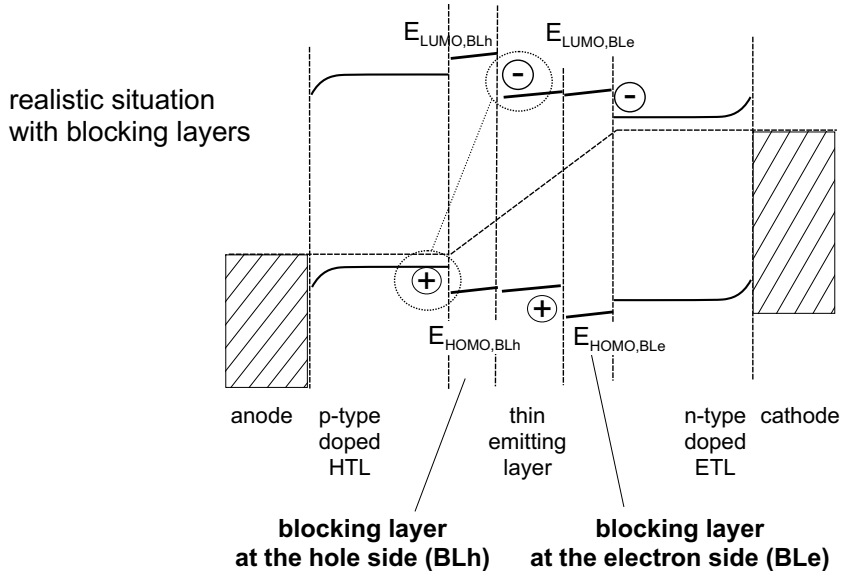

Figure 5.12: *The same situation like in figure 5.11 right side, but with additional thin blocking layers. Note that the distance between regions of higher charge densities of different signs are now separated, which effectively avoids the formation of an interface exciplex.*

exciplex at the interface can be transformed to bulk Frenkel excitons in the emission layer.

The equivalent conditions for the ETL and the blocking layer at the electron side (BLe) are obvious from figure 5.12. As a consequence of the use of a blocking layer between the doped charge transport layer and the emitting layer, regions with higher densities of charge carriers are separated by the thickness of the blocking layers, except in the emission region. Additionally, the direct quenching of excitons by dopant molecules is suppressed.

It should be noted here that the proper choice of the blocking materials is essential for the success of the concept of combining doped transport and undoped blocking layers. The prediction which material combination is suitable for this concept from the properties of the single materials is mostly not sufficient. The energetic HOMO and LUMO alignment at the interface might be changed by bringing both materials together (see Chapter 4 for more details). Therefore, the interface behavior regarding electroluminescence quenching has to be checked experimentally.

5.4 Preparation of OLEDs in a coupled UHV system

5.4.1 A comparison of OLEDs made in HV and in UHV

As explained in Chapter 3.4, the multiple chamber ultra high vacuum system (cluster-tool) has several advantages over the single chamber high vacuum preparation tool (used for all samples described up to here). This effect is evaluated in this Section. One has to keep in mind that not only the vacuum system was changed, but also the handling of the organic materials. As described in Chapter 3.4, all organic sources are kept under vacuum for a much longer time compared to the single chamber system where they were exposed to air after each sample preparation. Furthermore, the Alq_3 was stored in a separate high

vacuum environment after its purification by gradient sublimation and until shortly before filling the source in the cluster-tool. This handling should strongly improve the purity of Alq_3, which is most important for device efficiency. A third progress compared to the single chamber vacuum system is the use of new evaporators which now consist of graphite crucibles (for Alq_3, F_4-TCNQ, TPD) or newly designed quartz crucibles with a small top hole (for the Starburst molecules). This ensures a higher temperature evenness inside the sources during sublimation which decreases temperature stress. Hence, improvements in device efficiency can not be exclusively attributed to differences in the base pressure of the HV and the UHV system, but are rather the effect of all efforts to improve the organic material handling.

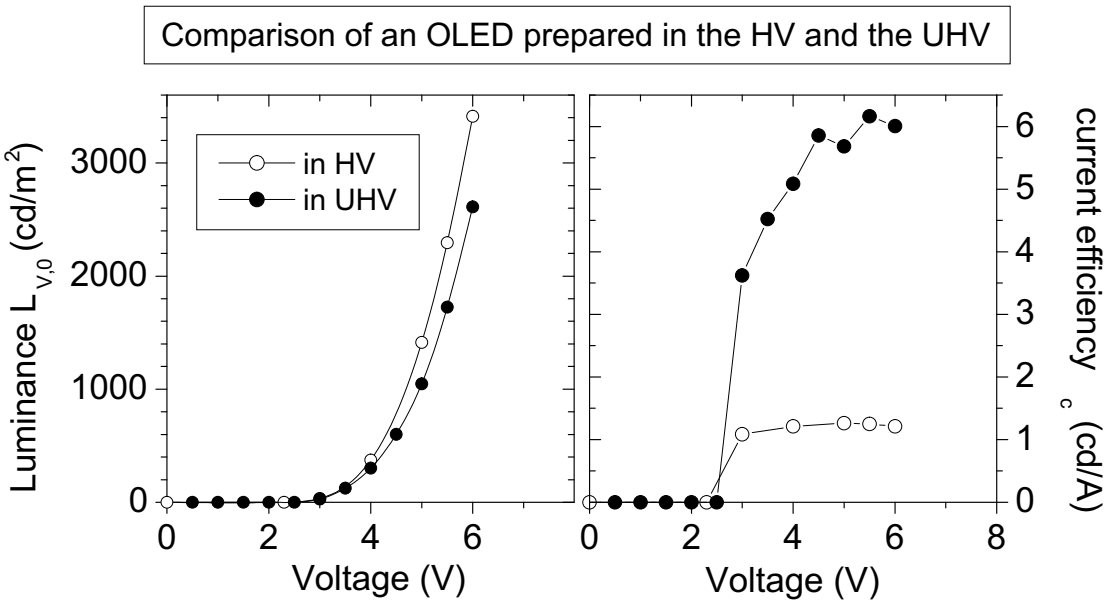

Figure 5.13: *Comparison of an OLED prepared in the single chamber HV-system and in the UHV-cluster tool. The luminance in forward direction $L_{V,0}$ vs. voltage V (left pictures) and current efficiency η_c vs. voltage curves (right pictures) are given. The layer structure is: ITO/100nm TDATA:F_4-TCNQ /x nm TPD/65nm Alq_3/1nm LiF/Al (doping ratios 1:50, TPD thickness x=10nm for the HV sample and 5nm for the UHV sample).*

For the comparison the OLED structure with doped TDATA as HTL, a TPD blocking layer and a LiF/Al cathode was chosen (layer structure: ITO / 100nm TDATA:F_4-TCNQ / 5nm TPD / 65nm Alq_3 / 1nm LiF / Al). Figure 5.13 compares the luminance in forward direction $L_{V,0}$ vs. voltage V and current efficiency η_c vs. voltage curves of the UHV-sample with a corresponding sample prepared in HV (see Section 5.2.3). In the UHV-system a 5nm TPD layer was needed to achieve a similar operating voltage. This difference in the nominal layer setup of the HV and the UHV sample might be caused by two effects: (i) a possible different absolute layer thicknesses due to differences in the calibration of the thickness monitors, or (ii) by an influence of the base pressure on the LiF interlayer effect.

Table 5.6: *Survey of the optoelectronic behavior of OLEDs made in HV and UHV.*

sample	V (V) for j = 10 mA/cm^2	V (V) for $L_{V,0}$ = 100 cd/m^2	j (mA/cm^2) for $L_{V,0}$ = 100 cd/m^2	η_c (cd/A) at $L_{V,0}$ = 100 cd/m^2 and max.	η_P (lm/W) at $L_{V,0}$ = 100 cd/m^2	η_Q (%) at $L_{V,0}$ = 100 cd/m^2
structure:	ITO/100nm TDATA:F_4-TCNQ (1:50)/x nm TPD/65nm Alq_3/1nm LiF/Al					
HV (x=10)	3.35	3.4	9.1	1.1 (1.3)	1.0	0.34
UHV (x=5)	4.5	3.4	2.2	4.5 (6.2)	4.1	1.4 (1.9)

The relevant optoelectronic properties of the two samples are listed in Table 5.6. Although the voltage to reach a given current density of 10mA/cm^2 is higher for the UHV-device (which can be due to the effects listed above), the following basic conclusion can be drawn: The device efficiency for the OLED prepared in the UHV system is approx. 4 times larger than that of the HV-sample. A maximum current efficiency of 6cd/A has been achieved, which is one of the best values reported for OLEDs using pure Alq_3 as emitter layer (around 5cd/A [53, 54, 55]). Thus, it can be concluded that devices made in the UHV system with a more careful handling of the organic materials reach higher efficiencies. The fact that the voltage at a fixed current density is higher for the UHV-sample might reflect a thicker Alq_3 layer in that device. This would not influence the device efficiency which was tested by a thickness dependence study not to be explained in detail, here.

One important point must be concluded from the comparison between nominally identical samples made in different vacuum systems: The scatter in the actual optoelectronic data of OLEDs with sophisticated layer structures featuring many interfaces is large. This can be understood if one keeps in mind that a little change in the properties of one interface can alter the whole behavior of the OLED. Thus, only OLEDs from one measuring series made under constant environmental conditions (e.g. material charge, purity, base pressure, geometric setup of the evaporation sources with respect to the sample etc.) should be compared quantitatively. This in turn means that the evaluation of the current-voltage curves and the luminance-voltage curves of sophisticated layer structures by means of analytical or numerical models can be misleading if environmental effects are not properly rated. As an example, the current efficiency vs. voltage curve for the OLED prepared in UHV do not show the decrease in efficiency after reaching a maximum value. The maximum value is not even reached at voltages, where the efficiency of the HV sample already decreased. Thus, it can be concluded that the efficiency decrease of the HV samples is related to charge carrier or exciton quenching at impurities in the Alq_3 or at one of its interfaces.

5.4.2 OLEDs with emitter layer doping

In the preceding Section, a maximum current efficiency of 6cd/A and a quantum efficiency of 1.9% was demonstrated for an OLED with pure Alq_3 as emitter material. Most likely,

this cannot be further improved due to the low fluorescence quantum yield of Alq_3 (10% [48] - 25% [49]). Taking into account the singlet emission statistics and classical ray optics outcoupling effects (according to equation 1.1, but with ideal backscattering at the non-transparent contact), this would result in a maximum quantum efficiency of 0.4-1.25%. The limit of this very rough estimation is already exceeded for the most efficient OLED presented in Figure 5.13 and Table 5.6. This discrepancy can be due to several reasons: (i) To exactly model the outcoupling efficiency, microcavity effects of the whole layer structure (including ITO and substrate) has to be taken into account. This can lead to a much larger outcoupling efficiency (see [19]). Thus, the theoretical external quantum efficiency limit may be substantially larger. (ii) The quantum efficiency of the OLEDs is slightly overestimated by the assumption of Lambertian emission [134]. (iii) Recent publications propose the invalidity of the simple 1:3 singlet:triplet statistics for Alq_3. This can be altered by different formation cross-sections of singlet and triplet excitons [61]. Thus, the 25% rule for singlet exciton creation may be not valid.

However, Tang et al. first demonstrated the use of emission layers doped with highly fluorescent molecules [48] to further improve the device efficiency. For singlet emitters, the energy of an exciton created on a matrix molecule through bipolar charge injection into the emission layer can be transferred to the dopant by means of a non-radiative Förster transfer. This process is efficient if the emission spectra of the matrix layer and the dopant diluted in this matrix overlap. The direct charge trapping at an emitter dopant molecule is a second path to emission from the dopant molecules as long as the energy levels of the dopant are appropriate. For further details see Appendix A, point j.

The fact that the stability and lifetime of OLEDs made with emitter doping exceeds that of OLEDs with a pure Alq_3 layer by far is another important reason for the use of emitter dopants in an Alq_3 matrix. It is thought that this is due to the degradation of Alq_3 by oxidation (hole injection) [120, 177]. Hence, trapping of holes on guest molecules in Alq_3 result in to longer lifetimes of the light-emitting devices [121, 178, 179].

The most prominent emitter dopants to be used in Alq_3 are coumarins like C540 which emit in the blue-green spectral region [48, 180], DCMs which emits in the orange-red [48, 181, 182], tetraphenylnaphthacene (rubrene) which emit in the yellow-red [49, 179] and quinacridone [49, 57, 183]. Mattoussi et al. [49] found photoluminescence efficiencies near 100% for rubrene in Alq_3 and around 80% for quinacridone (QAD) molecules in Alq_3 for molecular doping concentrations around 1%. At higher concentrations, the PL quantum yield decreases drastically due to exciton quenching by an accumulation of dopants leading to excimer formation. Fortunately, this molecular concentration is related to intermolecular distances well suited to Förster energy transfer.

We have chosen QADs as emitter dopant molecules to demonstrate the possibility to make very high efficient *and* very low voltage OLEDs by p-doped HTLs for the following reasons. Firstly, all QADs emit in the green spectral region, not very much shifted from the Alq_3 emission. Secondly, a variety of QAD derivatives can be purchased from Syntec (see QAD1 and QAD3 in Chapter 3.1). Furthermore, some comparison with literature data is possible. Jabbour et al. reported current efficiencies up to 7.4cd/A [69], Murata et al. reached efficiencies of 8cd/A [57], Wakimoto showed 9cd/A [183] and Shaheen et al. achieved 18cd/A [58] (all values at approx. $100 cd/m^2$). The molecular doping ratio in these studies was approx. 1%.

Three different quinacridone molecules, named QAD1, QAD2 and QAD3 for short (molecular structures see Chapter 3.1) were co-evaporated with the electron transport

molecule Alq_3. Due to their different molecular structure their absorption spectrum in Alq_3 is different. This result in different Förster transfer rates (Appendix A, point j). OLED current efficiencies between 5 and 12 cd/A could be reached using the three quinacridone molecules as emitter guest in OLEDs with a similar layer structure than in the Section before. However, QAD3 showed the highest values, i.e. the most efficient Förster energy transfer. The electroluminescence spectra of a typical QAD3 containing OLED is depicted in figure 5.14 (doping concentration 1:100). For comparison, the EL spectrum of a typical OLED with pure Alq_3 as emitter layer is shown. The maximum of the Alq_3:QAD3 electroluminescence spectrum is red shifted of about 15nm. The shoulder at $\lambda \approx 570$nm seems to be a typical feature of the quinacridone emitters. It should be noted here that a small change of the doping ratio between 1:80 and 1:120 did not show a significant influence neither on efficiency nor on the emission spectra.

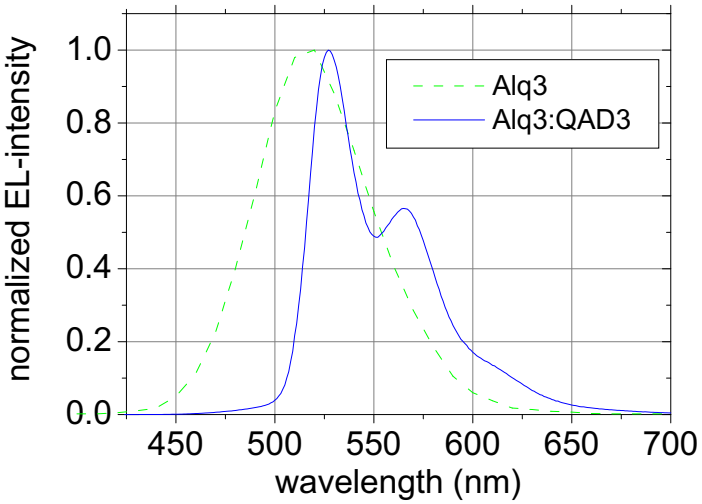

Figure 5.14: *left: Electroluminescence spectrum of an OLED containing QAD3 as emitter guest molecule (doping ratio approx. 1 mol.-%). For comparison, a typical EL spectrum of an OLED with pure Alq_3 as emitter is shown.*

The layer structure and thicknesses of OLEDs containing QAD3 as an emitter were varied to optimize the power efficiency. The luminance $L_{V,0}$ vs. voltage and efficiency vs. voltage curves of the two best OLEDs of this optimization are compared in Figure 5.15 with the best OLED with an emitter layer of pure Alq_3 (Figure 5.13, Table 5.6). Table 5.7 lists the optoelectronic data. The layer structures are:

(i) pure Alq_3: ITO/ 100nm TDATA:F_4-TCNQ 50:1/ 5nm TPD/ 65nm Alq_3/ 1nm LiF/ Al,
(ii) Alq_3:QAD3 I: ITO/ 100nm TDATA:F_4-TCNQ 50:1/ 5nm TPD/ 15nm Alq_3:QAD3 100:1/ 30nm Alq_3/ 1nm LiF/ Al, and
(iii) Alq_3:QAD3 II: ITO/ 100nm m-MTDATA:F_4-TCNQ 50:1/ 5nm TPD/ 12nm Alq_3:QAD3 100:1/ 33nm Alq_3/ 1nm LiF/ Al.

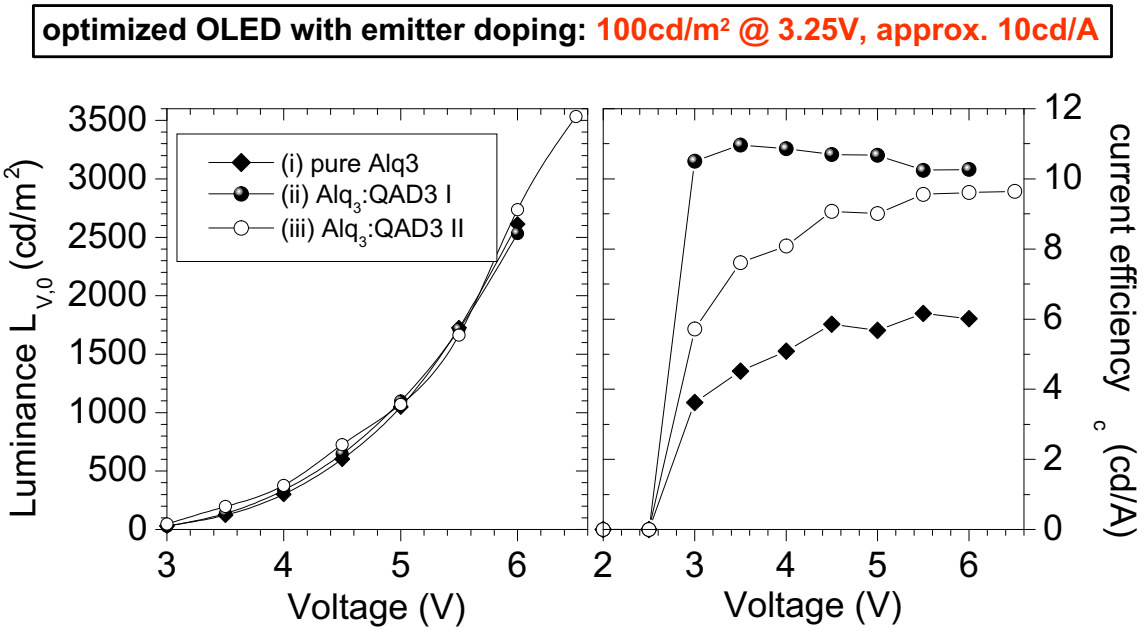

Figure 5.15: *Luminance in forward direction $L_{V,0}$ vs. voltage V and current efficiency vs. voltage curves for QAD doped samples compared with an undoped device. See text for the layer structures.*

Table 5.7: *Optoelectronic data of OLEDs containing QAD3 as emitter dopant (molecular doping ratio 1:100) after layer thickness optimization. The radiation luminous efficacy K_r for the QAD3 doped samples is 550 lm/W. Distinguishing features of the OLED setups and the leading shares of the optoelectronic properties are marked by fat letters.*

sample	V (V) for j = 10 mA/cm^2	V (V) for $L_{V,0}$ = 100 cd/m^2	j (mA/cm^2) for $L_{V,0}$ = 100 cd/m^2	η_c (cd/A) at $L_{V,0}$ = 100 cd/m^2 and max.	η_P (lm/W) at $L_{V,0}$ = 100 cd/m^2	η_Q (%) at $L_{V,0}$ = 100 cd/m^2
	ITO/100nm TDATA:F_4-TCNQ 50:1/5nm TPD/65nm **Alq_3**/1nm LiF/Al					
(i)	4.5	3.4	2.2	4.5 (6.2)	4.1	1.4
	ITO/100nm TDATA:F_4-TCNQ 50:1/5nm TPD/ **15nm Alq_3:QAD3** 100:1/30nm Alq_3/1nm LiF/Al					
(ii)	5.0	**3.4**	0.9	**10.8 (11.0)**	**10.0**	**2.6**
	ITO/100nm m-MTDATA:F_4-TCNQ 50:1/5nm TPD/ **12nm Alq_3:QAD3** 100:1/33nm Alq_3 /1nm LiF/Al					
(iii)	4.8	**3.2**	1.5	6.5 **(9.7)**	6.4	1.6

For the device (ii) with 15nm doped Alq_3 and 30nm undoped Alq_3 as electron transport layer, an operating voltage of 3.4V is achieved, similar to the best OLED without emitter layer doping (although the total Alq_3 thickness of the latter device was higher). A power efficiency of 10lm/W at 100cd/m^2 could be achieved and the quantum efficiency is 2.6%. A further decrease of the thickness of the QAD3 doped layer (12nm for device (iii), but total Alq_3 layer thickness was constant) leads to a slightly decreased current efficiency, but also a lowered operating voltage. Since the voltage to achieve a current density of 10mA/cm^2 is also decreased with decreasing the thickness of the doped Alq_3 layer, it can be concluded that the QAD dopant hinders charge carrier transport in the OLED. This is an evidence that the emitter dopant acts as a charge carrier trap with a possible direct exciton formation at a dopant molecule. The results of the Alq_3:QAD layer thickness optimization (here only shown for the thicknesses 12 and 15nm) showed that a further increase of the Alq_3:QAD layer thickness leads to no further increase in current efficiency but a drastically increased operating voltage. On the other hand, decreasing the doped Alq_3 layer even below 12nm strongly decreases the device efficiency (noticeable already for the 12nm doped Alq_3 device). Thus, it can be concluded that most excitons are created and decay within 10-20nm distance to the interface of TPD and doped Alq_3. This behavior is also favored by the fact that a diffusion of excitons on QAD into the layer of pure Alq_3 is impossible for energetic reasons. Furthermore, 15nm QAD3 doped Alq_3 are obviously enough to prevent holes from entering the pure Alq_3 layer. This is another hint for efficient hole trapping by QAD3. For this reason, the total thickness of the Alq_3 layer could be reduced to 45nm, here, without loosing efficiency by either exciton migration to the top contact or by holes reaching the top contact.

From the simple efficiency estimations at the beginning of this Section, a rough estimation leads to a maximum possible quantum efficiency of 5% for OLEDs with emitter dopants having 100% fluorescence quantum yield (assuming the 25% singlet spin statistics is valid). This limit was not reached in the above presented OLEDs. An improvement above this 5% level is only possible with structured substrates for a better outcoupling similar to the design of efficient inorganic LEDs. This would drastically increase the costs of a possible display manufacturing. The more appropriate way would be the use of phosphorescent emitters, enabling efficient emission from singlet and triplet states. This should allow a maximum efficiency of 20%, which corresponds to approximately 80lm/W in the green spectral region. Recent efforts in that direction gave results of around 20-30lm/W [24, 25, 62, 63, 64]. However, phosphorescent emitters have a series of disadvantages (shortly summarized in Appendix A, point j).

5.4.3 OLEDs with n-type doped electron transport layers

The introduction of a LiF layer between the electron transport layer and the contact metal was shown to lower the operating voltage of OLEDs (Sections 5.2.2b and 5.2.3). This was explained by a kind of n-doping effect of Li (released by hot Al atoms) in Alq_3. Such a n-type doped layer as electron transport layer should have similar advantages for the OLED behavior as demonstrated in this work for the p-type doped hole transport layer, i.e. the reduction of ohmic losses of the ETL and a drastic increase of the injection of electrons into the organic layers.

One might ask, if a stable and efficient n-type doping of an organic matrix material

with an organic donator molecule is possible. There is a principal restriction to that approach since the neutral n-type dopant molecule must have a HOMO level in the energy range of the LUMO level of the material to be doped. Organic materials with such low ionization potentials tend to be unstable. Additionally, typical electron transport matrix materials have a rather low electron affinity in the range of 3eV. For these reasons, a stable molecular n-type doping of the electron transport layers has not been successively applied for OLEDs. However, a demonstration of the n-type doping effect was done in our group by Nollau et al. for naphthalene-tetracarboxylic-dianhydride (NTCDA) as a matrix and bis(ethylenedithio)-tetrathiafulvalene (BEDT-TTF) as dopant [184]. NTCDA has an electron affinity of around 4eV. The conductivity of doped NTCDA layers could be enhanced by two orders of magnitude up to 10^{-6}S/cm (doping ratio 1:54 at room temperature). Simultaneously, the Seebeck coefficient raises from less than -1.9mV/K to -1.2mV/K upon doping. The latter corresponds in a simple approximation to a distance of 0.4eV between the Fermi-level and the electron conduction state. Thus, it can be concluded that n-type doping of organic matrix materials with organic dopants is possible, with similar electrical effects as for p-type doping.

However, because of the low lying LUMO level of NTCDA, this material is not suited as electron transport material in OLEDs. Thus, in order to test the effect of n-doped layers in OLEDs, the co-evaporation of Li-atoms was considered (metal doping). According to the effect of LiF on the OLED behavior, a better electron injection and transport of a mixed Alq_3:Li layer can be expected. Indeed, Kido et al. demonstrated a decrease of the operating voltage for OLEDs with Li doped Alq_3 as a 5nm thin electron injection layer [54]. The doping effect is caused by a reaction between Li and Alq_3 leading to radical anions or charge transfer complexes which give rise to an intrinsic carrier density. In order to achieve a noticeable effect, a molecular doping ratio of 1:1 had to be used. This completely quenched the Alq_3 photoluminescence. Parthasarathy et al. also found a positive effect of doping a BCP electron injection layer with Li in transparent OLED structures with ITO as anode and cathode material [185].

We measured the planar conductivity of a nominally 5:1 doped Alq_3:Li layer to be 10^{-6}S/cm at 100 ^{o}C and 2x10^{-8}S/cm at room temperature. The conductivity of an undoped Alq_3 layer was below 5x10^{-10}S/cm [186]. For comparison, Parthasarathy et al. found a conductivity in sandwich geometry of 3x10^{-5}S/cm for BCP thin films (10nm thick) doped by Li diffusion [187]. However, there conductivity determination includes contact contributions.

Figure 5.16 shows $j - V$ and $L_{V,0} - V$ curves measured for three samples (ii-iv) that feature a Li doped Alq_3 layer as electron injection and transport layer. The exact layer structure is given in Table 5.8. The main differences are:
Sample (i): Sample with the standard LiF interlayer for comparison. The emitter layer is 25nm thick QAD3 doped Alq_3 (as for all of the following samples). The total Alq_3 layer thickness is 40nm.
Sample (ii): Here the total not Li-doped Alq_3 layer thickness is reduced to 30nm. An additional 30nm thick heavily doped Alq_3:Li (2:1) layer should allow an efficient electron injection and transport.
Sample (iii): The total not Li-doped Alq_3 thickness is enhanced back to 40nm. A medium doped (6:1) 25nm thick Alq_3:Li layer should enable electron injection.
Sample (iv): This sample has a similar structure as (iii), but a 5nm thin BCP layer (for the chemical structure see Chapter 3.1) instead of a 15nm thick pure Alq_3 layer is

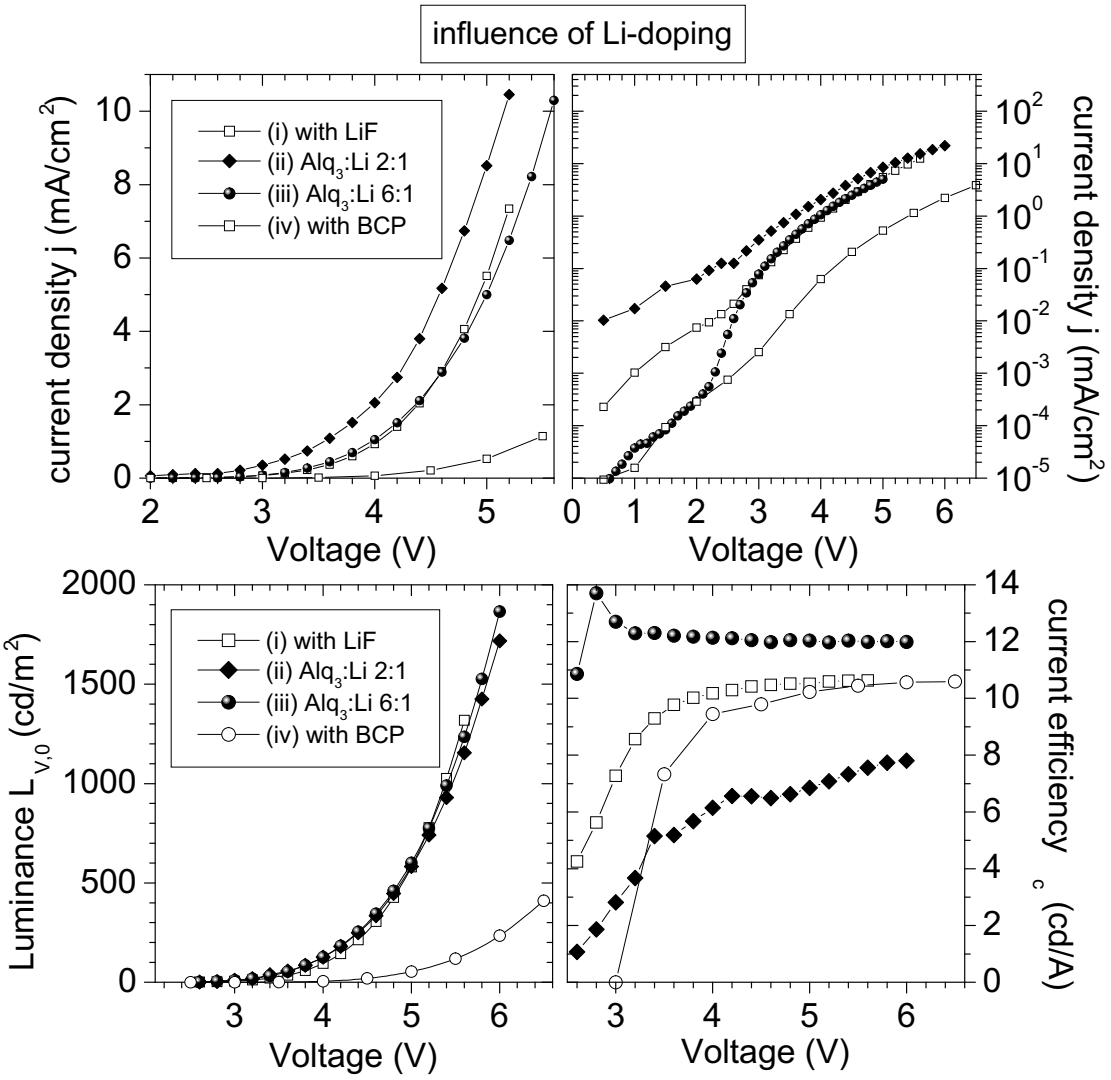

Figure 5.16: *Current density j vs. voltage V in a linear scale (top left) and a log-lin scale (top right). Luminance in forward direction $L_{V,0}$ vs. voltage V (bottom left) and current efficiency η_c vs. voltage curves (bottom right). The layer structures are described in Table 5.8. Shortly they are:* ***(i)*** *with LiF electron injection layer,* ***(ii)*** *highly Li-doped Alq_3,* ***(iii)*** *medium Li-doped Alq_3,* ***(iv)*** *with BCP blocking layer.*

introduced between the QAD and the Li doped Alq_3 layers.

Table 5.8 summarizes the relevant optoelectronic data of the OLEDs represented in Figure 5.16. First, the results of sample (i) to (iii) are interpreted. In contrast to sample (i), where the standard LiF interlayer is used as electron injection layer, sample (ii) has a heavily doped Alq_3 layer with reduced thickness of the undoped Alq_3 (30nm instead of 40nm). As expected, a higher current density is achieved indicating that the effect of electron injection enhancement by Li doping is indeed achieved. However, at the same time the device efficiency is strongly reduced. Furthermore, this OLED with an

Table 5.8: *Optoelectronic data of OLEDs with Li-doped Alq_3 layers for electron injection and transport. The radiation luminous efficacy K_r for the QAD3 doped samples is 550 lm/W.*

sample	V (V) for $j = 10$ mA/cm^2	V (V) for $L_{V,0} = 100$ cd/m^2	j (mA/cm^2) for $L_{V,0} = 100$ cd/m^2	η_c (cd/A) at $L_{V,0} = 100$ cd/m^2 and max.	η_P (lm/W) at $L_{V,0} = 100$ cd/m^2	η_Q (%) at $L_{V,0} = 100$ cd/m^2
	ITO/10nm VOPc:F_4-TCNQ 40:1/50nm m-MTDATA:F_4-TCNQ 45:1/10nm TPD/ 25nm Alq_3:QAD3 125:1/15nm Alq_3/0.75nm **LiF**/Al					
(i)	5.4	4.05	1.0	10.3 (10.7)	8.0	2.5
	ITO/10nm VOPc:F_4-TCNQ 45:1/50nm m-MTDATA:F_4-TCNQ 42:1/10nm TPD/ 20nm Alq_3:QAD3 80:1/10nm Alq_3/30nm **Alq_3:Li (2:1)**/Al					
(ii)	5.2	3.9	0.9	5.9 (7.7)	4.8	1.4
	ITO/10nm VOPc:F_4-TCNQ 65:1/50nm m-MTDATA:F_4-TCNQ 45:1/10nm TPD/ 25nm Alq_3:QAD3 108:1/15nm Alq_3/25nm **Alq_3:Li (6:1)**/Al					
(iii)	5.6	3.9	0.83	12.0 (12.5)	9.7	2.9
	ITO/10nm VOPc:F_4-TCNQ 48:1/50nm m-MTDATA:F_4-TCNQ 51:1/10nm TPD/ 25nm Alq_3:QAD3 98:1/**5nm BCP**/25nm **Alq_3:Li (6:1)**/Al					
(iv)	7.7	5.4	0.95	10.5 (10.6)	6.1	2.5

only 30nm thin not Li-doped Alq_3 layer was very unstable, indicating a negative effect of the Li atoms on device stability. Probably, because of their small size, Li-ions are able to diffuse through the Alq_3 layer, causing partial shorts and the decrease in device efficiency. This is in accordance with the observation of Parthasarathy et al. [187]. They determined an approx. 40nm diffusion length of Li in Alq_3 from SIMS depth profiling and transport measurements. Thus, sample (iii) was prepared having the same not Li-doped Alq_3 thickness as (i), but an additional 25nm thick Alq_3 layer doped by 6:1 molecular ratio with Li. Its behavior is similar to sample (i) with the LiF injection layer. The operating voltage to reach a brightness of 100cd/m^2 is a little bit lower for the Li doped device. At higher voltages, the current density of the LiF injection layer device (i) is higher. The reason for this behavior is not clear. The different current efficiencies of the samples (i) and (iii) might be related to the slightly different QAD3 doping ratios for the two devices. One advantage of device (iii) is that the current efficiency already reaches its maximum value at voltages where the first light could be detected. This behavior is in contrast to all previous presented OLEDs (except for device (ii) in Figure 5.15), which is an indication that Li-doping enhances electron injection already at very low bias voltages.

Since we observed that Li ion migration can cause a device degradation, the insertion of a blocking layer at the electron side may help to prevent such an effect. This approach corresponds to our concept of using a combination of doped transport and blocking layers given in Section 5.3 and the role of TPD as blocking layer at the hole side therein. With this idea in mind, a 5nm thin BCP (bathocuproine, see Section 3.1.1) layer was used as

blocking layer in sample (iv) of Figure 5.16. BCP is known to act as an hole blocking layer due to its low HOMO level of 6.7eV. In accordance to the work of Baldo et al. [24], who stated a LUMO position of 3.2eV, BCP should not form a barrier for electron injection. However, Hill et al. gave HOMO and LUMO positions from UPS experiments and optical absorption measurements of 6.4eV and 2.9eV, respectively [161], indicating an energy barrier for the injection of electrons from Alq_3 into BCP. The blocking layer BCP should combine two different properties: (a) a good electron injection and transport and (b) the effective prevention of Li ion migration into the emission zone. Despite the fact that sample (iv) has only a not Li-doped layer thickness of 30nm (25nm QAD3 doped Alq_3 and 5nm BCP) the current density is low in that device (see Figure 5.16). This indicates that condition (a) is not fulfilled for BCP as blocking layer. The fact that the efficiency of device (iv) is still high indicates that condition (b) is fulfilled. However, BCP is not a suitable blocking layer at the electron side to improve the behavior of Li doped devices.

In conclusion, it was confirmed that a Li doped electron injection layer act similar as a LiF interlayer between the electron transport layer (Alq_3) and the cathode metal (Al) [54]. However, at such high Li doping ratios where the Li doped layer should have superior properties in terms of bulk conductivity, the devices get unstable and the efficiency is strongly decreased. Hence, more efforts are necessary which may point in two directions. Firstly, the metal n-type doping might be improved by choosing other organic matrix materials (like bathophenanthroline, BPhen [54]), metal dopants (like cesium), and blocking layers. The second approach would be the development of a suitable organic dopant system. This might lead to stable n-type doped electron transport layers.

5.5 A lifetime test

A preliminary lifetime test was carried out for an OLED with the layer structure ITO/10nm VOPc:F_4-TCNQ 65:1/50nm m-MTDATA:F_4-TCNQ 45:1/10nm TPD/25nm Alq_3:QAD3 108:1/15nm Alq_3 /25nm Alq_3:Li 6:1/Al (sample (iii) in Figure 5.16 and Table 5.8). This should answer the question if the p-type doping of the hole transport layer by an organic dopant system and the medium metal doping of the electron injection and transport layer reduces the overall lifetime of such an OLED. For this purpose, the OLED was firstly stored in the UHV-chamber for 140 hours. There, the light emission and bias voltage for the current density of $j = 1.85\text{mA/cm}^2$ could be measured simultaneously. After 140 hours, the sample was transferred into the dry nitrogen glove box where an encapsulation was done by pressing a cleaned glass sheet onto the sample and glue the edges with a two-component fast hardening glue. Encapsulation is important to exclude environmental influences [188, 189, 190]. After some minutes, the sample was taken into air and was re-connected to the constant current source. Ex-situ, only the operating voltage could be measured. Figure 5.17 shows the gradual increase of device voltage with time.

During the first 140h in vacuum the voltage increase was 0.4mV/h and the luminance decreased only slightly from 220cd/m^2 to 210cd/m^2. No black spots could be observed with the eyes. After taking the (encapsulated) device into air the voltage rise was faster, namely 2.7mV/h. A part of this voltage rise can be attributed to growing non-emissive black spots clearly visible with the eyes. At a total lifetime of the device of 800 hours, these spots covered approx. 40% of the original area. Due to the constant current drive

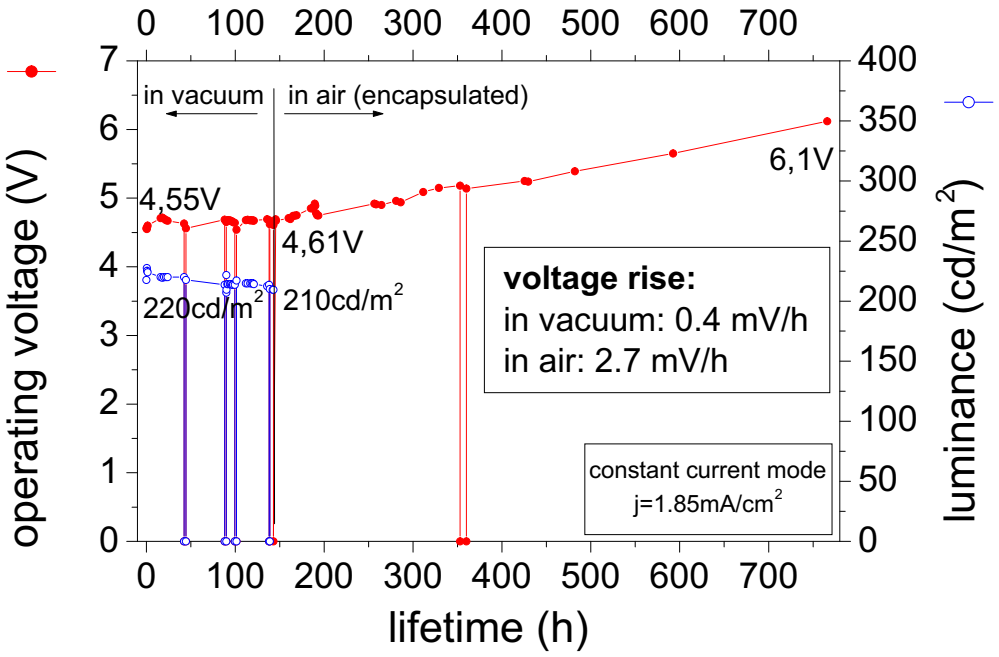

Figure 5.17: *Dependence of the bias voltage V and the luminance in forward direction $L_{V,0}$ from the operating time of the OLED: ITO/10nm VOPc:F_4-TCNQ 65:1/50nm m-MTDATA:F_4-TCNQ 45:1/10nm TPD/25nm Alq_3:QAD3 108:1/15nm Alq_3/25nm Alq_3:Li 6:1/Al at a constant drive current of $j = 1.85mA/cm^2$.*

mode, a higher current density flows through the still active area of the device. A 0.35V higher voltage had to be applied to compensate this effect (estimated from the j-V curve of Figure 5.16). This calculation lowers the voltage rise in air caused by intrinsic effects to 1.8mV/h.

The measured rise rate values can now be compared with literature data. Burrows et al. found for a similar encapsulated device a bias voltage increase of approx. 3mV/h (device structure ITO (no pre-treatment)/TPD/Alq_3/Mg:Ag, j =10mA/cm^2 [188]). Kim et al. reported voltage rise rates of 12mV/h for a polyfluorene based polymer LED (encapsulated device with pre-treated ITO in air at 200cd/m^2 initial brightness [191]). Sakamoto et al. found a voltage rise of 1.1mV/h for a device where both, the hole transport and the emission layer were doped with rubrene in a nitrogen atmosphere (pre-treated ITO, initial brightness 500cd/m^2 [179]). Steuber et al. reported voltage rises of below 0.4mV/h at the sample structure ITO (pre-treated)/CuPc/NPD/Alq_3/Mg:Ag (at 200cd/m^2 initial brightness and a pulsed current drive regime in dry nitrogen atmosphere [75]).

Although a comparison with these data suggest that doping is not a lifetime limiting factor, further experiments would be necessary to clarify this observation. For example, it is known that a voltage increase during operation of the OLED can be reversed by

a negative bias voltage (as was done for the Steuber-measurements with a pulsed drive scheme). This effect is explained by mobile ions in the organic layers which can built up space charges during operation [76] or due to the trapping of charge carriers in deep traps [192]. Both effect might be influenced by doping. Furthermore, it is known that pre-treatment of the ITO substrates by oxygen plasma ashing or ozone treatment improves the lifetime of OLEDs. This was applied for most of the above mentioned OLEDs. For the OLEDs represented in this work no special treatment of the ITO was applied.

5.6 A summary of the OLED experiments as a pathway to highly efficient OLEDs

In this Section, a summary of the OLED-experiments described before is given. Common to all prepared OLEDs is the use of p-type doped hole transport layers. The following principal OLED setups were demonstrated:

A Section 5.1.1: Two layer OLED with F_4-TCNQ doped VOPc as hole transport layer (HTL) and Alq_3 as emission layer (EML).

B Section 5.1.2: Three layer OLED based on A with an additional TPD blocking layer between the HTL and the EML.

C Section 5.2.2a: Two layer OLED analogously to A with doped Starburst as HTL.

D Section 5.2.2b: Three layer OLED based on C with a LiF layer as electron injection layer.

E Section 5.2.3: Four layer OLED based on D with an additional TPD blocking layer between the HTL and the EML (an analogous to B).

F Section 5.4.1: The same OLED as in E, but prepared in a multiple chamber UHV-system.

G Section 5.4.2b: Five layer OLED similar to E and F, where the Alq_3 emission and electron transport layer is split in an emitter layer doped with emitter molecules and a pure Alq_3 ETL.

H Section 5.4.3: A five layer OLED similar to G, where the layer next to the cathode is directly doped with Li instead of using LiF.

Only a detailed optimization of all layer thicknesses (including the effect of an ITO thickness change on the outcoupling efficiency [19]) and doping ratios would lead to the best results, every layer setup would be able to achieve. Such an optimization was not done, but some parameters of the basic setups have been varied as described in detail in the preceding Sections of this Chapter. A comparison of the best results achieved is given in Table 5.9. The essential conclusions from that Table are the following:

- For sample setup A, the basic effect of p-type doping the hole transport layer could be proven: the lowering of the operating voltage of OLEDs due to a better hole injection and transport.

Table 5.9: *A comparison of the best results achieved in this work for the basic OLED setups A to H (see text). Distinguishing features of the OLED setups and the best figures for each optoelectronic property are marked by fat letters.*

sample setup	V (V) for $j = 10$ mA/cm^2	V (V) for $L_{V,0} = 100$ cd/m^2	j (mA/cm^2) for $L_{V,0} = 100$ cd/m^2	η_c (cd/A) at $L_{V,0} = 100$ cd/m^2 and max.	η_P (lm/W) at $L_{V,0} = 100$ cd/m^2	η_Q (%) at $L_{V,0} = 100$ cd/m^2
	ITO/200nm **VOPc:F_4-TCNQ** 34:1/71nm Alq_3/Al					
A:	5.0	6.2	59	0.17 (0.19)	0.086	0.06
	ITO/200nm VOPc:F_4-TCNQ 34:1/**20nm TPD**/71nm Alq_3/Al					
B:	9.25	10.1	23	0.43 (0.57)	0.13	0.15
	ITO/200nm **TDATA:F_4-TCNQ** 62:1/65nm Alq_3/Al					
C:	6.2	9.5	69.5	0.14 (0.14)	0.046	0.04
	ITO/200nm TDATA:F_4-TCNQ 62:1/65nm Alq_3/**1nm LiF**/Al					
D:	4.05	6.7	64.5	0.16 (0.21)	0.08	0.05
	ITO/100nm TDATA:F_4-TCNQ 50:1/**10nm TPD**/65nm Alq_3/**1nm LiF**/Al					
E:	3.35	**3.4**	9.1	1.1 (1.3)	1.0	0.34
	ITO/100nm TDATA:F_4-TCNQ 50:1/5nm TPD/65nm Alq_3/1nm LiF/Al **in UHV**					
F:	4.5	**3.4**	2.2	**4.5 (6.2)**	4.1	**1.4**
	ITO/100nm TDATA:F_4-TCNQ 50:1/5nm TPD/ 15nm **Alq_3:QAD3** 100:1/30nm Alq_3/1nm LiF/Al					
G:	5.0	**3.4**	0.9	10.8 (11.0)	**10.0**	2.6
	ITO/10nm VOPc:F_4-TCNQ 65:1/50nm m-MTDATA:F_4-TCNQ 45:1/ 10nm TPD/25nm Alq_3:QAD3 108:1/15nm Alq_3/25nm **Alq_3:Li** 6:1/Al					
H:	5.6	3.9	0.83	**12.0 (12.5)**	9.7	**2.9**

- Sample setup B demonstrates the need for suitable blocking layers to enhance the device efficiency. In the case of the TPD-layer, electrons are hindered from entering the doped hole transport layer. The current efficiency could be enhanced by a factor of 3 compared to setup A. However, the operating voltage is increased due to the intrinsic TPD layer. The thickness of the TPD layer cannot be reduced, here, because electrons are able to tunnel through the layer into the low LUMO of VOPc.

- OLED setup C use for the first time a doped amorphous hole transport layer, namely the Starburst derivative TDATA. The basic doping effects could be verified for amorphous wide gap materials. The operating voltage of the OLEDs could be reduced compared with device B but, due to the nature of the TDATA/Alq_3 interface, the device efficiency was poor.

- An additional LiF electron injection layer in the setup D reduces the voltage (com-

pared to C) but does not remarkably change the device efficiency. Such an injection layer is also used in the sample structures E to G.

- With the insertion of the blocking layer TPD (setup E), the current efficiency was enhanced by a factor of 6. A very low operating voltage of 3.4V was achieved with such devices. It is crucial for these low operating voltage that the thickness of the TPD blocking layer could be as low as 5-10nm without loosing efficiency, here, because the high LUMO of the HTL prevents electron injection.

- Preparing the device with the layer sequence E in a multiple chamber UHV-system (device F) further improves the device efficiency. This indicates a very high quality of preparation in this new tool.

- To further improve the OLED power efficiency, an emission layer doped with emitter molecules was applied in the structure G. After a rough layer thickness optimization, this allows for 10lm/W power efficiency at the monitor brightness level of 100cd/m^2. The lowest operating voltages achieved in this study (3.25-3.4V) were realized with this setup.

- It was confirmed that the use of a Li-doped electron transport layer improves the electron injection (setup H). The optoelectronic properties of the sample structure G could be reproduced.

In closing this Section, it should be pointed out here that not only the layer setups and optimized layer thicknesses are important to prepare OLEDs with very high power efficiency. At least similarly important is the degree of purity of the organic materials, in particular the purity of the emitter molecules. This directly influences the device efficiency and also the lifetime of the device. Hence, every application of organic materials for commercial devices requires a proper material purification as described in Section 3.1.2 and a proper handling of the purified materials during storage and evaporation. The storage of all materials in high vacuum under slightly enhanced temperatures and the evaporation of the organic materials from sources with very even temperature distributions are inevitable.

6 Conclusions

6.1 Summary

In this work an operating voltage of *3.25-3.4 V for a luminance of 100cd/m*^{2} was achieved for an optimized OLED layer structure with a p-type doped hole transport layer. These results represent the lowest ever reported operating voltage for LEDs consisting of exclusively vacuum sublimed molecular layers. The current efficiency for this device is above 10cd/A, hence, the power efficiency at 100cd/m^2 is about 10lm/W. This high power efficiency could be achieved by the use of a blocking layer between the transport and the emission layer. Furthermore, it could be shown that the transport layer doping is stable at room temperature. This was deduced from a lifetime test on an encapsulated device. Hence, the use of the doping concept may lead in the near future to more efficient and stable devices for many applications, like large area flat screens.

The origin of the drastically decreased operating voltage of OLEDs with doped hole transport layers was investigated by means of a combination of UPS and XPS experiments. For the first time, the energetic alignment of intentionally doped organic layers on conductive substrates could be determined. A comparison of F_4-TCNQ doped and undoped layers of zinc-phthalocyanine on gold and ITO substrates showed that *electronically doped organic layers show a behavior similar to doped inorganic semiconductors*. The Fermi-level shifts towards the transport states and the depletion region of a doped organic semiconductor in front of a conductive substrate is reduced in accordance with classical inorganic semiconductor theory. Thus, a Schottky contact with quasi-ohmic behavior can be achieved by doping. However, doping of organic layers by organic molecules needs higher doping concentrations compared to the doping of inorganic semiconductors.

As a basic new result, we demonstrated the effect of p-type doped hole transport layers based on co-evaporated organic molecules in organic light emitting diodes. The effect of a varying dopant concentration on the optoelectronic properties of an OLED was shown on the model system of a phthalocyanine layer doped with the strong acceptor molecule F_4-TCNQ. It became clear that *doping lowers the operating voltage drastically and improves the power efficiency of an OLED*. The doping concept was further applied to energetically better suited hole transport materials like the Starbursts. Together with a very thin blocking layer between the doped transport and the emission layer of the OLED, both a very low operating voltage *and* a very high quantum efficiency could be achieved. The origin of this improvement was attributed to a more efficient charge carrier injection into the transport layers together with low ohmic losses in doped organic layers.

In the course of the present work, OLEDs were prepared in a (i) single chamber high vacuum system and in a (ii) multiple chamber ultra high vacuum system with improved handling of all organic materials. The differences in the optoelectronic properties shows the importance of material purity for highly efficient OLEDs as one of the most essential issues for device applications.

6.2 Outlook

In this work, only efficient p-type doping of organic layers with organic dopants and their use in OLEDs could be demonstrated. As a first approach to n-type doped electron transport layers, metal doped layers were investigated. They need very high doping ratios which lead to partially unstable devices. From this point of view, an organic doping system would be favorable. However, n-type doping of organic materials suitable for OLED applications is difficult to achieve, but is, without doubt, one of the main future issues. On a short time scale, the n-type doping with other metals than Li (e.g. cesium) should be addressed and other host materials than Alq_3 should be used (e.g. bathophenanthroline having a higher electron mobility than Alq_3).

Since the strong acceptor F_4-TCNQ is only stable until approx. $80\,^oC$, other dopant molecules are needed to enhance the operation temperature range of doped OLEDs. The synthesis of larger and more stable dopants is currently under investigation.

A further improvement of the quantum efficiency of OLEDs should be possible with the use of phosphorescent emitter molecules which avoid the spin statistics problem. P-type doping of the hole transport layer should be of special importance, here, to achieve low operating voltages, since the HOMO level of molecules, which are known to be appropriate host molecules for phosphorescent emitter dopants, are generally relatively low. A technological advantage of doped hole transport and metal doped electron transport layers is the possibility to invert the OLED layer structure. Common highly efficient OLEDs based on intrinsic undoped organic layers need a special pre-treatment of the ITO anode and the evaporation of Al on top of LiF to achieve low operation voltages. With intentionally doped transport layers, it is possible to use untreated ITO as anode materials. The inverted structure with low operating voltage should be demonstrated in the near future. The device setup with the transparent anode on top is by far more favorable for most integrated display applications.

The UPS/XPS investigations showed the effect of doping on the energetic alignment of the doping model system phthalocyanines:F_4-TCNQ on conductive substrates. However, further studies are necessary to clarify the behavior of organic/organic junctions with doping of one material and to clarify the energetic alignment of less efficient p-type doping systems like the Starbursts.

Doping was the key technology for inorganic semiconductor applications. Hence, doping of organic layers may also be the first step towards an electrically driven organic laser. However, many basic questions in that field still wait to be answered. The influence of the ionized dopants and the high density of intrinsic charge carriers on the loss mechanisms inside an OLED needs to be investigated. Additionally, the doping efficiency of some organic matrix/dopant systems has to be improved to allow for the extremely high current densities inside an organic laser setup. At current densities in excess of $100 A/cm^2$ which are needed for lasing operation [193, 194] the voltage drop over the doped wide gap hole transport layers becomes important. Nevertheless, doped organic layers will probably be applicable to a wide variety of devices known from the inorganic semiconductor technology, like transistors, solar cells and many others.

Appendix A Physical processes involved in OLED operation

The temporal and steady state behavior of an organic LED is mainly determined by the time dependent distribution of the density of electrons n and holes p, whether trapped (n_t, p_t) or free (n_f, p_f). They again are determined by the modification of the external field due to accumulation of charges inside the device. Possible efficiency reducing factors of the modeled device setup may be recognized from the steady state distribution of all relevant device variables calculated by an appropriate numerical model. From the time dependent change of the charge carrier densities and the electric field, one can derive the current density and light emission intensity as a function of time. These values can be directly compared to transient and steady state electroluminescence measurements. Figure A.1(left) shows an example for the steady state distribution of the charge carrier densities in a two layer OLED calculated from a numerical model and the right side shows the total internal field distribution in the two layers of an OLED determined by an electroabsorption measurement.

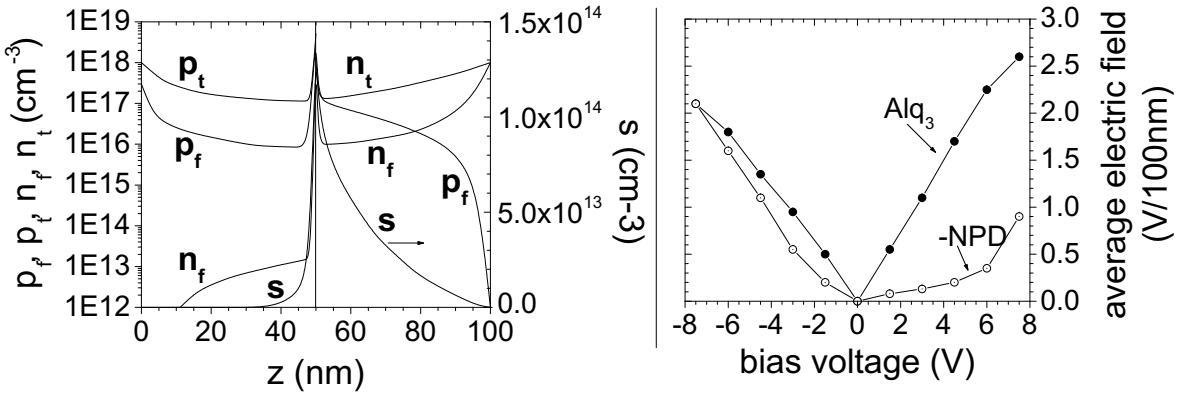

Figure A.1: ***(left)*** *Calculated spatial distribution of the free (p_f, n_f) and trapped (p_t, n_t) charge carrier densities and the singlet exciton density (s) derived from a numerical model for a two layer OLED consisting of a HTL and an ETL at a voltage where reasonable light is emitted (taken from Staudigel et al. [4]). Note the effect of hole and electron blocking at the internal interface.* ***(right)*** *The average electric field per layer of a double layer OLED (HTL=α-NPD, ETL=Alq_3) as a function of DC-bias derived from electroabsorption spectroscopy measurements (taken from Rohlfing et al. [195]). Note that the ratio of the electric field in the NPD and the Alq_3 layer changes at approx. 5V, where reasonable light emission starts to occur.*

Up to date, all efforts to model the complete OLED behavior restrict their calculation to a quasi one-dimensional model [4, 5, 6, 7, 8, 9, 10, 11]. This limitation hinders the simulation of effects due to laterally inhomogeneous charge carrier injection caused by surface roughness and localized high current flow caused by point defects. Nevertheless, the intrinsic properties of organic layers are thought to be dominated by the high field perpendicular to the surface of the device, since the layer thickness is much smaller than the lateral dimensions. Hence, a one-dimensional description of the relevant physical processes is appropriate.

a) built-in potential and electric field

For calculating the internal electric field, the external voltage V, space charge effects and the built-in potential V_{bi} between two electrodes with different work-functions have to be considered. The average electric field $\overline{F}$ in the sample is given by:

$$\overline{F} = \frac{V - V_{bi}}{L}\,, \tag{A.1}$$

where L is the total layer thickness. In the simplest case of a single layer device with contacts and bias voltages that cause an injection limited current, the internal electric field is uniform and equals the difference between the external field and the built-in potential [7].

A calculation of the built-in voltage from the difference of independently measured work-functions of the electrodes is only a first-order-approximation. Ionizable dopants may create an interfacial depletion layer, interface dipoles may give rise to an additional voltage and charged surface states may also act to pin the Fermi energy at the electrode interface. Hence, the actual energy alignment at an organic/metal interface has to be determined experimentally, e.g. by ultraviolet photoelectron spectroscopy (see Chapter 4). Alternatively, the actual built-in potential of an OLED can be determined by electro-absorption (EA) measurements [147, 196, 197] or the photovoltaic method of nulling the photocurrent [198, 199].

In order to calculate the local electric field distribution, the influence of free and trapped excess charges has to be considered. The excess charge or space charge density ρ at position x (distance from the anode/cathode) is:

$$\rho = e\left[(p_f(x) - p_{f,0}(x)) + (p_t(x) - p_{t,0}(x)) - (n_f(x) - n_{f,0}(x)) - (n_t(x) - n_{t,0}(x))\right]\,, \tag{A.2}$$

where e is the elementary charge and the densities of equilibrium free and trapped charge carriers are: $p_{f,0}(x)$, $p_{t,0}(x)$, $n_{f,0}(x)$ and $n_{t,0}(x)$. The local electric field at position x can then be calculated from the Poisson equation:

$$F(x) = \frac{1}{\epsilon_0}\int_0^x \frac{\rho(x')}{\epsilon(x')}\,dx' + \frac{\rho_A}{\overline{\epsilon}\epsilon_0}\,, \tag{A.3}$$

where ϵ_0 denotes the dielectric constant in vacuum, while $\epsilon(x)$ and $\overline{\epsilon}$ denote the local and averaged relative dielectric constants. For an example of the measured average electric field inside the two layers of a double layer OLED see Figure A.1 right.

Additionally, one has to make sure that the integrated Poisson-equation yields the external electric field reduced by the built-in voltage:

$$\int_0^L F(x)dx = V - V_{bi}\,, \tag{A.4}$$

If the charge injection is assumed to be ohmic (which means that there is a inexhaustible reservoir of charges at the interfaces), the condition (A.4) determines also the second term in equation (A.3) which is the anode surface charge density ρ_A [4, 11]. The corresponding cathode surface charge density ρ_C can be calculated taking into account the neutrality condition for the whole sample.

b) charge carrier drift

In evaporated organic semiconductor layers, charge carriers are transported by hopping, characterized by incoherent jumps between isolated molecular sites, possibly with the formation of a small polaron at each site. The mobilities are very low compared to inorganic semiconductors and strongly temperature and field dependent.

Transient electroluminescence experiments have shown that a model based on hopping in a Gaussian distribution of states (DOS) (Bässler et al. [200, 201]) is able to describe the temperature and field dependence of the mobility in organic semiconductors quite well. This model is based on the assumption that dispersive transport occurs through a manifold of localized states distributed in energy and distance (shallow traps). Polaronic effects are neglected, upward jumps are scaled with a Boltzmann factor, downward jumps have unity probability and the absence of deep traps is assumed. The model is also referred to as dipolar disorder model, since the width of the energy disorder is described with a random distribution of permanent dipoles [202]. The model yields:

$$\begin{aligned} \mu(F,\beta) \;&=\; \mu_0\, exp\left[-\left(\frac{2}{3}\,\beta\sigma\right)^2\right]\cdot \\ &\cdot \begin{cases} exp\,[C((\beta\sigma)^2-\Sigma^2)\sqrt{F}\,], & \Sigma > 1.5 \\ exp\,[C((\beta\sigma)^2-2.25)\sqrt{F}\,], & \Sigma \le 1.5 \end{cases}, \end{aligned} \tag{A.5}$$

where $\beta = 1/k_b T$, σ the energetic disorder parameter, Σ the spatial disorder parameter, μ_0 the zero field high temperature mobility, and C a constant which depends on the distance between adjacent hopping sites. To determine the mobility modeled above correctly, one has to keep in mind that equation (A.5) was derived for the hopping transport in an equilibrium state. Thus the equilibrium energetic distribution of the charge carriers and their average transport energy is determined by the interplay between a Boltzmann thermal exponent and the Gaussian distribution of states (for more details see [203]).

Another possibility to describe the field dependence of the mobility in organic materials over a reasonable voltage range is the Poole-Frenkel-like form, deduced from the assumption of a decreasing hopping energy with increasing local internal field:

$$\mu(F) \;=\; \mu_0\, exp\,(\sqrt{F/F_0}) \quad , \tag{A.6}$$

where μ_0 is the zero field mobility and F_0 the characteristic field [11]. Both parameters can be temperature dependent with different activation energies. For both models the logarithm of the mobility is proportional to the square root of the electric field.

All parameters of equation (A.5) and (A.6) have to be determined by independent measurements. This can be done by fitting the described mobility models to experimental mobility data derived from hole or electron only devices with ohmic majority charge injection (transient SCL currents, see e.g. [204, 205, 206]). To do so, the proper choice of the two electrodes is crucial. This is especially true, since injection limited currents can give the same voltage dependence as the field dependent mobility [10] due to the Schottky barrier lowering effect. Additional approaches to derive mobility data for organic materials experimentally are: (1) from transient time-of-flight measurements [126, 129, 207, 208, 209, 210] (which gives usually too high mobilities since the transport does not take place in the equilibrium energetic charge carrier distribution, except for large layer-thicknesses) and (2) capacity-frequency measurements [211, 212]. A prerequisite for these measurements is that the transient time of the current flow has to be less than the dielectric relaxation time (i.e. the screening of the electric field should not take place before the created or injected charge carriers reach the opposite electrode).

Another approach is to measure field effect mobilities [119, 213] in an organic field effect transistor setup. In this case, an effective mobility is measured, which is influenced by shallow *and* deep traps (in contrast to Bässlers model where only shallow traps are considered). Hence, the field effect mobility should differ from mobilities derived from the above mentioned methods (see [95]).

The drift current (here given for holes; electrons analogous) of free holes at the position x in the sample $j_{drift,p}$ can then be calculated to:

$$j_{drift,p}(x) = eF(x)\mu_p(x)p_f(x)\,. \tag{A.7}$$

Since μ is the mobility in the equilibrium distribution of a manifold of different transport states, the density $p_f(x)$ in equations (A.7) and (A.2) refers to all holes in that distribution, whereas $p_t(x)$ in equation (A.2) refers only to deep trap levels, e.g. caused by impurities.

In the framework of a discrete numerical model (e.g. Staudigel at al. [4]) the change of the free hole density at position x can be related to the hopping transport by the average waiting time $\overline{\tau}_p$ of a charge carrier between two consecutive hopping processes. The average waiting time is the quotient of the jump distance and the average local charge carrier velocity (determined by the above described mobility): $\overline{\tau}_p = d_h/(\mu_p(x)F(x))$. The change in free hole density at position x by hops from x to $x+d_h$ (d_h is an average hopping distance, mostly taken to be the molecular distance in x-direction) in the time Δt is then:

$$\Delta p_{drift}^{x\to x+d_h} = \frac{\mu_p(x)\,F(x)}{d_h}\,p_f(x)\,\Delta t \quad \text{for } F(x)>0 \quad \text{and} \quad \Delta p_{drift}^{x\to x+d_h} = 0 \quad \text{for } F(x)\le 0\,. \tag{A.8}$$

The total change of the free hole density at distance x from the anode has to be calculated by summing up the hopping processes from $x \to x+d_h$, $x \to x-d_h$, $x-d_h \to x$ and $x+d_h \to x$. The drift current is related to the change of the free hole density by $j_{drift,p} = e(\Delta p_{drift,total}/\Delta t)d_h$.

c) charge carrier diffusion

Since the electric field for an operating light-emitting diode is relatively high (0.1-10MV/cm) it is expected that the charge carrier drift exceeds the carrier diffusion by

far. Numerical simulations confirmed this assumption: Malliaras et al. found a minimal change in the current-voltage behavior by changing the diffusion constant over one order of magnitude [214].

Nevertheless, the diffusion current at position x can be obtained from (again for holes; electrons analogous):

$$j_{diff,p}(x) = D_p(\mu_h)\,\frac{dp_f(x)}{dx} \quad . \tag{A.9}$$

The diffusion constant D is related to the charge mobility by the Einstein relation:

$$e\,D \;=\; \mu\,k_B\,T \quad . \tag{A.10}$$

The change of the free hole density caused by diffusion can also be described equivalently to the drift current equation (A.8), however excluding the direction restriction due to the electric field. The average local diffusion velocity $v_{diff,p}(x)$ (equivalent to the drift velocity $\mu_p(x)F(x)$) is related to the diffusion coefficient by:

$$v_{diff,p}(x) = D_p(x)/d_h \qquad . \tag{A.11}$$

In general, to account for the field effect on the hopping probability, the Einstein-equation (A.10) would have to be modified into a non symmetric form [4]. Since for most OLED operation voltages the contribution of the drift current exceeds the diffusion current by far, such an exact description of the nature of the diffusion transport does not seem to be necessary.

d) charge carrier injection

In OLEDs, charge carriers are injected from the electrodes into a disordered organic dielectric. The rate at which this occurs depends upon either the injection process itself (injection limited current flow) or upon charge transport in the organic layer controlled by space charges therein (space charge limited current = SCLC). The latter case is realized if the net space charge near the interface is high enough that the electric field at the injection electrode vanishes. An electrode is then called ohmic, because it serves as an quasi-inexhaustible carrier reservoir. The analysis of very efficient OLEDs has lead to the conclusion that under bias voltages used to generate electroluminescence, the metal-organic junction serves as an ohmic contact [129, 205, 215]. If not, these devices would exhibit poor efficiencies and are therefore of no interest for modeling and optimizing their performance.

In a numerical model, the case of ideal ohmic injection can be accounted for by taking the density of charges near the electrode/semiconductor interface at least one order of magnitude higher than the space charge density in the bulk. Then the drift contribution to the change of the free hole density can be calculated according to equation (A.8).

Nevertheless, a proper description of the charge injection process is sometimes necessary especially at low voltages around threshold. In the early days of OLED research injection was thought to be best described in terms of Fowler-Nordheim tunneling over a triangular potential barrier [6, 9, 216]. Nowadays, it is believed that thermionic injection with image force barrier-lowering is the best model, at least for modest barrier heights (which are necessary for SCL currents) and most voltages of interest [10]. In this model

the number of charge carriers effectively entering the organic bulk is reduced by the image potential caused by the carriers themselves. The image potential forces most of the carriers to jump back into the electrode after entering the first organic layer. Only in the presence of an external electric field the charges are able to overcome the image potential. A more detailed description of charge injection is given in Appendix B.

e) bulk recombination

Keeping in mind the hopping nature of charge transport in OLEDs, recombination[1] should be describable with the Langevin-formalism [130]. This process occurs for small carrier mean-free-paths. There, an electron and a hole that approach each other within a distance such that their mutual Coulomb binding energy exceeds the thermal energy, $k_B T$, will inevitably recombine. Already Helfrich et al. [27] found that the recombination rate in anthracene single crystals is close to the Langevin-expectation. Since the mean-free-path of amorphous materials should be shorter than for crystalline anthracene, the Langevin-formalism should be even better applicable on such systems. Furthermore, for polymer LEDs the Langevin-type recombination was found experimentally by Blom et al. [217].

The Langevin type bimolecular recombination rate (here for free holes recombining with free electrons) can be described by:

$$R_{p_f,n_f}(x) \;=\; \frac{dp_f(x)}{dt} \;=\; -\gamma_f(x)\, p_f(x)\, n_f(x)\,, \tag{A.12}$$

where γ is the recombination coefficient in accordance with Langevin's theory:

$$\gamma_f(x) \;=\; \frac{e\,(\mu_p(x) \,+\, \mu_n(x)\,)}{\epsilon_0 \epsilon(x)}\,, \tag{A.13}$$

Additional contributions to the exciton formation by electron-hole recombination are due to a recombination with trapped charge carriers described in point f and g.

f) charge carrier trapping

In the low voltage regime, where few charges are injected into the organic semiconducting layer, traps drastically reduce the mobility. This is called trap charge limited transport (TCL). Increasing the forward bias leads to more injected carriers and hence to more and more filled traps. At a certain voltage, all traps are filled and therefore they no longer influence the charge carrier transport (trap filled limit). Then, the device behavior resembles the space charge limited current (SCLC). This threshold voltage depends strongly on the materials investigated. There is some experimental evidence that for most hole transporting molecular layers in very high efficient OLEDs, the trap free limit is reached for operating voltages where light emission occurs [10, 218].

Nevertheless, for multi-layer OLEDs the behavior of traps can not be neglected in all layers. Staudigel et al. [4] described a way to treat deep traps within the energy gap of the organic molecular layer. Such trap states may have origins like material impurities or local structural disorder [219]. The occupation of trap states (uncharged when empty) depends on the free charge carrier density and the trap depth (energetic distance to the next transport state). The decrease of free hole density (free electron density analogous)

[1] In this work the creation of an exciton from electrons and holes is named 'recombination' or creation, whereas the radiative or non-radiative decay of this exciton is named 'decay'.

due to increase of trapped hole density (trapped electron density analogous) at position x may then be described as:

$$\frac{dp_t(x)}{dt} = \underbrace{\left[\mu_p(x)\,\left(|F(x)| + \frac{k_B T}{e\,d_h}\right)\right]}_{v_{f,p}(x)}\,\sigma_t\,\cdot$$

$$\cdot\,\left[\underbrace{p_f(x)\,(N_{t,p}(x) - p_t(x))}_{trapping} - \underbrace{p_t(x)\,(N_{HOMO} - p_f(x))\,exp\left(-\frac{E_{t,p}(x)}{k_B T}\right)}_{detrapping}\right] \quad \text{(A.14)}$$

The change in the trapped and free hole density is proportional the the sum of drift and diffusion velocity of the free holes $v_{f,p}(x)$, to a trapping cross-section σ_t, which can be related to a multiple of the distance of the molecules in the layer (Staudigel et al. assumed $\sigma_t \approx 5\,d_h^2$) and to a trapping and detrapping term. Trapping is assumed to be proportional to the free hole density and the density of empty traps $N_{t,p} - p_t$ (where $N_{t,p}$ is the total concentration of hole traps). The detrapping is proportional to the density of trapped holes and the available transport states $N_{HOMO} - p_f$ (which is in a good approximation N_{HOMO}) and is thermally activated with the trap depth energy $E_{t,p}$.

Additionally, recombination effects can further reduce the density of trapped carriers. The recombination of a trapped hole with a free electron in the Langevin-picture is:

$$R_{p_t,n_f}(x) \;=\; \frac{dp_{t,n_f}(x)}{dt} \;=\; -\,\frac{e\,\mu_n(x)}{\varepsilon_0 \varepsilon(x)}\,p_t(x)\,n_f(x)\,. \quad \text{(A.15)}$$

The energetic depths of the dominant trap E_t and its density N_t can in principle be derived from thermally stimulated current (TSC) experiments [220]. For Alq_3, values of $E_{t,n} = 0.6eV$ and densities of $N_{t,n} = 2\text{x}10^{17}cm^{-3}$ were found. In a self consistent way, reasonable trap depth and energy values can also be obtained from model-fits to single layer hole- or electron-only devices. As an example, Staudigel et al. found $E_{t,p} = 0.7eV$ and $N_{t,p} = 1.9\text{x}10^{16}cm^{-3}$ for hole traps in m-MTDATA and $E_{t,n} = 0.25eV$ and $N_{t,n} = 10^{18}cm^{-3}$ for electron traps in Alq_3 and hole traps in 1-Naphdata. The difference in the Alq_3 trap depths and density might be caused by different suppliers and cleaning procedures.

g) crossing of internal interfaces and interface recombination

In multi-layer device structures, internal interfaces between different materials with different mobilities and molecular energy levels remarkably influence current flow, charge carrier balance and accumulation. The actual processes are not fully understood yet. This is especially true for the interaction between different types of molecules, like exciplex formation. For some material combinations, exciplex formation is known to influence device efficiency and emission color strongly [174, 175]. On the other hand, it is known from UPS/XPS investigations on organic/organic interfaces that for almost all relevant material combinations, no interface reaction takes place (surface states or charge-transfer complexes would lead to a change in the vacuum level alignment, see Chapter 4).

Two major effects are present at internal interfaces (compare Figure A.2): (1) charge carriers can cross the interface, either by a thermally assisted jump over the barrier or

by transition between tail states of the energetic distribution of states (DOS) at the interface, and (2) charge carriers may recombine to form charge transfer excitons followed by a possible transfer of their energy to a bulk exciton.

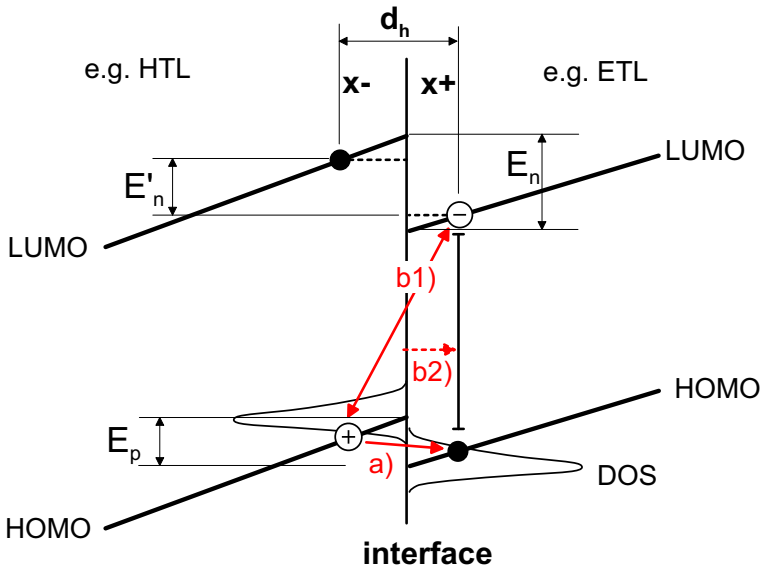

Figure A.2: *Possible processes at an internal interface: a) interface crossing through thermally stimulated hopping in a gaussian distribution of states (DOS), b1) charge carrier recombination (i.e. creation of a CT-exciton), b2) formation of a bulk exciton.* ΔE_p *and* ΔE_n *are interface barriers for holes and electrons, resp. (determined from HOMO and LUMO differences),* $\Delta E'_n$ *denotes the reduced interface barrier due to internal electric fields.*

The barrier heights, ΔE_p and ΔE_n for holes and electrons, respectively, are determined by the difference of the HOMO or LUMO levels decreased by the internal field on both sides of the barrier. If $x-$ and $x+$ denote molecular positions left and right from the interface, a simple approximation for the field lowering yields (cp. Figure A.2):

$$\Delta E'_p \;=\; \Delta E_p - e\,\frac{F(x-) + F(x+)}{2} d_h\,, \tag{A.16}$$

where d_h again gives the approximate distance of the molecules. In order to calculate the rate of thermally assisted jumps over the energy barrier given in equation (A.16), Staudigel et al. [4] included the effect of energetic disorder of states. Thus, a transition between tail states of that energy distribution is possible. The interface distribution of states (DOS) may differ from the bulk DOS due to inter-diffusion at the interface. The model of Staudigel et al. determines a hopping probability $G(\Delta E')$ over the barrier $\Delta E'$ based on some assumptions like a homogeneous occupation of the DOS at the interface. Downward jumps have the probability 1 and upward jumps are thermally activated. Effectively, the energetic distribution caused by disorder eases the barrier crossing. The actual change in the concentration of free carriers, respectively the barrier crossing current, can then be calculated according to bulk drift and diffusion currents (equations (A.7) and (A.9)) weighted with the barrier crossing probabilities.

On the other hand, electrons from one side ($x+$) and holes from the other ($x-$) can directly recombine to form charge-transfer (CT) excitons. Assuming that interface recombination follows the same Langevin formalism like bulk and trap recombination this yields:

$$R^{if}_{p_f,n_f} = \frac{e\,(\mu_n(x+) + \mu_p(x-))}{\varepsilon_0 \overline{\varepsilon}}\, p_f(x-)\, n_f(x+)\,, \tag{A.17}$$

where $\overline{\varepsilon}$ is an average dielectric constant in the two layers. Only a part of this CT-excitons can form bulk Frenkel excitons which may decay radiatively. The probability that an interface exciton leads to a bulk exciton left or right from the interface is also determined by the probabilities $G(\Delta E')$ calculated for the charge carrier barrier crossing (under the approximation that CT-excitons shows no energetic relaxation), since at least one carrier has to 'cross' the interface. CT-excitons which do not lead to bulk excitons are believed to decay non-radiatively (excimer formation process).

h) current density

The total current density in the OLED setup can be derived from the numerically calculated changes of the charge carrier densities (drift, diffusion, recombination), and, as long as steady state is not reached, from the change of the electric field (displacement current):

$$\begin{aligned} j(x) = & \underbrace{j_{drift,p}(x) + j_{drift,n}(x) + j_{diff,p}(x) + j_{diff,n}(x)}_{\text{drift \& diffusion}} + \\ & + \underbrace{e\, d_h \left[R_{pf,nf}(x) + R_{pt,nf}(x) + R_{pf,nt}(x) + R^{if}_{pf,nf}\right]}_{\text{recombination}} + \\ & + \underbrace{\epsilon_0 \epsilon(x) \frac{\partial F(x)}{\partial t}}_{\text{displacement}} \quad . \end{aligned} \tag{A.18}$$

It can be directly compared with the measured current density.

i) decay of singlet excitons = electroluminescence

In common organic molecules with weak spin-orbit coupling, only the radiative decay of singlet excitons is an allowed transition. Hence, it is assumed that triplet excitons decay non-radiatively. In order to reveal a quantitative value for the light output from an OLED, one has to consider singlet exciton creation (see the recombination processes described above), their transport and decay.

The change of singlet exciton density $s(x)$ due to creation and decay can be described by (see points f,g,h):

$$\left(\frac{ds(x)}{dt}\right)_{rad} = \frac{1}{4}\left[R_{pf,nf}(x) + R_{pt,nf}(x) + R_{pf,nt}(x) + R^{if}_{pf,nf,singlet}\right] - \frac{s(x)}{\tau_s}\,, \tag{A.19}$$

where $R^{if}_{pf,nf,singlet}$ means that part of the interface CT-excitons that became bulk excitons and τ_s denotes the singlet exciton lifetime, which may be derived from time

resolved photoluminescence measurements (a typical value for aromatic organic molecules is 10ns [4]). The pre-factor 1/4 accounts for the singlet/triplet spin statistics and is a first order approximation [61].

If one supposes that exciton transport only takes place by hopping to next neighbor molecules, the one-dimensional diffusion velocity $v_{diff,s}$ is related to the average number of hopping processes $\overline{N}_{hop}$ during its lifetime τ_s by $v_{diff,s} = (\overline{N}_{hop}\, d_h)/\tau_s$. The change of exciton density due to diffusion $(ds(x)/dt)_{diff}$ can then be calculated in the same manner as the free charge carrier diffusion in equation (A.11). The average hopping number $\overline{N}_{hop}$ might be derived from experiments regarding exciton diffusion lengths in organic materials. Reasonable values are in the order of 10-30nm [221, 222].

As long as the singlet excitons diffuse without getting quenched, they inevitable decay. The most prominent quenching mechanisms are: (1) quenching at the contacts, (2) quenching near the contacts, caused by inter-diffusion of electrode material (see [204]), and (3) quenching by free charge carriers. The latter process is believed to limit the quantum efficiency at very high operating voltages. Staudigel proposes a rate equation for the quenching of singlet excitons by free holes (free and trapped electrons and trapped holes are treated similarly) like:

$$R_{singlett,p_f}(x) \;=\; (v_{diff,s} + v_{f,p}(x))\, \sigma_q\, s(x) p_f(x)\,, \tag{A.20}$$

where $v_{f,p}(x)$ denotes the sum of the drift and diffusion velocity of a free hole (equation (A.14)) and σ_q gives a reaction cross-section. Staudigel et al. found from a parameter fit to experimental data of OLEDs with pure Alq_3 as emitter material a quenching cross-section of about $10^{-12}m^2$ (for comparison: 1nm area would lead to a cross-section of about $10^{-14}m^{-2}$).

The internal light emission can be derived from a summation of $s(x)/\tau_s$ over all organic layers:

$$S \;=\; \int_0^L \eta_{rad} \frac{s(x)}{\tau_s}\, dx \quad , \tag{A.21}$$

where η_{rad} is the material specific ratio of radiative decay of singlet excitons in the solid state (in a good approximation the photoluminescence efficiency). Hence, only the organic layers where η_{rad} is not zero contribute to light emission.

Several loss mechanisms decrease the external emission. In order to reveal a realistic and quantitative value for the light output, one would have to consider absorption losses, out-coupling losses due to (total) internal reflection and wave-guiding effects. They generally depend on the recombination profile throughout the device. In a simple approximation, the out-coupling efficiency can be calculated using equation (1.1) multiplied by 2 ($\eta_O \approx 1/2n^2$). This formula is valid under the neglect of absorption and microcavity effects, the assumption of total internal reflection at the non-transparent contact, and isotropic emission in the device. For more details regarding microcavity effects and out-coupling efficiencies see Lu [19], Greenham [134], Neyts [223], Tessler [224] and in refs. [225, 226, 227].

j) inclusion of emitter dopants

In order to enhance the quantum efficiency of an OLED, very often emitter dopants are used [48]. A certain amount of emitter dopant molecules (guest) is evaporated together

with the host molecules. If an energy transfer from the singlet excitons of the host to the singlet excitons of the guest is favorable, or free charge carriers can efficiently recombine directly on the guest molecules, almost all light emission originates from the guest molecules. These guest molecules are chosen due to their higher photoluminescence efficiency in a solid dispersion compared to the photoluminescence efficiency of the host molecules in the pure layer.

In the framework of the model described above, emitter dopants are traps for free charge carriers in the organic layer *and* traps for excitons of the host molecules. Their energetic position inside the HOMO-LUMO gap of the host molecule (position of the guest HOMO relative to the host HOMO: $E_{et,p}$, position of the guest LUMO relative to the host LUMO: $E_{et,p}$) and their densities ($N_{et,p} = N_{et,n} = N_{et}$) determine the density of occupied emitter trap states $p_{et}(x)$ and $n_{et}(x)$. The change of the density of occupied emitter traps due to free charge carriers can be calculated in accordance to equation (A.14).

There are two ways how an exciton can be created at an emitter dopant: (1) the recombination of a trapped hole with a free charge carrier and vice versa, and (2) the energy transfer from a host molecule to the guest molecule. Process (1) may be described in accordance to the treatment of normal traps by equation (A.15).

Process (2) is the resonant non-radiative (or Förster) energy transfer between molecules. The energy transfer rate K via induced anisotropic dipole-dipole interactions between a single pair of organic molecules is given by [130]:

$$K = \frac{1}{\tau_s}\frac{1}{R^6}\left(\frac{3}{4\pi}\int \frac{c^4}{\omega^4 n_H^4} F_H(\omega)\sigma_D(\omega)d\omega\right), \tag{A.22}$$

where $F_H(\omega)$ is the normalized fluorescence spectrum of the host material, $\sigma_D(\omega)$ the normalized optical absorption cross-section of the emitter dopant (which is proportional to the absorption coefficient), τ_s is the natural (without transport effects) radiative lifetime of the singlet excitons of the host materials, n_H is the index of refraction of the host and R is the mean distance between host and guest molecules, which can be calculated from the guest/host doping ratio. For an efficient energy transfer, the overlap between the emission spectra of the host and the absorption spectra of the guest has to be large. The Förster transfer rate is generally written in relation to a critical transfer distance R_0:

$$K = \frac{1}{\tau_s}\left[\frac{R_0}{R}\right]^6, \tag{A.23}$$

where R_0 is determined by the integral in equation (A.22). Equation (A.23) says that the rate of energy transfer between a guest and a host molecule separated by a distance R_0 is equal to the spontaneous emission rate of the host. A typical value for disordered organic materials is $R_0 \approx 30$Å [193].

The optimum concentration of the guest molecules in the host molecular film can be estimated from an analytic calculation of the total host-guest transfer rate accounting for the fact that each host can interact with a distribution of guest molecules (see [49]). Optimum concentrations are about 1 to 3 mol-%.

Recent attempts to increase the quantum efficiency in OLEDs use phosphorescent emitters as dopant molecules[24, 25, 62, 63, 64]. This avoids the spin statistic limitations, but adds some other difficulties:

(1) The triplet exciton diffusion length is long compared to the singlet diffusion length, hence, they more likely reach the quenching electrodes.

(2) The lifetime of the phosphorescent state is long, thus increasing the probability of energy back-transfer and triplet-triplet annihilation, reducing efficiency at higher operating voltages and limiting the device speed.

(3) Energy transfer is typically slower as compared to singlets. It can be described with the short-range Dexter-transfer mechanism based on diffusion of excitons to nearest neighbors [130, 228]. This effect makes the excitonic wave-function overlap between host and guest molecules more critical.

(4) Finally, it is difficult to obtain information about the triplet energy levels in the host and guest molecules [24].

Nevertheless, the treatment of triplet emitting dopants in a numerical model should be similar to the method described above for singlet excitons.

k) inclusion of dopants

The electronically doping of organic layers shifts the Fermi-level towards the transport states and, hence, increases the density of free charge carriers in equilibrium (without applied voltage). Thus, in equation (A.2), calculating the excess charge carrier density, the equilibrium charge carrier densities $p_{f,0}(x)$ and $n_{f,0}(x)$ are determined by the dopant concentrations: N_A for p-type doping with acceptor molecules and N_D for n-type doping with donator molecules. Two limiting cases can be distinguished:

(1) The Fermi-energy level crosses trap-energy levels (densities $N_{t,p}$ and $N_{t,n}$, see equation (A.14)) due to doping. Accordingly, these trap states are filled, and it follows: $N_t = 0$ and $p_{f,0} = N_A - N_{t,p}$, resp. $n_{f,0} = N_D - N_{t,n}$.

(2) If the dominant trap level E_t is still above the Fermi-level, the trap states N_t and the free charge carrier states N_μ will be occupied in accordance to a Boltzmann equation (assuming the Fermi-energy is still far away from the trap energy E_t and the transport energy E_μ). For the ratio of equilibrium free and trapped charge carriers follows: $p_{f,0}/p_{t,0} = N_\mu/N_t \, exp((E_\mu - E_t)/k_B T)$.

Owing to the increased equilibrium charge carrier densities due to doping, the effective charge carrier mobility described with equation (A.5) may also change. This is due to the fact that the dispersive transport in a disordered organic molecular layer takes place around a mean transport energy in the tail of the distribution of states (DOS) [203]. Upon doping, more states inside the DOS are filled which increases the mean transport energy. Here the concentration of states is higher and consequently the hopping rate is higher too. Thus, the effective mobility is increased. In fact, this behavior was already observed by Männig et al. [119], who observed a higher effective mobility in field-effect measurements on F_4-TCNQ doped ZnPc (zinc-phthalocyanine) compared to undoped ZnPc. In order to measure the mobilities of doped organic layers one has to keep in mind that the dielectric relaxation time is short, and thus, transient SCL, TOF and Cf-experiments used to determine the mobility in nominally undoped molecular layers (see point c of this Section) are generally not applicable for doped organic layers. It should be noted here that the effect that the effective mobility increases with the filling of the DOS can also occur for high injection levels in undoped materials.

Appendix B Simple approximations: j-V curves

As seen above, there is no general analytic solution for the bipolar current behavior in OLEDs. Only with severe restrictions, some numerical models are applicable. The most common simplifications are: (1) field independent hole and electron mobility, (2) diffusion and trapping completely ignored, (3) anode and cathode provide ohmic contacts and (4) restriction to one or two organic layers.

For the very simple case of an OLED with the layer sequence ITO/TPD/Alq_3/Mg:Ag or Al, which is an OLED with efficient hole injection and transport and comparably inefficient electron injection and transport, the qualitative behavior of an OLED is dominated by the electron current in the Alq_3 layer. The quantitative current flow is surely further influenced by recombination currents due to bipolar injection in the device. In dependence on the cathode material, injection limited or space charge limited currents (SCL) are expected. In the latter case, SCL current can be trap limited (TCL) or trap free SCL.

For very low voltages, one expects ohmic conduction via thermally generated free charges. In this case the current density is described by (for electrons):

$$j = e\mu_n n_0 \frac{V}{d} \tag{B.1}$$

where e is the elementary charge, μ_n is the electron mobility in the ETL, n_0 is the thermally generated background free charge density, V the applied voltage and d is the ETL thickness.

On the other hand, in the trap filled limit for SCL currents at high voltages (the Fermi level E_F lies below the trap energy), the current density follows the SCL model [130]:

$$j = \frac{9}{8}\mu_n \epsilon\epsilon_0 \frac{V^2}{d^3} \tag{B.2}$$

where ϵ is the dielectric constant and ϵ_0 the permittivity of free space. This equation is the solid state analogous of Child's-Law for SCL currents in vacuum.

In the intermediate case, where too many charges are injected to allow for ohmic conduction, but not enough charges to fill all trap levels, increasing the voltage leads to filling of traps below the rising quasi-Fermi level for electrons. This reduces the available density of empty trap states and thus successively increases the electron effective mobility, $\mu_{eff} = \mu_n(n_{inj}/n_t)$. Here, n_t is the total trapped charge density, n_{inj} the injected charge density. Therefore, in the TCL regime a higher power law dependence of the current on voltage is observed. If the traps are not discrete, but exponentially distributed in the gap, it was found that the current is governed by the density and energy distribution of the traps [5, 130]:

$$j = N_{LUMO}\,\mu_n\, e \left[\frac{\epsilon\epsilon_0 l \sin(\pi/l)}{eH_t(\pi/l)(1+l)}\right]^l \left(\frac{2l+1}{l+1}\right)^{(l+1)} \frac{V^{(l+1)}}{L^{(2l+1)}} \tag{B.3}$$

where N_{LUMO} is the density of states in the LUMO-levels and H_t is the total trap density if the trap distribution starts at E_{LUMO}=0. The empirical parameter $l \geq 1$ describes

how the concentration of traps changes with energy (for an exponential trap distribution l equals the ratio of the characteristic trap temperature to the ambient temperature). The value of l can be experimentally obtained from the slope of a $ln(j)$ versus V plot. For Alq_3, l is usually in the range of 6-8 [5].

For less efficient electron injection into the electron transport layer, injection limited currents might be observed. Two models known from inorganic semiconductors and insulators were proposed to treat field induced injection into an organic dielectric material: (1) Fowler-Nordheim-tunneling (FN), and (2) the Richardson-Schottky (RS) model for thermionic emission.

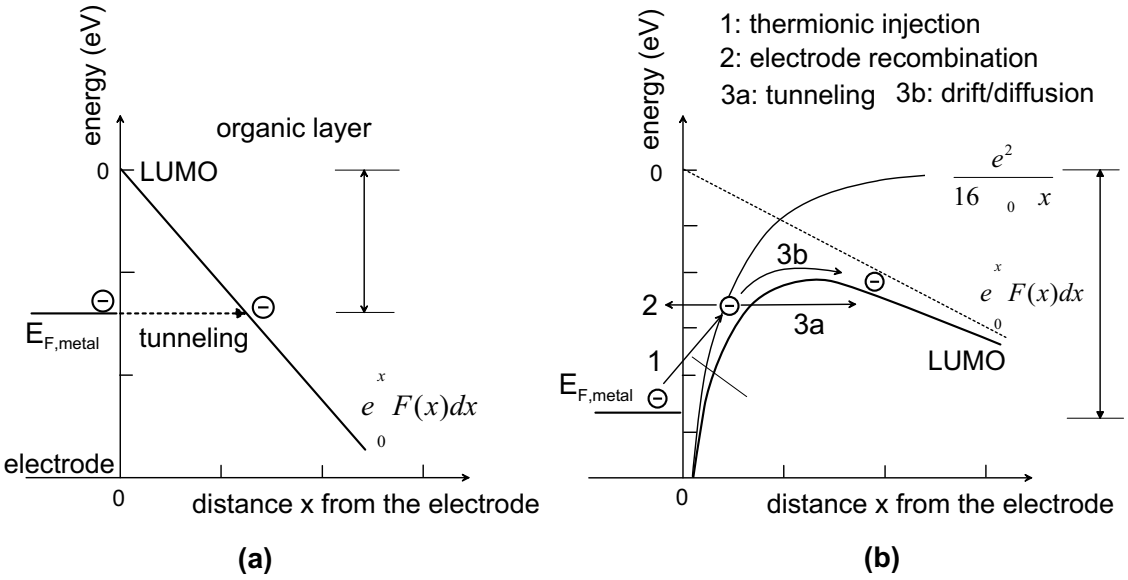

Figure B.1: *Schematic view of two possible models for the injection process of carriers into an organic dielectric material, (a) Fowler-Nordheim tunneling for electrons, (b) Richardson Schottky thermionic emission for electrons; here the 3 current parts of an extended model are schematically drawn (see text).*

The FN-model ignores image charge effects and assumes tunneling of charge carriers from the metal through a triangular barrier into unbound continuum states (see Figure B.1 (a)). It predicts a temperature independent injection current [28]:

$$j(F) \;=\; B\,F^2\,exp\left[-\frac{4(2m_{eff})^{1/2}\Phi^{3/2}}{3\hbar eF}\right] \quad , \tag{B.4}$$

where B denotes a field independent constant, m_{eff} is the effective mass of the charge carriers inside the barrier and Φ the potential barrier for charge injection at the interface. The FN-model sometimes gives reasonable values for the interface barrier (in the high field case) but this agreement is by chance [229].

In the RS-model (Figure B.1 (b)) carriers are injected when they acquire sufficient thermal energy to cross the potential maximum that results from the superposition of the external and the image charge potential [7]:

$$j(F) \;=\; C\,T^2\,exp\left[-(\Phi-(eF/4\pi\varepsilon_0\varepsilon)^{1/2}\right]\,/\,k_BT \quad , \tag{B.5}$$

where C is the field independent Richardson-constant. This approach neglects tunneling through the barrier and inelastic backscattering of the hot carriers before traversing the potential maximum. The latter is the reason why fits of the RS-model to experimental data usually give too high values for the Richardson constant C.

Recently there was considerable theoretical work going on to overcome the shortcoming of the two models described above. Mainly it deals with the optimization of the RS-model by including backscattering (which is particularly important for the short mean free path in disordered organics) and tunneling or diffusion through and over the barrier.

Davids and Campbell et al. proposed an analytic model [7], which basically rests on three current parts that together govern the injection current. The first and second part, charge injection by thermionic emission and back-flow of charges by interface recombination, are balanced and the third part, the tunneling current through the image charge modified potential wall, is modeled with a WKB-approach (see Figure B.1 (b)). They observed that for low fields the thermionic part of the injection current dominates, whereas at higher fields tunneling exceeds thermionic emission [230]. The group of Scott et al. proposed a similar model, where the field dependence of the tunneling part of the injection current is governed by Schottky-barrier lowering [10, 11, 231]. In their model, the mobility dependence of the injection current is also recovered.

Another model, the thermally assisted hopping injection into disordered solids, was proposed by the Bässler group [203, 215, 232, 233]. They calculate the probability of the first short distance carrier jump from the metal into a distribution of localized disordered states and their escape probability into the bulk, determined by the interplay of drift and diffusion in the presence of an image charge modified potential, treated in a one-dimensional Onsager picture. This model accounts also for the disorder dependence of the injection current. Namely, the probability to find a target site for the first carrier jump away from the metal is increased, if the energetic disorder of the organic material in contact is higher. The difference to the models mentioned above is that no tunneling is involved, but the disorder of the organics is regarded properly. For high electric fields the Bässler model approaches the RS-thermionic injection model since for that case the maximum of the image charge modified energy barrier is close to the first molecular lattice plane and disorder does not play an important role anymore [229].

In summary, the following shapes of current-voltage dependencies could be expected in cases where one charge carrier type in one layer dominates the current flow:

ohmic conduction	$j \sim V$
space charge limited current (SCL)	$j \sim V^2$
trap charge limited current (TCL)	$j \sim V^{l+1}$ with $l > 1$
injection limited current (FN tunneling)	$ln(j/F^2) \sim -1/F$
injection limited current (RS thermionic injection)	$ln(j) \sim \sqrt{F}$

(B.6)

Bibliography

[1] C.W. Tang, S.A. VanSlyke. *Appl. Phys. Lett.*, **51** (1987) 913–915.

[2] J. Yang, J. Shen. *J. Appl. Phys.*, **85** (1999) 2699–2705.

[3] M.S. Tyagi. *Introduction to semiconductor materials and devices*. John Wiley & Sons, New York, 1991.

[4] J. Staudigel, M. Stößel, F. Steuber, J. Simmerer. *J. Appl. Phys.*, **86** (1999) 3895–3910.

[5] P.E. Burrows, Z. Shen, V. Bulovic, D.M. McCarty, S.R. Forrest, J.A. Cronin, M.E. Thompson. *J. Appl. Phys.*, **79** (1996) 7991–8006.

[6] D.V. Khramtchenkov, H. Bässler, V.I. Arkhipov. *J. Appl. Phys.*, **79** (1996) 9283–9290.

[7] P.S. Davids, I.H. Campbell, D.L. Smith. *J. Appl. Phys.*, **82** (1997) 6319–6325.

[8] J. Shen, J. Yang. *J. Appl. Phys.*, **83** (1998) 7706–7714.

[9] Y. Kawabe, M.M. Morrell, G.E. Jabbour, S.E. Shaheen, B. Kippelen, N. Peyghambarian. *J. Appl. Phys.*, **84** (1998) 5306–5314.

[10] J.C. Scott, P.J. Brock, J.R. Salem, S. Ramos, G.G. Malliaras, S.A. Carter, L. Bozano. *Synthet. Metal.*, **111** (2000) 289–293.

[11] B. Ruhstaller, S.A. Carter, S. Barth, H. Riel, W. Riess, J.C. Scott. *J. Appl. Phys.*, **89** (2001) 4575–4586.

[12] F. Godler. *Colour image projector with time-controlled LED-light sources*. Patent Application WO00074390, 2000.

[13] C. Hosokawa, M. Eida, M. Matsuura, K. Fukuoka, H. Nakamura, T. Kusumoto. *Synthet. Metal.*, **91** (1997) 3–7.

[14] Z.A. Bao, S. Campbell. *Thin Solid Films*, **352** (1999) 239–242.

[15] K. Nagayama, S. Miyaguchi. *Organic electroluminescent display panel and method for manufacturing the same*. Patent Application EP732868A1, 1996.

[16] D.L. Mathine, H.S. Woo, W. He, T.W. Kim, B. Kippelen, N. Peyghambarian. *Appl. Phys. Lett.*, **76** (2000) 3849–3851.

[17] O. Madelung, Editor. *Semiconductors - Basic data*. Springer-Verlag, Berlin, 2. rev. Edition, 1996.

[18] P.E. Burrows, V. Khalfin, G. Gu, S.R. Forrest. *Appl. Phys. Lett.*, **73** (1998) 435–437.

[19] M.-H. Lu, J.C. Sturm. *Appl. Phys. Lett.*, **78** (2001) 1927–1929.

[20] R. Windisch, P. Heremans, A. Knobloch, P. Kiesel, G.H. Dohler, B. Dutta, G. Borghs. *Appl. Phys. Lett.*, **74** (1999) 2256–2258.

[21] C.W. Tang. *Appl. Phys. Lett.*, **48** (1986) 183–185.

[22] M. Pfeiffer, A. Beyer, B. Plönnigs, A. Nollau, T. Fritz, K. Leo, D. Schlettwein, S. Hiller, D. Wöhrle. *Solar Energ. Mater. Solar Cells*, **63** (2000) 83–99.

[23] M.G. Craford. *MRS Bulletin*, **25** (2000) 27–31.

[24] M.A. Baldo, S. Lamansky, P.E. Burrows, M.E. Thompson, S.R. Forrest. *Appl. Phys. Lett.*, **75** (1999) 4–6.

[25] T. Tsutsui, M. Yang, M. Yahiro, K. Nakamura, T. Watanabe, T. Tsuiji, Y. Fukuda, T. Wakimoto, S. Miyaguchi. *Jpn. J. Appl. Phys. Pt. 2*, **38** (1999) L1502–L1504.

[26] M. Pope, H. Kallman, P. Magnante. *J. Chem. Phys.*, **38** (1963) 2042–2043.

[27] W. Helfrich, W.G. Schneider. *Phys. Rev. Lett.*, **14** (1965) 229–231.

[28] S. Miyata, H.S. Nalwa, Editor. *Organic electroluminescent materials and devices*. Gordon and Breach Science Publishers, Amsterdam, 1997.

[29] J.H. Burroughes, D.D.C. Bradley, A.R. Brown, R.N. Marks, K. Mackay, R.H. Friend, P.L. Burns, A.B. Holmes. *Nature*, **347** (1990) 539–541.

[30] D. Braun, A. J. Heeger. *Appl. Phys. Lett.*, **58** (1991) 1982–1984.

[31] R.H. Friend, R.W. Gymer, A.B. Holmes, J.H. Burroughes, R.N. Marks, C. Taliani, D.D.C. Bradley, D.A. Dos-Santos, J.L. Brédas, M. Löglund, W.R. Salaneck. *Nature*, **397** (1999) 121–128.

[32] Y. Yang, A.J. Heeger. *Appl. Phys. Lett.*, **64** (1994) 1245–1247.

[33] S.A. Carter, M. Angelopoulos, S. Karg, P.J. Brock, J.C. Scott. *Appl. Phys. Lett.*, **70** (1997) 2067–2069.

[34] M. Gross, D.C. Müller, H.G. Nothofer, U. Scherf, D. Neher, C. Bräuchle, K. Meerholz. *Nature*, **405** (2000) 661–665.

[35] P.L. Burn, A.B. Holmes, A. Kraft, D.D.C. Bradley, A.R. Brown, R.H. Friend, R.W. Gymer. *Nature*, **356** (1992) 47–49.

[36] H. Spreitzer, H. Becker, E. Kluge, W. Kreuder, H. Schenk, R. Demandt, H. Schoo. *Adv. Mater.*, **10** (1998) 1340–1343.

[37] S. Janietz, D.D.C. Bradley, M. Grell, C. Giebeler, M. Inbasekaran, E.P. Woo. *Appl. Phys. Lett.*, **73** (1998) 2453–2455.

[38] D. Ammermann, C. Rompf, W. Kowalsky. *Jpn. J. Appl. Phys. Pt. 1*, **34** (1995) 1293–1297.

[39] T. Tominaga, K. Hayashi, N. Toshima. *Appl. Phys. Lett.*, **70** (1997) 762–763.

[40] S.A. Van Slyke, C.H. Chen, C.W. Tang. *Appl. Phys. Lett.*, **69** (1996) 2160–2162.

[41] Y. Shirota, T. Kobata, N. Noma. *Chem. Lett.*, (1989) 1145–1148.

[42] Y. Shirota, Y. Kuwabara, H. Inada. *Appl. Phys. Lett.*, **65** (1994) 807–809.

[43] Y. Shirota, Y. Kuwabara, D. Okuda, R. Okuda, H. Ogawa, H. Inada, T. Wakimoto, H. Nakada, Y. Yonemoto, S. Kawami, K. Imai. *Journal of Luminescence*, **72-74** (1997) 985–991.

[44] C.C. Wu, C.I. Wu, J.C. Sturm, A. Kahn. *Appl. Phys. Lett.*, **70** (1997) 1348–1350.

[45] J.S. Kim, M. Granström, R.H. Friend, N. Johansson, W.R. Salaneck, R. Daik, W.J. Feast, F. Cacialli. *J. Appl. Phys.*, **84** (1998) 6859–6870.

[46] K. Sugiyama, H. Ishii, Y. Ouchi, K. Seki. *J. Appl. Phys.*, **87** (2000) 295–298.

[47] Y. Hamada. *IEEE Transactions on Electron Devices*, **44** (1997) 1208–1217.

[48] C.W. Tang, S.A. VanSlyke, C.H. Chen. *J. Appl. Phys.*, **65** (1989) 3610–3616.

[49] H. Mattoussi, H. Murata, C.D. Merritt, Y. Iizumi, J. Kido, Z.H. Kafafi. *J. Appl. Phys.*, **86** (1999) 2642–2650.

[50] S.E. Shaheen, B. Kippelen, N. Peyghambarian, J.F. Wang, J.D. Anderson, E.A. Mash, P.A. Lee, N.R. Armstrong, Y. Kawabe. *J. Appl. Phys.*, **85** (1999) 7939–7945.

[51] C. Adachi, M.A. Baldo, S.R. Forrest. *J. Appl. Phys.*, **87** (2000) 8049–8055.

[52] M. Uchida, C. Adachi, T. Koyama, Y. Taniguchi. *J. Appl. Phys.*, **86** (1999) 1680–1687.

[53] L.S. Hung, C.W. Tang, M.G. Mason. *Appl. Phys. Lett.*, **70** (1997) 152–154.

[54] J. Kido, T. Matsumoto. *Appl. Phys. Lett.*, **73** (1998) 2866–2868.

[55] B.J. Chen, W.Y. Lai, Z.Q. Gao, C.S. Lee, S.T. Lee, W.A. Gambling. *Appl. Phys. Lett.*, **75** (1999) 4010–4012.

[56] J. Kido, Y. Iizumi. *Appl. Phys. Lett.*, **73** (1998) 2721–2723.

[57] H. Murata, C.D. Merritt, H. Inada, Y. Shirota, Z.H. Kafafi. *Appl. Phys. Lett.*, **75** (1999) 3252–3254.

[58] S.E. Shaheen, G.E. Jabbour, B. Kippelen, N. Peyghambarian, J.D. Anderson, S.R. Marder, N.R. Armstrong, E. Bellmann, R.H. Grubbs. *Appl. Phys. Lett.*, **74** (1999) 3212–3214.

[59] V. Cleave, G. Yahioglu, P. Le Barny, R. Friend, N. Tessler. *Adv. Mater.*, **11** (1999) 285–288.

[60] R.J. Curry, W.P. Gillin. *J. Appl. Phys.*, **88** (2000) 781–785.

[61] M. Wohlgenannt, K. Tandon, S. Mazumdar, S. Ramasesha, Z.V. Vardeny. *Nature*, **409** (2001) 494–497.

[62] M.A. Baldo, D.F. O'Brien, Y. You, A. Shoustikov, S. Sibley, M.E. Thompson, S.R. Forrest. *Nature*, **395** (1998) 151–154.

[63] C. Adachi, M.A. Baldo, S.R. Forrest, M.E. Thompson. *Appl. Phys. Lett.*, **77** (2000) 904–906.

[64] C. Adachi, M.A. Baldo, S.R. Forrest, S. Lamansky, M.E. Thompson, R.C. Kwong. *Appl. Phys. Lett.*, **78** (2001) 1622–1624.

[65] F. Li, H. Tang, J. Anderegg, J. Shinar. *Appl. Phys. Lett.*, **70** (1997) 1233–1235.

[66] H. Tang, F. Li, J. Shinar. *Appl. Phys. Lett.*, **71** (1997) 2560–2562.

[67] M.B. Huang, K. McDonald, J.C. Keay, Y.Q. Wang, S.J. Rosenthal, R.A. Weller, L.C. Feldman. *Appl. Phys. Lett.*, **73** (1998) 2914–2916.

[68] Y. Kurosaka, N. Tada, Y. Ohmori, K. Yoshino. *Synthet. Metal.*, **102** (1999) 1101–1102.

[69] G.E. Jabbour, Y. Kawabe, S.E. Shaheen, J.F. Wang, M.M. Morrell, B. Kippelen, N. Peyghambarian. *Appl. Phys. Lett.*, **71** (1997) 1762–1764.

[70] R. Schlaf, B.A. Parkinson, P.A. Lee, K.W. Nebesny, G. Jabbour, B. Kippelen, N. Peyghambarian, N.R. Armstrong. *J. Appl. Phys.*, **84** (1998) 6729–6736.

[71] U. Wolf, H. Bässler. *Appl. Phys. Lett.*, **74** (1999) 3848–3850.

[72] H. Heil, J. Steiger, S. Karg, M. Gastel, H. Ortner, H. v. Seggern. *J. Appl. Phys.*, **89** (2001) 420–424.

[73] T. Osada, P. Barta, N. Johansson, T. Kugler, P. Broms, W.R. Salaneck. *Synthet. Metal.*, **102** (1999) 1103–1104.

[74] M.G. Mason, C.W. Tang, L.-S. Hung, P. Raychaudhuri, J. Madathil, D.J. Giesen, L. Yan, Q.T. Le, Y. Gao, S.-T. Lee, L.S. Liao, L.F. Cheng, W.R. Salaneck, D.A. dos Santos, J.L. Brédas. *J. Appl. Phys.*, **89** (2001) 2756–2765.

[75] F. Steuber, J. Staudigel, M. Stössel, J. Simmerer, A. Winnacker. *Appl. Phys. Lett.*, **74** (1999) 3558–3560.

[76] J. Shen, D. Wang, E. Langlois, W.A. Barrow, P.J. Green, C.W. Tang, J. Shi. *Synthet. Metal.*, **111** (2000) 233–236.

[77] L.M. Do, C. Ganzorig, A. Koike, M. Fujihira. *Mol. Cryst. Liq. Cryst. Sci. Tec. A*, **294** (1997) 333–336.

[78] T. Mori, K. Obata, T. Mizutani. *J. Phys. D - Appl. Phys.*, **32** (1999) 1198–1203.

[79] T. Mori, H. Tsuge, T. Mizutani. *J. Phys. D - Appl. Phys.*, **32** (1999) L65–L69.

[80] Z.D. Popovic, S. Xie, N. Hu, A. Hor, D. Fork, G. Anderson, C. Tripp. *Thin Solid Films*, **363** (2000) 6–8.

[81] H. Ochi, S. Kawami, H. Ohata, K. Nagayama, R. Murayama, Y. Okuda, H. Nakada, T. Tohma, T. Naito, H. Abiko. *J. SID*, **5** (1997) 235.

[82] *Pioneer electronic corporation press release, September 28, 1998 (www.pioneer.co.jp/press/index-e.html).* 1998.

[83] G. Rajeswaran, M. Itoh, M. Boroson, S. Barry, T.K. Hatwar, K.B. Kahen, K. Yoneda, R. Yokoyama, T. Yamada, N. Komiya, H. Kanno, H. Takahashi. *SID 00 Digest*, (2000) 40.1.

[84] G.H. Gelinck, T.C.T. Gneus, D.M. deLeeuw. *Appl. Phys. Lett.*, **77** (2000) 1487–1489.

[85] C.D. Dimitrakopoulos, S. Purushothaman, J. Kymissis, A. Callegari, J.M. Shaw. *Science*, **283** (1999) 822–824.

[86] H. Sirringhaus, N. Tessler, R.H. Friend. *Science*, **280** (1998) 1741–1744.

[87] J.H. Schön, Ch. Kloc, B. Battlogg. *Appl. Phys. Lett.*, **77** (2000) 3776–3778.

[88] B.K. Crone, A. Dodabalapur, R. Sarpeshkar, R.W. Filas, Y.-Y. Lin, Z. Bao, J.H. O'Neill, W. Li, H.E. Katz. *J. Appl. Phys.*, **89** (2001) 5125–5132.

[89] H. Ishii, K. Sugiayama, E. Ito, K. Seki. *Adv. Mater.*, **11** (1999) 605–625.

[90] Y. Park, V. Choong, E. Ettedgui, Y. Gao, B.R. Hsieh, T. Wehrmeister, K. Müllen. *Appl. Phys. Lett.*, **69** (1996) 1080–1082.

[91] I.H. Campbell, D.L. Smith, C.J. Neef, J.P. Ferraris. *Appl. Phys. Lett.*, **75** (1999) 841–843.

[92] V.R. Nikitenko, V.I. Arkhipov, Y.-H. Tak, J. Pommerehne, H. Bässler, H.-H. Hörhold. *J. Appl. Phys.*, **81** (1997) 7514–7525.

[93] T.R. Hebner, C.C. Wu, D. Marcy, M.H. Lu, J.C. Sturm. *Appl. Phys. Lett.*, **72** (1998) 519–521.

[94] K. Book, H. Bässler, V.R. Nikitenko, A. Elschner. *Synthet. Metal.*, **111** (2000) 263–267.

[95] Martin Pfeiffer. *Controlled doping of organic vacuum deposited dye layers: basics and applications.* PhD thesis TU-Dresden, 1999.

[96] Y. Yamamoto, K. Yoshino, Y. Inuishi. *J. Phys. Soc. of Jap.*, **47** (1979) 1887–1891.

[97] D.R. Kearns, G. Tollin, M. Calvin. *J. Chem. Phys.*, **32** (1960) 1020–1025.

[98] B. Boudjema, N. El-Khatib, M. Gamoudi, G. Guillaud, M.Maitrot. *Rev. Phys. Appl.*, **23** (1988) 1127–1134.

[99] T.J. Marks. *Science*, **227** (1985) 881–889.

[100] M. Maitrot, G. Guillaud, B. Boudjema, J.J. André, J. Simon. *J. Appl. Phys.*, **60** (1986) 2396–2400.

[101] N. El-Khatib, B. Boudjema, G. Guillaud, M. Maitrot. *J. Less Comm. Metals*, **143** (1988) 101–112.

[102] E.J. Lous, P.W.M. Blom, L.W. Molenkamp, D.M. deLeeuw. *Phys. Rev. B - Condensed Matter*, **51** (1995) 17251–17254.

[103] Y.-W. Park, A.J. Heeger, M.A. Druy, A.G. MacDiarmid. *J. Chem. Phys.*, **73** (1980) 946–957.

[104] S. Hiller, D. Schlettwein, N.R. Armstrong, D. Wöhrle. *J. Mater. Chem.*, **8** (1998) 945–954.

[105] S. Hayashi, H. Etoh, S. Saito. *Jap. J. Appl. Phys.*, **25** (1986) L773–L775.

[106] H. Antoniadis, D.B. Roitman, J.N. Miller. *Organic electroluminescent device*. Patent Application US 5 719 467, 1995.

[107] D.B. Romero, M. Schaer, L. Zuppiroli, B. Cesar, B. Francois. *Appl. Phys. Lett.*, **67** (1995) 1659–1661.

[108] F. Huang, A.G. MacDiarmid, B.R. Hsieh. *Appl. Phys. Lett.*, **71** (1997) 2415–2417.

[109] A. Yamamori, C. Adachi, T. Koyama, Y. Taniguchi. *Appl. Phys. Lett.*, **72** (1998) 2147–2149.

[110] A. Yamamori, C. Adachi, T. Koyama, Y. Taniguchi. *J. Appl. Phys.*, **86** (1999) 4369–4376.

[111] J. Kido, J. Endo, T. Matsumoto. *Polym. Prepr. (Am. Chem. Soc. Div. Polym. Chem.)*, **47** (1998) 1940.

[112] C. Ganzorig, M. Fujihara. *Appl. Phys. Lett.*, **77** (2000) 4211–4213.

[113] T. Kugler, W.R. Salaneck, H. Rost, A.B. Holmes. *Chem. Phys. Lett.*, **310** (1999) 391–396.

[114] B. Plönnigs. *Elektrische und strukturelle Charakterisierung dotierter Farbstoffaufdampfschichten*. Diplomarbeit, TU Dresden, 1999.

[115] M. Meneghetti, C. Pecile. *J. Chem. Phys.*, **84** (1986) 4149–4162.

[116] J.S. Chapell, A.N. Bloch. *J. Amer. Chem. Soc.*, **103** (1980) 2442–2443.

[117] M. Pfeiffer, A. Beyer, T. Fritz, K. Leo. *Appl. Phys. Lett.*, **73** (1998) 3202–3204.

[118] M. Pfeiffer, T. Fritz, J. Blochwitz, A. Nollau, B. Plönnigs, A. Beyer, K. Leo. *Advances in Solid State Physics*, **39** (1999) 77–90.

[119] B. Männig, M. Pfeiffer, A. Nollau, X. Zhou, K. Leo. *Organic Electronics*, (2001) submitted.

[120] F. Papadimitrakopoulos, X.-M. Zhang, D.L. Thomsen III, K.A. Higginson. *Chem. Mater.*, **8** (1996) 1363–1365.

[121] Z.D. Popovic, H. Aziz, N.-X. Hu, A.-M. Hor, G. Xu. *Synthet. Metal.*, **111-112** (2000) 229–232.

[122] T. Mori, K. Miyachi, T. Kichimi, T. Mizutani. *Jpn. J. Appl. Phys. Pt. 1*, **33** (1994) 6594–6598.

[123] E.I. Maltsev, M.A. Brusentseva, V.A. Kolesnikov, V.I. Berendyaev, B.V. Kotov, A.V. Vannikov. *Appl. Phys. Lett.*, **71** (1997) 3480–3482.

[124] A. Rajagopal, C.I. Wu, A. Kahn. *J. Appl. Phys.*, **83** (1998) 2649–2656.

[125] C. Hosokawa, H. Tokailin, H. Higashi, T. Kusumoto. *Appl. Phys. Lett.*, **60** (1992) 1220–1222.

[126] S. Naka, H. Okada, H. Onnagawa, Y. Yamaguchi, T. Tsutsui. *Synthet. Metal.*, **111** (2000) 331–333.

[127] R.G. Kepler, P.M. Beeson, S.J. Jacobs, R.A. Anderson, M.B. Sinclair, V.S. Valencia, P.A. Cahill. *Appl. Phys. Lett.*, **66** (1995) 3618–3620.

[128] A.J. Ikushima, T. Kanno, S. Yoshida, A. Maeda. *Thin Solid Films*, **273** (1996) 35–38.

[129] C. Giebeler, H. Antoniadis, D.D.C. Bradley, Y. Shirota. *Appl. Phys. Lett.*, **72** (1998) 2448–2450.

[130] M. Pope, C.E. Swenberg. *Electronic processes in organic molecular crystals*. Oxford University Press, New York, 1982.

[131] N. Karl. Organic Semiconductors. In *Landolt-Börnstein (New Series), Group III, 17i*, p. 106–218. Springer-Verlag, Berlin, Heidelberg, New York, Tokyo, 1985.

[132] E.A. Silinsh. Organic Molecular Crystals - Their Electronic States. In M. Cardona, P. Fulde, H.-J. Queisser, Editor, *Springer Series in Solid-State Sciences*. Springer-Verlag, Berlin, Heidelberg, New York, 1980.

[133] W.R. McCluney. *Introduction to radiometry and photometry*. Artech House, Boston, London, 1994.

[134] N.C. Greenham, R.H. Friend, D.D.C. Bradley. *Adv. Mater.*, **6** (1994) 491–494.

[135] G. Ertl, J. Küppers. *Low Energy Electrons and Surface Chemistry*. VCH Verlagsgesellschaft mbH, Weinheim, Deerfield Beach, 2nd Edition, 1985.

[136] G. Svehla, Editor. *Comprehensive Analytical Chemistry: Ultraviolet Photoelectron and Photoion Spectroscopy*, Chapter 1. Number IX. Elsevier Scientific Publishing Comp., Amsterdam, Oxford, New York, 1979.

[137] S.T. Lee, X.Y. Hou, M.G. Mason, C.W. Tang. *Appl. Phys. Lett.*, **72** (1998) 1593–1595.

[138] I.G. Hill, A. Rajagopal, A. Kahn. *J. Appl. Phys.*, **84** (1998) 3236–3241.

[139] T. Mori, H. Fujikawa, S. Tokito, Y. Taga. *Appl. Phys. Lett.*, **73** (1998) 2763–2765.

[140] R. Schlaf, B.A. Parkinson, P.A. Lee, K.W. Nebesny, N.R. Armstrong. *Appl. Phys. Lett.*, **73** (1998) 1026–1028.

[141] R. Schlaf, B.A. Parkinson, P.A. Lee, K.W. Nebesny, N.R. Armstrong. *J. Phys. Chem. B*, **103** (1999) 2984–2992.

[142] S.T. Lee, Y.M. Wang, X.Y. Hou, C.W. Tang. *Appl. Phys. Lett.*, **74** (1999) 670–673.

[143] I.G. Hill, A. Kahn. *J. Appl. Phys.*, **84** (1998) 5583–5586.

[144] D. Briggs, M.P. Seah, Editor. *Practical Surface Analysis*. John Wiley and Sons, Chichester, New York, Brisbane, Toronto, Singapore, 1983.

[145] Y. Hirose, C.I. Wu, V. Aristov, P. Soukiassian, A. Kahn. *Appl. Surf. Sci.*, **113-114** (1997) 291–298.

[146] R. Schlaf, C.D. Merritt, L.A. Crisafulli, Z.H. Kafafi. *J. Appl. Phys.*, **86** (1999) 5678–5686.

[147] I.H. Campbell, T.A.Z.S. Rubin, J.D. Kress, R.L. Martin, D.L. Smith, N.N. Barashkov, J.P. Ferraris. *Phys. Rev. B - Condensed Matter*, **54** (1996) R14321–R14324.

[148] A. Kahn. *private communication*.

[149] R. Schlaf, P.G. Schroeder, M.W. Nelson, B.A. Parkinson, C.D. Merrit, L.A. Crisafulli, H. Murata, Z.H. Kafafi. *Surf. Sci.*, **450** (2000) 142–152.

[150] H. Peisert, T. Schwieger, M. Knupfer, M.S. Golden, J. Fink. *J. Appl. Phys.*, **88** (2000) 1535–1540.

[151] Y. Park, V.-E. Choong, B.R. Hsieh, C.W. Tang, T. Wehrmeister, K. Mullen, Y. Gao. *J. Vac. Sci. Technol. A*, **15** (1997) 2574–2578.

[152] I.G. Hill, A.J. Mäkinen, Z.H. Kafafi. *J. Appl. Phys.*, **88** (2000) 889–895.

[153] I.G. Hill, J. Schwartz, A. Kahn. *Organic Electronics*, **1** (2000) 5–14.

[154] H. Ishii, H. Oji, E. Ito, N. Hayashi, D. Yoshimura, K. Seki. *J. Lum.*, **87-89** (2000) 61–65.

[155] I.G. Hill, A.J. Mäkinen, Z.H. Kafafi. *Appl. Phys. Lett.*, **77** (2000) 1825–1827.

[156] K.F. Brennan. *The Physics of Semiconductors*. Cambridge University Press, Cambridge, New York, 1999.

[157] D. Schlettwein, K. Hesse, N.E. Gruhn, P.A. Lee, K.W. Nebesny, N.R. Armstrong. *J. Phys. Chem. B*, (2001) accepted.

[158] F.R. Fan, L.R. Faulkner. *J. Chem. Phys.*, **69** (1978) 3334–3340.

[159] J. Simon, J.-J. André. *Molecular Semiconductors*. Springer Verlag, Berlin, Heidelberg, New York, Tokyo, 1985.

[160] E.C. Chen, W.E. Wentworth. *J. Chem. Phys.*, **63** (1975) 3183–3191.

[161] I.G. Hill, A. Kahn. *J. Appl. Phys.*, **86** (1999) 4515–4519.

[162] C. Giebeler, H. Antoniadis, D.D.C. Bradley, Y. Shirota. *J. Appl. Phys.*, **85** (1999) 608–615.

[163] A. Werner. *Untersuchung des Dotiermechanismus von Farbstoffschichten anhand optischer und elektrischer Messungen*. Diplomarbeit, TU Dresden, 1999.

[164] P.E. Burrows, S.R. Forrest. *Appl. Phys. Lett.*, **64** (1993) 2285–2287.

[165] Z.L. Shen, P.E. Burrows, V. Bulovic, D.M. McCarty, M.E. Thompson, S.R. Forrest. *Jpn. J. Appl. Phys.*, **35** (1996) L401–L404.

[166] M.A. Lampert, P. Mark. In H.G. Booker, N. DeClaris, Editor, *Current Injection in Solids*. Academic Press, New York, 1970.

[167] M. Matsumura, A. Ito, Y. Miyamae. *Appl. Phys. Lett.*, **75** (1999) 1042–1044.

[168] L.B. Lin, R.H. Young, M.G. Mason, S.A. Jenekhe, P.M. Borsenberger. *Appl. Phys. Lett.*, **72** (1998) 864–866.

[169] P. Piromreun, H. Oh, Y. Shen, G.G. Malliaras, J.C. Scott, P.J. Brock. *Appl. Phys. Lett.*, **77** (2000) 2403–2405.

[170] M. Stößel, J. Staudigel, F. Steuber, J. Blässing, J. Simmerer, A. Winnacker, H. Neuner, D. Metzdorf, H.-H. Johannes, W. Kowalsky. *Synthet. Metal.*, **111-112** (2000) 19 – 24.

[171] K. Itano, H. Ogawa, Y. Shirota. *Appl. Phys. Lett.*, **65** (1994) 807–809.

[172] Y. Shirota. *Proc. SPIE*, **3148** (1997) 186.

[173] K. Itano, H. Ogawa, Y. Shirota. *Appl. Phys. Lett.*, **72** (1998) 636–638.

[174] T. Noda, H. Ogawa, Y. Shirota. *Adv. Mater.*, **11** (1999) 283–285.

[175] K. Okumoto, K. Wayaku, T. Noda, H. Kageyama, Y. Shirota. *Synthet. Metal.*, **111** (2000) 473–476.

[176] M. Pfeiffer, K. Leo, J. Blochwitz, X. Zhou. *Lichtemittierendes Bauelement mit organischen Schichten*. Patent Application DE 100 58 578.7, 2000.

[177] H. Aziz, Z.D. Popovic, N.-X. Hu, A.-M. Hor, G. Xu. *Phys. Status Solidi A - Appl. Res.*, **283** (1999) 1900–1902.

[178] Y. Hamada, T. Sano, K. Shibata, K. Kuroki. *Jpn. J. Appl. Phys. Pt. 2*, **34** (1995) L824–L826.

[179] G. Sakamoto, C. Adachi, T. Koyama, Y. Taniguchi, C.D. Merritt, H. Murata, Z.H. Kafafi. *Appl. Phys. Lett.*, **75** (1999) 766–768.

[180] K. Yamashita, J. Futenma, T. Mori, T. Mizutani. *Synthet. Metal.*, **111** (2000) 87–90.

[181] Y. Hamada, H. Kanno, T. Tsujioka, H. Takahashi, T. Usuki. *Appl. Phys. Lett.*, **75** (1999) 1682–1684.

[182] D. Ammermann, A. Böhler, J. Schöbel, W. Kowalsky. Device structures and materials for organic light emitting diodes. In *Annual Report 1996*, p. 9–23. Braunschweig, 1996.

[183] T. Wakimoto. Organic electroluminescent cells with high luminous efficiency. In S. Miyata, H.S. Nalwa, Editor, *Organic electroluminescent materials and devices*, p. 289–310. Gordon and Breach Science Publishers, Amsterdam, 1997.

[184] A. Nollau, M. Pfeiffer, T. Fritz, K. Leo. *J. Appl. Phys.*, **87** (2000) 4340–4343.

[185] G. Parthasarathy, C. Adachi, P.E. Burrows, S.R. Forrest. *Appl. Phys. Lett.*, **76** (2000) 2128–2130.

[186] A. Werner. *private communication*. 2001.

[187] G. Parthasarathy, C. Shen, A. Kahn, S.R. Forrest. *J. Appl. Phys.*, **89** (2001) 4986–4992.

[188] P.E. Burrows, V. Bulovic, S.R. Forrest, L.S. Sapochak, D.M.McCarthy, M.E. Thompson. *Appl. Phys. Lett.*, **65** (1994) 2922–2924.

[189] M. Schaer, F. Nesch, D. Berner, W. Leo, L. Zuppiroli. *Adv. Funct. Mater.*, **11** (2001) 116–121.

[190] S.F. Lim, L. Ke, W. Wang, S.J. Chua. *Appl. Phys. Lett.*, **78** (2001) 2116–2118.

[191] J.S. Kim, R.H. Friend, F. Cacialli. *Appl. Phys. Lett.*, **74** (1999) 3084–3086.

[192] P.E. Burrows, S.R. Forrest, T.X. Zhou, L. Michalski. *Appl. Phys. Lett.*, **76** (2000) 2493–2495.

[193] V.G. Kozlov, V. Bulovic, P.E. Burrows, M. Baldo, V.B. Khalfin, G. Parthasarathy, S.R. Forrest, Y. You, M.E. Thompson. *J. Appl. Phys.*, **84** (1998) 4096–4108.

[194] N. Tessler, P.K.H. Ho, V. Cleave, D.J. Pinner, R.H. Friend, G. Yahioglu, P. Le Barry, J. Gray, M. de Souza, G. Rumbles. *Thin Solid Films*, **363** (2000) 64–67.

[195] F. Rohlfing, T. Yamada, T. Tsutsui. *J. Appl. Phys.*, **86** (1999) 4978–4984.

[196] T. Yamada, F. Rohlfing, T. Tsutsui. *Jpn. J. Appl. Phys. Pt. 1*, **39** (2000) 1382–1386.

[197] M. Hiramoto, K. Koyama, K. Nakayama, M. Yokoyama. *Appl. Phys. Lett.*, **76** (2000) 1336–1338.

[198] G.G. Malliaras, J.R. Salem, P.J. Brock, J.C. Scott. *J. Appl. Phys.*, **84** (1998) 1583–1587.

[199] X. Wei, M. Raikh, Z.V. Vardeny, Y. Yang, D. Moses. *Phys. Rev. B - Condensed Matter*, **49** (1994) 17480–17483.

[200] H. Bässler. *Phys. Status Solidi B - Basic Res.*, **175** (1993) 15–56.

[201] H. Bässler. *Phys. Status Solidi B - Basic Res.*, **107** (1981) 9–54.

[202] S.A. Visser, W.T. Gruenbaum, E.H. Magin, P.M. Borsenberger. *Chem. Phys.*, **240** (1999) 197–203.

[203] V.I. Arkhipov, U. Wolf, H. Bässler. *Phys. Rev. B - Condensed Matter*, **59** (1999) 7514–7520.

[204] J. Staudigel, M. Stössel, F. Steuber, J. Simmerer. *Appl. Phys. Lett.*, **75** (1999) 217–219.

[205] J. Staudigel, M. Stößel, F. Steuber, J. Blässing, J. Simmerer. *Synthet. Metal.*, **111-112** (2000) 69–73.

[206] A.J. Campbell, D.D.C. Bradley, H. Antoniadis, M. Inbasekaran, W.W. Wu, E.P. Wo. *Appl. Phys. Lett.*, **76** (2000) 1734–1736.

[207] E.H. Magin, P.M. Borsenberger. *J. Appl. Phys.*, **73** (1993) 787–791.

[208] T. Mühl. *Transiente Photostrommessungen an dünnen Schichten aus organischen Halbleitermaterialien*. Diplomarbeit, TU Dresden, 1996.

[209] U. Bach, K. De Cloedt, H. Spreitzer, M. Graetzel. *Adv. Mater.*, **12** (2000) 1060–1063.

[210] S. Barth, P. Müller, H. Riel, P.F. Seidler, W. Rieß, H. Vestweber, H. Bässler. *J. Appl. Phys.*, **89** (2001) 3711–3719.

[211] H.C.F. Martens, H.B. Brom, P.W.M. Blom. *Phys. Rev. B - Condensed Matter*, **60** (1999) R8489–R8492.

[212] H.C.F. Martens, J.N. Huiberts, P.W.M. Blom. *Appl. Phys. Lett.*, **77** (2000) 1852–1854.

[213] F. Garnier, G. Horowitz, X.Z. Peng, D. Fichou. *Synthet. Metal.*, **45** (1991) 163–171.

[214] G.G. Malliaras, J.S. Scott. *J. Appl. Phys.*, **83** (1998) 5399–5403.

[215] U. Wolf, S. Barth, H. Bässler. *Appl. Phys. Lett.*, **75** (1999) 2035–2037.

[216] I. D. Parker. *J. Appl. Phys.*, **75** (1994) 1656–1666.

[217] P.W.M. Blom, M.J.M. deJong, S. Breedijk. *Appl. Phys. Lett.*, **71** (1997) 930–932.

[218] L. Bozano, S.A. Carter, J.C. Scott, G.G. Malliaras, P.J. Brock. *Appl. Phys. Lett.*, **74** (1999) 1132–1134.

[219] A.J. Campbell, D.D.C. Bradley, D.G. Lidzey. *J. Appl. Phys.*, **82** (1997) 6326–6342.

[220] A. Werner, J. Blochwitz, M. Pfeiffer, K. Leo. *J. Appl. Phys.*, (2001) accepted.

[221] V.E. Choong, Y. Park, Y. Gao, T. Wehrmeister, K. Müllen, B.R. Hsieh, C.W. Tang. *J. Vac. Sci. Technol. A*, **15** (1997) 1745–1749.

[222] H.R. Kerp, E.E. van Faassen. *Phys. Chem. Chem. Phys.*, **1** (1999) 1761–1763.

[223] K.A. Neyts. *J. Opt. Soc. Am. A - Opt. Image Sci.*, **15** (1998) 962–971.

[224] N. Tessler. *Appl. Phys. Lett.*, **77** (2000) 1897–1899.

[225] G. Gu, D.Z. Garbuzov, P.E. Burrows, S. Venkatesh, S.R. Forrest, M.E. Thompson. *Optics Letters*, **22** (1997) 396–398.

[226] C.F. Madigan, M.-H. Lu, J.C. Sturm. *Appl. Phys. Lett.*, **76** (2000) 1650–1652.

[227] K.B. Kahen. *Appl. Phys. Lett.*, **78** (2001) 1649–1651.

[228] D.F. O'Brien, M.A. Baldo, M.E. Thompson, S.R. Forrest. *Appl. Phys. Lett.*, **74** (1999) 442–444.

[229] U. Wolf, V.I. Arkhipov, H. Bässler. *Phys. Rev. B - Condensed Matter*, **59** (1999) 7507–7513.

[230] I.H. Campbell, P.S. Davids, D.L. Smith, N.N. Barashkov, J.P. Ferraris. *Appl. Phys. Lett.*, **72** (1998) 1863–1865.

[231] J.C. Scott, G.G. Malliaras. *Chem. Phys. Lett.*, **299** (1999) 115–119.

[232] V.I. Arkhipov, E.V. Emelianova, Y.H. Tak, H. Bässler. *J. Appl. Phys.*, **84** (1998) 848–856.

[233] S. Barth, P. Müller, H. Riel, P.F. Seidler, W. Riess, H. Vestweber, U. Wolf, H. Bässler. *Synthet. Metal.*, **111** (2000) 327–330.

List of the most important mathematical symbols and abbreviations

Alq_3	aluminium-tris-(8-hydroxy-quinolate), emitter and electron transport material
BLh, BLe	blocking layer at the hole/electron side
c	speed of light (=3x10^{8}m/s)
c_{dop}	molar concentration of dopants in a matrix
CT	charge transfer
d_h	hopping distance or intermolecular distance in an organic layer
DOS	distribution of states
e	elementary charge (1.602x10^{-19} C)
E_a	energy level of the anode
E_A	energy level of an acceptor state
E_B	binding energy of a CT-complex
E_c	energy level of the cathode
E_e	electron transport level or radiometric irradiance in W/m^2
E_F	Fermi level energy
E_g	gap energy of a semiconductor
E_h	hole transport level
$E_{t,p}$	hole trap depths with respect to the transport level
$E_{et,p}$	HOMO position of an emitter trap with respect to the transport level
EL	electroluminescence
E_{vac}	vacuum energy level
EIL	electron injection layer
EML	emission layer
ETL	electron transport layer
ϵ_0	dielectric constant of vacuum (8.85x10^{-12} As/Vm)
ϵ	relative dielectric constant of a material
F	electric field
FN	Fowler-Nordheim (tunneling)
F_4-TCNQ	2,3,5,6-tetrafluoro-7,7,8,8-tetracyano-quinodimethane, acceptor molecule
FTIR	Fourier transformed infrared (spectroscopy)
$\phi(\lambda)$	emission spectra of an OLED
Φ	potential barrier for charge injection
Φ_e	radiant flux in Watts
Φ_V	luminous flux in Lumens
γ	Langevin recombination rate
h	$h = 6.626$x10^{-34} Js is the Planck action constant
HIL	hole injection layer
HTL	hole transport layer
HOMO	highest occupied molecular orbital
$I_{V,0}$	luminous intensity in forward direction (in cd)
ITO	indium tin oxide - the prototypical transparent anode material
j	current density
K	Förster energy transfer rate
K_m	radiometric-photometric conversion constant (=683lm/W)
K_r	radiometric-photometric conversion efficacy
K_S	system luminous efficacy in lm/W
k_B	Boltzmann constant (1.381x10^{-23} J/K=8.62x10^{-5} eV/K)

L	total organic layer thickness of an OLED
$L_{V,0}$	luminance in forward direction (in cd/m^2)
λ	wavelength
LED	light emitting diode
Li, LiF	lithium, lithium-fluoride
LUMO	lowest unoccupied molecular orbital
$\mu_{p,n}$	mobility of charge carriers (holes or electrons)
n	density of electrons or index of refraction
n_f, n_t	free and trapped electron density
$n_{f,0}$, $n_{t,0}$	equilibrium free and trapped electron density
n_{et}	density of occupied LUMO-states of the emitter dopant (per volume)
$N_{A,D}$	density of acceptor/donator molecules (per volume)
$N_{HOMO,h}$	density of hole transport states (per volume)
N_μ	density of the relevant free charge carrier states (per volume)
$N_{t,p}$	density of hole traps (per volume)
N_{et}	density of emitter traps (per volume)
η_c	current efficiency of an OLED in cd/A
η_P	luminous or power efficiency of an OLED in lm/W
η_o	outcoupling efficiency
η_Q	quantum efficiency of an OLED in %
OLED	organic light emitting diode
p	density of holes
p_f, p_t	free and trapped hole density
$p_{f,0}$, $p_{t,0}$	equilibrium free and trapped hole density
p_{et}	density of occupied HOMO-states of the emitter dopant (per volume)
Pc's	phthalocyanines
PEDOT:PSS	poly(3,4-ethylenedioxythiophene):poly(4-styrenesulfonate)
PLED	polymer light emitting diode
PPV	poly(para-phenylene-vinylene), a typical emitter material in PLEDs
QAD	quinacridone, an emitter dopant molecule
RS	Richardson-Schottky (injection)
s	singlet exciton density
S	total internal light emission or Seebeck coefficient
SCL	space charge limited (current)
σ	conductivity or energetic disorder parameter
Σ	spatial disorder parameter
sr	steradian, unit of solid angle
t	time
T	absolute temperature
TCL	trap charge limited (current)
TFL	trap filled limit
TPD	tri-phenyl-diamine, a typical hole transport material
τ_s	singlet exciton lifetime
UPS	ultraviolet photoelectron spectroscopy
V, V_{bi}	voltage, built-in voltage of a diode
$v_{drift,diff}$	drift or diffusion velocity of charge carriers
V_{see}	Seebeck voltage
VOPc, ZnPc	vanadyl-phthalocyanine, zinc-phthalocyanine
XPS	X-ray photoelectron spectroscopy
Z	degree of charge transfer

Acknowledgements

First of all, I want to thank all the people and inanimate stuff that gives the 'Institut für Angewandte Photophysik' such a nice and pleasant atmosphere. It was - and it still is - a pleasure for me to work here.

In more detail, I want to thank my supervisor Prof. Karl Leo for his constant help and support with both scientific and organizational problems. It were his outstanding skills and courage in collecting money for the institute what made this work possible. I want to thank Dr. Martin Pfeiffer for his help to catch up with the theory of organic semiconductors, his 'stand by' help in every suddenly strange situation, only appearing too often if one works experimentally, and for our outstanding co-operation over the last 3 years. I would like to thank Dr. Torsten Fritz for being the best group-leader i can imagine and for helping me with at least some of the 'English problems' in his direct and friendship way. We all had the vision of doing a good job in the field of organic semiconductors and devices. Pleasingly enough, our work is now earning growing attention by the community.

The new 'UFO-system' would have not been possible without the efforts of all people working with it, as there are Ansgar Werner (thanks also for helpful discussions on technical and physical problems; you have been a nice guy to share the room with), Jens Drechsel, Maik Koch (it was a great pleasure to see you handle some UFO-'catastrophes'), and all others. Naturally, I also would like to thank all people from Bestec for the construction and delivery of a good working tool and Volker Trepte for his outstanding mechanical work in his little basement workshop.

For helping me out with the OLED experiments with TDATA in the old vacuum chambers i want to thank Dr. Xiang Zhou from the P.R. of China. For optimization of our OLED structures, Michael Hofmann deserves my greatest thanks (I still owe you a bottle of wine, you know). Thank you, Katja Floreck, for help with the AFM imaging, and you, Birk Plönnigs, for doing most of the FTIR experiments.

It was a great pleasure for me to have the opportunity to carry out the UPS/XPS-experiments in Tucson, Arizona. My gratitude goes to Dana, Paul, Prof. Neal Armstrong, and all the others for their plentiful scientific and technical support; the warmness of their welcome were only exceeded by the hotness of the desert.

Because i do not want to write endless acknowledgements - even I should probably do so - now only short thanks to all of the following: Kai Schmidt and Sven (the computer anti-trouble task force), Eva Schmidt (the good spirit of the institute), Tobias, Ben and Holger (hanging around in the cafeteria makes the head free for further lab experiences), Silke and Annette (sorry for some mess I caused), Andreas, Hartmut Fröb, Prof. Lukas Eng (for electronic support), and Stefan Grafström. I surely forget some, thanks to them, too. Still, there are people not belonging to our institute I'm surely indebted to. To name just a few of them: Prof. Dr. Kowalsky (Braunschweig) for providing us with the first OLED wide gap materials and Dr. Martin Knupfer for fruitful discussions about UPS/XPS.

I gratefully acknowledge the financial support by the 'Freistaat Sachsen' which provide

me with a 'Graduiertenstipendium'. For help in arranging additional financial support I thank J. Amelung from the 'Fraunhofer Intitut für mikroelektronische Schaltungen' in Dresden.

My scientific work would not have been possible without familiar and friendship background. Thus, thanks to my parents for all they have done. Finally, Anikke, thank you for your love and your ability to bring me back from work to real live.